THE UNIVERSITY OF CHICAGO

TRANSIENT TERRESTRIAL PLANET HABITABILITY: INSIGHTS FROM MODELS AND MEASUREMENTS OF MARTIAN CRATERS AND THE EVOLUTION OF VENUS' ATMOSPHERE

A DISSERTATION SUBMITTED TO
THE FACULTY OF THE DIVISION OF THE PHYSICAL SCIENCES
IN CANDIDACY FOR THE DEGREE OF
DOCTOR OF PHILOSOPHY

DEPARTMENT OF THE GEOPHYSICAL SCIENCES

BY
ALEXANDRA OKSANA WARREN

CHICAGO, ILLINOIS
AUGUST 2023

Copyright © 2023 by Alexandra Oksana Warren

All Rights Reserved

This dissertation is dedicated to my cats, Nook and Tishka, who reminded me that no sentence, thought, or line of code is ever more important than dinner.

"You never really summon all of your strength until you know that there's no way back, no way to go but onward." — Kim Stanley Robinson, Red Mars

TABLE OF CONTENTS

LIST OF FIGURES viii

LIST OF TABLES xi

ACKNOWLEDGMENTS xii

ABSTRACT xiii

1 INTRODUCTION 1

I MARS

2 THROUGH THE THICK AND THIN: NEW CONSTRAINTS ON MARS PALEO-PRESSURE HISTORY 3.8 - 4 GA FROM SMALL EXHUMED CRATERS . . . 12
- 2.1 Abstract 12
- 2.2 Introduction 13
- 2.3 Geological Context 17
  - 2.3.1 Mawrth Phyllosilicates 17
  - 2.3.2 Meridiani Planum 20
- 2.4 Method 21
  - 2.4.1 Crater Counts 21
  - 2.4.2 Model 23
- 2.5 Results 30
- 2.6 Discussion 31
  - 2.6.1 Modification of CSFDs over geologic time: sedimentation, erosion, and changes in impactor population 34
  - 2.6.2 Constant and time-varying atmospheric pressure both fit data 38
  - 2.6.3 Single-site atmospheric pressure upper limits are globally representative 45
- 2.7 Integrating new constraints with existing data using a 2-component atmospheric evolution model 49
- 2.8 Conclusions 55

3 OVERSPILLING SMALL CRATERS ON A DRY MARS: INSIGHTS FROM BREACH EROSION MODELING 58
- 3.1 Abstract 59
- 3.2 Introduction 60
- 3.3 Methods 62
  - 3.3.1 Breach Erosion Model 63
- 3.4 Results 70
  - 3.4.1 Mars Tadpole Craters: Measurements & Implications 70
  - 3.4.2 Application of the Model to Terrestrial Breaching Events 71
- 3.5 Runaway Erosion: Predicted but not observed 75

3.5.1 Sediment transport on steep slopes . . . 76
3.5.2 Barriers to crater rim erosion . . . 77
3.5.3 Pre-event vs. measured breach morphology . . . 79
3.6 Are all tadpole craters consistent with a single overspill event? . . . 81
3.6.1 Climate Tadpole Crater Overspill Scenarios . . . 82
3.6.2 Groundwater Tadpole Crater Overspill Scenarios . . . 85
3.7 Conclusions . . . 87

4 MULTIPLE OVERSPILL FLOOD CHANNELS FROM YOUNG CRATERS REQUIRE SURFACE MELTING AND HUNDREDS OF METERS OF MID-LATITUDE ICE LATE IN MARS HISTORY . . . 89
4.1 Abstract . . . 89
4.2 Introduction . . . 90
4.3 Tadpole Crater Distribution and Geomorphology . . . 96
4.3.1 Tadpole crater dataset . . . 96
4.3.2 Tadpole crater DEMs . . . 103
4.4 Subaerial Overspill . . . 115
4.4.1 Water-filled crater . . . 115
4.4.2 Ice-filled crater . . . 125
4.5 Subglacial Overspill . . . 131
4.5.1 Water Volume . . . 131
4.5.2 Ice Sheet Slope . . . 133
4.5.3 Water Sources for Subglacial Flow . . . 135
4.6 Discussion . . . 141
4.6.1 Terrestrial analogs . . . 141
4.7 Conclusions . . . 146

II VENUS

5 NARROW RANGE OF EARLY HABITABLE VENUS SCENARIOS PERMITTED BY MODELING OF OXYGEN LOSS AND RADIOGENIC ARGON DEGASSING 151
5.1 Abstract . . . 151
5.2 Introduction . . . 152
5.3 Oxygen Loss Model . . . 155
5.3.1 Initial Conditions . . . 158
5.3.2 Runaway Greenhouse . . . 159
5.3.3 Atmospheric Escape . . . 162
5.3.4 Degassing . . . 166
5.3.5 Oxidation of basalt . . . 170
5.4 Argon Degassing Model . . . 172
5.5 Results . . . 177
5.5.1 Oxygen Loss Model . . . 177
5.5.2 Argon Degassing Model . . . 181
5.6 Discussion . . . 186

5.6.1 Habitable Era Water Recycling . . . 186
5.6.2 Limitations . . . 193
5.6.3 Implications for upcoming Venus missions . . . 196
5.7 Conclusions . . . 197

6 SYNTHESIS . . . 199

REFERENCES . . . 202

A SUPPLEMENTARY INFORMATION FOR CHAPTER 2 . . . 241
A.1 Fitting Procedure . . . 241
A.2 Synthetic time-varying, modified cumulative size frequency distributions . . . 242

B SUPPLEMENTARY INFORMATION FOR CHAPTER 3 . . . 245
B.1 Justification of Model Assumptions . . . 245
B.2 Supplementary Tables . . . 247

C SUPPLEMENTARY INFORMATION FOR CHAPTER 4 . . . 248
C.1 Groundwater Model Output . . . 248
C.2 Pond Overspill Model Output . . . 249

D SUPPLEMENTARY INFORMATION FOR CHAPTER 5 . . . 252
D.1 Oxygen loss model . . . 252
D.1.1 Crustal production upper limit . . . 252
D.1.2 Runaway Greenhouse Surface Temperature . . . 252
D.1.3 Drag of Heavy Species During H Escape . . . 253
D.1.4 Explosive Volcanism . . . 254
D.2 Supplementary Figures . . . 256

LIST OF FIGURES

1.1 Venus and Mars in the context of the habitable zone for planets with CO_2, H_2O, and N_2 atmospheres. . . . 2
1.2 Schematic illustration of a planetary geochemical evolution model. . . . 5
1.3 Geologic record of surface liquid water on Mars. . . . 6

2.1 Schematic illustration of cratering process for impactors passing through thin and thick atmospheres. . . . 16
2.2 Global and local context for Mawrth Vallis and Meridiani Planum study sites. . 17
2.3 Examples of ancient craters in the 2 main units in our Mawrth Vallis site. . . . 19
2.4 Sedimentary features at Meridiani site. . . . 21
2.5 Example ancient embedded craters on Mawrth paleosurface. . . . 24
2.6 Fits of measured crater size frequency distributions to synthetic data from atmosphere-impactor interaction model. . . . 32
2.7 Updated paleopressure constraints for Mars showing our new upper limits in context. . . . 33
2.8 Schematic illustrating the effect that depositional and erosional processes have on cumulative size frequency distribution shape. . . . 35
2.9 Model crater size frequency distributions produced by variations in atmospheric pressure and preferential obliteration of small craters. . . . 39
2.10 Comparison of measured cumulative size frequency distributions to synthetic distributions for varying atmospheric pressures and preferential obliteration of small craters. . . . 41
2.11 Comparison of measured cumulative size frequency distributions to synthetic distributions for varying atmospheric pressures and preferential obliteration of small craters. . . . 42
2.12 Minimum time needed for the observed number of craters in the diameter bin 15.6-22.1 m to accumulate as a function of minimum atmospheric pressure. . . . 44
2.13 Schematic illustrating three atmospheric pressure histories for Mars between $\sim$4 Ga and 3.8$\pm$0.2 Ga. . . . 46
2.14 Solution density contour plots of pressure histories allowed by existing paleopressure estimates from our basic, 2-component atmospheric evolution model. . . . 52
2.15 Schematic illustration of one possible pressure history for Mars that satisfies all existing paleopressure constraints. . . . 57

3.1 Tadpole crater HiRISE Digital Elevation Models and global context. . . . 62
3.2 Schematic illustration of preferred tadpole crater overspill mechanisms. . . . 63
3.3 Schematic illustration of crater breach erosion model and breach cross section. . 66
3.4 Lake size relative to outlet valley length plotted against valley width and steepness for tadpole craters and terrestrial analogues. . . . 72
3.5 Model-predicted evolution of transport stage and erosion rate. . . . 74
3.6 Measured tadpole crater exit breach depth vs. crater diameter. . . . 79

3.7 Water flux into the crater per unit lake area and required duration to erode observed breach depth. 83

4.1 Digital Elevation Models and topographic rim profiles of multiple breach tadpole craters. 93
4.2 Sketch of four overspilling mechanisms for tadpole craters. 95
4.3 Map of reliable tadpole craters overlaid on MOLA topography. 96
4.4 Percentage of craters in each degradation state classification that are single and multiple breach tadpole craters. 98
4.5 Histograms of proportions of all craters that are tadpole craters as a function of diameter. 100
4.6 Histograms of proportions of all craters that are tadpole craters as a function of MOLA elevation and residual topography for a range of smoothing radii. 105
4.7 Digital Elevation Models of multiple breach tadpole craters showing measurement areas for other figures. 107
4.8 HiRISE imagery of crater floor fill interpreted as crater-filling ice. 111
4.9 HiRISE imagery of unincised portions of multiple breach crater rims showing rim textures and topographic rim profiles. 113
4.10 HiRISE imagery of crater rim breaches infilled with discontinuous material resembling crater-filling ice-rich deposits and downstream topographic profiles of breaches. 115
4.11 Sketch illustrating simultaneous erosion of multiple rim breaches in a water-filled crater compared to topographic rim profile of *Hellas* multiple breach tadpole crater. 118
4.12 Schematic illustration of a retreating ice sheet progressively exposing lower rim topography for breach formation. 122
4.13 Sketch illustrating our groundwater model. 123
4.14 Example time evolution of instantaneous and cumulative groundwater water fluxes into *Noachis* multiple breach tadpole crater. 127
4.15 Groundwater fluxes into *Arabia Terra 2* after 0.1 and 1 crater volumes of water have discharged into the crater. 128
4.16 Meltwater pond overspill modelling results for *Noachis*. 129
4.17 Sketch of 1D intrusion model, example evolution of vertical temperature profile, and total melt thicknesses generated in melting model. 138
4.18 Minimum required intrusion thickness as a function of intrusion depth. 141
4.19 Digital Elevation Model of Pingualuit Crater. 143
4.20 Sketch of the three remaining multiple breach tadpole crater forming mechanisms consistent with our morphological and modeling constraints on tadpole breach forming climate. 147

5.1 Schematic illustration of model for Venus' atmospheric evolution starting from the end of a hypothetical early habitable era. 157
5.2 Magmatism rates as a function of time in our model. 169
5.3 Schematic illustration of our ^{40}Ar degassing model based on: (Kaula, 1999; O'Rourke and Korenaga, 2015). 172

5.4 Time evolution of column masses of H_2O, H_2, O_2, CO_2, CO, and CH_4 for two post habitable era evolutions ending at different times. 179
5.5 Example evolution of column masses of H_2O and O_2 in baseline Venus oxygen loss model. 182
5.6 Example time evolution of atmospheric species in Venus oxygen loss model for variable melt oxygen fugacities. 183
5.7 Example atmospheric ^{40}Ar accumulation for a range of crustal production rates. 184
5.8 Percentage of model runs that end with atmospheric H_2O, O_2, and CO concentrations consistent with data for modern Venus. 187
5.9 Comparison of fraction of successful runs compatible with modern Venus atmosphere for models without runaway greenhouse melting, and with runaway greenhouse melting. 188
5.10 Steady-state pressure-temperature profiles for Venus lithosphere compared to phase boundaries for serpentinite dehydration and eclogite formation. 191

A.1 Synthetic cumulative size frequency distributions for Mawrth phyllosilicates. . . 242
A.2 Synthetic cumulative size frequency distributions for Meridiani. 243
A.3 Synthetic cumulative size frequency distributions for Meridiani for atmospheric pressures above calculated upper limits. 244

C.1 Groundwater flux into each multiple exit breach tadpole crater when 0.1 crater volumes of water have been discharged from the aquifer. 248
C.2 Meltwater pond overspill modelling results for *Arabia Terra 1*. 249
C.3 Meltwater pond overspill modelling results for *Arabia Terra 2*. 250
C.4 Meltwater pond overspill modelling results for *Hellas*. 251

D.1 Summary of ^{40}Ar degassing model results consistent with modern Venus atmosphere. 256
D.2 Example evolutions of habitable era water inventory. 257
D.3 Evolution of final and time-averaged habitable era water inventories on Venus. . 258
D.4 Example sensitivity tests for different values of the binary diffusion coefficient of hydrogen through the background atmosphere. 259
D.5 Example sensitivity tests for different values of top of the atmosphere temperature. 260

LIST OF TABLES

2.1 Image and DTM numbers for Mawrth Vallis and Merdiani Planum crater counting locations. . . . 18
2.2 Impact model parameters. . . . 27
2.3 Impact crater scaling parameters. . . . 29
2.4 Crater diameters and paleopressure upper limits from models and full fitting procedure. . . . 31

3.1 Digital Elevation Model numbers and locations. . . . 64
3.2 Measured tadpole crater exit breach parameters from Digital Elevation Models. 65

4.1 Summary of multiple breach tadpole craters investigated in this study. . . . 106
4.2 Breach measurements for each tadpole crater in this study. . . . 116
4.3 Modelling results for subaerial crater overspill mechanisms. . . . 120
4.4 Parameter values used for models of radial groundwater flow, ice melting above an intrusion, and overspill from a melt pond on the surface of an ice-filled crater. 126
4.5 Calculations for subglacial breach scenarios for all tadpole craters. . . . 134

5.1 Parameter values used in O_2 loss model. . . . 156
5.2 Parameter values used in ^{40}Ar degassing model. ^{a}Kaula 1999, ^{b}O'Rourke and Korenaga 2015, ^{c}Arevalo Jr et al. 2009 . . . 173

B.1 Compilation of potential tadpole crater terrestrial analogue data. . . . 247

D.1 Coefficient values used in calculation of surface temperature during runaway greenhouse. . . . 253

ACKNOWLEDGMENTS

Thank you to my advisor Edwin Kite for encouraging me to read widely, teaching me how to tell the difference between open doors and dead ends, and helping me to sculpt my science into the best (and most readable) version of itself. I would also like to thank my committee, Fred Ciesla and Douglas MacAyeal, for their time, wisdom, curiosity, and encouragement, even when my research ventured 70 million miles from the planet I originally told them I would be working on. I am grateful to my collaborators Briony Horgan, Jean-Pierre Williams, Sharon Wilson-Purdy, Samuel Holo, Alan Howard, and Axel Noblet for sharing the ideas and data without whom none of the work in this thesis would have been possible. I would also like to thank the NASA FINESST program for funding three years of my research, and GSA, NSF, AGU, and IAS for providing support for my attendance at so many conferences and workshops throughout my PhD.

I am endlessly grateful to Ben Austen, Benjamin Lytal, Rachen Cohen, and Kathleen Blackburn for welcoming me into their creative writing classrooms and helping me find and my voice for what I couldn't say in my academic papers. Thank you also to Louise Lerner, the Astrobites collaboration, the AAAS Mass Media Fellowship, Sarah Lewin-Frasier, and all of the editors at Scientific American for believing in the science writer behind the scientist.

Thank you mum, dad, and Misha, for trusting me enough to move halfway across the planet to do my own thing, and for always forgiving me when I left it too long between phone calls. To Annissa Zak, Carolyn Ashley, David Zak, Duncan Clark, Tim and Heather Ratigan, Quin McLaughlin, Ross Mansouri-Rad, and – of course – James Zak: there are no words for how grateful I am to you all. This thesis may be built from equations and citations, but you hold together every line.

ABSTRACT

If, when, and how other terrestrial planets were (or are) habitable is one of the primary foci of planetary science. The catalog of known planets around other stars has exploded in recent years, and there is more data than ever before that might be usable to determine whether any of these exoplanets are habitable or inhabited. The habitability of a planet through time – where habitable conditions are defined as those enabling surface liquid water to be present on the planet's surface – is the product of many interconnected processes spanning the core to the upper atmosphere. The abundance and resolution of data available for Mars and Venus make these the only planets besides the Earth where we can identify and interpret the geologic imprints of these processes and their resulting climates. In this thesis, I use Mars topographic data, measurements of Venus' atmospheric composition, statistical analysis, and numerical modeling to integrate proxies for past conditions on both planets into our understanding of their overall evolution. In the first part of this thesis, I focus on the climate record provided by Martian geomorphology. In Chapter 2, I compare the size distribution of ancient buried craters to impact model results to constrain atmospheric pressure during one of the wettest eras in Mars' history. In Chapters 3 and 4, I use measurements and models of valleys exiting small, relatively young craters with overspill channels but no visible inlets to constrain the volume of water needed to explain their formation under a range of climate conditions, and infer that Mars' climate has been ice-dominated but transiently and locally habitable for billions of years. In the second part of this thesis, I turn to the evolution of Venus as constrained by its modern atmospheric composition. I present models of bulk atmospheric composition and radiogenic argon degassing which I use to explore the narrow range of parameter space that enables a past habitable Venus to be reconciled with the planet's present, and make recommendations for future spacecraft observations that may reveal the likelihood of clement past conditions on Earth's sister planet.

CHAPTER 1

INTRODUCTION

Of the four terrestrial planets in our Solar System, the Earth is the only one currently known to have surface conditions suitable for life. Mercury hurtles around the Sun at a distance of only 0.39 AU and is too small to hold onto an atmosphere, rendering it largely desiccated and sterile since its formation (Schulze-Makuch and Irwin, 2018). The surface conditions of terrestrial planets in our Solar System today range from Mars' arid, frozen wasteland (Murphy and Koop, 2005) challenging for crewed and robotic mission design alike (e.g. Huntsberger et al. 2000) to Venus' hellish pressure cooker atmosphere that is downright murderous to spacecraft (Amato and Williams, 2015), let alone organisms. Despite these less-than-promising appearances, however, Venus and Mars both skim the edges of our solar system's "habitable zone," the just-right region around a star where planets with atmospheres primarily composed of CO_2, H_2O, and N_2 can have stable liquid water on their surfaces (e.g. Kasting et al. 1993; Hart 1979, Fig. 1.1).

Uncovering if, when, and how other terrestrial planets were (or are) habitable is one of the overarching goals in planetary sciences, as outlined in the 12 Priority Science Questions in the 2023-2032 Planetary Science Decadal Survey (National Academies of Sciences, 2022). Although the number and diversity of known terrestrial planets has exploded in recent years (e.g. Ostberg et al. 2023; Grimm, Simon L. et al. 2018; Petigura et al. 2013) with the James Webb Space Telescope (JWST) now enabling more detailed observations than ever before (e.g. Lustig-Yaeger et al. 2023; Whittaker et al. 2022), the relative accessibility of the terrestrial planets orbiting our own sun provides opportunities to study rocky planets more closely than is possible for distant exoplanets. More than half a century of observing both Mars and Venus has revealed complex geologic histories suggesting that one or both planets ventured into habitable states over the past 4.5 Gyrs (e.g. Kite 2019; Pollack 1971; Donahue et al. 1982; Pollack et al. 1987). The next step towards a more robust understanding of plane-

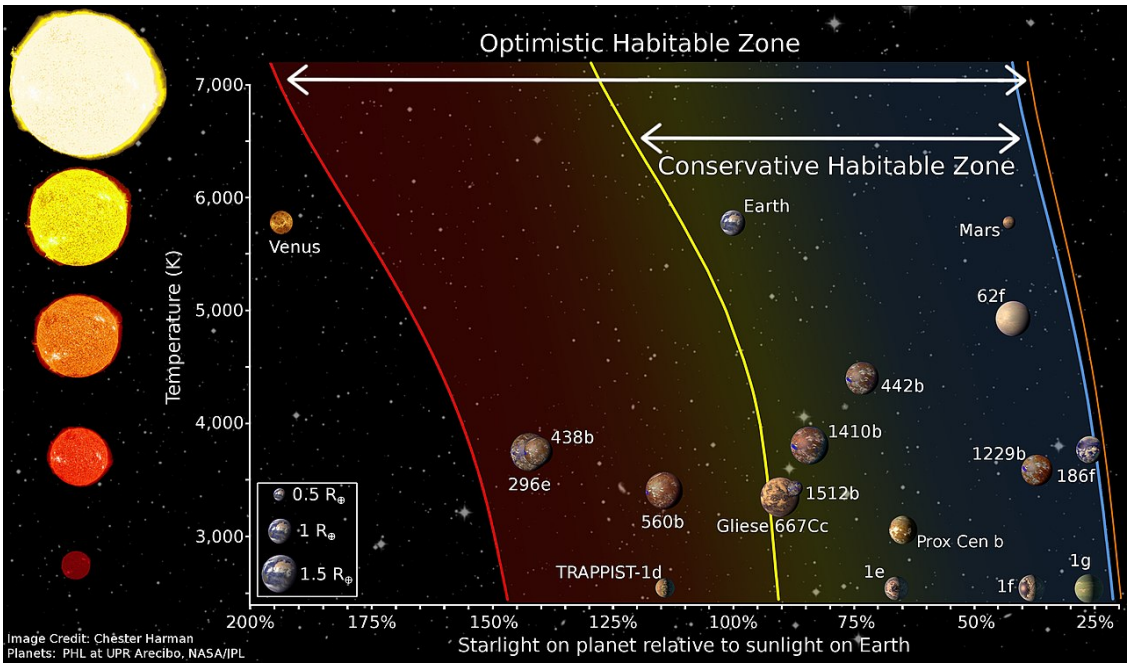

Figure 1.1: Illustration of the boundaries of the habitable zone for planets with CO_2, H_2O, and N_2 atmospheres orbiting different types of star, showing selected exoplanets, Solar System terrestrial planets, and past Mars and Venus. Y-axis shows temperature of host star surface. Blue curve indicates the outer edge of the "conservative" habitable zone where the CO_2 greenhouse effect can no longer maintain surface temperatures above freezing. Yellow curve indicates the inner edge of the conservative habitable zone where insolation is so strong it triggers a runaway greenhouse climate (Ingersoll, 1969). Red and orange curves indicate the bounds of the "optimistic" habitable zone, based on empirical evidence for past water on Mars and Venus (Kopparapu et al., 2013). Image credit: Chester Harman. Planets: Planetary Habitability Lab (PHL) at University of Puerto Rico (UPR) Arecibo, NASA/JPL.

tary habitability is to unravel the mechanisms that may have enabled clement conditions to arise on Mars and Venus, and understand why they disappeared (e.g. Ehlmann et al. 2016; Kane et al. 2019; Lasne 2021; Way et al. 2023). In this thesis, I use high-resolution imagery and topography data for Mars, measurements of Venus' atmospheric composition, statistical analysis, and numerical modeling to explore not only the likelihood of past surface liquid water on both planets at different times in their evolution, but also the processes that enabled or ended these habitable conditions.

Achieving habitable surface conditions on any planet – the Earth included – is a delicate balance between time-dependent, interrelated processes spanning the planet's core to its upper atmosphere (e.g. Lammer et al. 2009; Zahnle and Catling 2017; Noack et al. 2014; Meadows and Barnes 2018; Cockell et al. 2016, Fig. 1.2). Gas retained from the circumplanetary disc during formation (Saito and Kuramoto, 2017; Lammer et al., 2018), early degassing (e.g. from a magma ocean, (Elkins-Tanton, 2008; Lammer et al., 2013; Pahlevan et al., 2019)), continued volcanism (Phillips et al., 2001; Jakosky et al., 2018), impacts (Sakuraba et al., 2019), and metamorphic processes such as burial decarbonation (Foley and Smye, 2018; Pollack et al., 1987; Glotch and Rogers, 2013) can provide volatiles to planetary atmospheres. An atmosphere can then be modified by reactions between atmospheric constituents (Mills et al., 2021; Zahnle et al., 2008), escape of species to space (Gronoff et al., 2020; Chassefière et al., 2007; Dong et al., 2018; Tian, 2015a; Kulikov et al., 2006), impact erosion (Schlichting et al., 2015; Pham and Karatekin, 2016; Sakuraba et al., 2019), and interactions between the atmosphere and the surface (and oceans, if present), including carbonate formation (Stephens and Stevenson, 1990; Wray et al., 2016) and oxidation of fresh rock (Heard and Kite, 2020; Baker, 2017). These processes are modulated by factors like the planet's size (Kopparapu et al., 2014), composition and volatile inventory (Pepin, 2006; Horner et al., 2009; Bergin et al., 2015; Ciesla et al., 2015), tectonic regime (Foley, 2015; Kruijver et al., 2021; Jellinek and Jackson, Jellinek and Jackson; Way et al., 2023),

presence or absence of a magnetic field (Lundin et al., 2007; Brain et al., 2016), and the host star's type and evolution (Airapetian et al., 2020; Ramirez and Kaltenegger, 2014). Then, atmospheric dynamics determine the spatial distribution of volatiles on the surface and in the atmosphere (Kaspi and Showman, 2015; Nowajewski et al., 2018; Fastook et al., 2008; Wordsworth et al., 2013), the presence/absence of clouds (Kite et al., 2021; Yang et al., 2014, 2013), and the resulting energy balance that ultimately sets surface temperatures and whether surface water is stable anywhere on the planet (Hoffert et al., 1981), i.e. whether the planet is habitable at any given time.

The habitability of a planet through time, or its transient habitability, is a complicated function of all of these factors (Lammer et al., 2009; Zahnle and Catling, 2017; Kopparapu et al., 2014; Ehlmann et al., 2016), and perhaps more that haven't been identified yet. Planetary science is still in the early stages of narrowing down a recipe for habitability, and even which processes are most important (Ehlmann et al., 2016; Lasne, 2021); debates continue over the likelihood that distant exoplanets are habitable (Vida et al., 2017; Wolf, 2017; Vinson and Hansen, 2017), and which atmospheric gases might be reliable signatures of habitable and inhabited worlds (Krissansen-Totton et al., 2022; Zhan et al., 2021; Meadows et al., 2018). Fortunately, the processes that conspire to render a planet habitable – and to strip that habitability away – leave their mark. Water-logged sediments can lithify into rocks whose stratigraphy can be read, even from orbit (e.g. Grant et al. 2008; Grotzinger and Milliken 2012), and atmospheric escape processes can leave tell-tale combinations of species behind (e.g. Pepin 2006; Cassata et al. 2022; Hu et al. 2015; Donahue et al. 1982). Piecing together these records for the Earth, we can reconstruct one planetary history, and understand what has enabled the habitability of an Earth-sized planet 1 AU from its star for billions of years (Lunine, 2006; Mueller and Nutman, 2017). Until humans master interstellar travel, though, Mars and Venus are the only other planets where we have the abundance and resolution of data to do the same for two worlds more (Ehlmann et al., 2016; Kane et al.,

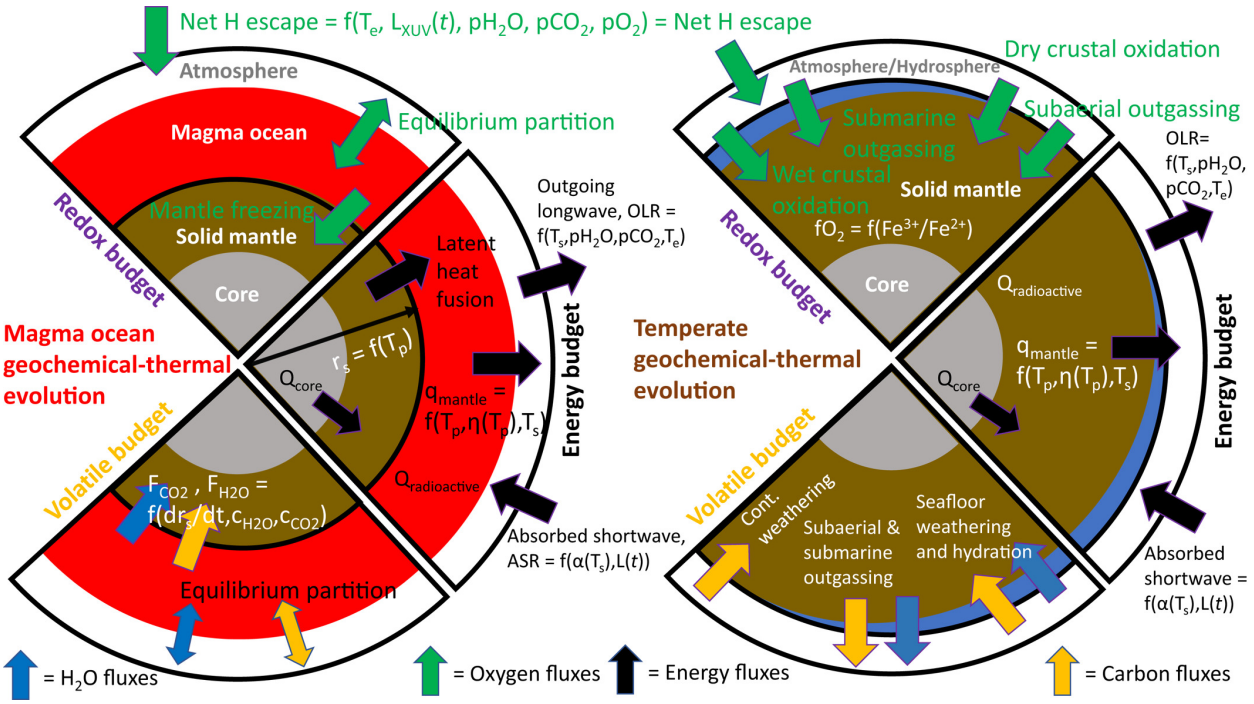

Figure 1.2: Reproduced from Fig. 1 in (Krissansen-Totton et al., 2021). Schematic illustration of a planetary geochemical evolution model showing some of the many processes that affect whether a planet is habitable. t is time, T_e is temperature in the upper atmosphere where escape is occuring, OLR is outgoing longwave radiation, T_s is surface temperature, T_p is mantle potential temperature, L_{XUV} is extreme ultraviolet (XUV) luminosity, L is solar luminosity, $p\mathrm{H_2O}/p\mathrm{CO_2}/p\mathrm{O_2}$ are partial pressure of $\mathrm{H_2O}/\mathrm{CO_2}/\mathrm{O_2}$ in the atmosphere, r_s is the solidified radius within the magma ocean, $F_{\mathrm{CO_2}}/F_{\mathrm{H_2O}}$ are mass fractions of $\mathrm{H_2}O/\mathrm{CO_2}$ in solid mantle, $c_{\mathrm{CO_2}}/c_{\mathrm{H_2O}}$ are concentrations of $\mathrm{H_2O}/\mathrm{CO_2}$ in the magma ocean melt, $f\mathrm{O_2}$ is mantle oxygen fugacity, $Q_{radioactive}$ is radiogenic heat production in the mantle, Q_{core} is heat flow from the metallic core, q_{mantle} is heat flow out of interior to the surface, η is mantle viscosity.

2019; Lasne, 2021; Way et al., 2023).

Without the rapid recycling provided by plate tectonics on Earth, Mars has preserved evidence for surface liquid water since as early as 4.1 Ga (Bottke and Andrews-Hanna, 2017; Nimmo and Tanaka, 2005), with earlier habitable conditions potentially recorded by ancient Martian meteorites (e.g. Moser et al. 2019). From the morphological features preserved on Mars' surface, the planet has experienced multiple periods in its history wet enough to form rivers and other fluvial features (Kite 2019, Fig. 1.3). The wettest of these is the Late Noachian to Early Hesperian Valley Network forming period (3.2-3.9 Ga) (Hartmann, 2005).

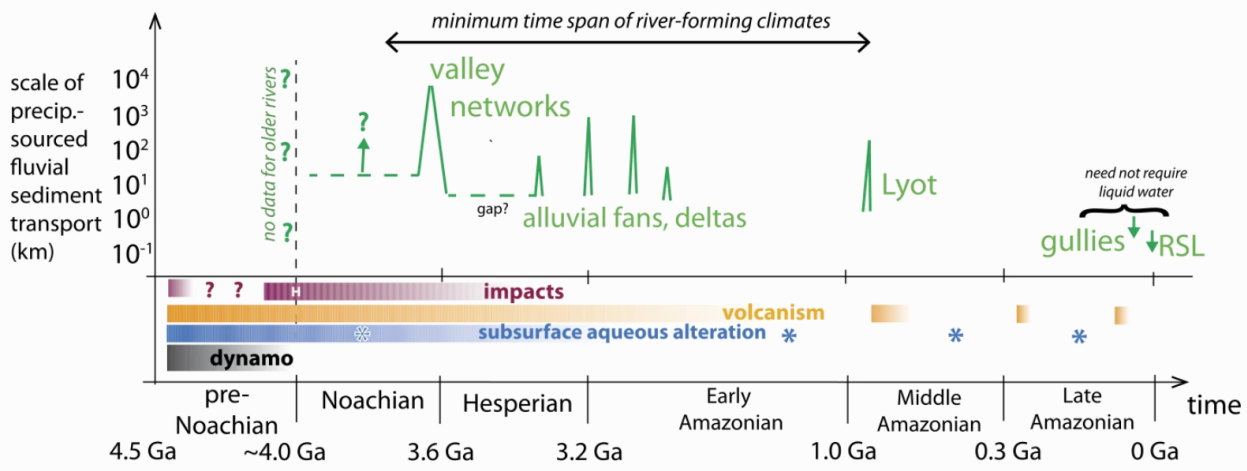

Figure 1.3: Reproduced from Fig. 1 in Kite (2019). Schematic summary of relative wetness in terms of column thickness of precipitation-sourced water required to explain observed fluvial features (y-axis) and timing (x-axis, not to scale) of river-forming climates on Mars. H indicates the Hellas basin forming impact event. *s indicate meteorite-based evidence for aqueous alteration. RSL - recurring slope lineae (McEwen et al., 2011).

During this time, surface water carved regionally-integrated river channels (Mangold et al., 2008; Moore et al., 2003; Fassett and Head, 2008), filled and overspilled crater lakes (Fassett and Head, 2005; Grotzinger et al., 2014; Morschhauser et al., 2011; Goudge et al., 2016), and may even have pooled in an ocean covering the entire northern hemisphere (di Achille and Hynek, 2010; Citron et al., 2018; Cardenas and Lamb, 2022). These wet periods have also been ground-truthed by rover observations in Gale Crater, which was host to a Late Noachian to Early Hesperian lake (or lakes) from around 3.6 to 3.2 Ga (e.g. Grotzinger et al. 2015, 2014; Palucis et al. 2016), and Jezero Crater, whose delta deposits record a deep lake environment and flood deposits 3.6-3.8 Gyr old (e.g. Mangold et al. 2021; Sun, Hand, Stack, Farley, Simon, Newman, Sharma, Liu, Wiens, Williams, Tosca, Alwmark, Beyssac, Brown, Calef, Cardarelli, Clavé, Cohen, Corpolongo, Czaja, Del Sesto, Fairen, Fornaro, Fouchet, Garczynski, Gupta, Herd, Hickman-Lewis, Horgan, Johnson, Kinch, Kizovski, Kronyak, Lange, Mandon, Milkovich, Moeller, Núñez, Paar, Pyrzak, Quantin-Nataf, Shuster, Siljestrom, Steele, Tice, Toupet, Udry, Vaughan, and Wogsland Sun et al.).

Mars' subsequent climate evolution shows evidence for a great drying from both orbital

and rover data (e.g. Kite and Noblet 2022; Rapin et al. 2021). This more arid period in Mars' history is etched onto the surface by features like alluvial fans and shallower valleys that become increasingly spatially patchy and require less and less water over time (Holo et al., 2021; Grant and Wilson, 2011; Kite et al., 2019; Wilson et al., 2021; Hauber et al., 2013).

The climate conditions implied by this multi-billion-year assortment of morphological features range from earlier Martian climates analogous to the Great Basin on Earth during the Pleistocene (Kite, 2019) to more arid climates like Western Nevada (Kite, 2019) and polar deserts like the Antarctic Dry Valleys (Head and Marchant, 2014), trending towards increasing aridity and spatial patchiness over time (Kite and Noblet, 2022). They all, however, require some amount of surface liquid water. At 1.5 AU from the Sun, the challenge for Mars is understanding how the planet warmed to at least 273 K to enable liquid water on its surface, particularly under a fainter young Sun (Haberle, 1998) – even the greenhouse warming from a multi-bar CO_2 atmosphere with the added warming provided by H_2O vapor at 100% relative humidity is insufficient for Mars to reach habitable temperatures (Wordsworth, 2016). So, other warming mechanisms have been proposed to explain the geology, including short-lived heating after impacts (e.g. Turbet et al. 2020; Toon et al. 1997; Palumbo and Head 2018) and non-CO_2 greenhouse warming by species including H_2, CH_4, SO_2, and clouds (Ramirez, 2017; Kite et al., 2017; Kerber et al., 2015; Kite et al., 2021; Madeleine et al., 2014).

Compared to Mars, the proposed evidence for past habitable conditions on Venus is sparse and hotly debated. Unfortunately for geomorphologists, Venus' surface has been completely refreshed by basaltic eruptions within the past 1 Gyr (Phillips et al., 1992; Bottke et al., 2016; Strom et al., 2005), with evidence for ongoing volcanism (Herrick and Hensley, 2023). Venus' early geologic record may be entirely lost to observations, or preserved only in snippets of older crust present in highly deformed tesserae (Byrne et al., 2020; Khawja et al.,

2020). However, the atmospheric record of Venusian evolution remains. Venus' elevated deuterium/hydrogen (D/H) ratio (around 150 times higher than that of the Earth) has been proposed to suggest escape of as much as an Earth ocean of water (around 3000 m GEL, Donahue et al. 1982; Kulikov et al. 2006), although this water need not necessarily have been present as a liquid water layer on the planet's surface (Grinspoon, 1993; Selsis et al., 2007). Additional support for past Venusian habitability has come from climate modeling studies (e.g. Way and Del Genio 2020; Krissansen-Totton et al. 2021), but the research community remains divided. Some authors argue that habitable conditions could have lasted until as recently as 0.7 Ga (e.g. Way and Del Genio 2020; Kasting 1988; Pollack 1971; Salvador et al. 2017), whereas others propose that liquid water may not have condensed on the planet's surface at any time since its formation (e.g. Gillmann et al. 2009; Hamano et al. 2013; Turbet et al. 2021).

At around 30 % closer to the Sun than the Earth, Venus faces the opposite problem to Mars: habitable conditions are only possible if Venus can reflect enough sunlight to prevent *too much* heating. Even a faint young Sun is insufficient to keep Venus' surface below 273 K as the planet would still have received around 40% higher insolation than the modern Earth (Lammer et al., 2008), triggering a "runaway greenhouse" effect (Ingersoll, 1969). During a runaway greenhouse, initial warming leads to increased evaporation of surface liquid water. The additional water vapor now in the atmosphere leads to further greenhouse warming, which leads to more evaporation, and an even stronger greenhouse effect. Eventually, this positive feedback effect evaporates all water on the planet into the atmosphere where photochemistry can fragment H_2O into its constituent H and O. As the H escapes to space, preventing H_2O from re-forming, the planet dries out permanently (Ingersoll, 1969; Kasting, 1988). To avoid runaway greenhouse conditions, researchers have invoked a global, high-albedo cloud deck to reflect solar radiation back into space (Way et al., 2016; Yang et al., 2014; Way and Del Genio, 2020). These models also appeal to an early

Venusian atmosphere much thinner than the present-day 93 bar, 95% CO_2 atmosphere to reduce the insulating greenhouse effect that keeps Venus's surface today above the melting point of lead.

However, the discovery of mechanisms that can generate habitable conditions on both Mars and Venus does not mean we understand planetary habitability. Modeled mechanisms, no matter how successful on paper, must be compatible with observations, and integrated into our understanding of a planet's long-term evolution. For example, was the atmospheric pressure during the wettest period in Mars' history high enough to increase the potency of CH_4 or H_2 as greenhouse gasses through collision-induced absorption (Turbet et al., 2019)? Or, if Venus had surface liquid water and a thin atmosphere until 0.7 Ga (Way and Del Genio, 2020), how could a mass of CO_2 equivalent to all the carbonate deposits on Earth today have made its way into the atmosphere?

In this thesis, I aim to integrate climate proxies from both Mars and Venus into our broader understanding of how these planets may have evolved over time. This thesis is divided into two parts. In the first part, I focus on Mars. In Chapter 2, I use the size distribution of small craters buried in ancient stratigraphy related to a wet environment on Mars to constrain atmospheric pressure at the time these sediments were being deposited. I build upon previous work using this paleopressure proxy (Kite et al., 2014) by measuring crater populations at two new sites, considering time-variable atmospheric pressures during sediment deposition, and by exploring atmospheric pressure histories for Mars compatible with known paleopressure constraints using a simplified, process-agnostic source vs. sink model of atmospheric pressure evolution from Mars formation to present. In Chapters 3 and 4, I use measurements and models of small craters with overspill channels eroded during the more recent, drier portion of Mars' record of surface liquid water to constrain the sources of water, and therefore the climate, when these features formed. In the second part, I turn to Venus. In Chapter 5 I use a novel model of Venus' bulk atmospheric composition to explore

the likelihood that Venus could have evolved from a habitable state to its modern thick, dry atmosphere without violating measurements of the modern atmospheric H_2O, O_2 and ^{40}Ar abundances. In addition to advancing our knowledge of Mars and Venus as individual planets, this work contributes towards the growing view of all terrestrial planets as complex systems whose habitability can – and should be expected to – vary both in space and in time.

Part I

Mars

CHAPTER 2

THROUGH THE THICK AND THIN: NEW CONSTRAINTS ON MARS PALEOPRESSURE HISTORY 3.8 - 4 GA FROM SMALL EXHUMED CRATERS

This chapter was originally published as: Warren, A. O., Kite, E. S. Williams, J-P., and Horgan, B. "Through the thick and thin: New constraints on Mars paleopressure history 3.8–4 Ga from small exhumed craters." *Journal of Geophysical Research: Planets* 124, no. 11 (2019): 2793-2818.

J-P.W. wrote the forward model of impactor-atmosphere interactions and provided model results to which measured crater populations were fitted. B.H. contributed CRISM-based mineralogic maps for distinguishing between different crater-bearing sedimentological units on Mars. E. S. K. provided MATLAB code for bootstrap fits of observed craters to impact model results, which a. O. W. modified and expanded. All authors contributed to editing the paper and the revisions.

2.1 Abstract

Mars' climate history depends in part on its atmospheric pressure evolution, but most existing constraints on atmospheric pressure are indirect. Thin atmospheres allow small objects to reach the surface and form impact craters, therefore ancient impact craters can constrain past atmospheric pressure. To identify ancient craters preserved in sedimentary rocks and exhumed by wind erosion we use HiRISE orthoimages, anaglyphs, and digital terrain models (DTMs). We compare measured crater populations from two sites to predictions from an atmosphere-impactor interaction model for atmospheres of different pressures. Our upper limits on continuous atmospheric pressure are 1.9 ± 0.1 bar around 4 Ga and 1.5 ± 0.1 bar at 3.8 ± 0.2 Ga. We demonstrate that atmospheric pressure cannot have been continuously

above these upper limits. During the interval 3.8 ± 0.2 Ga, our crater counts require that atmospheric pressure was less than 5% of Earth's modern pressure for at least 10^4 yrs, or at higher pressure for a correspondingly longer duration of time (at least $10^5 - 10^6$ yrs at 1.5 bar for our Mawrth phyllosilicates and Meridiani Planum data respectively). Therefore, atmospheric pressure around 4 Ga was either continuously 1.9 ± 0.1 bar, or varied between higher (> 1.9 bar) and lower (< 1.9 bar) pressures. Similarly, atmospheric pressure at 3.8 ± 0.2 Ga was either continuously 1.5 ± 0.1 bar, or varied between higher (> 1.5 bar) and lower (< 1.5 bar) pressures. Finally, we synthesize all available paleopressure estimates for early Mars to constrain a 2-component model of Mars' long-term atmospheric pressure evolution. In our model, atmospheric pressures < 1 bar early in Mars' history best fit existing paleopressure constraints.

2.2 Introduction

Changes in Mars' atmospheric pressure over time are an important control on climate evolution. Today, Mars' annual mean atmospheric pressure is 6 mbar. At these low atmospheric pressures, liquid water is not stable because it will boil at 273K and is frozen at lower temperatures (Murphy and Koop, 2005). During the Late Noachian (3.84-3.7 Ga) and Early Hesperian (3.7-3.4 Ga), however, there is abundant geologic evidence for liquid water on the surface of Mars including fluvial landforms (e.g. Mangold et al. 2008; Moore et al. 2003), lake deposits (e.g. Fassett and Head 2005; Grotzinger et al. 2014), and potentially a hemispheric ocean (e.g. di Achille and Hynek 2010; Citron et al. 2018; Oehler and Allen 2012). There is further evidence that the water that fed these lakes and channels was precipitation-derived (Hynek et al., 2010; Mangold et al., 2004; Ansan and Mangold, 2006). This implies that surface temperatures must have at least transiently reached 273K. Another important control on the stability of water at the Martian surface is evaporitic cooling (Hecht, 2002), which efficiently removes heat from ice that would otherwise melt at 273K, particularly at

low atmospheric pressures e.g. on the present day Martian surface. To achieve the required, elevated surface temperatures, models of early Mars climate invoke greenhouse warming by thick (1-2 bar), CO_2 atmospheres with some water vapor content (e.g. Haberle 1998; Wordsworth et al. 2013, 2015), or CO_2 atmospheres with some fraction of H_2, SO_2, or CH_4 (e.g. Ramirez et al. 2014; Wordsworth et al. 2017; Halevy and Head 2014; Kite et al. 2014). Paleopressure estimates throughout Martian history are therefore important for constraining the maximum pressure of the atmosphere available at any given time for greenhouse warming.

One basic upper limit on Martian atmospheric pressure is the pressure at which CO_2 would condense into ice. This process depends on the minimum temperature on Mars' surface. The lowest temperatures are found at high latitudes and high elevation, for example the South Pole and Tharsis Rise today. Using the relationship between elevation and latitude from Fastook and Head (2015), we can calculate the minimum temperature on the Martian surface during the deposition of various sedimentary units on Mars. The hydrous minerals observed at Mawrth Vallis require seasonal surface temperatures of at least 273K to form (Bishop and Rampe, 2016), possibly approaching 300K (Bishop et al., 2018). If Mawrth Vallis is assumed to be at an annual average temperature of 273K, this gives a minimum temperature at the South Pole of 240K. At this temperature, a $\sim$12 bar CO_2 atmosphere would need to exist for condensation into ice caps to occur (Bryson et al., 1974; Fernández-Fassnacht and Río, 1984). We can apply the same approach to the sinuous ridge (interpreted to be an inverted channel by Davis et al. 2016) observed at our Meridiani site. Observations from the Antarctic McMurdo Dry Valleys suggest that 255K is the lowest annual average temperature at which fluvial processes can occur (Marchant and Head, 2007; Head and Marchant, 2014). Assuming an annual average temperature of 255K at Meridiani, this gives a minimum temperature of 225K at the coldest point on Mars, which would require a $\sim$7 bar CO_2 atmosphere for condensation to occur. Here, we present results for each site that lower

these upper limits on atmospheric pressure by a factor of 5.

To make a direct estimate of atmospheric pressure during crater accumulation, we can use ancient crater populations embedded in Martian stratigraphy (Kite et al., 2014). The thickness and density of the atmosphere determine the minimum size of an impactor that can reach the planetary surface and form a hypervelocity impact crater (Tauber and Kirk, 1976). In a thinner atmosphere, a greater propotion of smaller objects will be able to reach the surface travelling at high velocities, producing more small impact craters (Fig. 2.1). Therefore, for the same impactor population, different atmospheric pressures will produce different CSFDs. For craters embedded in ancient Martian sedimentary rocks, the ratio of small to large craters records atmospheric pressure during deposition. We use a model of atmosphere-impactor interactions (Williams et al., 2014) to generate synthetic crater populations. We fit measured CSFDs from craters preserved in ancient sedimentary units to the expected CSFDs to find upper limits on continuous atmospheric pressure during the accumulation of crater populations in Mawrth Vallis and Meridiani Planum. In contrast to existing indirect paleopressure constraints from thermodynamic studies of mineral stability at the Martian surface (Hu et al., 2015; van Berk et al., 2012; Bristow et al., 2017), our upper limit is insensitive to atmospheric composition and surface temperature. This is important because modeling studies show that it is not possible to warm early Mars to 273K with a pure CO_2 atmosphere (Forget et al., 2013). A single site (e.g. Kite et al. 2014) is sufficient to get a global estimate of past atmospheric pressure. However, finding paleopressure estimates for sites of multiple ages gives us better temporal coverage of Martian atmospheric pressure evolution. Changes in atmospheric pressure may also occur during crater population accumulation. By considering the effect of different geologic processes on crater populations we establish 3 end-member scenarios for paleopressure evolution from $\sim$4-3.8 Ga constrained by our new results. To investigate Mars' paleopressure history as a whole, we integrate our new upper limits on continuous atmospheric pressure with existing

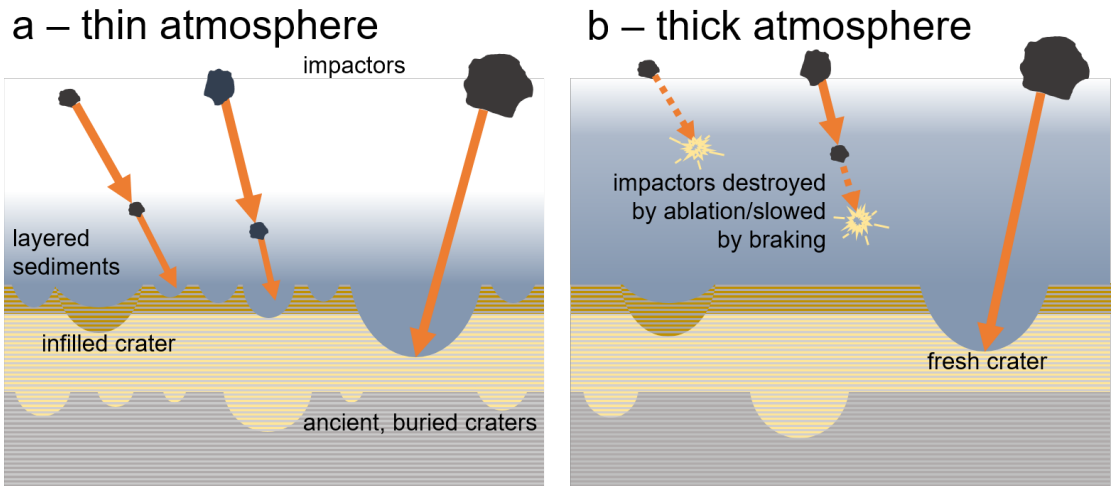

Figure 2.1: Schematic illustration of cratering due to impactors passing through a) a thin atmosphere, b) a thick atmosphere, also showing infill of ancient craters by layered sediments (example labelled"infilled crater"). The thin atmosphere case has a much higher proportion of smaller craters than the thick atmosphere case.

paleopressure estimates and use these to constrain a basic, 2-component model of Mars' atmospheric pressure evolution. Our model results highlight where new data is needed and motivate the search for new Martian paleopressure estimates, particularly between 3.6 Ga and present.

The remainder of this paper is organized as follows. Section 2.3 will describe the geological context of the sedimentary units that preserve the ancient crater populations we are interested in. Section 2.4 will describe our criteria for crater identification, and give a brief summary of our chosen atmosphere-impactor interaction model (Williams et al., 2014). Section 2.5 will summarize the results from fitting model-predicted CSFDs to our measured CSFDs and states our new upper limits on *constant* atmospheric pressure. Section 2.6 will discuss processes that can modify CSFDs, the effect of *time-varying* atmospheric pressure, and demonstrates that our results are globally-representative upper limits on continuous atmospheric pressure. In Section 2.7 we use a 2-component atmospheric evolution model to integrate our new paleopressure estimates with existing data. Section 2.8 will summarize our conclusions.

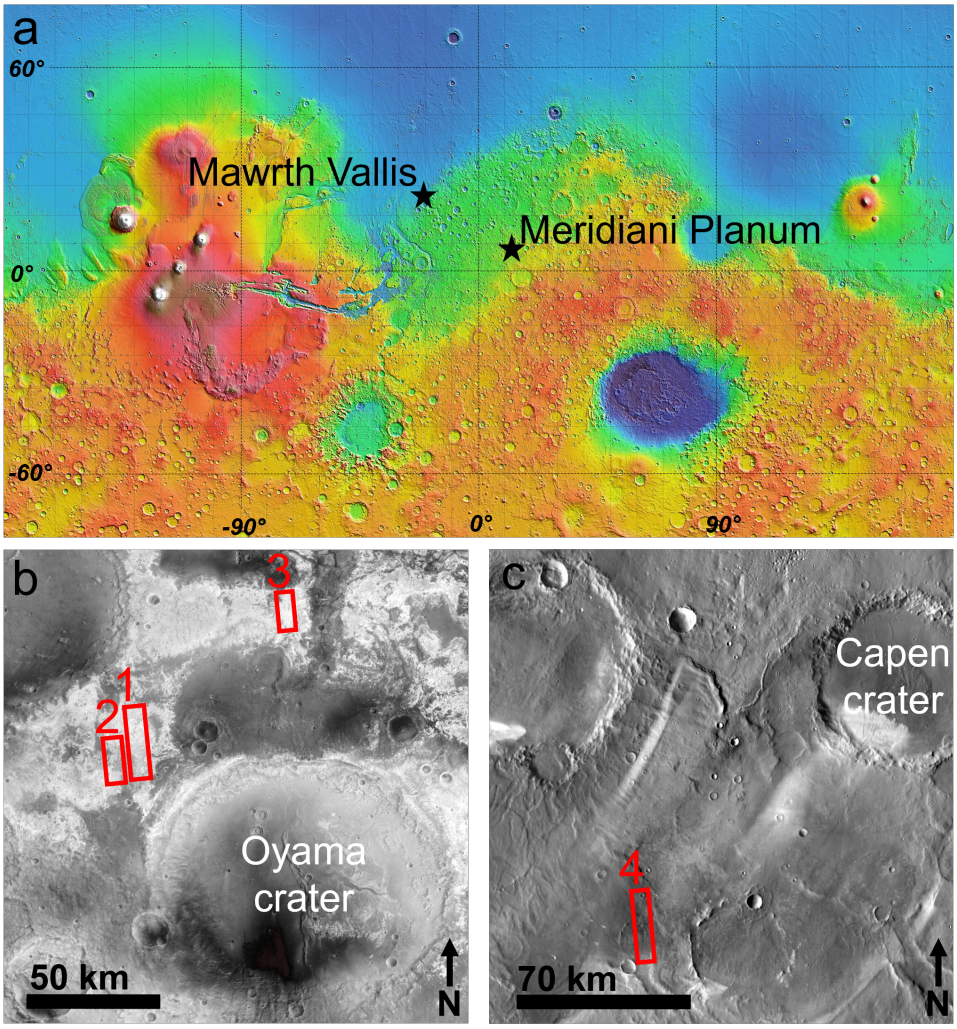

Figure 2.2: a) Global map of Mars showing locations of Mawrth Vallis and Meridiani Planum sites from this study and Aeolis Dorsa site from Kite et al. (2014) (Image credit: MOLA science team. Color scale shows elevation relative to Mars geoid overlain on shaded relief. Purple (e.g. 35° S 55° W) corresponds to -8km, white (e.g. 10° S 120° E) corresponds to 8km), b) HRSC Mawrth Vallis mosaic showing Mawrth HiRISE DTM locations (image credit: ESA/DLR/FU Berlin), c) THEMIS daytime IR mosaic showing Meridiani Planun HiRISE DTM location (image credit: NASA/USGS, ESA/DLR/FU Berlin). Numbering corresponds to location numbers (#) in Table 2.1.

2.3 Geological Context

2.3.1 Mawrth Phyllosilicates

Site	#	Image(s)	DTM
Mawrth	1	ESP_023488_2050/ ESP_023554_2050	DTEEC_023488_2050_023554_2050_A01 (PDS-released)
	2	PSP_008245_2045/ ESP_016394_2045	DTEEC_008245_2045_016394_2045_A01 (PDS-released)
	3	ESP_028011_2055/ ESP_028288_2055	DTEEC_028011_2055_028288_2055_A01 (PDS-released)
Meridiani	4	ESP_022221_1850/ ESP_039667_1850	ESP_022221_1850_ESP_039667_1850_align_1_DEM

Table 2.1: Image and DTM numbers for Mawrth Vallis and Merdiani Planum crater counting locations. Location numbers (#) correspond to labels shown in Fig. 2.2. Mawrth paleosurface crater counts come from location 1 only. Mawrth phyllosilicate crater counts are a composite of all ancient embedded craters found in visually similar phyllosilicate units in locations 1-3. Meridiani crater counts come from all sedimentary units in location 4 only.

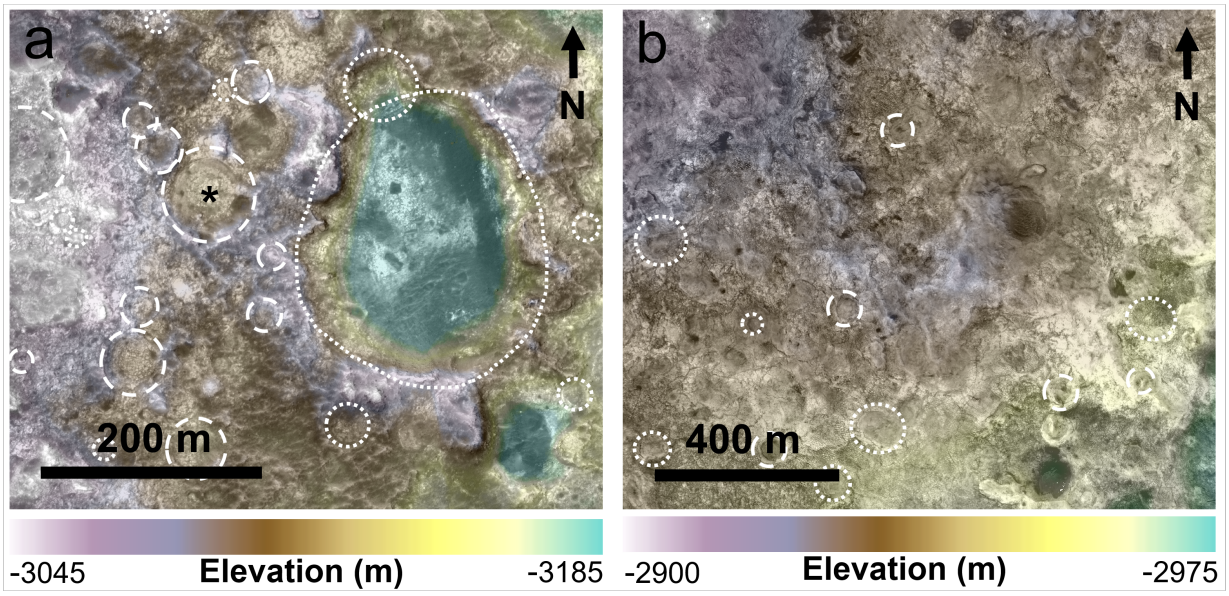

Figure 2.3: Examples of ancient craters in the 2 main units in our Mawrth Vallis site: a) 'Dark paleosurface' (image #1, crater with black asterisk in center shown in Fig. 2.5), b) phyllosilicates (image #2, dark-bottomed crater in bottom left (near letter m) centered at 21°12′52.89W, 24°30′50.53N). Dashed ellipses outline exhumed ancient craters. Dotted ellipses outline candidate exhumed craters that are not included in our final ancient crater counts.

The Noachian phyllosilicates north/northwest of Oyama crater (24.5° N, 21.0° W, Fig. 2.2b, 'Mawrth' herein) are comprised of thick units (>150m; Loizeau et al. 2007) of little-deformed (Michalski et al., 2010), finely layered sedimentary deposits. Hydrous clay minerals (Bishop et al., 2008) make these phyllosilicates of interest for constraining the atmospheric pressure during the Early Noachian (4.10 - 3.95 Ga), when liquid water must have been present for alteration to occur. These minerals suggest that surface temperatures must have been at least 273K according to Bishop and Rampe (2016), but may have been as high as 310K (Bishop et al., 2018). Additionally, the Mawrth phyllosilicates overlie a dark paleosurface (Loizeau et al. 2010, Fig. 2.3a), which traps an even more ancient crater population. These craters are infilled with layered phyllosilicates and therefore must pre-date the main phyllosilicate deposition (Loizeau et al., 2012). The preservation of >100m diameter craters on this paleosurface shows that it was exposed long enough to be impacted by bolides (Loizeau

et al., 2010). Stratigraphic relationships (Loizeau et al., 2012) and cratering ages for the overlying phyllosilicate units give an age for the heavily cratered paleosurface of >4 Gyr. Therefore, this surface cannot be dated directly using cratering ages. The phyllosilicates themselves are dated to $3.8^{+0.2}_{-0.2}$ Ga (Loizeau et al., 2012). The greatest density of well-preserved embedded craters occurs on the underlying paleosurface. Embedded craters in the overlying phyllosilicates are more sparse, perhaps due to dilution of the crater population by sedimentation. During periods of rapid sedimentation, there is less time for craters to accumulate on the same stratigraphic level (Kite et al., 2013). The lower density of craters in the phyllosilicates necessitated crater counting over a larger area. Initially, we compile crater counts from only images 1 and 2 (Table 2.1). We use textural features occurring in aluminum-rich phyllosilicates in HiRISE images 1 and 2 to identify outcrops of the same phyllosilicates in nearby regions (i.e. image 3).

2.3.2 Meridiani Planum

Our study region in Meridiani Planum (Fig. 2.2c, 'Meridiani' herein) is located to the southwest of Capen crater. We adopt the crater age of Hynek and di Achille (2017), who date these deposits to $3.82^{+0.10}_{-0.18}$ Ga. Our DTM includes a sinuous ridge, interpreted as an inverted channel by Davis et al. (2016) (Fig. 2.4a), with some craters embedded in the layered deposits that make up the inverted channel itself. In this study, we are interested in crater populations preserved in sedimentary units. We identify several sedimentary units at our Meridiani site (image #4, Table 2.1). Light-toned units in the south of the region have horizontal layering (Fig. 2.4b). These light units overlie mid-toned material which has regularly spaced, morphologically consistent ridges with m-scale wavelengths. These have different orientations on different stratigraphic levels (Fig. 2.4b) — this suggests that these are a deposition-era feature re-exposed by more recent differential erosion. We interpret these units as being of sedimentary origin. These units overlie a darker surface with no evidence for a sedimentary

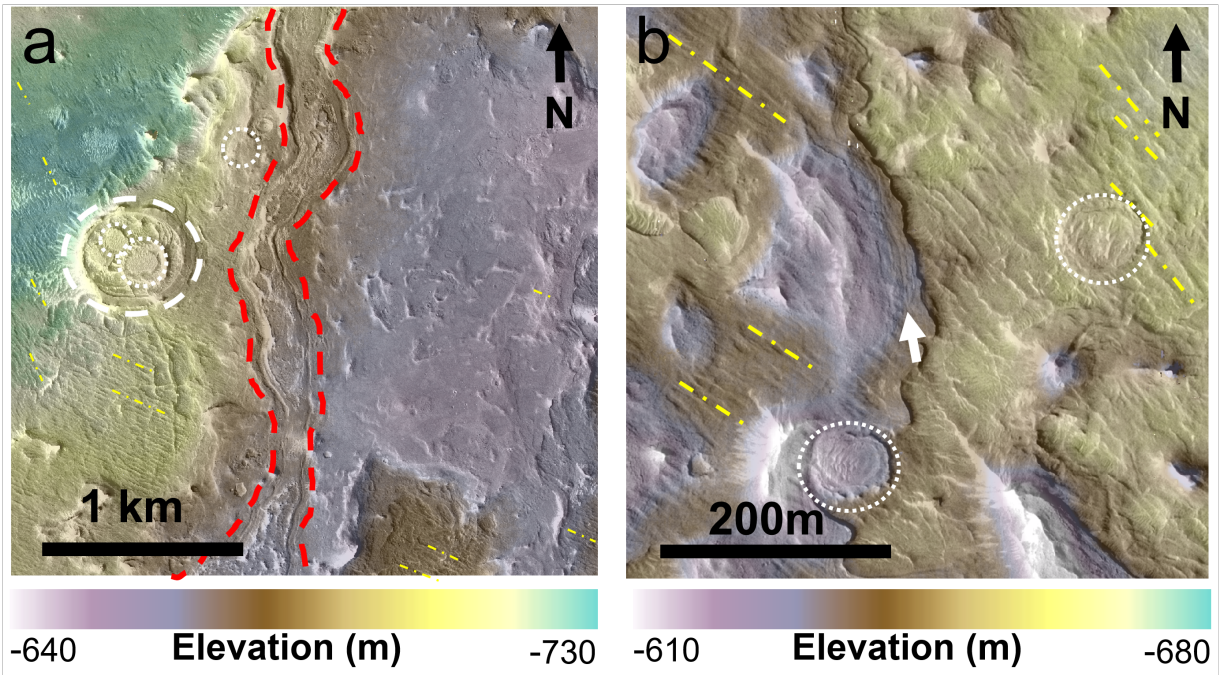

Figure 2.4: Sedimentary features at Meridiani site (image #4): a) sinuous ridge (outlined in dashed red, large crater in left of image centered at 12°36′45.768W, 4°58′11.911N) and b) layering (white arrow, points at 12°36′26.065W, 4°46′56.299N). A selection of linear ridges (not interpreted as fluvial) on various stratigraphic levels are marked with yellow dashed-dotted lines. Ancient embedded craters are shown by dashed, white ellipses. Candidate ancient embedded craters (not included in final counts) are marked with a dotted ellipse.

origin from HiRISE images. For this study, we only include embedded craters occurring in units with visible sedimentary features, and exclude those in areas covered by modern wind-blown material.

2.4 Method

2.4.1 Crater Counts

We identify definite ancient embedded craters (Fig. 2.5) according to the following criteria:

1. Approximately circular topographic depression.

2. Topographic feature appears convex-up in anaglyph.

3. <50% of crater depression obscured by sand/dust infill.

4. Center of the crater sand/dust free.

5. Maximum crater depth $\ll 0.2\times$crater diameter.

6. Preservation of a topographically elevated rim spanning at least a 150° arc outside the topographic depression (arc may be discontinuous).

Additional support for a crater being ancient and embedded is the presence of disk-shaped, layered sedimentary deposits inside the crater. However, few embedded craters preserve this feature and we primarily rely on the criteria listed above. We do not attempt to discriminate between primary and secondary craters in our counts. While secondary craters are observed on Mars (McEwen et al., 2005), secondary craters are not observed in Earth's geologic record. We assume that at atmospheric pressures $\geq$1 bar, secondary craters do not significantly affect the observed CSFDs. Additionally, our chosen atmosphere-impactor interaction model (Williams et al., 2014) closely reproduces modern Mars CSFDs without including secondary craters.

We measured ancient embedded craters by placing points along the exposed crater rim in ArcGIS (Fig. 2.5). We fit these points to circles using the MATLAB code `circfit`, generating a best-fit circle as well as the largest and smallest possible circles that fit the measured points. We have attempted to reduce the human errors associated with the crater counts by making at least 2 passes of each DTM. To ensure in-lab consistency, a second person performed an independent crater count within a test-region in each DTM. After two independent counts, differences in selections of definite and candidate craters were discussed and were recategorised accordingly. In an 11 km^2 test patch in DTM #1, Analyst A identified 36 ancient craters, and Analyst B identified 26. Of these, 25 were agreed upon. 11 craters were identified by Analyst A that were not identified by Analyst b. These craters have a mean diameter 40m and are all < 75m in diameter. Due to the small average size of these craters,

this difference in identification is likely due to 2 passes of the DTM by Analyst A and only 1 check pass by Analyst b. 1 crater with diameter > 100m is identified by Analyst B and not by Analyst a. Our fitting procedure is most sensitive to the smallest craters in the population, therefore the inclusion/exclusion of this crater is unlikely to affect our results. We only use CSFDs with more than ∼50 craters to reduce the impact of misidentifying erosion-era craters as ancient on the paleopressure fit, and to improve our confidence that our measured population more closely represents the erosion-modified ancient crater population (Williams et al., 2017).

2.4.2 Model

Impactors passing through planetary atmospheres experience ablation and decceleration, and can also undergo catastrophic disruption or fragmentation. These processes have been extensively modelled for both the Earth's atmosphere (Passey and Melosh, 1980; Melosh, 1981; Hills and Goda, 1993; Svetsov et al., 1995; Lyne et al., 1996; Bland and Artemieva, 2006; Boslough and Crawford, 2008) and the atmospheres of other bodies in the Solar System (Ivanov et al., 2001; Popova et al., 2003; Korycansky and Zahnle, 2004, 2005; Chappelow and Sharpton, 2005). In this study, we employ a numerical model of ablation and decelaration of impactors passing through atmospheres of different pressures written by Williams et al. (2014). This model closely reproduces geologically recent crater populations on Mars when zero elevation corrected atmospheric pressure is set to the present day value. To estimate paleopressure, we treat impacts as a Poisson process (Aharonson et al., 2003) and use the pipeline of Kite et al. (2014) to bayesian fit the observed CSFD to model crater distributions at a range of atmospheric pressures from 0.006 to 5 bar, as generated for Kite et al. (2014) using the methodology described in Williams et al. (2014). We briefly summarize the model here.

Synthetic crater populations are generated using a forward model of impactor-atmosphere

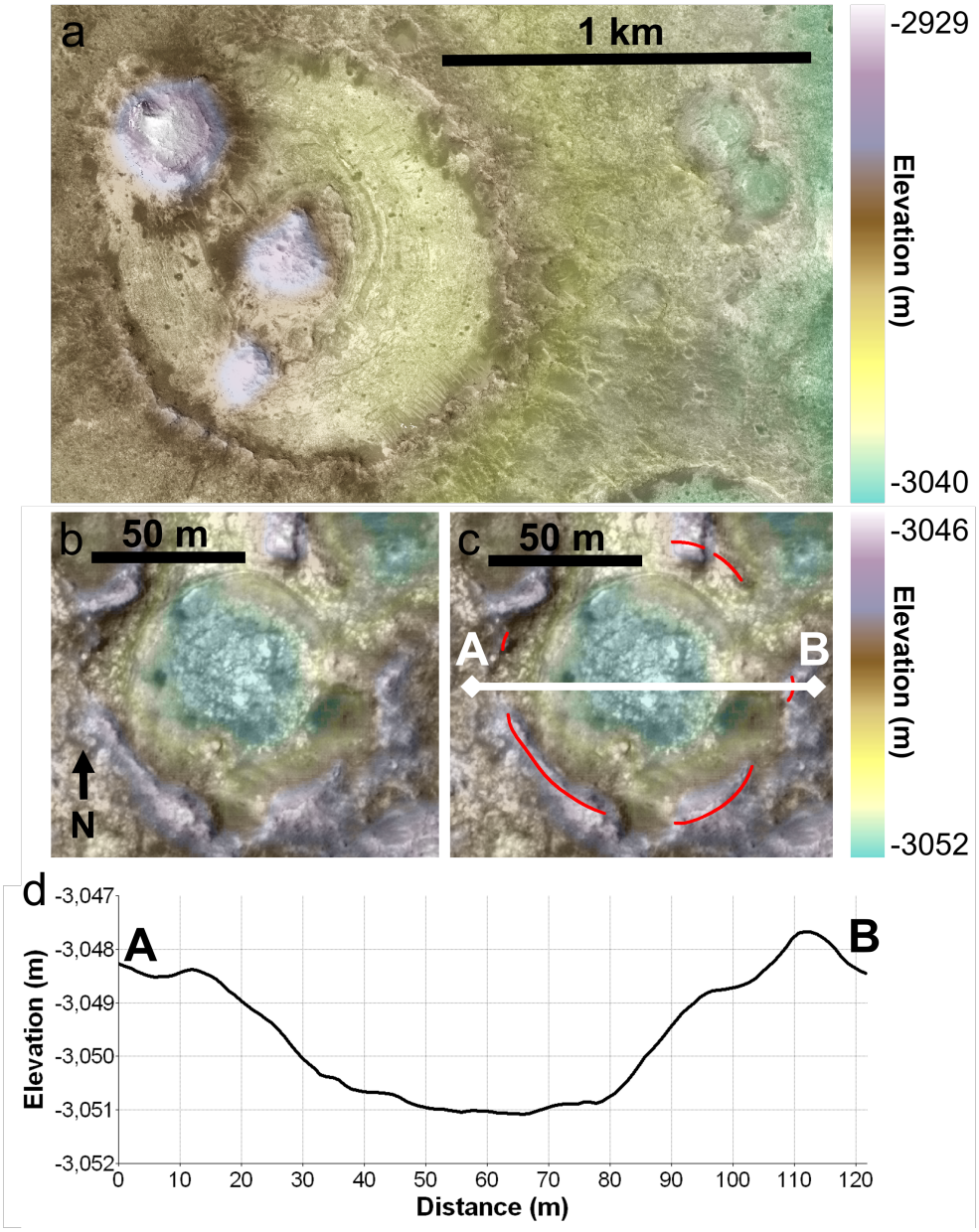

Figure 2.5: Example ancient embedded craters on Mawrth paleosurface (centered at 21°10′5.252W, 24°23′30.842N). a) Large ancient crater, previously identified by Loizeau et al. (2010) (their Fig. 8, #2 in Table 2.1 of this paper), b) typical, small ancient crater without interpretation, b) topographically elevated rim outlined in red, c) cross section showing depth $\ll 0.2\times$ diameter. #1 in Table 2.1 and Fig. 2.2. Solar incidence angle 45° . Illuminated by sunlight from NW.

interactions for an ensemble of 10^6 impactors with properties drawn from distributions of size (Brown et al., 2002), velocity (Davis, 1993), density, and strength (i.e. irons, chondrites

etc.) (Ceplecha et al., 1998) based on terrestrial fireball network observations (Ceplecha et al., 1998) using a Monte Carlo approach. Each impactor starts at an altitude of 100 km and passes through an atmosphere with scale height:

$$H = \frac{R\bar{T}}{g} \tag{2.1}$$

where R is the specific gas constant for CO_2, and $\bar{T}$ is a characteristic atmosphere temperature. We assume that the atmosphere is isothermal, and use surface temperature T_s as our value for $\bar{T}$. The local atmospheric density, ρ_a is:

$$\rho_a = \rho_0 \exp\left(\frac{-z}{H}\right) \tag{2.2}$$

where ρ_0 is the surface atmospheric density calculated using the ideal gas law ($p_0 = \rho_0 RT$). p_0 is surface pressure. We assume a flat surface geometry, and therefore do not allow impactors to skip out of the atmosphere (Williams et al., 2014).

As an impactor passes through the atmosphere, it loses kinetic energy through drag (Equation 2.3) and ablation (Equation 2.4):

$$\frac{\mathrm{d}v}{\mathrm{d}t} = -\left(\frac{C_D \rho_a v^2 A}{2m}\right) + g(z)\sin\theta \tag{2.3}$$

(where t is time, v is speed, z is height above Mars' surface, θ is the angle of the impactor trajectory measured from the horizontal, $g(z)$ is local gravitational acceleration at z, C_D is the drag coefficient, ρ_a is atmospheric density at z, A is cross-sectional area of the impactor). The impactor is assumed to be spherical and in the high Reynolds number, continuum flow regime, therefore $C_D \sim 1$ (Podolak et al., 1988).

$$\frac{\mathrm{d}m}{\mathrm{d}t} = -\frac{C_h \rho_a v^3 A}{2\zeta} \tag{2.4}$$

(where m is mass, C_h is heat transfer coefficient, and ζ is the heat of ablation; Williams

et al. 2014). C_D, C_h, and ζ are related through the ablation coefficient σ (Ceplecha et al., 1998):

$$\sigma = \frac{C_h}{2\zeta C_D} \tag{2.5}$$

In addition to ablation, the model includes fragmentation of impactors through aerodynamic breakup. Fragmentation occurs when the dynamic pressure from the impactor passing through the atmosphere ($\rho_a v^2$) exceeds the bulk strength of the impactor (σ_m). All impactors are assumed to have the same bulk strength. $\sigma_m = 0.65$ MPa best reproduces the present-day SFD of small craters on Mars (Williams et al., 2014). The model limits fragmentation to a single event producing < 100 individual fragments, each of which are followed to the end of their flight. As described in Williams et al. (2014), the number of fragments generated in each fragmentation event follows a power-law probability distribution with slope -1.5. Fragment masses are determined by iteratively subtracting random mass fractions from the initial impactor mass.

When an impactor reaches the surface, final mass and velocity can be used to calculate the size of the resulting crater (Holsapple, 1993):

$$V_t = K_1 \left(\frac{m_f}{\rho_t}\right) \left[\pi_2 \left(\frac{\rho_m}{\rho_t}\right)^{\frac{1}{3}} + K_2 \left(\pi_3^{\frac{2+\mu}{2}}\right)\right]^{-\frac{3\mu}{2+\mu}} \tag{2.6}$$

where V_t is transient crater volume, m_f is final mass, ρ_t is target density, ρ_m is impactor density, and K_1, K_2 and μ are empirical coefficients that vary between target material (Table 2.3). This expression for V_t smoothly spans the transition between the the strength regime (crater size primarily determined by target strength) and the gravity regime (crater size primarily determined by surface gravity) (Holsapple, 1993). π_2 and π_3 are dimensionless numbers given by:

Table 2.2: Numerical model parameters. Target-dependent parameters are given in Table 2.3.

Symbol	Units	Description
H	m	scale height
R	J kg^{-1} K^{-1}	specific gas constant
$\bar{T}$	K	characteristic atmospheric temperature
g	m s^{-1}	gravitational acceleration
ρ_a	kg m^{-3}	local atmospheric density
ρ_0	kg m^{-3}	surface atmospheric density
z	m	elevation
v	m s^{-1}	speed
t	s	time
C_D	—	drag coefficient
A	m^2	cross sectional area of impactor
m	kg	impactor mass
σ	kg J^{-1}	ablation coefficient
σ_m	MPa	impactor bulk strength
V_t	m^3	transient crater volume
m_f	kg	final impactor mass
v_f	m s^{-1}	final impactor velocity
D_t	m	transient crater diameter
D_f	m	final crater diameter

$$\pi_2 = \frac{gR_p}{v_f^2} \tag{2.7}$$

$$\pi_3 = \frac{Y}{\rho_t v_f^2} \tag{2.8}$$

where v_f is final velocity, R_p is projectile diameter, and Y is target yield strength. Impactors with $v_f < 500$m s^{-1} are removed from the simulation because they are travelling too slowly to produce hypervelocity impact craters (Kite et al., 2014; Williams et al., 2014). Transient crater diameter, D_t is then:

$$D_t = 2K_r V_t^{\frac{1}{3}} \tag{2.9}$$

The final diameter of the crater $D_f = 1.3D_t$ (Holsapple, 1993). When crater clusters form after fragmentation events, their effective diameters (D_{eff}) are calculated from individual crater diameters (D_i) using $D_{eff} = \left(\sum_i D_i^3\right)^{\frac{1}{3}}$. The synthetic CSFD assumes target properties for dry soil (Williams et al., 2014). We follow Kite et al. (2014) and assume that target properties for dry soil/soft rock (Table 2.3) are likely to be appropriate for ancient craters preserved in the Mawrth phyllosilicates and at our Meridiani Planum site because the craters formed during the deposition of loose material. However, the cratering model may be strongly sensitive to target strength (Fig. S4 in Kite et al. 2014). The lithology of the Mawrth 'dark paleosurface' is poorly constrained (Loizeau et al., 2012) and therefore values for hard rock may be more appropriate. Additionally, if the sediments deposited at Mawrth Vallis and Meridiani Planum were wet, their strength would be greater (Table 2.3). Both of these would introduce a systematic underestimate of atmospheric pressure. An increase in target yield strength from dry alluvium ($Y = 65 \times 10^3$ Pa) to hard rock ($Y = 7 \times 10^6$ Pa) without changing any other parameters could increase our upper limit paleopressure estimates by as much as a factor of 2. This only holds if μ (an experimentally derived empirical coefficient related to porosity) is kept constant at $\mu = 0.41$. However, a more appropriate value for μ for hard rock may be $\mu = 0.55$. With this Y-dependent adjustment for the value of μ, our paleopressure estimates would only increase by a factor of $\sim 25\%$ for a hard rock surface.

Table 2.3: Impact crater scaling parameters. Values as given in Williams et al. (2014) from material published online (keith.aa.washington.edu/craterdata/scaling/theory.png)

Parameter	**Dry soil/soft rock**	**Wet soil/hard rock**	**Description**
ρ_t (kg m^{-3})	2000	3200	Target density
μ	0.41	0.55	Empirical constant related to target porosity (Equation 2.6)
Y (kPa)	65	6900	Yield strength
K_1	0.132	0.095	Empirically-derived scaling parameter (Equation 2.6)
K_2	0.26	0.257	Empirically-derived scaling parameter (Equation 2.6)
K_r	1.1	1.1	Empirically-derived scaling parameter (Equation 2.4.2)

Our final paleopressure estimates are corrected for elevation to zero-elevation atmospheric pressure:

$$p_{corr} = \frac{p}{\exp\left(\frac{-|\Delta z|}{H}\right)} \tag{2.10}$$

where p_{corr} is the new elevation corrected atmospheric pressure and $\mid \Delta z \mid$ is the change in elevation of the site. Assuming $H = 10.7$ km, this corresponds to a systematic error of $\sim$10% for every 1 km change in elevation. At present, our crater counting sites are 3100 m (Mawrth) and 670 m (Meridiani) below the Mars geoid. Large (km-scale) changes in the elevation of these sites are not expected between the time of crater population accumulation and present, even taking into account the growth of Tharsis and true polar wander (Citron et al., 2018).

2.5 Results

Our paleopressure estimates are 1.9±0.1 bar for the Mawrth paleosurface, 1.5±0.1 bar for the Mawrth phyllosilicates, and 1.5±0.1 bar for the Meridiani data (Table 2.4). The fitted synthetic CSFDs are shown alongside the real data in Fig. 2.6. Our new upper limits on continuous atmospheric pressure are shown alongside existing paleopressure estimates in Fig. 2.7. Our impactor-atmosphere interaction model produces synthetic CSFDs with 10-20m diameter craters under a 1 bar atmosphere. This is consistent with observations of small (<100m diameter), hypervelocity craters on Earth (Shoemaker et al., 2005; Folco et al., 2011), including 2 that are <20m in diameter within the past 5 kyrs: the Haviland crater (15 m, Nininger and Figgins 1933), and the Carancas crater (13.5m, Tancredi et al. 2009).

Using the same method as described here, Kite et al. (2014) stated a paleopressure upper limits of 0.9 ± 0.1 bar and $p < 1.9 \pm 0.2$ bar with and without rimmed circular mesas

	Min. crater diameter	Paleopressure upper limits	
Site	$D_{\min}$ (m)	$\mathbf{p}^N_{\mathrm{sfd}}$ (bar)	$\mathrm{p}^F_{\mathrm{sfd}}$ (bar)
Mawrth paleosurface	$21.2\pm^{0.6}_{0.7}$	**1.9± 0.1**	1.3±0.1
Mawrth phyllosilicates	$15.2\pm^{0.7}_{0.9}$	**1.5± 0.1**	1.0±0.1
Meridiani	$15.7\pm^{1.2}_{2.0}$	**1.5± 0.1**	1.0±0.1

Table 2.4: Crater diameters and paleopressure upper limits from models and full fitting procedure. $D_{\min}$ - minimum measured crater diameter, error bars give upper and lower limits from `circfit` pressure estimates from the full CSFD with ($\mathrm{p}^F_{\mathrm{sfd}}$) and without ($\mathrm{p}^N_{\mathrm{sfd}}$) fractalcorrection for each study region. All pressures are zero-elevation corrected.

(potential but not confirmed preserved ancient impact craters) respectively. To do this, the senior author (E. S. Kite) used the p_0 (zero-elevation corrected atmospheric pressure) from the National Space Science Data Center (0.20 kg m^{-3}). However, this greater than the p_0 given by the Mars Climate Database and is not self-consistent. With self-consistent p_0, the limits become $p < 1.1\pm^{0.2}_{0.1}$ and $p < 2.4 \pm 0.2$ bar. We plot the corrected values (7b[a] and 7a[a]) in Fig. 2.7 onwards. Our paleopressure estimates at 3.8±0.2 Ga agree with the constraint of van Berk et al. (2012) (4[c]) from thermodynamic models of carbonate cation compositions, and the modelled upper bound on $\mathrm{pCO_2}$ from Hu et al. (2015) (5[c]). Including a fractal correction (described in Section 2.6.1) lowers our paleopressure estimates; we discuss whether the fractal correction is appropriate in Section 2.6.1. We assume that local, elevation-independent variations in pressure are negligible (we justify this assumption in Section 2.6.3) and consider the impact of both long-term (10^8-yr timescale) and short-term (on the timescale of obliquity changes) changes in atmospheric pressure on our upper bounds in Section 2.6.2.

2.6 Discussion

Our main points in this section are as follows:

1. Section 2.6.1 — CSFDs can be modified by multiple processes including changes in impactor population and preferential obliteration of smaller craters. This supports the

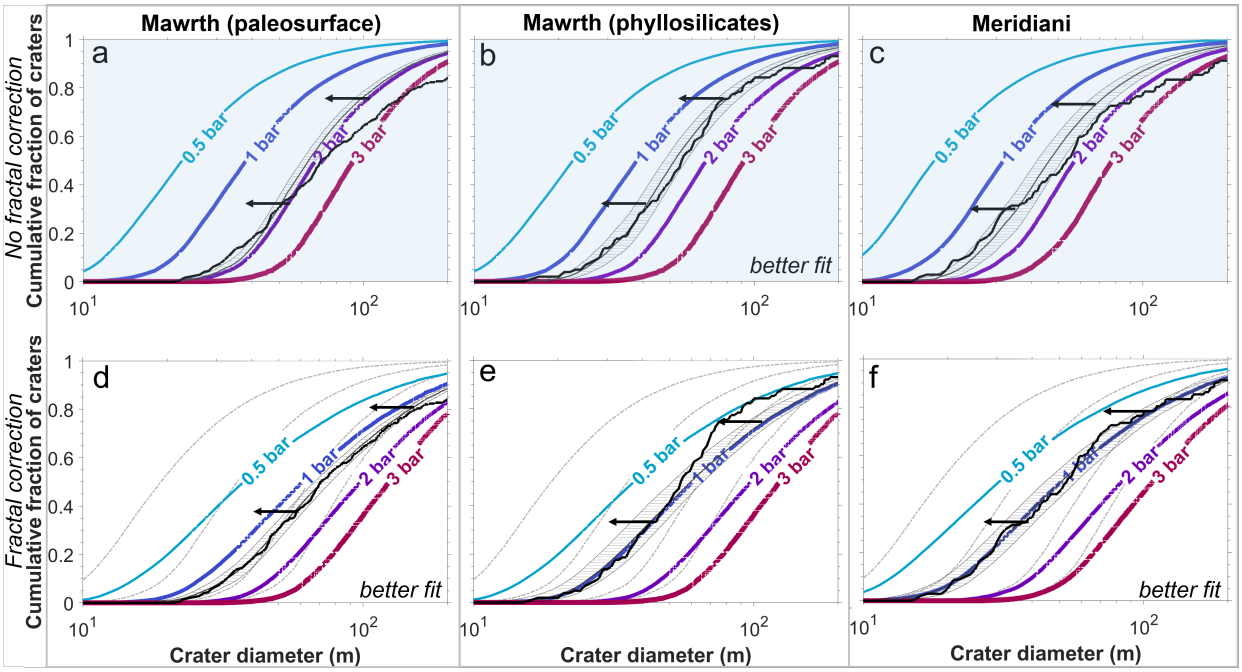

Figure 2.6: Fits of measured crater size frequency distributions (CSFDs, black) to synthetic data from atmosphere-impactor interaction model (colored lines) without the fractal correction (described in Section 2.6.1, a-c, blue tint) and with the fractal correction (d-f, see discussion in Section 2.6.1) for the Mawrth paleosurface (a, d), Mawrth phyllosilicates (b, e), and Meridiani (c, f). x-axis upper limit is 200m because fitting procedure is most sensitive to smallest craters in distribution (15-50m scale). Dashed-dotted, gray lines in d-f show synthetic CSFDs without the fractal correction (from left to right: 0.5, 1, 2 and 3 bars). Hatched areas show 2-σ bootstrap error envelope on fit ($\pm$0.1 bar). Black horizontal arrows indicate that paleopressure fits are upper bounds, due to the possibility of preferential obliteration/non-recognition of small craters, (Section 2.6.3).

interpretation of our paleopressure fits as upper limits on atmospheric pressure, rather than best estimates.

2. Section 2.6.2 — Our measured CSFDs cannot be produced through atmospheric pressures persistantly above our upper limits. However, our measured CSFDs can be matched by crater population accumulation in either an atmosphere with constant pressure, or in an atmosphere that has varied in time between high and low atmospheric pressures. Therefore, our paleopressure estimates from Section 2.5 cannot simply be taken as fixed upper bounds on atmospheric pressure. We can constrain the

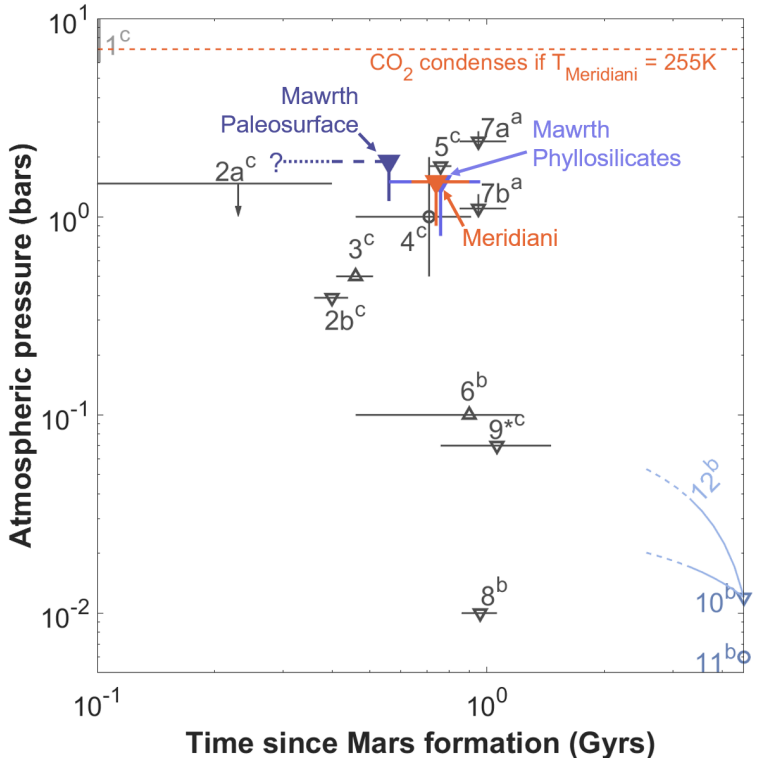

Figure 2.7: Updated paleopressure constraints for Mars showing our new upper limits (orange, light purple, and dark purple symbols) in context. Superscripts: a - constraints from small, ancient, embedded craters, b - constraints from remote sensing, c - constraints from all other techniques (meteorite analyses, modeling, etc.). Upward (downward)-pointing triangles indicate lower (upper) bounds. Circles indicate estimates of absolute atmospheric pressure or direct measurements. Downward arrows from a horizontal line indicate that pressure is constrained to have been below the given value for the entire time interval. 1^c) Cosmochemical estimate based on scaling Earth's C abundance to Mars (Lammer et al., 2013), 2^c) atmospheric evolution model results based on Ar isotope measurements from Mars meteorite ALH 84001 and from modern Mars (Cassata et al., 2012) (a - maximum atmospheric pressure for first 400 Myr of Mars' history, b - pressure at age of meteorite), 3^c) atmospheric evolution model results based on Ne, Ar and Xe isotope measurements from ALH 84001 and modern Mars (Kurokawa et al., 2018), 4^c) thermodynamic modeling of Mg-Fe-Ca carbonate formation (van Berk et al., 2012), 5) atmospheric evolution model results (Hu et al., 2015), 6^b) pressure calculated from impact structure from bomb sag in pyroclastic deposits (Manga et al., 2012), 7) pressure estimates from CSFDs in Aeolis Dorsa (corrected from Kite et al. 2014) (a/b - with/without rimmed circular mesas), 8^b) pressure calculated from wind ripple size (Lapotre et al., 2016), 9^{*c}) thermodynamic modeling of siderite formation (Bristow et al., 2017) (since superseded by experimental results, see Tosca et al. 2018), 10^b) annual mean modern atmospheric pressure + CO_2 stored in polar ice (Bierson et al., 2016), 11^b) annual mean modern atmospheric pressure, 12^b) absolute upper and lower bounds of MAVEN escape rates extrapolated backwards in time (Lillis et al., 2015). Only studies that explicitly find paleopressure estimates are included here.

minimum accumulation time at any pressure < 1.5 bar recorded by each outcrop by using crater production functions.

3. Section 2.6.3 — Our results are not affected by local variations in zero-elevation-corrected pressure, as the early Martian atmosphere is unlikely to have been able to sustain annual mean zero-elevation corrected atmospheric pressure gradients greater than a few percent.

2.6.1 Modification of CSFDs over geologic time: sedimentation, erosion, and changes in impactor population

There are 3 key processes that contribute to the removal of smaller craters:

1. The likelihood of intersecting a crater on an erosion surface through a 3D volume containing craters is proportional to crater diameter (Smith et al. 2008, Fig. 2.8a & b).

2. Erosion and sedimentation processes preferentially remove small craters because of their smaller topographic expression (Öpik, 1966; Jerolmack and Sadler, 2018), Fig. 2.8 c & d) (a more complete summary of the issues associated with crater modification and preservation can be found in Williams et al. (2017)).

3. Craters may be excluded from counts because the resolution of HiRISE images and DTMs is insufficient for us to resolve the smallest preserved craters.

These effects increase the likelihood that the smallest craters in any population will be missed in crater counts. As a result, paleopressure estimates based on our measured CSFDs represent upper-bounds. Additionally, degradation of craters can widen the apparent crater diameter by up to 10% through backwasting of the crater rim (Grant and Schultz, 1993; Craddock et al., 1997a). Watters et al. (2015) also report rim span widening with increasing crater modification for small, recent craters, that may be in a more representative size regime

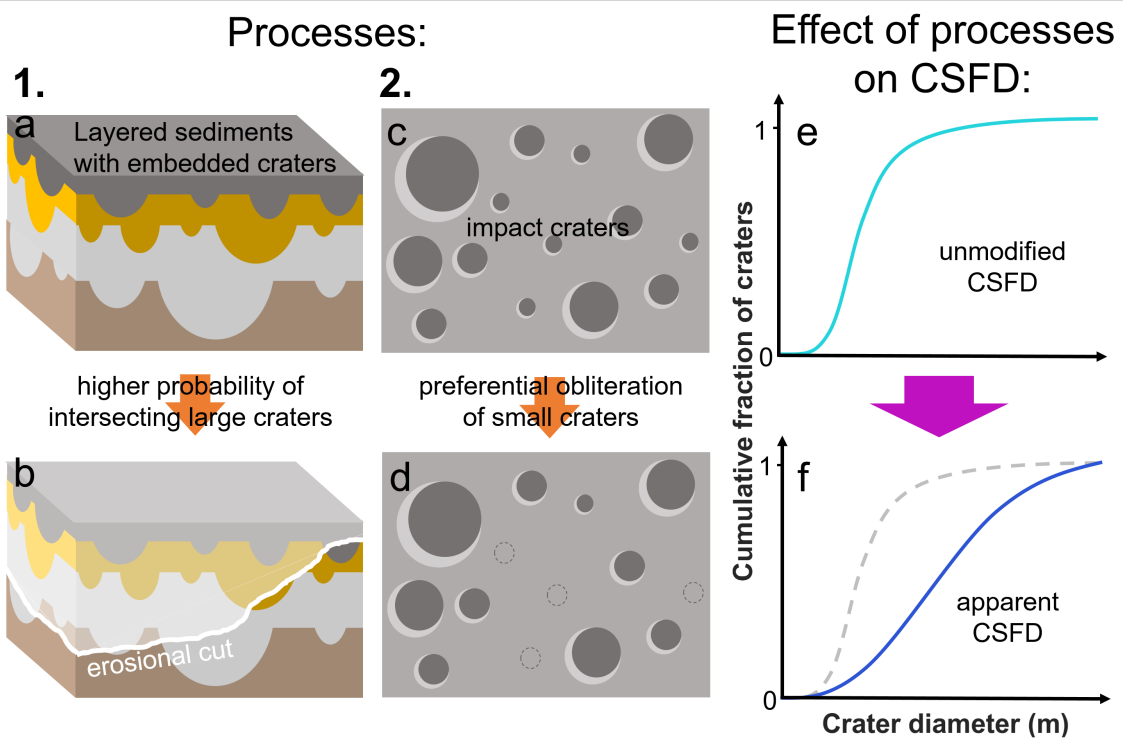

Figure 2.8: Schematic illustrating the effect that depositional and erosional processes have on CSFD shape. Process 1: a) initial cratered volume before modification, b) intersection of erosional cut with cratered volume, cut intersects more large craters than are represented by the underlying crater population. We refer to the correction for this effect as the "fractal correction." Process 2: c) initial cratered surface, d) cratered surface after modification by sedimentary processes with obliterated smaller craters indicated by dashed circles. Effect of these two processes on CSFD: e) initial CSFD for a & c (pre-modification), f) observed CSFD for b & d after modification by processes 1 & 2. The grey dashed curve is the original, unmodified CSFD from e.

for the craters that most strongly affect our paleopressure estimates (<100 m diameter). The effect of this is to shift the entire CSFD to larger crater diameters (i.e. displacing the schematic CSFD in Fig. 2.8e to the right), which may mean that our upper bounds on paleopressure are conservative. It is also possible for an erosional cut to occur below the original crater rim. This would lead to apparent shrinkage of the bowl. However, our ancient embedded crater criteria (Section 2.4) specify that a topographically elevated rim must be preserved for a crater to be included in our counts and therefore this effect is unlikely to be important for our crater counts. We assume that a preserved topographic rim represents the

original crater diameter regardless of the orientation of an erosional cut. If the cut destroys the rim — modifying the apparent crater diameter — the crater does not meet the selection criteria and is not included in this study.

To correct for the increased probability of not intersecting smaller craters in an erosional cut that spans many stratigraphic levels (1), we can compensate for the preferential loss of the smallest craters in each population. This can be done by implementing a "fractal correction" (Kite et al., 2014). This fractal correction reduces the weight of each crater in our modelled CSFDs in proportion to its diameter, with the greatest down-weighting of the largest craters, so that each diameter range is an equally good probe of the underlying CSFD throughout the cratered volume that we are only seeing a small part of. To ensure that our paleopressure upper limits are as conservative (high) as possible, we choose not to apply this correction by default. The Mawrth paleosurface data is fit much better by the model data with the fractal correction (accounting for processes 1 & 2) included (Fig. 2.6a-d). The paleosurface dips only 1-2° to the north east, and the erosion surface does not visibly cut any stratigraphic layers. Therefore, we propose that the Mawrth paleosurface represents a single stratigraphic level that has been exposed at the surface by the erosional cut. If this is the case, the fractal correction does not apply.

While we do not rule out the possibility of size-selective crater obliteration (2) as an explanation for this observation on the Mawrth paleosurface, a fourth process may contribute to the difference in observed CSFD:

4. The impactor population in our atmosphere-impactor interaction model might not be representative of the impactor flux at Mars' orbit at ∼4 Ga (Strom et al., 2005).

The impactor population used in the forward model is adapted from satellite observations of the annual flux of objects colliding with Earth. This is scaled to Mars and can closely reproduce recent crater populations on Mars (Williams et al., 2014). However, it may not be representative of Mars' impactor population over the past 4 Gyr. The Mawrth paleosurface

CSFD may record a difference in the impactor population reaching Mars earlier in its history, as a reduction in the relative proportion of smaller impactors for a given atmospheric pressure would have the same sign as the fractal correction, acting to flatten the cumulative CSFD. Additionally, the Mawrth phyllosilicates and Meridiani CSFDs may also encode a changing impactor population component, as their ages place them close to the end of the Late Heavy Bombardment, for which evidence suggests an impactor CSFD richer in massive impactors by 1 log unit (Strom et al., 2005, 2015).

The Meridiani data is also better fit when the fractal correction is implemented (Fig. 2.6c vs. f). This is consistent with the fact that the Meridiani crater counts are a composite of ancient embedded craters in sedimentary deposits that span multiple stratigraphic levels, few of which are as exposed at the surface over as large a continuous area as the Mawrth paleosurface. However, the Hynek and di Achille (2017) age for this region also places it towards the end of the Late Heavy Bombardment. Therefore, a change in impactor population (4) may partially explain the shape of the CSFD by increasing the proportion of large impactors, flattening the CSFD. Conversely, the Mawrth phyllosilicate data is fit best by the model CSFDs when no fractal correction is applied (Fig. 2.6b vs. e). This is surprising because, like Meridiani, the Mawrth phyllosilicates crater counts also span multiple stratigraphic levels, which we would expect to flatten the observed CSFD due to the greater probability of an erosional cut intersecting larger craters (1). The difference in the 2 CSFDs may reflect differences in crater preservation between the two sites. Alternatively, the dominant effect may be changes in impactor population between the deposition of the Mawrth phyllosilicates and Meridiani sediments, as the Mawrth phyllosilicates could predate the Meridiani deposits by up to $\sim$300 Myr.

2.6.2 Constant and time-varying atmospheric pressure both fit data

Crater populations do not record an instantaneous atmospheric pressure, and atmospheric pressure need not remain constant over time. Long-term changes in the balance between atmospheric source and sink processes may have changed atmospheric pressure over the course of crater accumulation. The large number of craters on the Mawrth paleosurface suggests that it was exposed for >100 Myr (Loizeau et al., 2010). This is not much shorter than the timescales of degassing, weathering, and atmospheric escape for early Mars. Additionally, climate models have demonstrated that, depending on Mars' obliquity history, its atmosphere may have undergone periods of collapse (Kreslavsky and Head, 2005; Forget et al., 2013; Soto et al., 2015; Saito and Kuramoto, 2017) and reinflation. This provides a mechanism for atmospheric pressure to vary on 10^3 yr timescales, provided that the atmospheric pressure falls below the threshold pressure for atmospheric collapse ($\sim$ 0.5 bar according to Forget et al. 2013). If either of these processes occurred, then our measured CSFDs may represent time-varying atmospheric pressures.

We used synthetic crater populations generated by the atmospheric filtering model to create 'time-varying pressure' CSFDs (S_{mix}). We achieve this by combining CSFDs for a chosen maximum and minimum pressure. These are weighted by the fraction f of time spent at the minimum pressure. CSFDs at high and low pressures are normalized so that the number of large impactors reaching the surface after passing through either atmosphere are the same. We test combinations of 0.007, 0.3, 0.5, 1.2, 2.3 and 3.5 bar atmospheres. No fractal correction is applied to these CSFDs.

$$S_{mix} = fS_{low} + (1 - f)S_{high} \tag{2.11}$$

When the atmosphere is thin, a greater number of small impactors are able to reach the surface over any given time period. Spending as little as 0.1% of the crater accumula-

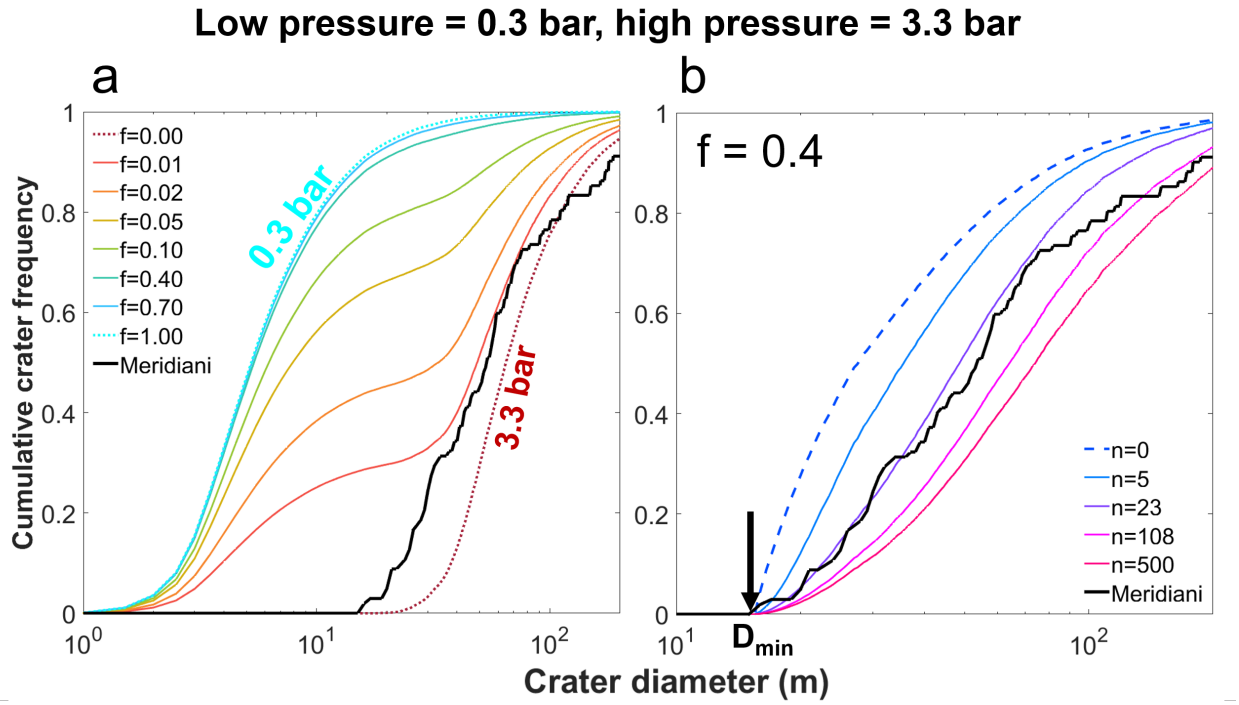

Figure 2.9: Model crater size frequency distributions (CSFDs) produced by a) variations in atmospheric pressure from 0.3 to 3.5 during the time of crater population accumulation b) degree of preferential obliteration of small craters. Dashed colored lines correspond to nonvarying 0.3 (cyan) and 3.5 bar (red) atmospheres. f is the fraction of time spent at minimum atmospheric pressure. Thick black line shows measured Meridiani CSFD. To illustrate the effect of simulated crater population modification on synthetic CSFDs, b) shows a time-varying pressure CSFD with f=0.4 and different degrees of preferential obliteration of small craters (n).

tion period at the lower pressure can form a substantial 'tail' of small craters (Fig. 2.9a). However, we may not actually be able to resolve the small crater tail in our data because of observational limitations (the resolution of HiRISE images and DTMs), and because the crater population has been modified by sedimentation and erosion.

We approximate the effects of sedimentation and erosion on a given CSFD (S) by multiplying through by an arbitrary crater removal factor (c) that is a function of crater diameter.

$$c = \begin{cases} 0, & D < D_{min} \\ 1 - \exp\left(\frac{D_{min} - D}{n}\right), & D \geq D_{min} \end{cases} \tag{2.12}$$

We use this to generate a 'modified' CSFD, S_{mod}:

$$S_{mod} = c(D)S \tag{2.13}$$

where D_{min} is the smallest observed crater diameter for a given dataset and n is the 'e-folding' crater diameter, such that ~60% of craters with $D = n + D_{min}$ are preserved. This simple approximation of small crater removal is justified based on the possible CSFD modification mechanisms outlined in Section 2.6.2, all of which act to preferentially remove smaller craters. Our approach also gives the worst case scenario for crater preservation because we assume that the smallest possible crater in each CSFD is the smallest observed crater in our crater counts. We take D_{min} from each CSFD rather than using an overall D_{min} because ancient embedded craters on the Mawrth paleosurface are visually distinct from those preserved in the Mawrth phyllosilicates or Meridiani units. Therefore, we cannot assume that all of the crater populations have been preserved in the same way or have undergone the same modification.

To compare our artificial, cumulative CSFDs for time-varying atmospheric pressure to our measured CSFDs, we plot the 5th and 25th (Mawrth paleosurface and phyllosilicates) and 5th and 35th (Meridiani) percentile crater diameters from the artificial populations and our real data (Fig. 2.10). If our measured crater diameters fall within the range of diameters for each percentile that can be achieved by changing the fraction of time spent at low pressure (f) and changing the degree to which the population is modified by the preferential removal of small craters (n) for a combination of pressures, then our data can be reproduced by having an atmosphere varying between these two pressures during crater accumulation. We demonstrate that it is not possible to match the 5th and 25th (35th) percentile crater diameter for any combinations of pressures greater than the upper limit on continuous atmospheric pressure presented in Section 2.5 (Fig. 2.10). This is because the CSFDs for a high pressure atmosphere are more strongly dominated by larger craters, and

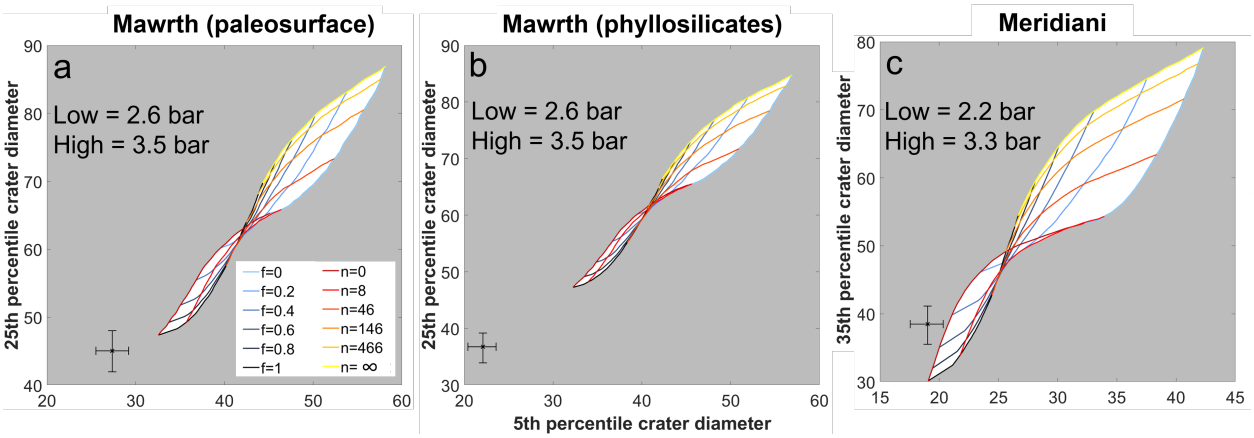

Figure 2.10: Our measured crater size frequency distributions (CSFDs) cannot be produced by any combination of atmospheric pressures above our continuous paleopressure upper limits, even when the CSFDs are modified by preferential removal of small craters. Contours of 5th and 25th (Mawrth paleosurface and Mawrth phyllosilicates data) and 5th and 35th (Meridiani) crater diameter for different fractions of time spent at low pressure (f, cool colours) and degrees of CSFD modification by preferential obliteration of small craters (n, warm colors) plotted on the same axes as the actual 5th and 25th percentile crater diameters for each site (black crosses with error bars). The 5th and 25th (35th) percentiles correspond to the small craters in the distribution. Error bars indicate mean difference between best-fit crater diameter and maximum and minimum crater diameters found using `circfit`. Greyed out areas are regions of parameter space for which it is not possible to reproduce the shape of the measured CSFD. High and low pressures are corrected to planet datum elevation (i.e., pressures are corrected from local site elevation to 0m elevation).

our population modification function preferentially removes smaller craters. This acts to flatten the CSFD and causes high pressure CSFDs to rotate clockwise relative to our data. This generates a greater apparent paleopressure. We conclude that our measured CSFDs cannot be produced by atmospheric pressures continuously above our paleopressure upper limits. This is a key finding which validates our main results in Section 2.5.

However, many different combinations of maximum and minimum pressures can reproduce our observed CSFDs (Fig. 2.11). Therefore, our method cannot rule out changes in atmospheric pressure during crater population accumulation. These changes in atmospheric pressure can occur through:

1. Large scale changes in sources and sinks

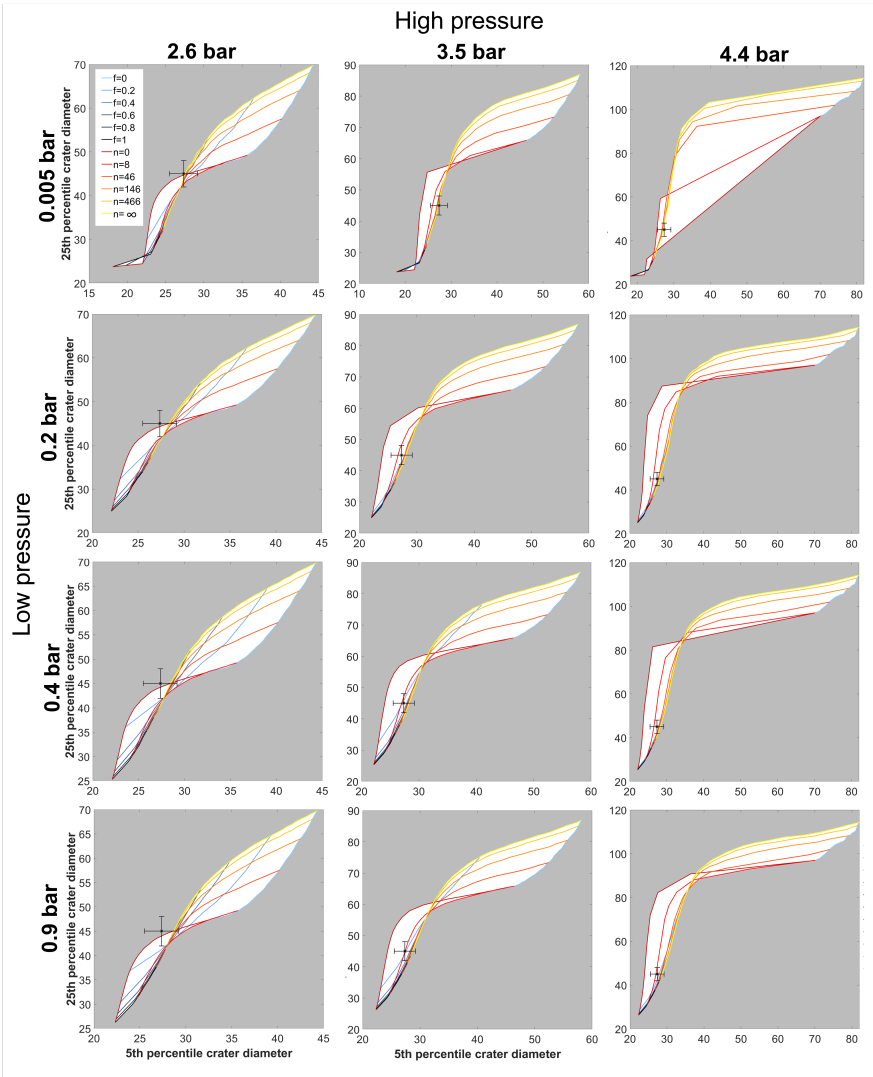

Figure 2.11: Our measured crater size frequency distributions (CSFDs) can be produced by time varying atmospheric pressure, provided that at least the minimum pressure is below our continuous paleopressure upper limits. Contours of 5th & 25th crater diameter for different fractions (f) of time spent at low pressure (cool colours) and degrees of CSFD modification (n) by preferential removal of small craters (warm colors) plotted on the same axes as the actual 5th and 25th percentile crater diameters for the Mawrth paleosurface (black crosses with error bars). Error bars indicate mean difference between best-fit crater diameter and maximum and minimum crater diameters found using `circfit`. Greyed out areas are regions of parameter space for which it is not possible to reproduce the shape of the measured CSFD. All pressures are corrected to planet datum elevation (i.e., pressures are corrected from local site elevation to 0m elevation).

2. Atmospheric collapse

Using crater production functions, we can estimate the minimum duration of time spent at present day atmospheric pressure. By selecting a diameter bin in a crater population of a known age, we can estimate the minimum accumulation time needed for the number of craters in that bin to accumulate at present-day atmospheric pressure. We observe seventeen 15.6 to 22.1m diameter craters (bin -1 Michael 2013) at our Meridiani site. This is the first diameter bin to have > 5 craters. This is important because it means that the crater diameter bin used does not represent the smallest possible crater than can form at 1.5 bar (this would yield an infinite accumulation time). Using the production and chronology functions given in Michael (2013), under a paleo-atmospheric pressure of 6 mbar that does not vary during the period of crater accumulation recorded by the embedded craters in our study, our observed crater populations would have accumulated over a minimum of 10^4 years (Mawrth phyllosilicates site) to 10^5 years (Meridiani). At higher atmospheric pressures, fewer craters of this size are expected to form, and a correspondingly longer time must be spent at high pressure to accumulate the observed craters (Fig. 2.12). We can multiply the accumulation time by the ratio of the flux of craters in the chosen diameter bin at present day pressure to the flux of craters in the same bin at a higher pressure. For a paleo-atmospheric pressure of 1.5 bar that does not vary during the period of crater accumulation recorded by the embedded craters in our study, our observed crater populations would have accumulated over a minimum of 10^5 years (Mawrth phyllosilicates site) to 10^6 years (Meridiani site). This calculation cannot be performed for the Mawrth paleosurface because crater production functions do not extend to before 4 Ga. All accumulation time estimates are subject to the uncertainties associated with the dating of the Mawrth phyllosilicates and Meridiani site, as well as uncertainties in the crater production functions used to calculate past cratering rate. If the crater population is older (younger), the flux of craters km^{-2} Ga^{-1} is higher (lower) (Michael, 2013), and the observed craters will need a shorter (longer) minimum accumulation time at any given pressure.

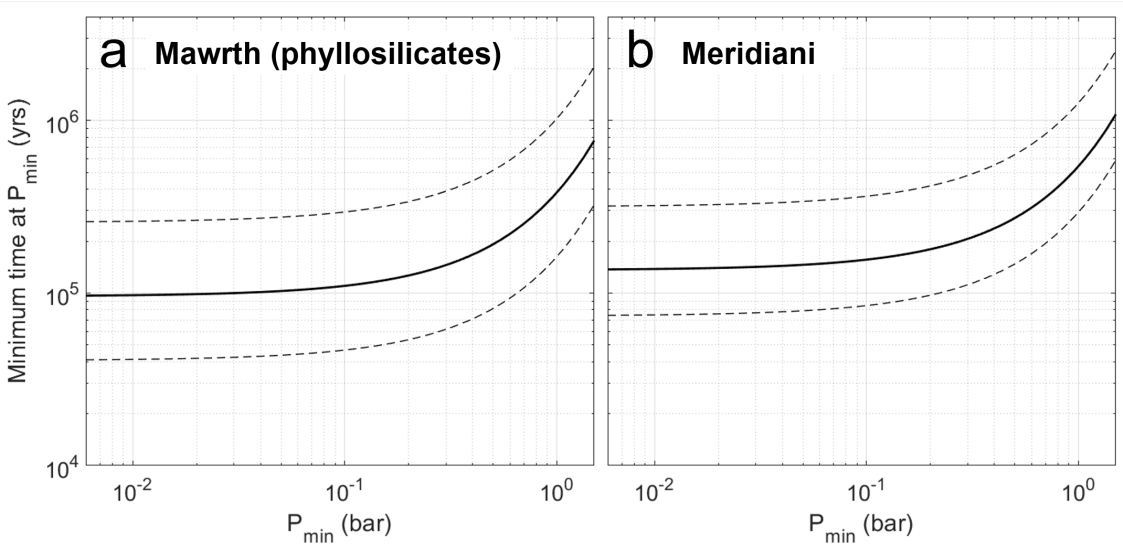

Figure 2.12: Minimum time needed for the observed number of craters in the diameter bin 15.6-22.1 m to accumulate as a function of minimum atmospheric pressure (P_{min}) for crater populations a) in the Mawrth phyllosilicates, b) at Meridiani. Solid curves show minimum accumulation times at each pressure if both sites are at their best-fit ages (3.8 ± 0.2 and $3.82^{+0.10}_{-0.18}$ Ga respectively). Dashed curves show minimum accumulation times at each pressure for the upper and lower limits on the ages of each site. X-axis range is 0.006 to 1.5 bar.

We expect smaller craters to be preferentially removed or missed in our crater counts. Therefore we consider it more likely that our measured CSFD for Meridiani corresponds to continuously low ($\ll 1.5$ bar) pressures rather than long periods spent at pressures $\gg 1.5 \pm 0.1$ bars with short (10^4 yr), low pressure excursions. This is further supported by the models of Forget et al. (2013) and Soto et al. (2015), which suggest that there are two different ways that the saturation vapor pressure of CO_2 can affect Mars' atmospheric pressure:

1. Obliquity-independent buffering of high atmospheric pressures to values below the saturation vapor pressure of CO_2 at the coldest point on Mars

2. Obliquity-dependent collapse into CO_2 icecaps between <0.1 and ∼0.5 bar.

This suggests that rapid oscillation between pressures >1.5 bar and <0.5 bar is unlikely to be possible through atmospheric collapse because the upper bound on atmospheric pressure for collapse to occur at any obliquity is relatively low (0.5 bar; Forget et al. 2013). Therefore,

for any time during crater population accumulation to have been spent at pressures >1.5 bar, 100 Myr-timescale changes in atmospheric pressure due to processes such as outgassing, impact delivery/erosion of volatiles, carbonate formation, and escape to space must also have occurred. These processes all leave imprints on Mars' geologic record that can potentially be compared to the timing of our measured crater populations to assess the feasibility of different atmospheric pressure histories and are constrained by factors such as the growth of Tharsis Phillips et al. (2001), shutdown of the Martian geodynamo, and reduction in atmospheric escape rates over time (Tian et al., 2009).

We can therefore identify 3 very different, pressure histories for Mars between ∼4 and 3.8±0.2 Ga that are equally consistent with our new results:

1. Pressure continuously at our upper limits on continuous atmospheric pressure.

2. Pressure continuously below the upper limit for atmospheric collapse (∼ 0.5 bar), with low pressure intervals caused by collapse.

3. Fluctuations in atmospheric pressure of several bar due to changes in the balance of atmosphere sources and sinks. The minimum atmospheric pressure must be below our upper limits on continuous atmospheric pressure.

2.6.3 Single-site atmospheric pressure upper limits are globally representative

Having demonstrated that our paleopressure estimates do in fact constrain atmospheric pressure at the time of crater population accumulation, we show that paleopressure at an individual site is representative for all of Mars once corrected for the exponential decrease in local surface pressure with increasing local elevation. On Earth, zero-elevation-corrected annual mean pressures vary only by several percent (Trenberth et al., 1987). As our paleopressure estimates are similar to the surface pressure of present day Earth, we expect that pressure gradients in the ancient Martian atmosphere would be of a similar order. However, on some

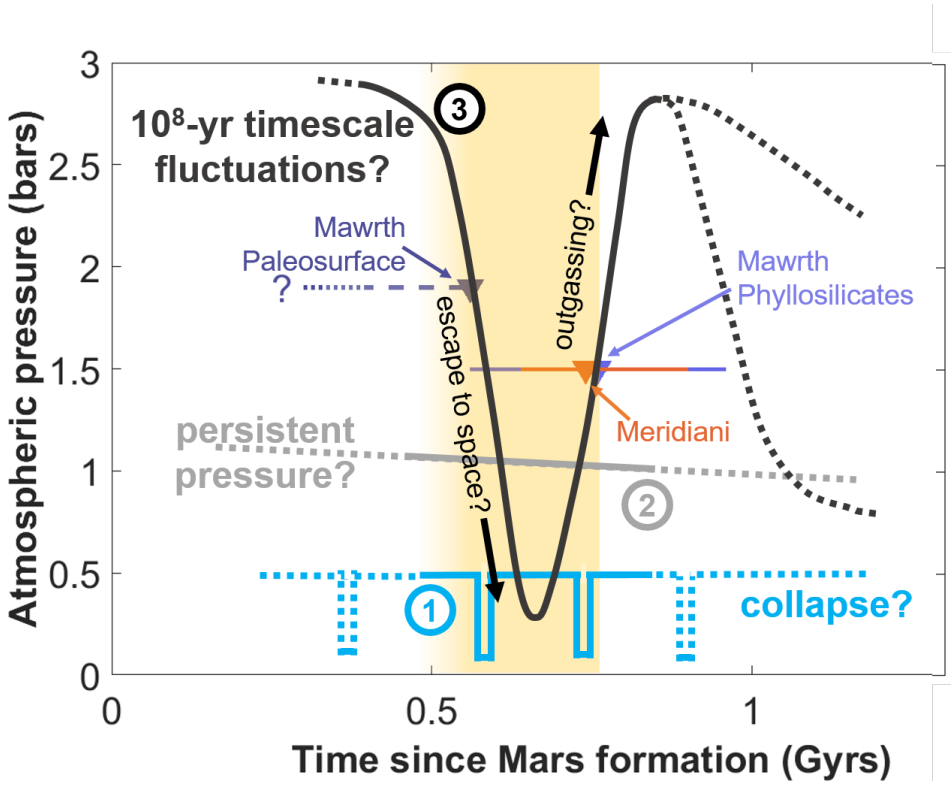

Figure 2.13: Schematic illustrating three atmospheric pressure histories for Mars between ∼4 Ga and 3.8±0.2 Ga (yellow area). Triangles with age uncertainties are our new upper bounds on continuous atmospheric pressure (dark purple at 4 Ga - Mawrth paleosurface, light purple - Mawrth phyllosilicates, orange - Meridiani). The blue box-car function illustrates a <0.5 bar atmosphere that undergoes periods of collapse. The grey line illustrates an atmosphere that remains continuously at our constant pressure upper limits. The black curve illustrates several bar of atmospheric pressure changes due to changes in atmospheric sources and sinks. Dotted lines/curves indicate time that is not covered by our new results.

Solar System bodies, such as Io, it is possible to sustain gradients in zero-elevation-corrected pressures on the order of 10 times mean atmospheric pressure (Jessup et al., 2004; Buratti et al., 2011). Assuming geostrophic balance (latitudinal pressure gradients balanced by Coriolis force) in a 1 bar Martian atmosphere, we can calculate a geostrophic wind velocity, u_g, for a pressure difference of $\Delta p = \frac{1}{5} p_{atm} \sim 2 \times 10^4$ Pa:

$$u_g = \frac{1}{\rho_0 f} \frac{\partial p}{\partial y} \tag{2.14}$$

where f is the Coriolis parameter $f = 2\Omega sin\phi$ (Ω - Mars rotation rate $\sim 7.1 \times 10^{-5}\,\mathrm{rad\,s^{-1}}$, ϕ - latitude ($^\circ$)).

$$p_{atm} = \rho_0 g h \tag{2.15}$$

The density of Earth's atmosphere is $\approx 1\,\mathrm{kg\,m^{-3}}$, and Mars' gravity is approximately 3 times less of the Earth. Assuming the scale heights to be comparable for both planets, we take $\rho_0 \approx 3\,\mathrm{kg\,m^{-3}}$ for Early Mars. For $\phi = 30^\circ$, and using the equator-pole distance as a representative length scale $L \sim 5 \times 10^6$m, $u_g \approx 30\,\mathrm{m\,s^{-1}}$. If the Rossby number $Ro = \frac{U}{fL} \ll 1$, then geostrophic balance is a valid assumption. For $u_g = 20\,\mathrm{m\,s^{-1}}$ $Ro \approx 0.1$.

Assuming that the ideal gas law holds and the difference in pressure is sufficiently small, we can say that:

$$\frac{\Delta T}{T} \propto \frac{\Delta p}{p} \tag{2.16}$$

This allows us to define a pressure relaxation timescale τ_p:

$$\tau_p \propto \frac{T}{u_g \left(\frac{\Delta T}{\Delta y}\right)} \propto \frac{pL}{u_g \Delta p} \tag{2.17}$$

This gives $\tau \sim 12$ days.

Maintaining a pressure gradient requires an energy input. Pressure has units of energy density. We can imagine a simple case where energy (Q) is supplied via a region of high surface temperature that heats the overlying CO_2 atmosphere with mass $m = \frac{p}{g}$ initially at ~ 300 K to a temperature sufficient to produce the pressure difference of 2×10^4 Pa (Equation 2.18). This area needs to supply energy above that supplied to the rest of the atmosphere to maintain the pressure gradient.

$$Q = \frac{p}{g} c_{p_{CO_2}} T \frac{\Delta p}{p} \tag{2.18}$$

This energy needs to be supplied on a timescale $\leq \tau$, which tells us the rate at which energy

needs to be supplied to the atmosphere to sustain the pressure difference, $\sim 1.3\times10^3$ W m^{-2}. It is very difficult to devise a mechanism to maintain a rate of energy supply on this scale. From the Stefan-Boltzmann equation, $F = \sigma T^4$, this would require the region of elevated surface temperature to be at around 420K: 120K higher than the background. The lower the background surface temperature, the greater this difference would need to be. This surface temperature anomaly would need to span an area comparable to the area of the p anomaly in order to sustain it, otherwise all heat would rapidly dissipate in the surrounding atmosphere. Alternatively, the source of the anomaly would need to be immediately adjacent to one of our study regions. Additionally, for the pressure anomaly to have a significant effect on the observed CSFD, the energy source would need to persist for millions of years. For comparison, typical cooling timescales for magmatic intrusions are on the order of kyrs (Costa et al., 2008). Additionally, lavas could not supply the required power due to the formation of chill crusts (Matson et al., 2006). Giant impacts have been proposed as a mechanism for raising the surface temperature through the delivery of large amounts of kinetic energy (Segura et al., 2012). However, modeling studies of impacts on this scale suggest that the heating effect would be 1) global, and 2) short-lived (< 10 yrs) (Turbet et al., 2020; Steakley et al., 2019).

We also consider the maximum pressure gradient that could be sustained on Early Mars by differences in insolation across the surface. Assuming an obliquity of 0°, insolation will vary from a maximum at the equator to 0 at the poles. Taking Earth's Solar Constant to be $G_{SC_{Earth}}$ =1361 W m^{-2} and a Sun at 70% of its current brightness at ~ 4 Ga (Gough, 1981; Bahcall et al., 2001), we can construct an expression for maximum insolation (F_{max}) on Mars:

$$F_{max} = \frac{G_{SC_{Earth}}}{\left(\frac{R_{Earth}}{R_{Mars}}\right)^2} \times \frac{0.7}{\pi} = 131.7\,\mathrm{W\,m^{-2}} \tag{2.19}$$

where R_{Earth} and R_{Mars} are distances to each planet from the Sun. Using the pressure relaxation timescale from Equation 2.18 gives $Q = 5.83 \times 10^6$ J m^{-2}. Rearranging Equa-

tion 2.18 and assuming an average surface temperature of 273 K, the maximum possible zero-elevation corrected pressure difference is only of order 1190 Pa, or ∼1.2% of the total atmospheric pressure. Even in the most extreme case where the average Martian surface temperature is low (210 K) and the sun at 4 Ga is assumed to be as bright as at present, this value only rises to 2160 Pa, or less than 2.2% p_{atm}. Therefore, we conclude from these order of magnitude estimates that the paleopressure estimates in this study can be taken as representative of the global Martian atmosphere.

2.7 Integrating new constraints with existing data using a 2-component atmospheric evolution model

Detailed atmospheric evolution models rely on balancing fluxes from atmospheric sources and sinks (Pepin, 1994; Haberle et al., 1994; Slipski and Jakosky, 2016; Cassata et al., 2012; Kurokawa et al., 2018; Dong et al., 2018; Jakosky, 2019). The main sources for the Martian atmosphere are mantle outgassing and impact delivery of volatiles (Jakosky et al., 2018; Sakuraba et al., 2019). There may be additional contributions from retention of a nebular atmosphere (Saito and Kuramoto, 2017), and thermal decomposition of carbonates (Pollack et al., 1987; Glotch and Rogers, 2013). Mantle outgassing throughout Mars' history can be estimated from the rate of crustal production, which has decreased over time, as suggested by geologic evidence (Nimmo and Tanaka, 2005; Tanaka et al., 2003; Greeley and Schneid, 1991), and thermal evolution models (Morschhauser et al., 2011; Hauck and Phillips, 2002). The amount of volatiles outgassed depends strongly on the volatile content of Mars' mantle, which is not well constrained. Phillips et al. (2001) suggest that the growth of Tharsis may have contributed up to 1.5 bar of CO_2, however, depending on Martian mantle redox state, outgassed CO_2 may not have been sufficient to make a significant difference to atmospheric pressure (Stanley et al., 2011). The possible major sinks for the atmosphere are escape to space (Chassefière et al., 2007; Dong et al., 2018; Jakosky et al., 2018), impact erosion of

the atmosphere (Schlichting et al., 2015; Pham and Karatekin, 2016), carbonate formation (Stephens and Stevenson, 1990; Wray et al., 2016), surface weathering (Baker, 2017), transport of CO_2 into the subsurface (Manning et al., 2019; Kurahashi-Nakamura and Tajika, 2006), and condensation into ice caps (Bierson et al., 2016). Ion escape, sputtering, and photochemical loss mechanisms such as dissociative recombination are all strongly dependent on Solar EUV flux and solar wind mass flux (Ayres, 1997; Chassefière and Leblanc, 2004; Brain et al., 2016) which have both decreased over geologic time (Dorren and Guinan, 1994; Tu, Lin et al., 2015). However, many of these processes are poorly constrained. We therefore chose to construct a basic, 2-component, process-agnostic model that gathers all sources and all sinks into one term each. The purpose of this exercise is to explore the most simple possible pressure evolution tracks for Mars' atmosphere that satisfy existing paleopressure constraints.

In our model, we express sources and sinks as either a power-law of the form:

$$\frac{\mathrm{d}p}{\mathrm{d}t}_{(source,sink)} = k_{(1,3)} t^{-k_{(2,4)}} \tag{2.20}$$

or an exponential:

$$\frac{\mathrm{d}p}{\mathrm{d}t}_{(source,sink)} = k_{(1,3)} \exp\left(\frac{-t}{-k_{(2,4)}}\right) \tag{2.21}$$

where k_1, k_2 (sinks), k_3 and k_4 (sources) are free parameters. For the case shown in Fig. 2.14 (10,000 combinations of k_{1-4}), we select 10 uniformly spaced values of k_{1-2} between maximum and minimum values tuned to span the range that gives the greatest density of solutions in pairs plots for each source-sink set-up. For k_{3-4}, 10 uniformly logarithmically spaced values are selected between maxima and minima found in the same way. This gives 4 possible source-sink set-ups (1. exponential source + exponential sink, 2. powerlaw source + exponential sink, 3. exponential source + powerlaw sink, 4. powerlaw source + powerlaw sink). From our tuning process, k_{1-4} are always positive. This is appropriate because we expect

both sources and sinks to diminish forwards in time (Jakosky and Phillips, 2001). Overall change in atmospheric pressure at each timestep is given by:

$$\frac{\mathrm{d}p}{\mathrm{d}t\,(net)} = -\frac{\mathrm{d}p}{\mathrm{d}t\,(sink)} + \frac{\mathrm{d}p}{\mathrm{d}t\,(source)} \tag{2.22}$$

We integrate Equation 2.22 To find k_{1-4}, we use the upper limits of existing paleopressure estimates as hard constraints (shown in Fig. 2.7), and implement the constraint that $\frac{dP}{dt}$ at $t = 0$ must be less than the maximum observed MAVEN loss rate (12^b). We exclude the cosmochemical estimate for Mars' initial CO_2 inventory (1^c) because this value is an estimate, and an unknown proportion of the initial volatiles may remain in the mantle. We exclude the constraint given by Kurokawa et al. (2018) (3^c). Their models conclude that the atmosphere must have been uncollapsed at 4.1 Ga to reproduce observed noble gas isotopic compositions in ALH84001 and the modern Martian atmosphere. In their models, the collapse threshold is fixed at 0.5 bar. However, the collapse threshold varies depending on obliquity (Nakamura and Tajika, 2003; Forget et al., 2013; Soto et al., 2015). Mars' obliquity history is chaotic and poorly constrained (Touma and Wisdom, 1993; Laskar et al., 2004), and therefore the Kurokawa et al. (2018) lower limit may in fact be several times lower. Finally, we exclude the paleopressure estimate of Bristow et al. (2017) (9^{*c}) which was based on reaction-transport modeling of siderite stability. Their models have been superseded by more recent experimental results of Tosca et al. (2018). Tosca et al. (2018) demonstrate that siderite can in fact form at higher pCO_2 under expected early Mars conditions.

We integrate Equation 2.22 backwards in time, starting at a present day atmospheric pressure of $p_0 = 0.012$ bar (i.e. including CO_2 stored in ice caps) with the maximum atmospheric loss rate constrained by the upper limit of the observed MAVEN loss rates (Lillis et al., 2015). This means that we do not prescribe an initial atmospheric pressure for Mars. However, we do force $p > 0$ bar at 4.16 Ga, as this is the age of the earliest paleopressure constraint from the isotopic composition of ALH84001 (Cassata et al., 2012),

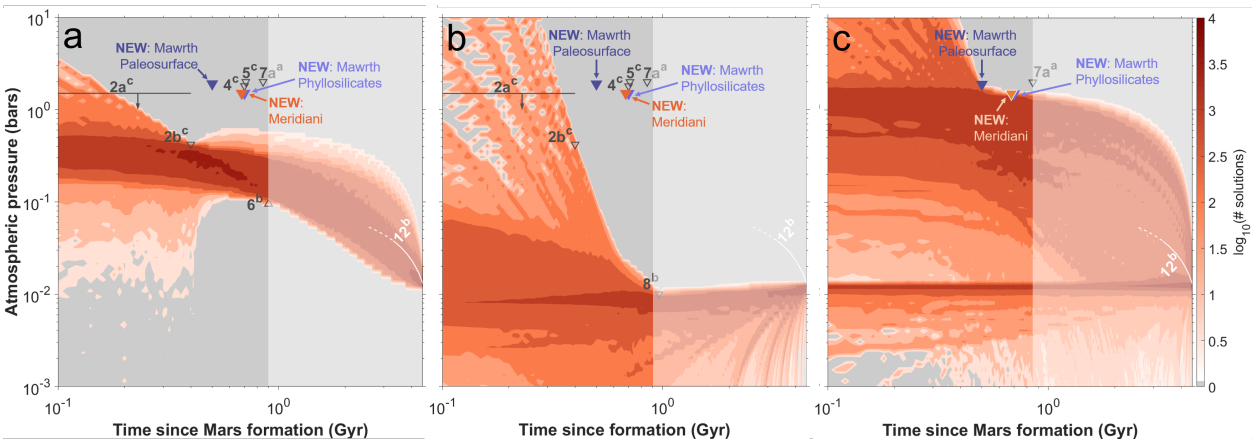

Figure 2.14: Solution density contour plots of pressure histories allowed by existing paleopressure estimates from our basic, 2-component atmospheric evolution model. All possible source/sink combinations are superimposed on one another for 10,000 possible combinations of k_{1-4}. Dark grey areas do not match data. Washed out (light grey) region indicates area of graph from ~3.6 Ga to present where no paleopressure estimates exist and solutions are not well constrained. $\log_{10}(\#\text{ solutions}) = 4$ indicates that 10,000 possible solutions pass through point. a) lower bound on paleo-atmospheric pressure comes from Manga et al. (2012) (6^b), pressure calculated from bomb sag structure at Home Plate at $3.66\pm^{0.44}_{0.31}$ Ga and b) Lapotre et al. (2016) (8^b), pressure calculated from large wind ripples in the Burns formation as the maximum constraint /3.6 ± 0.1 Ga respectively c) only paleopressure constraints from ancient crater size frequency distributions (methods used in this paper). 12^b is the upper limit on MAVEN escape rate extrapolated backwards through time. This is only enforced as a constraint at $t = 4.56$ Gyr (i.e. Neumann boundary condition at present day). All other constraints are as for Fig. 2.7.

so we assume that some atmosphere must have been present at this time in order for an 'atmospheric component' to be trapped in the meteorite. Our model does not allow negative atmospheric pressures. If pressure becomes negative at any timestep it is re-set to 0 bar.

The four possible exponential-powerlaw combinations for sources and sinks generate a wide variety of possible pressure histories for Mars. We treat each of the four combination as equally likely. While we do not seek to accurately reproduce Mars' atmospheric pressure history, these models give a qualitative impression of pressure histories allowed by the current data. Therefore, due to the lack of constraints after 3.6 Ga — with the exception of measured MAVEN loss rates — we limit our discussion to atmospheric pressure between 4.3 and 3.6 Ga.

As expected, our model is most strongly affected by the lowest implemented paleopres-

sure constraint. However, a common feature of our initial paleopressure tracks is a low initial atmospheric pressure, typically < 0.5 bar (Fig. 2.14). This agrees with constraints from modeling of noble gas isotope evolution from ALH84001 to present (Cassata et al., 2012), which suggest that atmospheric pressure was <1.5 bar for the first 400 Myr of Mars' history. However, it does not agree with the thick atmospheres invoked in current models of greenhouse warming of early Mars to $\sim$ 273K (Wordsworth et al., 2013; Ramirez, 2017; Turbet et al., 2019). Although there is no region of parameter space for which our set-up can include both the Home Plate bomb sag constraint (Manga et al. 2012, 6^b) and wind ripple constraints (Lapotre et al. 2016, 8^b), it is possible to imagine a pressure history involving rapid changes in atmospheric pressure to satisfy both constraints at their published ages (Fig. 2.15). If the wind ripple estimate (Lapotre et al. 2016, 8^b) is implemented as a constraint, the only other paleopressure estimate that affects the permitted solutions is from the Cassata et al. (2012) result ($2b^c$) (Fig. 2.4b). This set-up also gives rise to many solutions in which atmospheric pressure $<$ present for much of Mars' history. In the case where the Home Plate bomb sag constraint (Manga et al. 2012, (6^b) is implemented, the Cassata et al. (2012) result ($2b^c$) is the dominant control on the permitted paleopressure histories. This is most likely because this is the earliest constraint and therefore sets the effective maximum pressure because the majority of values for k_{1-4} generate pressure histories that decrease towards the present (we do not implement episodes of atmospheric collapse in our maximally simple model). As discussed in Section 2.4, applying a fractal correction to our synthetic CSFDs lowers our paleopressure estimates. However, when Cassata et al. (2012) ($2b^c$) is implemented as a constraint, pressure is already too low by 4 Ga for our new estimates to impact the allowed paleopressure histories, regardless of whether Manga et al. (2012) (6^b) or Lapotre et al. (2016) (8^b) are implemented as constraints. This emphasizes the impact of early paleopressure estimates on our understanding Mars' atmospheric evolution over time. This is inconsistent with geologic evidence for surface liquid water on Mars,

as present day annual mean temperatures and pressures do not allow for channel-forming quantities of liquid water to be stable on Mars' surface even at higher solar luminosities. It is currently unclear whether the existing rock record on Mars extends before 4 Ga, therefore it is not possible to apply the technique used in this paper to this time period, if indeed the interpretable-from-orbit Martian sedimentary rock record extends back this far.

Figure 2.14c shows the permitted pressure histories if only paleopressure upper limits from small exhumed crater methods (i.e., this paper and Kite et al. 2014) are enforced as constraints. The narrow time window covered by our new upper limits means that the majority of Mars' atmospheric evolution is poorly constrained by these data and a much wider range of paleopressure histories are permitted. This gives rise to two separate regions of maximum solution density in time-pressure space. The first cluster of solutions starts between 0.5 and 1.8 bar early in Mars history and remains steady $\sim$ 4 Ga when pressure begins to decreae towards present day values. The second cluster starts at $\sim$0.012 bar (i.e. modern atmospheric pressure if ice caps are included (Bierson et al., 2016) and remains at aproximately constant pressure for all of Mars history. There is also a third cluster with a lower density of solutions that start off at very high initial atmospheric pressure (of order 10s of bars). This exceeds the cosmochemical estimate of Mars' initial volatile inventory (Lammer et al., 2013), but these pressure histories cannot be ruled out by CSFD-based paleopressure estimates alone due to the absence of cratering ages before 4 Ga, and because Mars' sedimentary record may not extend this far back in time.

The lack of paleopressure estimates prior to 4 Ga and after 3.6 Ga makes it difficult to meaningfully assess the sensitivity of our model to each individual constraint. Once again, this motivates a search for more paleopressure constraints both between 3.6 Ga and present, and deep in Mars' history. Our CSFD method can only be applied where craters are embedded in stratigraphy. While we have focused on using orbiter data to investigate sedimentary rocks that may preserve evidence for liquid water on or near the Martian surface

during deposition (Malin and Edgett, 2000), it may be possible to apply the technique to aeolian sediments in the search for more recent paleopressure estimates (Vasavada et al., 1993; Nuno and Paige, 2019).

2.8 Conclusions

Our objective in this study was to obtain new constraints on Mars' paleopressure history 3.8-4 Ga. To do this, we compared crater populations preserved in ancient sedimentary rocks in Mawrth Vallis (>4 Ga & 3.8 ± 0.2 Ga) and Meridiani Planum ($3.82^{+0.10}_{-0.18}$ Ga) to predicted crater populations generated from a forward model of atmosphere-impactor interactions. At 3.8 ± 0.2 Ga, our results are consistent with two end-member cases:

1. Continuous paleo-atmospheric pressure of 6 mbar during the period of crater accumulation. Observed crater populations accumulated over a minimum of 10^4 years (Mawrth phyllosilicates site) to 10^5 years (Meridiani).

2. Continuous paleo-atmospheric pressure of 1.5 bar during the period of crater accumulation. Observed crater populations accumulated over a minimum of 10^5 years (Mawrth phyllosilicates site) to 10^6 years (Meridiani).

Our measured CSFDs indicate that paleoatmospheric pressure on Mars >4 Ga was either continuously below 1.9±0.1 bar, or varied between pressures above and below this upper limit on continuous atmospheric pressure. Theerefore, our new data are consistent with either continuously low (< 1.5 bar) atmospheric pressures, or alternatively variations of several bar in atmospheric pressure due to the changing balance between atmospheric sources and sinks. Thus, a diverse range of paleopressure histories for Mars in the interval 4-3.8±0.2 Ga are all consistent with our new data (Fig. 2.13. Source and sink processes leave imprints on Mars' geologic record that we can potentially compare to the timing of our measured crater populations to assess the feasibility of different atmospheric pressure histories. The feasibility

of pressure oscillations with amplitudes of several bar between pressures above and below our upper limits on continuous pressure due to changes in processes such as outgassing, impacts, escape to space, and carbonate formation from 4-$\pm$0.2 Ga could be constrained through better dating of our ancient embedded crater counting sites (e.g. through sample return missions), improved understanding of the extent and duration of carbonate deposition on Mars, and better relative and absolute age-dating for events such as the growth of Tharsis.

Our results agree with existing paleopressure constraints, including sedimentary features such as the Home Plate bomb sag (Manga et al., 2012) (6^b), and modeling studies based on mineral stability and carbonate deposition (Hu et al. 2015 (5^c), van Berk et al. 2012 (4^c), where superscripts refer to Fig. 2.7). We also demonstrate that paleopressure estimates for a single site are representative of global zero-elevation corrected surface pressure. However, due to the effects of sedimentation and erosion on observed crater populations, our results give conservative (high) upper bounds.

We combine our new paleopressure upper limits with existing constraints, and compare the combination to the output from a basic model of Mars atmospheric pressure evolution. Our process-agnostic, 2-component model of sources and sinks of volatiles (CO_2) to the atmosphere is very strongly sensitive to constraints that give lower bounds on atmospheric pressure (Fig. 2.14). Additionally, our method cannot constrain rapid changes in atmospheric pressure due to collapse (Fig. 2.15). Thus, more paleopressure constraints for Mars are needed, particularly between 3.6 Ga and present where the only existing constraints are the measured MAVEN escape rate and Mars' existing surface and atmospheric CO_2 reservoirs. The greatest density of possible solutions for Mars' atmospheric pressure history suggest atmospheric pressures on Early Mars between 0.01 and 1 bar. This agrees with the earliest upper bounds on atmospheric pressure as modelled using data from ALH84001 (Cassata et al., 2012) ($2a^c$ & $2b^c$, Fig. 2.7). This range is significantly lower than our new paleopressure upper bounds.

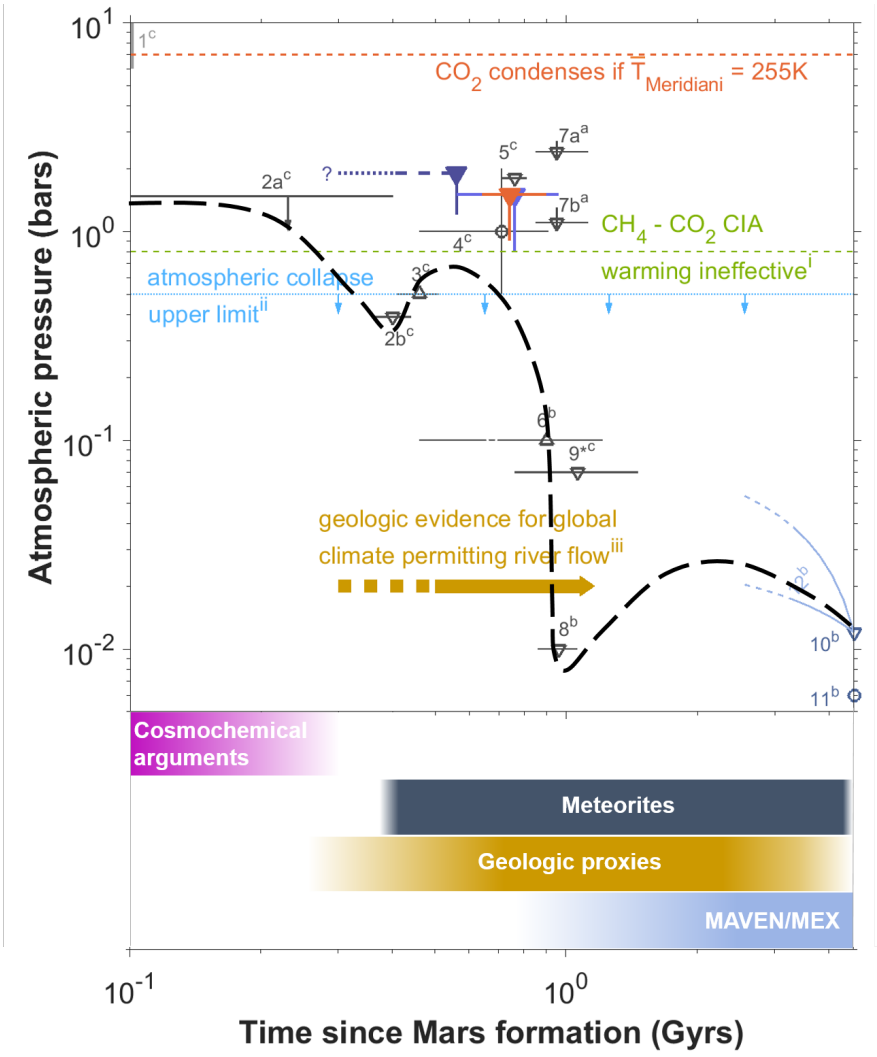

Figure 2.15: Schematic illustration of one possible pressure history for Mars that satisfies all existing paleopressure constraints. Superscripts: a - constraints from small, ancient, embedded craters, b - constraints from remote sensing, c - constraints from all other techniques (meteorite analyses, modeling, etc.). Upward (downward)-pointing triangles - lower (upper) bounds. Circles - estimates of absolute atmospheric pressure or direct measurements. Downward arrows from a horizontal line - pressure must have been below the given value for the entire time interval. Numbers for paleopressure constraints are as for Fig. 2.7. i) CH_4-CO_2 collision-induced absorption warming is ineffective below atmospheric pressures of 0.8 bar (Turbet et al., 2019), ii) from GCMs, the upper bound on atmospheric pressure for atmospheric collapse into CO_2 ice caps to occur is 0.5 bar (Soto et al., 2015; Forget et al., 2013), iii) the last year that widespread fluvial activity on Mars was permitted by global climate was <3.4 Ga (Kite, 2019) (additionally, there is evidence for <1 Ga Amazonian supraglacial channels (Dickson et al., 2009) and late (< 2 Ga) alluvial fan activity in Gale Crater (Grant and Wilson, 2019))

CHAPTER 3

OVERSPILLING SMALL CRATERS ON A DRY MARS: INSIGHTS FROM BREACH EROSION MODELING

This chapter was originally published as: Warren, A. O., Holo, S., Kite, E. S., and Wilson., S. A. "Overspilling small craters on a dry Mars: Insights from breach erosion modeling." *Earth and Planetary Science Letters* 554 (2021): 116671. The term “pollywog" (a small, relatively young crater with one or more overspill channels but no visible inlet) used in the publication has been replaced with “tadpole crater" for consistency throughout this thesis.

S.A.W. contributed a database of tadpole craters from the Arabia Terra region of Mars. S.H. designed the original breach erosion modeling approach and wrote the original MATLAB code, which was significantly modified by A.O.W. to include drawdown of the lake surface before the breach and a procedure to iteratively find the optimal grainsize for erosion. All authors contributed to editing the paper and the revisions.

We thank Caleb Fassett for pointing out low latitude tadpole craters, and the HiWish program for targetting requested tadpole craters. We would also like to thank Tim Goudge and an anonymous reviewer for their insightful comments and suggestions which helped clarify the manuscript. We thank Shavonne Morin at the University of Arizona for producing the DEM in Fig. 3.1. All stereopairs are publicly available on the HiRISE website. Our DEMs are publicly available at https://uchicago.box.com/v/tadpole crater-DEMs2020. We acknowledge the use of University of Chicago Research Computing Center resources.

Grants: NASA NNX16AG55G (E.S.K.), NASA 80NSSC19K1221 (S.A.W.), and NASA NNX15AM49G (E.S.K.).

3.1 Abstract

Understanding when, where, and how frequently liquid water was stable on Mars since the Late Noachian/Early Hesperian (3.2-3.9 Ga) is important for understanding the evolution of Mars' climate and hydrology. Some relatively young features on Mars require multiple wetting events to form, whereas others are consistent with single wetting events. Small and rare exit breach craters or "tadpole craters" are craters between 0.5 and 15 km in diameter with valleys leading away from the lowest point on their rims but no visible inlet valleys. These craters must have been filled with water to the point of overspill to form the observed valleys. The two possible water sources are precipitation and groundwater. In this paper we use measurements from Digital Elevation Models (DEMs) of 18 tadpole craters (21 outlet valleys) and a fixed channel width 0-D breach erosion model to determine whether tadpole crater exit breach valleys are consistent with a single crater overspill event, or if their formation requires multiple overspill events. Our model, which we compare to a selection of dam breaching events on Earth, predicts runaway erosion for two tadpole crater exit breaches. No runaway erosion is observed. We discuss potential explanations for this mismatch between the data and our model. We show that the majority of tadpole craters on Mars are consistent with formation during a single crater overspill event, incorporating a work around for the long-standing problem of unknown grainsize into our approach. Three tadpole craters require either multiple events or sustained water supply to drive erosion. We discuss potential source mechanisms for crater-filling water and conclude that tadpole craters either formed in a single erosion event, driven by groundwater discharge, or through many small erosion events, driven by draining of small meltwater lakes formed on crater-filling bodies of ice.

3.2 Introduction

Surface liquid water on Mars requires conditions very different from the present day; either temperatures > 273 K resulting from different climate conditions, or transport of water out of the subsurface for example by groundwater outflows Rodriguez et al. (2015). If the water source is known, morphological features (e.g. fluvial channels, lake deposits) can be used to understand either the evolution of the Martian climate and atmosphere, or the evolution of the hydrosphere. Wet events on Mars since the Valley Network forming period (<3.2-3.9 Ga, Hartmann 2005) are recorded by the formation of features such as alluvial fans Kite et al. (2019); Hauber et al. (2013), and small exit breach craters or "tadpole craters" (Wilson et al., 2016). These features indicate a trend from an earlier, wetter climate with intense fluvial erosion (Matsubara et al., 2013), to arid conditions punctuated by occasional surface liquid water (Kite et al., 2019). Tadpole craters have outlet valleys extending from well-preserved crater rims, but no inlet valleys (Wilson et al., 2016) e.g. Fig. 3.1a. The outlet valleys formed by overspill of water from within the crater. Fresh tadpole crater rims indicate that tadpole crater outlet incision post-dates the intense Late Noachian and Early Hesperian fluvial activity (Wilson et al., 2016). Tadpole breach formation requires a water source that left crater rims intact, but was intense enough to supply $> 10^7$ m^3 of water under dry climate conditions. Two possible sources of this water are groundwater (e.g. from a pressurized aquifer at depth), and precipitation and/or melting (Fig. 3.2). If erosion during a single tadpole crater overspill event can be constrained, then the observed erosion from tadpole crater overspill events is an important constraint on the number, duration, and intensity of mid-latitude surface liquid water events on Mars since the Late Noachian/Early Hesperian (3.9-3.2 Ga) (Hartmann, 2005).

Low-latitude alluvial fans require multiple episodes of wetting (Hauber et al., 2013; Kite et al., 2019). Groundwater modeling has shown that outflow channel formation may be more consistent with multiple, smaller-magnitude groundwater discharge events than a single flood

(Andrews-Hanna and Phillips, 2007). However, other features are consistent with a single wet event, for example impact-driven melting and precipitation in Mojave and Hale craters (Goddard et al., 2014). Do tadpole craters belong to the first group of features (Gale, alluvial fans) that record signatures of global climate conditions during the Hesperian? Or do they result from localized groundwater or impact-induced conditions?

Global climate and local conditions are plausible explanations for tadpole craters. Accumulating sufficient surface liquid water to overspill a tadpole crater through precipitation and snowmelt is challenging in a climate that is consistent with low erosion rates (Golombek et al., 2006) and valley distributions and morphologies consistent with reduced precipitation rates relative to the Noachian (>3.6-3.7 Ga) (Harrison and Grimm, 2005). Models of Martian climate under different orbital conditions can produce ice accumulation in midlatitudes (Mischna et al., 2013), and some melting (Kite et al., 2013). This makes ice-filled craters with melt ponds on their surfaces a plausible watersource for tadpole crater outlet valley erosion (e.g. Fig. 3.2). Orbital changes provide a potential mechanism for pacing surface liquid water activity (Jakosky et al., 1995). Large impacts (Steakley et al., 2019; Turbet et al., 2020) may also be able to induce short-lived climates enabling surface liquid water. Groundwater discharge from pressurized aquifers is an alternative mechanism for supplying liquid water to the surface during the Hesperian (Andrews-Hanna and Phillips, 2007; Rodriguez et al., 2015), e.g. in Xanthe Terra (Coleman, 2005), and some large (D >30 km) crater lake breach valleys (Warner et al., 2010).

The expected valley floor erosion from a single tadpole crater overspill event compared with observed erosion depths is an important constraint on Mars' climate and hydrology since the Late Noachian/Early Hesperian (Fig. 3.1a) because it can be used to infer the properties of the tadpole crater-overspilling water source. In this paper, we determine whether tadpole crater exit breach valleys are consistent with a single overspill event, or if their formation requires multiple overspill events. We use a new fixed channel width 0-D model

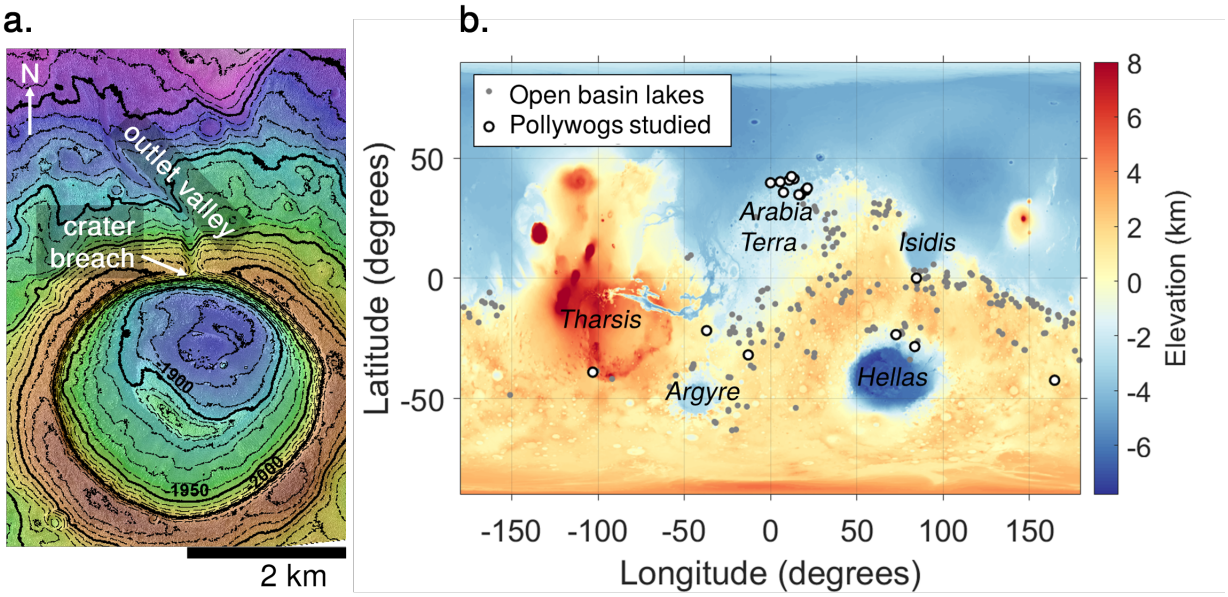

Figure 3.1: a. Tadpole crater HiRISE Digital Elevation Model (DEM) centered at 34.797°N, 17.398°E (ESP_053222_2150/ESP_052945_2150) overlain on orthophoto. Elevations relative to Mars geoid. Thick contour spacing is 50m. Thin, dashed contour spacing is 10m. b. Topographic map of Mars showing locations of DEMs of exit breach craters (tadpole craters) used in this study (Table 3.1) and Valley Network-fed open basin lakes (i.e. lakes with outlet valleys) (Fassett and Head, 2008) for comparison with older, climate-driven Noachian features. Topography data comes from the Mars Orbiter Laser Altimeter (MOLA).

(Section 3.3.1) and tadpole crater measurements from HiRISE Digital Elevation Models (DEMs) (Section 3.4.1) to predict the erosion that can occur in a single crater overspill event. The model is ground-truthed using terrestrial dam breach flood data (Section 3.4.2). We compare model predictions and observed breaches (Section 3.5), and consider the climate and hydrological conditions under which all studied tadpole craters could be consistent with a single overspill event (Section 3.6).

3.3 Methods

In Section 3.3.1 we describe our new model for breach erosion. In Section 3.4.1 we describe our tadpole crater measurements, their implications, and how they are used in the breach erosion model. In Section 3.4.2 we test the model against terrestrial exit breach erosion

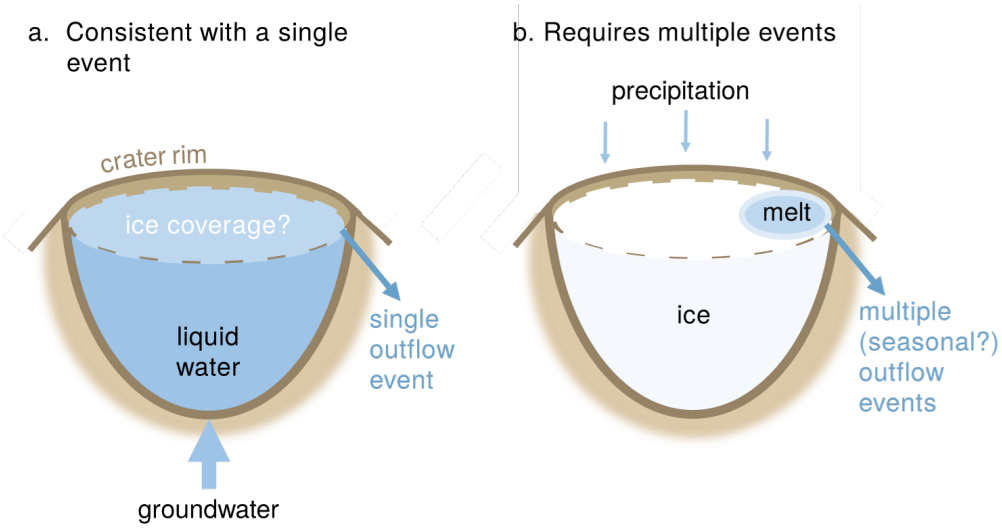

Figure 3.2: Schematic illustration of preferred tadpole crater overspill mechanisms. a. Crater fills and overspills during a single groundwater discharge event. $Q_{in} > 0$ is required for some craters (Section 3.6). b. Crater fills gradually with ice. Favorable climate conditions enable a melt pond/annulus smaller than the crater to form, which drains over the crater rim, contributing a small amount of erosion per overspill event. This mechanism repeats until the full breach depth is eroded.

events.

3.3.1 Breach Erosion Model

Previous studies of crater overspill erosion on Mars (Goudge et al., 2019) have adapted models of terrestrial flooding, e.g. dam failure and weir flow (Walder and O'Connor, 1997). These models work well for flow breaching small barriers within a pre-existing channel (Morris et al., 2009; Walder and O'Connor, 1997). However, when the dam (the crater rim for tadpole craters) extends for a greater distance down the valley, the cross section of the newly eroded channel restricts the flow of water downstream, affecting how the channel cross section varies over time through erosion (Morris et al., 2009). This is important for erosion into crater ejecta with no pre-existing valley. We used a new fixed channel width 0-D model, adapted from Holo and Kite (2019), to investigate breach erosion processes.

Our model couples lake drainage to breach erosion by combining conservation of mass,

Breach		DEM (Left Image)	Lat (° N)	Long (° E)	Diameter (D, km)
1		ESP_049860_2160	35.800	7.546	10.1 ± 0.20
2		ESP_053367_2220	41.438	13.633	1.8 ± 0.04
3		ESP_055330_1565	-23.410	72.793	0.7 ± 0.01
4		ESP_061037_1375	-42.399	164.775	9.6 ± 0.31
5		ESP_061782_1480	-31.851	-12.883	10.9 ± 0.24
6		ESP_052112_1800	0.096	84.656	11.2 ± 0.37
7		ESP_053169_2170	36.703	20.651	5.6 ± 0.06
8		ESP_055147_2170	36.683	20.538	4.2 ± 0.07
9		ESP_055266_2210	40.887	10.838	3.8 ± 0.09
10		ESP_059541_1580	-21.751	-37.027	2.5 ± 0.05
11		ESP_034014_1405	-39.052	-103.026	10.4 ± 0.33
12		ESP_052945_2150	34.797	17.398	3.6 ± 0.10
13	a	ESP_053736_2180	37.573	21.404	6.3 ± 0.37
	b				6.3 ± 0.37
	c				6.3 ± 0.37
14	a	ESP_052510_2150	34.841	16.476	3.8 ± 0.19
	b				3.8 ± 0.19
15		ESP_062045_2200	39.794	0.035	2.3 ± 0.09
16		ESP_050585_2225	42.385	12.184	6.3 ± 0.22
17		ESP_061715_2205	40.199	5.687	0.4 ± 0.02
18		ESP_059352_1515	-28.399	83.651	0.7 ± 0.02

Table 3.1: Table of DEM numbers and locations (Fig. 3.1). Latitude and longitude give center of left HiRISE observation. Error estimates are standard deviations of diameter (D) measurements. DEMs made using University of Chicago HiRISE pipeline.

and equations for flow resistance and transport-limited erosion. We assume no downstream changes in channel/valley geometry, flow depth, or flow velocity. We also assume that all sediment eroded is advected perfectly downstream and removed from the system, i.e. there is no modification of the flow through re-deposition. The elevation head (J) available to drive outflow and erosion in the tadpole crater channel is given by the difference between lake level (E), and breach floor elevation (B) (Fig. 5.1):

$$J = E - B \tag{3.1}$$

During lake draining, water accelerates from negligible velocity within the lake to a higher

Breach		L (km)	w_v (m)	z_v (m)	$S_{channel}$	S_{rim}	V (km^3)
1		5.8 ± 0.4	549 ± 48	41 ± 12.2	0.03 ± 0.01	0.17 ± 0.07	135.61 ± 3.06
2		1.4 ± 0.0	100 ± 8	5 ± 0.8	0.10 ± 0.01	0.10 ± 0.03	0.47 ± 0.03
3		2.5 ± 0.1	35 ± 15	1 ± 0.8	0.09 ± 0.02	0.15 ± 0.02	0.07 ± 0.00
4		4.4 ± 0.1	208 ± 12	44 ± 4.3	0.09 ± 0.02	0.10 ± 0.00	38.07 ± 1.32
5		20.7 ± 0.1	474 ± 34	71 ± 4.9	0.13 ± 0.02	0.29 ± 0.02	213.34 ± 4.65
6		8.5 ± 0.5	878 ± 42	116 ± 15.1	0.12 ± 0.06	0.17 ± 0.05	56.74 ± 11.06
7		1.5 ± 0.0	297 ± 17	35 ± 1.9	0.07 ± 0.03	0.11 ± 0.05	19.37 ± 2.13
8		1.4 ± 0.0	254 ± 56	40 ± 3.7	0.07 ± 0.01	0.09 ± 0.01	8.45 ± 0.34
9		2.0 ± 0.2	247 ± 23	34 ± 2.0	0.14 ± 0.03	0.09 ± 0.03	4.78 ± 0.75
10		4.5 ± 0.1	300 ± 44	25 ± 1.7	0.11 ± 0.01	0.14 ± 0.04	3.05 ± 0.06
11		10.7 ± 0.2	453 ± 85	46 ± 2.7	0.06 ± 0.02	0.09 ± 0.03	141.50 ± 16.01
12		3.1 ± 0.1	265 ± 37	18 ± 1.8	0.07 ± 0.01	0.08 ± 0.02	5.03 ± 0.23
13	a	3.7 ± 0.1	257 ± 23	31 ± 0.7	0.15 ± 0.03	0.22 ± 0.06	16.50 ± 1.17
	b	5.4 ± 0.2	308 ± 35	46 ± 4.6	0.08 ± 0.02	0.16 ± 0.01	
	c	3.7 ± 0.2	249 ± 21	28 ± 2.8	0.10 ± 0.01	0.13 ± 0.07	
14	a	3.3 ± 0.1	227 ± 52	20 ± 4.2	0.10 ± 0.01	0.19 ± 0.04	10.11 ± 1.96
	b	1.8 ± 0.1	197 ± 12	19 ± 3.6	0.11 ± 0.01	0.21 ± 0.03	
15		0.8 ± 0.0	228 ± 35	28 ± 1.4	0.15 ± 0.01	0.16 ± 0.03	0.62 ± 0.05
16		3.9 ± 0.1	265 ± 13	31 ± 4.2	0.08 ± 0.03	0.09 ± 0.03	22.09 ± 3.28
17		0.3 ± 0.0	145 ± 3	16 ± 2.0	0.14 ± 0.04	0.14 ± 0.03	0.01 ± 0.00
18		1.4 ± 0.1	200 ± 27	21 ± 1.0	0.07 ± 0.00	0.16 ± 0.05	0.12 ± 0.01

Table 3.2: Measured tadpole crater exit breach parameters from DEMs. L is outlet valley length. w_v is valley width, measured as the distance between the upper breaks in slope of the valley walls in cross sections of the exit breach. z_v is breach depth relative to the adjacent crater rim, measured using cross sections of the exit breach. $S_{channel}$ is the maximum valley bed slope, measured using long profiles down the center of the exit breach valley. S_{rim} is the average crater rim slope measured either side of the exit breach valley. Error estimates are standard deviations of 4 measurements. V is the volume of the crater. Breach numbers map to Table 3.1.

velocity at the breach. This causes drawdown of the lake level near the breach, so the flow depth at the breach (H) is less than the elevation head (J). Assuming critical flow at the breach, and a rectangular breach and channel, conservation of energy (French, 1985) gives:

$$H = \frac{2}{3}J \tag{3.2}$$

We assume that outlet channel flow depth and breach flow depth are equal, and use H to

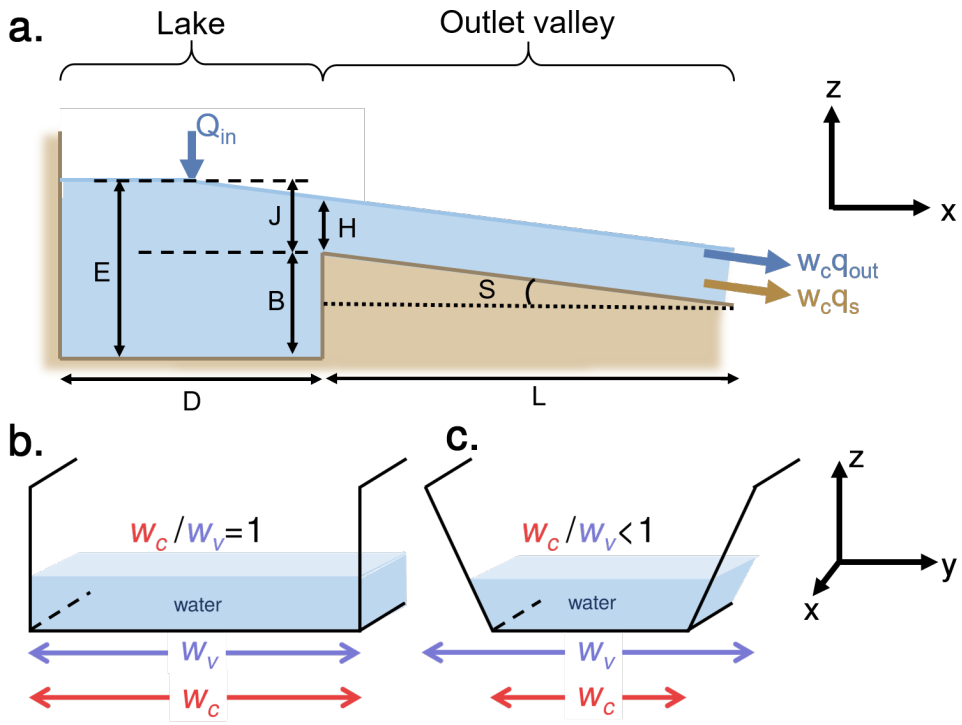

Figure 3.3: a. Schematic illustration of crater breach erosion model. E is water level in the lake. B is breach floor elevation. J is the difference in elevation between lake level and the channel floor, also known as the elevation head. H is the water depth in the channel. L is channel length, D is lake diameter, S is channel slope, w_v is valley width, w_c is channel width, q_{out} is flow of water out of the crater, q_s is sediment flux out of the channel, and Q_{in} is flux of water into the crater. b. Rectangular trough shaped channel with $w_c = w_v$. This is assumed in all models in this study. c. Trapezoidal channel with $w_c < w_v$. This shape favours runaway erosion.

calculate both lake drainage and channel floor erosion.

We select a value of initial flow depth $1 < H < 10$ m for each model run. E is controlled by the water flux into (Q_{in}) and out of the lake (q_{out}). B is controlled by downwards erosion of the valley floor, which is controlled by the sediment flux (q_s) out of the channel per unit length (L). Our model assumes that $H \ll w_v$. All of q_s/L contributes to deepening the channel through erosion. Differentiating Eq. 3.1 gives:

$$\frac{dJ}{dt} = \frac{dE}{dt} - \frac{dB}{dt} \tag{3.3}$$

where:

$$\frac{dE}{dt} = \frac{4(Q_{in} - w_c q_{out})}{\pi D^2} \tag{3.4}$$

$$\frac{dB}{dt} = -\left(\frac{w_c}{w_v}\right)\frac{q_s}{L} \tag{3.5}$$

using Manning's Law for water discharge in a channel:

$$q_{out} = \frac{H^{5/3} S^{1/2}}{n} \tag{3.6}$$

and a standard scaling for Manning's n (Brownlie, 1983):

$$n = \frac{k^{1/6}}{8g^{1/2}} \tag{3.7}$$

where k is the channel bed roughness lengthscale. In alluvial channels, k is typically larger than grainsize d (Kamphuis, 1974). The k used depends on whether d represents the grainsize for which 50% of grains are smaller (for d_{50}, $k = 2.5d_{50}$), or 90% of grains are smaller (for d_{90}, two common approximations are $k = d_{90}$ and $k = 3d_{90}$) (Van Rijn, 1984). We assume a uniform grainsize ($d_{50} = d_{90}$) and $k = d$ because $k > d$ disfavors erosion, therefore assuming $k = d$ provides an upper limit.

For sediment transport, we use the Meyer-Peter Mueller relation (MPM) (Meyer-Peter and Mueller, 1948):

$$q_s = 8\sqrt{Rgd^3}\,(\tau_* - \tau_{*c})^{3/2} \tag{3.8}$$

The appearance of g in this equation scales the model to Martian gravity. Substituting Eqs 3.4-3.8 into Eq. 3.3:

$$\frac{dJ}{dt} = \frac{4}{\pi D^2}\left(Q_{in} - \frac{8w_c H^{5/3}\sqrt{gS}}{d^{1/6}}\right) + \left(\frac{w_c}{w_v}\right)\frac{8\sqrt{Rgd^3}\left(\tau_* - \tau_{*c}\right)^{3/2}}{L} \tag{3.9}$$

Dimensionless Shield's stress τ_* in the channel is found using:

$$\tau_* = \frac{HS}{Rd} \tag{3.10}$$

where R is submerged specific gravity, a dimensionless measure of sediment buoyancy in water ($R = \frac{\rho_{sediment} - \rho_{fluid}}{\rho_{fluid}}$). The ratio of Shields stress τ_* to critical Shields stress stress τ_{*c} can be expressed in terms of the transport stage (T), where $T < 1$ indicates no bedload sediment transport:

$$T = \frac{\tau_*}{\tau_{*c}} \tag{3.11}$$

To solve Eq. 3.9 we discretize Eq 3.9 such that:

$$J_{i+1} = J_i + \Delta t\left[\frac{4}{\pi D^2}\left(Q_{in} - \frac{8w_c\left(\frac{2}{3}J_i\right)^{5/3}\sqrt{gS}}{d^{1/6}}\right) + \left(\frac{w_c}{w_v}\right)\frac{8\sqrt{Rgd^3}\left(\left(\frac{2J_i S}{3Rd}\right) - \tau_{*c}\right)^{3/2}}{L}\right] \tag{3.12}$$

where the subscript i indicates the ith timestep. We numerically integrate Eq. 3.12 from $t = 0$ to $t = 1$ year with $\Delta t = 100$ s.

In the first part of our analysis, we assume $Q_{in} = 0$, i.e. no flow into the crater during overspill. Under these conditions, our model predicts 2 possible regimes for breach erosion:

1. *Runaway erosion*

   Favoured by large lakes with narrow, steep channels and short valleys (large D and S, small w_v and L). At the onset of erosion, the outlet channel erodes downwards faster than q_{out} reduces lake level. Eq. 3.3 is positive. Water depth H in the channel increases.

This increases erosion rate in the channel (Eqs. 3.8 & 3.10), but q_{out} increases more rapidly (Eq. 3.6). H increases until the rate of lake level change dE/dt matches channel floor erosion rate dB/dt (i.e. Eq. 3.3 goes to zero). Erosion continues at a constant rate until the lake is drained, i.e. all available topography is consumed, corresponding to erosion of the valley floor through the entire elevated crater rim.

2. *Self-arrest erosion*

   Favoured by small lakes with wide, gently-sloping channels and long outlet valleys (small D and S, large w_v and L). At the onset of erosion, q_{out} reduces lake level faster than the valley floor erodes. Eq. 3.3 is negative. Water depth in the channel decreases. This reduces sediment transport rate in the channel more rapidly than it reduces q_{out} of the channel (Eqs. 3.8 & 3.10 vs. 3.6), so Eq. 3.3 remains negative. Once H drops below the sediment transport threshold, erosion stops and $dB/dt = 0$. q_{out} asymptotes to 0 before the lake is drained, i.e. not all available topography is consumed.

When there is flow into the lake ($Q_{in} > 0$), a third, sustained erosion regime occurs (discussed in Section 3.6), where the channel is able to accommodate q_{out}, but Q_{in} exceeds the sediment transport threshold. This causes continuous erosion in the channel at a fixed rate.

Exit breach channel and eroded valley widths are indistinguishable in most tadpole crater DEMs. We assume that the channel width does not change during the overspill event, and that the channel occupied the full valley width, i.e. $w_c = w_v$ and $\frac{w_c}{w_v} = 1$. This represents a rectangular, trough-shaped channel. If initial channel widths were much narrower than the observed valley width, or $w_c < w_v$, runaway is more likely because less water will drain from the lake at each timestep. This keeps water depth and erosion rates in the channel high (Eq. 3.10). In the natural case we would expect channel width to vary with time as H evolves. In the event of self-arrest erosion, H decreases over time so we expect channel widening to occur early in the overspill event. $w_v \approx w_c$ is also likely a good approximation

for tadpole craters based on analogue experiments of crater breaches (Marra et al., 2014), which suggest channel width and valley width are similar during crater rim breach floods.

The most important uncertainties in our model are initial flow depth and grainsize. These parameters set initial Shields stress τ_* (Eq. 3.10), which determines the initial rate of channel incision (Eq. 3.8). When $\tau_* > \tau_{*c}$, sediment transport can occur. $\frac{dB}{dt}$ decays rapidly during self-arrest erosion (Fig 3.5). Higher initial transport stages lead to more rapid initial erosion and allow erosion to occur for longer. The measured breach channel depth for the tadpole crater in Fig. 3.1b is 17.6±1.8 m. We assume initial flow depth must be much smaller and use initial breach depths of 1 and 10 m, where 10 m is approximately 10% of the deepest measured tadpole crater breach. We use a shear stress parameterization and τ_{*c} appropriate for gravel-sized grains. The only constraint on grainsize is that individual clasts cannot be seen at a 25 cm pixel^{-1} resolution in HiRISE images. Observations of impact breccia from Victoria Crater suggest most clasts are <1 m in diameter (Squyres et al. 2009, Fig. 3). To avoid assuming a grainsize, we find the optimal grainsize for erosion (i.e. the grainsize for which maximum erosion occurs) for each tadpole crater numerically. As a result, we likely overestimate erosion. Application of the Meyer-Peter Mueller relation (Eq. 3.8) is discussed in Section 3.5.1.

3.4 Results

We apply our model to Mars tadpole craters (Section 3.4.1) and terrestrial breach erosion events compiled from the literature (Section 3.4.2).

3.4.1 Mars Tadpole Craters: Measurements & Implications

We constructed DEMs for 18 craters with exit breaches (Table 3.1) using PDS-released HiRISE stereopairs and tools developed by Mayer and Kite (2016) (tools streamlined by S. Holo). We used these DEMs to measure tadpole crater exit breaches (Table 2). We

mark tadpole craters as consistent with runaway erosion if our model predicts runaway for all combinations of measured parameters (D, S, L, w_v) (Fig. 3.4). In our fixed channel width 0-D model, runaway is independent of grainsize because whether the lake can drain fast enough to cause water depth in the channel to drop is controlled by channel geometry and lake size (Eq. 3.4). We find the runaway threshold numerically for each tadpole crater by varying S for $H_0 = 1$ m. Our model predicts runaway erosion for two tadpole craters (breaches 4 and 13a, Table 3.1 and Fig. 3.4). The measured fraction of eroded relief for these tadpole craters is <0.65, so the channels did not erode through their crater rims. This model–data disagreement is discussed in Section 3.5.

We used valley geometry measurements as inputs to our breach erosion model and calculated eroded breach depth for initial flow depths $1 < H_0 < 10$ m and grainsizes $0.01 < d < 1$ m. A tadpole crater is consistent with a single erosion event if model-predicted total eroded depth meets or exceeds measured breach depth z_v for any grainsize d. To quantify the single to multiple event threshold, we found the critical value of $w_v/S^{7/6}$ required for each tadpole crater to erode in a single event for 3 logarithmically-spaced initial flow depths (10^0, $10^0.5$, and 10^1 m). We assumed a log-uniform prior for initial flow depth and a linear relationship between $w_v/S^{7/6}$ and D^2/L to perform 15,000 bootstraps to find the 95% confidence interval for a tadpole crater breach eroding in a single, self-arrest overflow event (Fig 3.4). Assuming $Q_{in} = 0$, three tadpole craters fall outside this region of parameter space. These three tadpole craters require multiple events to erode the observed breaches, or $Q_{in} \neq 0$. We discuss this in Section 3.6.

3.4.2 Application of the Model to Terrestrial Breaching Events

We tested our model against some potential tadpole crater terrestrial analogues, including outburst floods from moraine-dammed lakes, landslide dams, and caldera lakes (Fig. 3.4). Our model results are sensitive to breach length and channel slope, so we selected his-

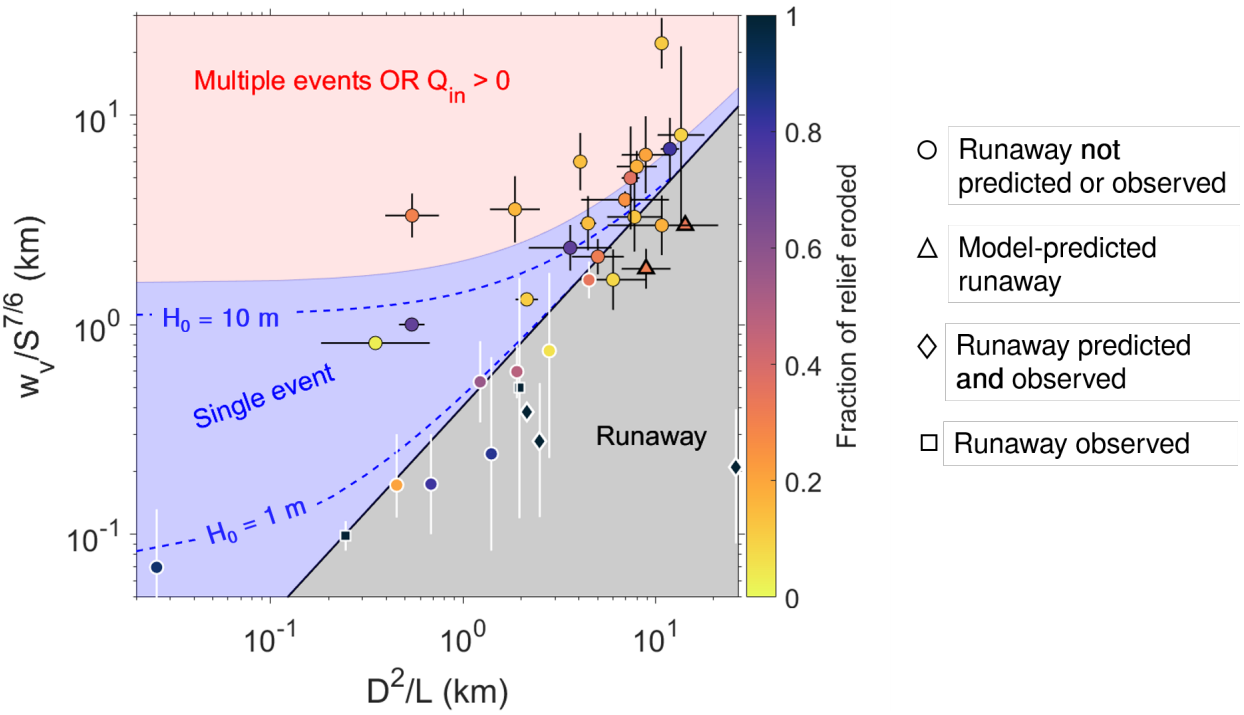

Figure 3.4: Lake size relative to outlet valley length plotted against valley width and steepness for tadpole craters and terrestrial analogues. Thresholds for runaway erosion and multiple erosion events/erosion events with continued water supply to the crater are found numerically by comparing model predicted erosion depth to measured tadpole crater outlet breach depths. Black outlines/bars are Mars tadpole crater data (Table 2). Bars show the range between maximum and minimum measured values (individual measurement errors are negligible by comparison). Markers are at the logarithmic mean of maximum and minimum values. White outlines/bars are Earth dam breach events. Markers are plotted at the mean measured value if available, or at the logarithmic mean of the measured range. Black line indicates the runaway threshold. Triangular markers: runaway is always predicted by the model. Square markers: runaway erosion is observed (i.e. all available relief consumed). Diamond markers: runaway is predicted by the model and measured in reality. Blue shaded area: 95% confidence interval from 15,000 bootstraps for transition between an eroded breach being consistent with a single overspill event to requiring multiple events for initial flow depths $1 < H_0 < 10$ m assuming a log-uniform prior for H_0. 3 Mars tadpole craters require multiple erosion events or continuous input of water into the crater to erode the observed outlet breach depth. Our model predicts runaway erosion for 2 tadpole craters.

torical events with well-documented pre- and post-breach topography to test the model. Where breach valleys connect to pre-existing channels, we used pre-breach dam width (where available) as a lower bound on eroded channel length. Otherwise, we assume a conservative (i.e. short) channel length $L = D/2$. This favours runaway. Most well-documented moraine/ landslide dammed lake breaches erode all available relief. Our model predicts runaway erosion under all conditions for 3 out of 5 known to be runaway events based on relief consumed during flooding (Fig 3.4). The remaining two events are consistent with runaway in the model within the range of measured slopes and channel widths. This slight underprediction of terrestrial runaway erosion reinforces our conclusion that two of the measured tadpole craters would be expected to undergo runaway breach erosion during crater overspill.

Using moraine/ landslide dams and volcanic caldera lake breaching events to test our model has several limitations. Firstly, our model assumes that abundant, loose sediment is available in the channel (transport-limited erosion). This might not apply to volcanic calderas where the caldera walls are formed primarily of lava flows. Intact rock needs to be broken into clasts before sediment transport can occur (detachment-limited erosion). Secondly, our model assumes uniform grainsizes between 0.01 and 1 m. Moraine deposits, landslides, and caldera walls can have a wide range of grainsizes, and a large proportion of fines (Lagmay et al., 2007; Clague and Evans, 2000). Gravel-sized clasts may be a poor approximation to the real dam grainsize distribution. This also applies to impact ejecta. Thirdly, interstitial ice in some morraine dams (Clague and Evans, 2000) may change the erodibility of dam materials by freezing clasts together. Additionally, ice melting during breaching this would lower the channel floor faster than erosion alone. Finally, available terrestrial examples of lakes draining through erosion of an exit breach and outlet valley are much smaller than the majority of tadpole craters measured on Mars ($D_{terrestrial} = 1.44$ km, $D_{Mars} = 5.26$ km). These differences in size may mean that different lake draining behaviours should be expected.

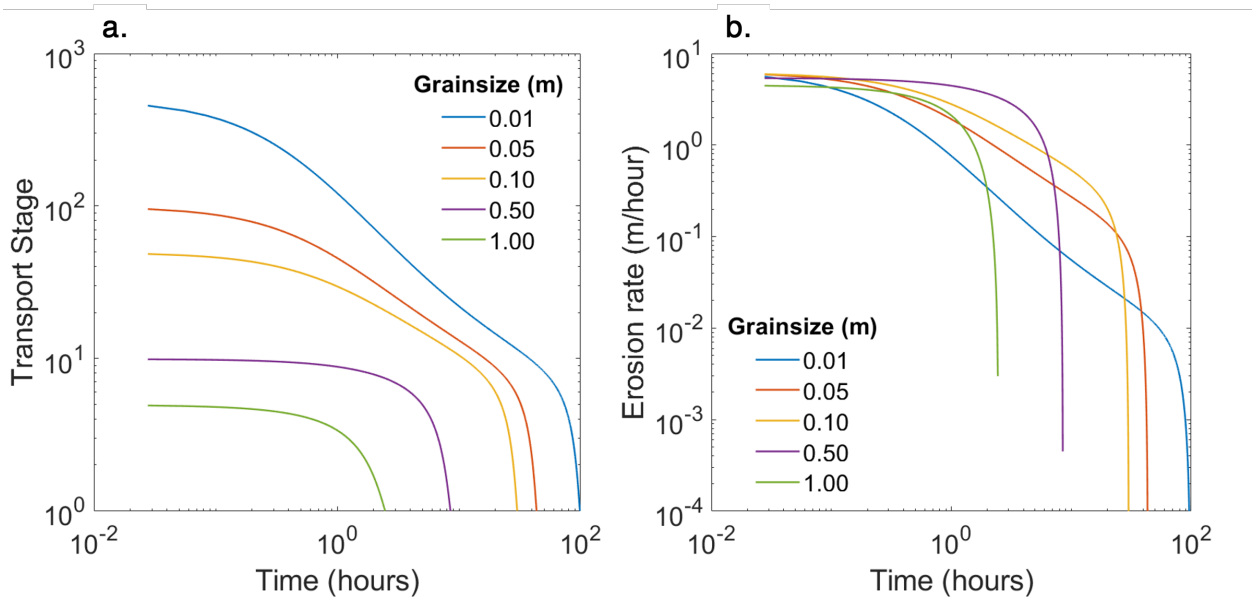

Figure 3.5: Model-predicted evolution of a. transport stage T (the ratio between Shields stress τ_* and the critical Shields stress for sediment transport τ_{*c}) and b. erosion rate over time since breach initiation for the Pinatubo Caldera breaching event in 2002 (Lagmay et al., 2007), assuming $H_0 = 1.54$ m and $Q_{in} = 0$. No erosion occurs when the transport stage falls below 1. The duration of the real event was <24 hours. This illustrates the general evolution of self-arrest erosion.

3.5 Runaway Erosion: Predicted but not observed

Runaway erosion is observed for many terrestrial moraine/ landslide dam breaching events (i.e. erosion to the base of the dam), whether the dam is a landslide deposit, terminal moraine, or crater rim. Runaway erosion is not observed for any tadpole crater valleys. Tadpole crater exit breaches do not erode deeply relative to crater floor depth (Fig. 3.1). By contrast, megaflood-formed valleys in Xanthe Terra erode hundreds of meters of crust (Coleman, 2005), representing 80 to 100% of the available relief (e.g. Shalbatana Valles, Masursky Crater outflow valleys at 12.964° N, -32.497° E). The water supply mechanism for tadpole craters cannot be both intense and long-lived. Our model predicts runaway erosion for at least two tadpole crater exit breaches. However, our model likely overestimates erosion. Firstly, measured w_v is an upper limit on channel width. If active channel width, which cannot be measured directly, was smaller than valley width, this would favor runaway. Setting $w_c/w_v = 1/3$, the number of runaway breaches predicted by the model increases sixfold (to 13/22). Secondly, our baseline model assumes no water flux into the crater during erosion ($Q_{in} = 0$). This minimizes dH/dt, disfavoring runaway erosion. Therefore, if tadpole crater overspill occurs during a climate event with increased runoff, or during a groundwater outflow event, runaway will be more likely than captured by the model. Typical measured breach depths are <50% (mean = 0.4, median = 0.3) of the available relief. This lack of observed runaway erosion may provide additional information about whether tadpole crater breaches can form in a single event, and whether or not tadpole craters were predominantly ice-filled. There are three possible explanations for the lack of observed runaway erosion:

- **Hypothesis 1:** The Meyer-Peter Mueller equation (MPM) for capacity bedload transport overpredicts tadpole crater valley erosion (Section 3.5.1).
- **Hypothesis 2:** - The stratigraphic transition from crater rim ejecta to uplifted bedrock is sufficient to halt runaway erosion (Section 3.5.2).

- **Hypothesis 3:** - Channel length (L), channel slope (S), or crater diameter (D) measured from DEMs are not representative of crater overspill conditions (Section 3.5.3).

3.5.1 Sediment transport on steep slopes

The empirical MPM equation for bedload transport was determined for well-sorted, gravel-bedded, terrestrial rivers, with shallow slopes ($\ll$0.1) (Meyer-Peter and Mueller, 1948). Measured tadpole crater valley floor/ crater rim slopes fall in the range $0.03 < S < 0.29$. There is some debate whether MPM under or overpredicts erosion in steep channels (Damgaard et al., 1997; Cheng and Chen, 2014). Increased τ_{*c} on steep slopes disfavors runaway (Eq. 3.9). Flume experiments by Lamb et al. (2008), and τ_{*c} measurements made in terrestrial gravel bedded streams/rivers (Mueller et al., 2005), suggest τ_{*c} reaches 0.1 at slopes $S > 0.02$. Even with $\tau_{*c} = 0.1$, our model predicts runaway for the two tadpole craters identified in Fig. 3.4. Our results are not strongly sensitive to the value of τ_{*c}. Given uncertainty in the correction for τ_{*c}, agreement between our model and terrestrial observations, and the small effect of doubling τ_{*c}, we do not modify τ_{*c}.

The mean sediment:water ratio for tadpole craters consistent with a single overspill event is 0.07 by volume. 0.04 is expected for water floods (Pierson, 2005). High sediment concentrations can lead to strongly non-Newtonian behaviours in sediment-water mixtures (Pierson, 2005). High sediment concentrations increase flow density, which may increase bedload transport. However, the primary effect of hyperconcentration on sediment transport is a decrease in suspended sediment settling rates. MPM performs well for hyperconcentrated flows up to high ($\sim$20%) sediment concentrations on steep slopes in analogue and numerical experiments (Rickenmann, 1991; Abderrezzak and Paquier, 2011). We disfavor Hypothesis 1 to explain the lack of runaway, and do not adjust our sediment transport equation for hyperconcentration.

3.5.2 Barriers to crater rim erosion

Crater rims are composed of uplifted bedrock overlain by ejecta. The contact between crater ejecta and bedrock is visible in the fresh impact crater visited by the Mars Exploration Rover Opportunity (Victoria Crater) (Squyres et al., 2009). The transition from poorly consolidated ejecta to intact bedrock could inhibit runaway erosion by a change in the erosion mechanism, or a change in grainsize. Our model assumes breach erosion is limited by whether the shear stress at the base of the channel is strong enough to move loose sediment clasts (transport-limited erosion). In bedrock, erosion is limited by whether the shear stress is sufficient to break off new clasts from the intact rock (detatchment-limited erosion; Whipple et al. 2013). Moving pre-existing clasts requires lower Shields stress than breaking off new clasts. Recent bedrock river studies suggest that plucking is one of the primary mechanisms of bedrock erosion (Lamb et al., 2015; Whipple et al., 2013). Plucking occurs when water breaks up bedrock along joint planes (Lamb et al., 2015). (Larsen and Lamb, 2016) apply a plucking threshold (τ^*_{pc}) to bedrock erosion in the Channeled Scablands:

$$\tau^*_{pc} = \frac{\cos\theta\left[\tan\phi - \tan\theta\right] + 2\tau^*_w}{\left[1 + \frac{1}{2}C_D\left(\frac{u}{u_*}\right)^2\frac{P}{L}\right]\left[1 + F^*_L\tan\phi\right]} \tag{3.13}$$

where θ is bed angle in degrees ($S_{channel} < \theta < S_{rim}$), ϕ is bed friction angle (wet basalt), τ^*_w is dimensionless block sidewall stress (caused by friction along the sides of a block of fractured bedrock), C_D is a local drag coefficient for fractured bedrock blocks related to particle Reynolds number (Lamb et al., 2015), $\frac{P}{L}$ is the ratio of protrusion height of basalt blocks above the channel floor to the length of each block, $\frac{u}{u_*}$ is the ratio of flow velocity to bed shear velocity, and F^*_L is the dimensionless hydraulic lift (force exerted perpendicular to the channel bed by flow of water over bedrock). We adopt the same values for these parameters as (Lamb et al., 2015) to find an upper limit on τ^*_{pc}, setting $\cos\theta \approx 1$, $\tan\theta \approx 0$ (i.e. a very gently sloping channel), and letting $\frac{P}{L}$ approach 0 (i.e. blocks protrude very little

above the bed). This gives $\tau^*_{pc} \approx 0.65$, equivalent to $T \approx 13$. $T > 13$ is readily achieved in all tadpole crater exit breach valleys at the beginning of a breach event, assuming optimal grainsize for erosion (Section 3.6). During runaway erosion, T increases over time as the lake drains through a breach that is not large enough to accommodate $q_{w,out}$. A transition from transport-limited to detatchment-limited, plucking-dominated erosion would be insufficient to inhibit runaway. If the ejecta-bedrock transition inhibits runaway through a change from transport-limited to detatchment-limited erosion, we would expect to see only multiple erosion event tadpole crater breaches incising into bedrock.

A change in grainsize at the ejecta-bedrock boundary could also inhibit runaway erosion. Large grainsizes (approaching 1 m) erode less efficiently in the model (Fig. 3.5) because $T \propto \frac{1}{d}$. During runaway erosion, T initially increases rapidly, then plateaus at a maximum value. If this maximum transport stage is less than the maximum ratio of $\frac{d_{bedrock}}{d_{ejecta}}$ (the range of grainsizes in the model gives $\left(\frac{d_{bedrock}}{d_{ejecta}}\right)_{max} = 100$), then a change in grainsize could halt runaway erosion, because T would fall below 1 when the grainsize change occurs (assuming an instantaneous ejecta to bedrock transition), this corresponds to cessation of erosion. However, this is not the case for either tadpole crater for which our model predicts runaway (Table 3.1). For breach 4 ($T_{max} \approx 2800$), and for breach 13 ($T_{max} \approx 600$). However, we select a grainsize to maximise erosion, so T_{max} during crater overspill was likely less than predicted. If the ejecta-bedrock transition inhibits runaway through an abrupt, order of magnitude change in grainsize, we would not expect to see tadpole crater exit breach valleys incise into bedrock. To test this prediction, we can compare breach depths to predicted ejecta thickness (Fig. 3.6). There are only a handful ejecta thickness observations for Martian craters (Sturm et al., 2016), and the contact between ejecta and bedrock is not visible in the tadpole crater HiRISE images. From existing data, there is no clear relationship between fraction of eroded relief and number of overspill events required (Fig. 3.4). The uncertainty in the ejecta thickness/ crater diameter relationship means that the ejecta-bedrock transition

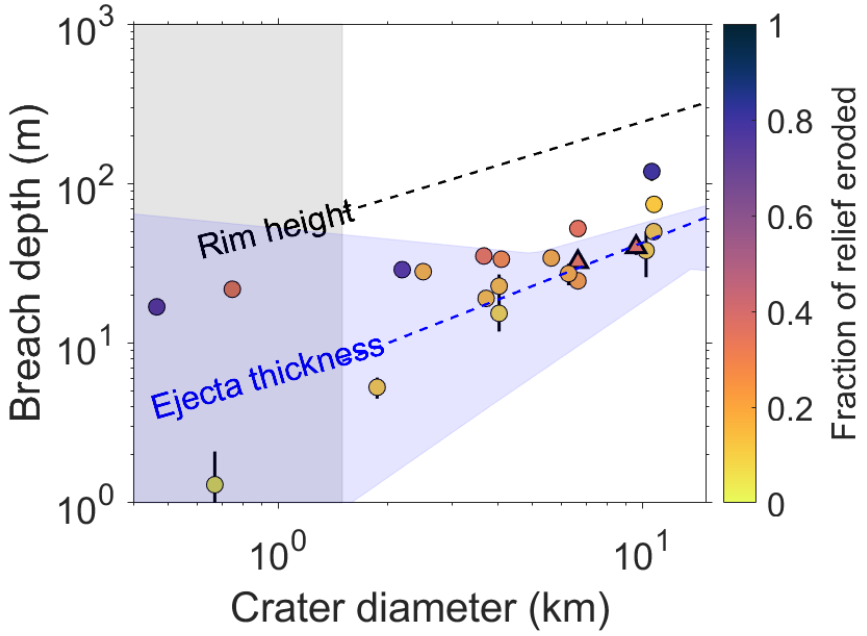

Figure 3.6: Measured tadpole crater exit breach depth vs. crater diameter. Marker color indicates fraction of available relief eroded by the breach. Dashed black line shows an empirically derived relationship between crater diameter and rim height for pristine craters (Mouginis-Mark et al., 2018). Dashed blue line shows a powerlaw fit to ejecta thickness and crater diameter measurements in Sturm et al. (2016). Grey shaded area indicates diameter range not covered by rim height and ejecta thickness relationships. Blue shaded area shows a bootstrapped 95% confidence interval on Sturm et al. (2016) based on crater measurements ($n = 5000$).

– Hypothesis 2 – cannot be ruled out as a mechanism for halting breach erosion.

3.5.3 Pre-event vs. measured breach morphology

tadpole crater measurements from DEMs may not be representative of crater and channel morphology during overspill. We assume $w_c = w_v$, likely overestimating active channel width during erosion. This disfavors runaway. There are three remaining parameters that could explain the lack of runaway erosion if their present day values are not representative of the breaching event.

1. *Slope (S)*

If channel slope during overspill was less than DEM measured $S_{channel}$ runaway would be less likely. For a crater overspilling for the first time, the initial channel slope would be the slope of the crater rim. S_{rim} is typically steeper than $S_{channel}$, therefore shallower initial breach channels are unlikely, favoring runaway. Slope cannot explain the data-model discrepancy.

2. *Channel Length (L)*

   Increasing channel length L decreases likelihood of runaway because erosion occurs over a larger area. This decreases the magnitude of dB/dt, making lake draining more likely to outpace downward erosion in the channel (Eq. 3.3). This favours self-arrest erosion (Section 3.3.1). For most tadpole craters, $L = (0.8 \pm 0.8)D$. Tadpole craters are identified, in part, by the fresh appearance of their crater rims, precluding extensive erosion (Wilson et al., 2016) as an explanation for the short exit breach valleys observed. The two tadpole craters for which runaway is predicted do not connect to a larger drainage network, so a difference in L is unlikely to explain the lack of runaway.

3. *Lake Diameter: Water-filled vs. Ice-filled craters*

   Measured crater diameter D may overestimate the size of the lake that drained to form the tadpole crater exit breach. Some tadpole craters have debris-covered icy deposits on their crater floors. If the crater was predominantly ice-filled during overspill, formation of a melt pond could form a lake with a much smaller equivalent diameter than the crater. Ice could also act as a barrier to crater rim erosion. If tadpole craters were predominantly ice filled (discussed in Section 3.6.1) with a meltwater lake, runaway could be prevented simply by the meltwater lake volume being too small to supply water to erode through the crater rim. This is an attractive mechanism for tadpole breach formation because it does not require the full crater volume to be filled with liquid water.

3.6 Are all tadpole craters consistent with a single overspill event?

The transition between breaches consistent with a single overspill event and breaches that require multiple breaching events or continuous supply of water (termed "multiple event" breaches) depends on how fast the lake can drain relative to the size of the lake. This can be quantified using the $w_v/S^{7/6}$ ratio of an outlet valley, and D^2/L of the tadpole crater and outlet valley. The power of 7/6 is inherited from Eqs. 3.6 & 3.8. We define the transition as the value of $w_v/S^{7/6}$ that allows for the observed breach depth to be eroded in a single event. This critical $w_v/S^{7/6}$ ratio is found numerically. At large D^2/L, the single-multiple event transition is close to the runaway threshold. Based on our modeling results, three tadpole crater exit breach valleys cannot be eroded through a single breaching event (Fig. 3.4). These tadpole craters require water flux into the crater during overspill, or multiple overspill events. The required water flux into the crater, flux duration, and the implied annual average flux can be compared to previously published estimates of potential tadpole crater water sources, such as groundwater, rainfall, and snowmelt runoff.

Water flux into the lake (Q_{in}) must be large enough that $\tau_* > \tau_{*c}$ (Eqs. 3.10 & 3.8) for erosion to continue. To ensure we only reject a hypothesis if absolutely necessary, we total required water volume by assuming the most favorable grainsize for erosion for each tadpole crater. This maximises eroded depth during the self-arrest portion of erosion (i.e. the initial breach). We solve for critical $Q_{in,crit}$ using a bisection method. When $Q_{in} = Q_{in,crit}$, the breach will take an infinite amount of time to erode. We ran our model with $Q_{in} = XQ_{in,crit}$, where X is a multiplier from 1.1 to 100, and found the time t_z at which total modelled eroded depth was equal to measured breach depth (Fig. 3.7). We found flux of water per unit lake area q_w using:

$$q_w = \frac{4Q_{in}}{\pi D^2} \tag{3.14}$$

q_w and t_z were used to calculate the implied annual average water supply rate. This can be compared to predictions for annual average precipitation/snowmelt under various climate scenarios (Kite et al., 2019; Turbet et al., 2020) (Section 3.6.1), and estimates of groundwater discharge (Section 3.6.2). None of the three tadpole crater exit breaches are consistent with formation in a single event with water input to the crater from energy limited snowmelt (4 m yr^{-1}). They are only consistent with a single event if there is groundwater discharge into the crater.

In future work, we aim to determine whether tadpole craters with multiple, deep exit breach valleys (e.g. craters 13 & 14 in Table 3.2) are consistent with formation during a single event. In single outlet tadpole craters, the exit breach is always on the crater rim's lowest point. If a crater overspilled multiple times, we would expect water to flow throguh the pre-existing valley. The terrestrial tadpole crater overspill analogues in this study (Section 3.4.2) only have one outlet valley. Possible explanations for multiple outlet valleys include blockages of a pre-existing exit breach by ice (as there are no blockages visible at present in DEMs), regional tilting between overspill events due to lithospheric loading (ice sheets, volcanic edifices), and formation of multiple, spatially isolated melt ponds on the surface of a crater-filling ice body (similar to Fig. 3.2b). Understanding how multiple valleys can drain the same crater may be critical to understanding whether or not tadpole craters were predominantly ice filled, and whether multiple-exit breach craters can ever be formed in a single overspill event.

3.6.1 Climate Tadpole Crater Overspill Scenarios

If tadpole crater overspills are climate-induced, then climate during their formation must have supplied large volumes of water as rain or snowfall. Large impacts are frequently proposed for inducing short term increased precipitation rates on Mars. Mars General Circulation Models (GCMs) seeded with impact model outputs produce precipitation rates up

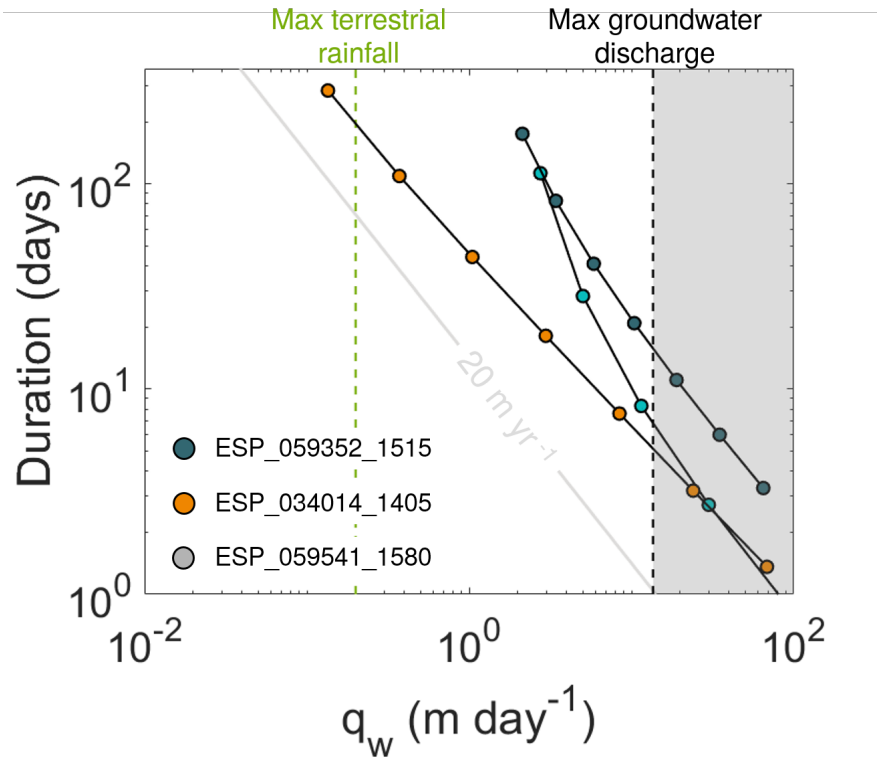

Figure 3.7: Water flux into the crater q_w per unit lake area and required duration to erode observed breach depth. Grey contour shows an annual average water flux per unit lake area of 20 m year^{-1}. 4 m year^{-1} is the maximum for energy limited snowmelt (Kite et al., 2019). Green dashed line shows maximum daily precipitation rate for extreme terrestrial rainfall events (Chien and Kuo, 2011). This precipitation rate is only sustained for hours to days, not a full year. Dashed black line shows the maximum possible discharge from a 1 km deep ice-pressurized aquifer (Section 3.6).

to 3 m yr^{-1} (Steakley et al., 2019; Turbet et al., 2020). For impacts producing craters ∼600 km, this precipitation can last decades (Steakley et al., 2019; Turbet et al., 2020). There are several problems with an impact trigger for tadpole crater overspill. Firstly, the 6 largest Hesperian and Amazonian impact craters have diameters <250 km (Irwin, 2013). Secondly, the impact generated precipitation would mostly fall as snow rather than rainfall (Steakley et al., 2019), so the maximum volume of surface liquid water would still depend on energy-limited, melt-derived runoff. The total integrated precipitation following a large bolide impact is modest even for bolides forming ∼ 600 km diameter craters entering a 1 bar Mars atmosphere; with a maximum of 10 m (Steakley et al., 2019) to 50 m (Turbet

et al., 2020). This would only be sufficient to overspill the five smallest tadpole craters in this study, which all have rim to floor depths of <50 m. Precipitation from a large impact would be insufficient to sustain erosion in an exit breach channel. Even if impact induced precipitation is much more intense than predicted by models, the most extreme rainfall rates recorded on Earth (Chien and Kuo, 2011) would also not be able to provide the required q_w. Additionally, impact induced precipitation is not globally uniform (Turbet et al., 2020; Steakley et al., 2019). Steakley et al. (2019) show that precipitation following a large impact is concentrated in the Northern midlatitudes, regardless of impact location, which may be consistent with the high density of tadpole craters observed in Arabia Terra (Wilson et al., 2016), but not the global tadpole crater distribution. However, a bolide impact could increase Mars' surface temperature even in a 150 mbar atmosphere (Steakley et al., 2019), which could contribute to snowmelt runoff.

Without extreme, isolated changes in climate generating large volumes of precipitation or melting, orbitally-driven climate oscillations are a more plausible explanation if tadpole crater overspill is primarily climate-driven. The most important climate constraint provided by tadpole craters is that a crater must first be filled in order to overspill. This requires accumulation of large volumes of ice or liquid water. This is consistent with observations of ice-related features in the Martian midlatitudes (Fassett et al., 2010), and models of ice accumulation under different orbital conditions (Mischna et al., 2013). Ice-related formation mechanisms have also been proposed for features associated with tadpole crater occurence in Arabia Terra such as fresh shallow valleys (Wilson et al., 2016).

Ice accumulation in mid latitudes during the Hesperian could gradually fill tadpole craters. Once ice-filled, seasonally or orbitally driven meltwater production (i.e. an excursion to temperatures above freezing) would enable some exit breach erosion through draining of a meltwater lake on the ice surface. This hypothesis is consistent with erosion of <60% of the available relief by 80% of tadpole crater exit breach valleys because a meltwater lake

would have a smaller volume of water available for erosion. If tadpole crater overspill was caused by warming and increased melt production, the effects would not be localized to regions with tadpole craters, but would leave a global signature. Low latitude alluvial fan activity is evidence for surface liquid water during the Hesperian and Amazonian (Hauber et al., 2013). However, the preferential occurrence of tadpole craters in midlatitudes (Wilson et al., 2016) indicates that these potentially contemporaneous alluvial fan forming wet events were insufficient to lead to overspill of low latitude craters. Latitudinal differences in ice availability (e.g. snowpack vs. crater-filling ice pods) would make equatorial craters less likely to overspill, while still making meltwater available for alluvial fan deposition.

In this scenario, however, it is more difficult for all exit breach erosion to occur during a single overspill event for any of the tadpole craters because the water depth must extend to at least the base of the channel. To melt ice filling a tadpole crater to the measured breach depth across the entire crater area would exceed the energy limited snowmelt rate of 4 m yr^{-1} (Kite et al., 2013) for all but one tadpole crater (Table 3.1 & 2, breach 3). Therefore, either a shallower meltwater lake would form or the diameter of the meltwater lake would be smaller, reducing the eroded depth in a single event. This favors multiple events for tadpole crater breach erosion if tadpole crater overspill was climate driven, and is consistent with the lack of observed runaway erosion.

3.6.2 Groundwater Tadpole Crater Overspill Scenarios

Previous work on Mars hydrology and groundwater outburst floods (e.g. Hanna and Phillips 2005) sets an upper limit on groundwater discharge from a pressurized aquifer. Assuming that the conduit between the aquifer and the crater floor is already water saturated, we can use Darcy's law:

$$q_{max} = \frac{K \Delta P_{max}}{\mu z_{min}} \tag{3.15}$$

where K is aquifer permeability, and $\mu = 8.9 \times 10^{-4}$ Pa s is the dynamic viscosity of water. The maximum pressure P_{max} within a Martian aquifer is set by the tensile strength of the bedrock. For Mars, we assume a basaltic crust with tensile strength 2-14 MPa (Schultz, 1993). From existing estimates for Hesperian surface temperatures and heat flux, (Harrison and Grimm, 2005) predict a cryosphere thickness of several kilometers. The cryosphere must be >1 km thick to achieve superlithostatic pressures, but more likely >3 km (Wang et al., 2006). This is a lower limit on aquifer depth z_{min}. Assuming the fractured basalt megaregolith model of Hanna and Phillips (2005), Mars' crust has a permeability of order $K = 10^{-11}$ m^2. For an aquifer depth of 1 km, and a tensile strength of 14 MPa, $q_{max} \approx$ 10 m day^{-1} per unit crater floor area. More realistically, the flow of water would be focused through high permeability fractures ($\sim 10^{-9}$ m^2 Wang et al. 2006) with small cross sectional areas.

A groundwater trigger for tadpole crater overspill has several potential problems. Superlithostatic pressures are most easily achieved in a global aquifer (Hanna and Phillips, 2005), however, high aquifer pressures would enable high discharge rates to persist for days to months (Wang et al., 2006). This is inconsistent with the observation that no tadpole crater exit breaches have eroded through all the available topography, as would be expected for prolonged $Q_{in} > 0$. In a regionally dissected hydrological system with small, local aquifers, superlithostatic pressures may not be possible due to pressure diffusion out of the aquifer (Hanna and Phillips, 2005), so aquifer discharge would quickly decay (Wang et al., 2006), limiting the ability of the aquifer to both fill the tadpole crater and sustain $Q_{in} > 0$. Specific regional aquifer conditions would be required for a groundwater source to be consistent with tadpole crater breach depth observations. Finally, many tadpole craters occur on regional or local highs (e.g. Fig. 3.1b), which is inconsistent with a groundwater source.

The size, latitude, and altitude distributions of tadpole craters can also be used to constrain tadpole crater climate conditions and hydrology. Firstly, all known tadpole craters are

small (D <15 km). This apparent size cut-off has two possible explanations. Either water accumulation was insufficient to overspill craters D >15 km, or there was a lack of larger craters. From the tadpole craters identified by Wilson et al. (2016) and the Robbins and Hynek (2012b) crater database, 3% of craters in Arabia Terra with $D < 15$ km are tadpole craters, i.e. the probability of any crater not being a tadpole crater is 0.97. There are 87 craters $D > 15$ km in the region studied by Wilson et al. (2016). The probability of not finding a tadpole crater $D > 15$ km is 0.97^{87}, or 7%. While this suggests that there may be an upper limit on tadpole crater size, repeating this calculation with a global tadpole crater inventory is necessary. Secondly, ice accumulation is more strongly affected by latitude and altitude than groundwater. In the case of a global pressurized aquifer, the control on tadpole crater distribution would be the occurrence of conduits between the surface and the crater floor, which may not have any latitude/altitude preference at all. Conversely, ice accumulation is strongly sensitive to surface temperature and moisture distribution (Mischna et al., 2013).

3.7 Conclusions

tadpole craters are relatively young Martian craters with outlet valleys puncturing fresh crater rims, but no visible inlet valleys. Our new fixed channel width, 0-D model of breach erosion predicts runaway erosion for 2 of 21 measured tadpole crater exit breaches, but evidence for runaway erosion (defined here as erosion through the entire crater rim thickness) is not observed for any tadpole craters. The mismatch between our model predictions and the measured tadpole crater valleys cannot be explained by increased critical dimensionless Shields stress (τ_{*c}) typical of steep slopes, different sediment transport equations, or differences in channel slope or outflow valley length. The remaining hypotheses are that runaway erosion is halted by the transition between impact ejecta and fractured, uplifted bedrock in the crater rim (either by a change in grainsize or a change in erosion style), or that the crater

was predominantly ice-filled. There are two main scenarios for the observed eroded depths of tadpole crater outlet valleys that are consistent with our modeling results:

1. Lots of erosion, once: Groundwater discharge infilled the crater with liquid water until it overspilled the rim, eroding the full valley depth in a single overspill event.

2. A little erosion, many times: tadpole craters were predominantly filled with ice that underwent a small amount of melting many times (e.g. seasonally). This formed small melt ponds that drained over the crater rim, contributing a small amount of valley floor erosion each time the climate enabled meltwater to form.

While it is possible to fill and overspill a tadpole crater through a single groundwater discharge event, many tadpole craters are located on local or regional highs which may argue against groundwater as a filling mechanism. No existing climate models for Hesperian Mars or impact-induced climates are capable of providing the precipitation rates or snowmelt rates required to fill and overspill a tadpole crater in a single event, which likely rules out the possibility of a single climate-induced tadpole crater-forming erosion event.

CHAPTER 4

MULTIPLE OVERSPILL FLOOD CHANNELS FROM YOUNG CRATERS REQUIRE SURFACE MELTING AND HUNDREDS OF METERS OF MID-LATITUDE ICE LATE IN MARS HISTORY

This chapter will be submitted to The Planetary Science Journal for publication as: Warren, A. O., Wilson, S. A., Howard, A., Noblet, A. and Kite, E. S. (2023). Multiple overspill flood channels from young craters require surface melting and hundreds of meters of mid-latitude ice late in Mars history. A.H. and S.A.W. provided the tadpole crater database used in this chapter, which A.O.W. manually checked and used to make additional measurements. A.N. provided two of the Digital Elevation Models used in this study.

We would like to thank Frances Butcher and Anna Grau-Galofre for helpful conversations about terrestrial analogs and both terrestrial and Martian subglacial systems, Marc Hesse for productive discussions that guided our groundwater modeling approach, the HiRISE HiWish program for fulfilling observation requests, and the University of Chicago Research Computing Center resources. Grants: NASA NNH19ZDA001N-FINESST (F.I. A.O. Warren)

4.1 Abstract

Mars' tadpole craters are small, young craters whose crater rims are incised by one or more exit breaches but lack visible inlets. The tadpole forming climate records the poorly understood drying of Mars since the Early Hesperian. A third of tadpole craters have multiple breaches, therefore the climate must have been able to generate crater rim incision in multiple locations. We use HiRISE data for four multiple breach tadpole craters to measure their crater fill, rims, and exit breaches. We compare these measurements and other data to our calculations of liquid water supply by rain, surface melting, groundwater discharge,

and basal ice sheet melting to discriminate between four proposed formation mechanisms for tadpole breaches, favoring scenarios with ice-filled craters and supraglacial melting. We conclude that multiple breach tadpole craters record hundreds of meters of mid-latitude ice and climate conditions enabling intermittent melting in the Late Hesperian and Amazonian, suggesting that liquid water on Mars has only been available in association with water ice for billions of years.

4.2 Introduction

The surface of Mars records a climate catastrophe. A planet with enough liquid water to carve canyons and overspill lakes in the Noachian (∼3.6 Ga) (Fassett and Head, 2008) became a cold, arid desert where water is so unstable it seldom occurs as anything but ice or vapor (Murphy and Koop, 2005). This great drying of Mars (Kite, 2019; Kite and Noblet, 2022; Scheller et al., 2021) is recorded by water-worn features that become increasingly spatially patchy and imply increasingly arid concitions over time (Holo et al., 2021; Grant and Wilson, 2011; Kite et al., 2019; Wilson et al., 2021). This evolution has been driven by the progressive loss of the atmosphere to space or carbonate formation (Hu et al., 2015), changes in the available surface and atmospheric water inventory (Mahaffy et al., 2015), loss of non-CO_2 greenhouse forcing (Wordsworth et al., 2021; Kite et al., 2022), and changes in orbital parameters (Haberle et al., 2017). However, the precise causes, timing, duration, and spatial pattern of this drying out of Mars are still poorly constrained (Kite and Noblet, 2022). In this paper, we examine the climate constraints on the cooling and drying of Mars provided by "tadpole craters."

We define tadpole craters (also known as "pollywogs") as small craters, extending up to 32 km across but typically ranging from 0.5-15 km in diameter, with at least one outlet breach leading away from their rims and no visible inlets. Outlet breaches indicate that at one time the rims of these craters were incised by liquid water (Wilson et al., 2016; Warren et al.,

2021). Unlike other preserved overspilling (i.e. hydrologically open) paleolakes on Mars (Bamber et al., 2022; Goudge et al., 2016; Fassett and Head, 2008; Bamber et al., 2022; Goudge et al., 2023), tadpole craters do not have inlet breaches and do not appear to form integrated chains of lakes. Tadpole craters occur in the mid-latitudes in both hemispheres (Wilson et al., 2016; Howard et al., 2022), with the best-studied group of tadpole craters in Arabia Terra (Wilson et al., 2016; Warren et al., 2021). Tadpole craters exist close to the equator (Warren et al., 2021) but these appear to be unusual.

In this paper, we focus on tadpole craters with multiple breaches. These represent about one-third of the overall tadpole crater population in the latitude band 24-52° S. Multiple breach tadpole craters are difficult to understand because the most common cause of dam breaches on Earth is overtopping of the dam wall by water (Costa and Schuster, 1988; Neupane et al., 2019). The lowest point on the crater rim is the most likely location for overtopping to occur, however, we observe tadpole craters with tens of meters of vertical separation between the breach floors of their multiple outlets (Fig. 4.1). Therefore, a mechanism must exist that can fill craters, generate liquid water, and route that water to multiple elevations around a crater rim. This constrains the climate during multiple breach tadpole crater overspill.

Although tadpole craters are too small to apply crater dating methods (Michael and Neukum, 2010; Warner et al., 2015), few $\leq$4 km craters pre-date the Noachian-Hesperian boundary (Irwin III et al., 2013), whereas many tadpole craters have diameters of $\leq$4 km. Additionally, tadpole crater rim breaches appear fresher than the more degraded valley networks (Wilson et al., 2016), and tadpole craters have topographically elevated, and sharp to rounded, crater rims (Wilson et al., 2016; Warren et al., 2021). These lines of evidence suggest that tadpole craters post-date the most intense episodes of fluvial erosion on Mars, and therefore formed since the Late Hesperian (Wilson et al., 2016). Alongside other Hesperian and Amazonian fluvial and glacial features such as alluvial fans (Holo et al., 2021;

Grant and Wilson, 2011), Fresh Shallow Valleys (FSVs, Wilson et al. 2016), midlatitude eskers (Butcher et al., 2017), and buried glaciers (Butcher et al., 2023; Holt et al., 2008; Head et al., 2005; Fassett et al., 2010), tadpole craters record a step in the long-term evolution of Mars' climate from the warmer, wetter Noachian to the planet's cold and arid present state (Kite and Noblet, 2022; Mangold et al., 2012; Jakosky and Phillips, 2001).

To carve breaches, tadpole craters must first fill with either water or ice, and then generate enough liquid water at least once (Warren et al., 2021) to erode the observed rim breach(es). Therefore, the Martian climate must have been able to generate liquid water in the midlatitudes during the Late Hesperian/Amazonian despite a colder, drier climate than that of the Late Noachian/Early Hesperian. A global aquifer protected by a cryosphere has been suggested as a mechanism for sustaining subsurface water under colder conditions (e.g. Clifford et al. 2010; Hanna and Phillips 2005). Additionally, climate models predict that high obliquity (e.g. 45°) can enable accumulation of ice in the midlatitudes, and even further equatorward, as late as the Amazonian (Forget et al., 2006; Madeleine et al., 2009; Steele et al., 2017; Mischna et al., 2003).

To better understand the climate requirements of multiple breach tadpole craters, we consider four mechanisms for tadpole crater overspill that can also explain how multiple breaches form (Fig. 4.2):

- **H1. Crater-filling water:** Craters fill to the brim with liquid water from precipitation, meltwater, or groundwater flow and overspill their rims. Either the lowest points on the rims were modified over time by erosion, creating new low points, or water inputs were sufficient to activate multiple breaches simultaneously (Sections 4.4.1 & 4.4.1).

- **H2. Shallow melt ponds on crater-filling ice:** Craters fill to the brim with ice. Transient melting forms ice surface ponds of sufficient volume to overspill the crater rim and carve breaches (Section 4.4.2).

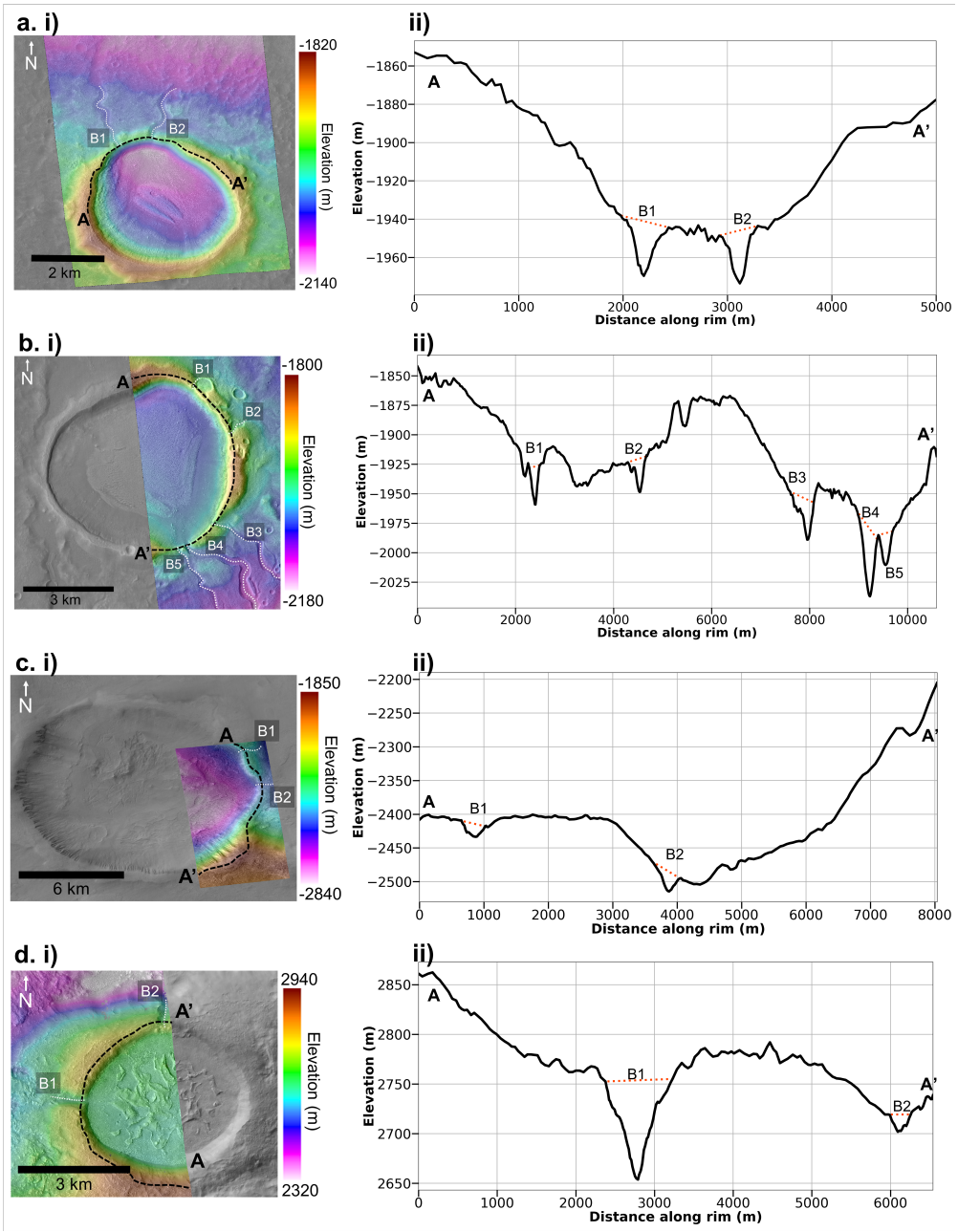

Figure 4.1: i) Digital Elevation Models (DEMs) and ii) topographic rim profiles of multiple breach tadpole craters **a.** *Arabia Terra 1* (left: ESP_052510_2150), **b.** *Arabia Terra 2* (left: ESP_053736_2180), **c.** *Hellas* (DEM: a. Noblet, left: ESP_012014_1335), **d.** *Noachis* (DEM: a. Noblet, left: ESP_074112_1455) (Table 4.1). B1-B5 mark breaches incised into the rim. Solid black lines show measured rim topography from A to A', dotted red lines show interpolated pre-incision topography between fresh-appearing (i.e. unincised) rim sections either side of each breach.

- **H3: Retreating ice sheet:** A retreating ice sheet partially fills craters with ice, routing meltwater into the crater in sufficient volumes to overspill exposed sections of the rim. The ice sheet then retreats further, exposing lower areas of the rim and causing previous, higher breaches to be abandoned. (Section 4.4.1)

- **H4. Subglacial flow:** A regional ice sheet covers the tadpole craters. Water from basal or surface melting pools at its base to drive subglacial streams out of craters (Section 4.5).

In this paper, we aim to test these mechanisms and determine the climate constraints implied by tadpole craters with multiple breaches. To do this, we first analyze the size and elevation distribution of all tadpole craters, including those with both single and multiple breaches, in the latitude band 24-52° S (Section 4.3.1). Busy readers may skip this section. Next, we focus on four multiple breach tadpole craters (Fig. 4.1). We provide detailed descriptions of the rim, breach, and crater floor morphologies of these craters, which busy readers may also skip. We use observations of these four craters (Section 4.3.2) to test our four proposed tadpole breach formation mechanisms (Fig. 4.2). We use breach morphometry to calculate water flow rate under subaerial (Section 4.4.1) and subglacial conditions (Section 4.5), and the eroded volumes of each exit breach. We compare the results of these calculations to:

1. Predicted precipitation and melting rates (Section 4.4.1)

2. Water supply rates from meltwater routed from an ice sheet larger than the crater (Section 4.4.1)

3. Discharge from a radially symmetrical, homogeneous, cryosphere-confined pressurized aquifer (Section 4.4.1)

4. The rim incising potential of meltwater ponds smaller than the crater area draining from the surface of a crater-filling ice body (Section 4.4.2)

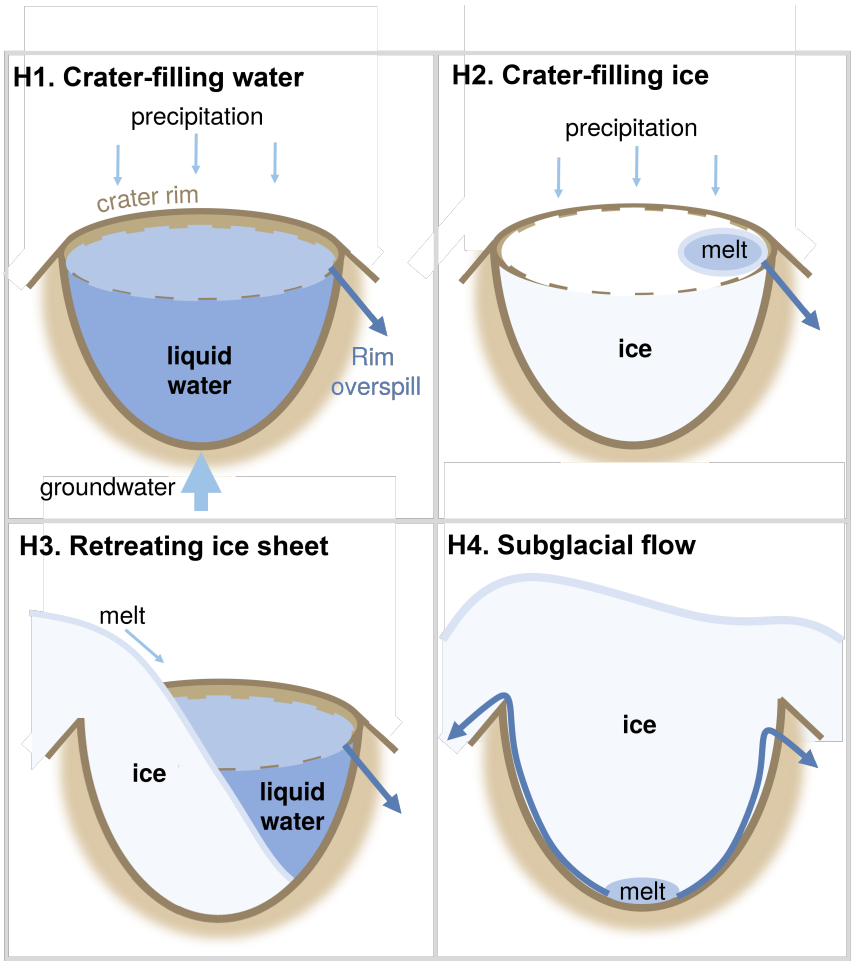

Figure 4.2: Sketch of four overspilling mechanisms for tadpole craters. H1. Crater filled to rim with liquid water - breaches form when water level exceeds topographic lows on rim. H2. Ice-filled crater - breaches form when localized melt pond(s) overspill the crater rim. H3. Crater at the margins of a retreating regional ice sheet - breaches form when meltwater in crater exceeds topographic lows on rim, new topographic lows are exposed as the ice sheet retreats. H4. Crater buried beneath regional ice sheet - breaches form as subglacial channels. All breaches may form in a single overspilling event, or sequentially as rim topography is modified or exposed by changing ice extent and topography or erosion.

5. Melt volumes generated by supraglacial meltwater (Section 4.5.3)

6. Melting rates and total melt thicknesses caused by a magma body intruded beneath a subglacial crater (Section 4.5.3)

Finally, we discuss potential terrestrial analogs for multiple breach tadpole craters (Section 4.6.1).

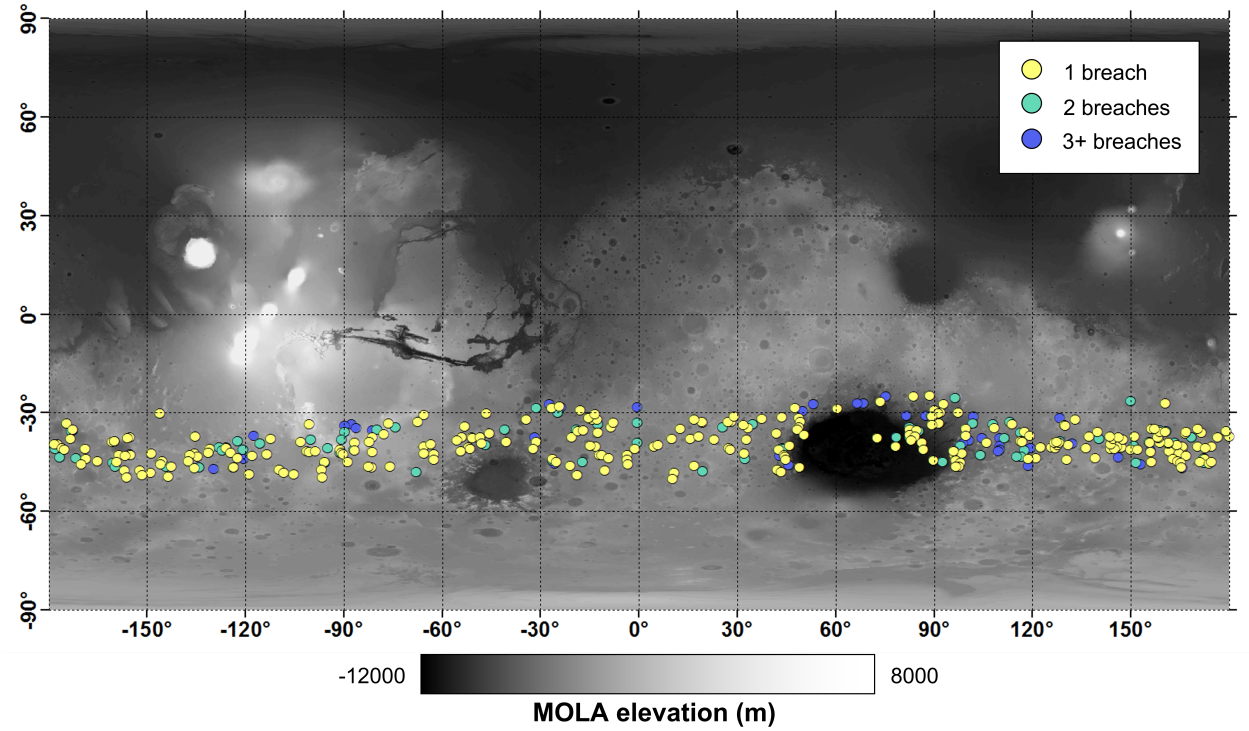

Figure 4.3: Map of reliable tadpole craters identified by A. Howard and checked by A. O. Warren in the latitude band 24-52° S overlaid on MOLA topography. White circles indicate craters with a single exit breach, grey circles craters with 2 exit breaches, and black circles craters with ≥3 exit breaches.

4.3 Tadpole Crater Distribution and Geomorphology

4.3.1 Tadpole crater dataset

Tadpole craters were observed in a latitude band between 24 and 52° S and assigned a reliability score between 'a' (most reliable) and 'c' (least reliable) by A. Howard using a global CTX mosaic (Howard et al., 2022) (Fig. 4.3). Every tadpole crater with $D_c \geq 1$ km was cross-referenced with the Robbins crater database (Robbins and Hynek, 2012a) to find its crater ID, circular fit diameter, latitude/longitude coordinates, and degradation state (Robbins and Hynek, 2012a). A. O. Warren independently reviewed all tadpole craters with reliability 'a' to remove any less reliable observations and count the number of rim breaches using a global CTX mosaic (Dickson et al., 2018) and global merged MOLA 128ppd and

64ppd mosaic (Smith et al., 2001).

In this subsection, we present evidence that:

1. Tadpole breaches preferentially occur in smaller craters
2. Tadpole craters preferentially occur on local highs relative to surrounding topography across a range of spatial scales

The preference for small crater overspill may reflect the total surface/atmosphere water inventory available during the tadpole breach forming climate (Fastook and Head, 2013). We suggest that the trend towards a greater proportion of tadpole craters at higher relative elevations reflects preferential accumulation of snow and ice at higher elevations, either through decreasing temperature with altitude favoring snow/ice accumulation at high points during the breach eroding climate (e.g. Wordsworth et al. 2013; Forget et al. 2006), or through orographic precipitation (Scanlon et al., 2013).

Busy readers may skip the remainder of this subsection.

Diameter Dependence of Tadpole Craters

To determine whether there is a crater diameter preference for tadpole breach formation, we compare the tadpole crater dataset to all Robbins crater database craters in the same latitude band (24-52° S). Following Head et al. (2010), we first performed a 2-sample Kolmogorov-Smirnov test using the `scipy.stats` package to determine whether the crater size-frequency distribution (SFD) of tadpole craters is consistent with being drawn from the same distribution as the SFD of all craters in the region. A p-value of 1.14×10^{-4} suggests with >98% confidence that the SFD of tadpole craters is distinct from that of all craters. We conclude that tadpole craters form by a process that does not uniformly affect craters of all sizes present in the studied latitude band. Rather, tadpole breaches preferentially form in smaller craters.

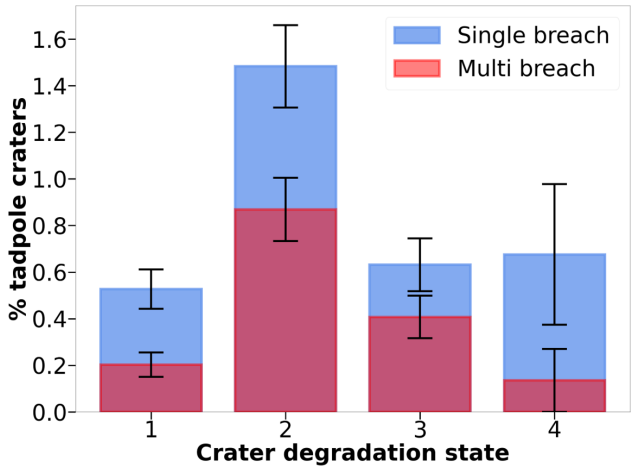

Figure 4.4: Percentage of craters in each degradation state classification (Robbins and Hynek, 2012a) that are tadpole craters, separated into tadpole craters with a single exit breach (blue), and those with multiple breaches (red). The total tadpole crater fraction is the sum of the two bars, i.e. 2.4% for degradation state 2. Error bars show fractional error corresponding to $\sqrt{n}$ where n is number of single breach (blue) or multiple breach (red) tadpole craters in each degradation state category. A degradation state of 4 corresponds to a pristine, fresh crater, and a degradation state of 1 corresponds to the most degraded craters which are highly infilled/modified by fluvial and aeolian processes with no preserved topographic rims or ejecta.

To further examine the difference between SFDs, we then normalized the Robbins crater dataset by degradation state (Robbins and Hynek, 2012a) to match the degradation state distribution of the tadpole craters (Fig. 4.4). Older crater populations have a greater proportion of larger craters (Hartmann, 2005) and older craters tend to be more degraded (Tanaka et al., 2014). A degradation state of 4 corresponds to a pristine, fresh crater, and a degradation state of 1 corresponds to the most degraded craters which are highly infilled/modified by fluvial and aeolian processes with no preserved topographic rims or ejecta. Normalizing by degradation state allows us to subtract the effect of changing crater size-frequency distributions over time and determine whether the tadpole crater forming process(es) had a crater size preference, rather than just seeing size patterns associated with tadpole formation during a particular epoch in Mars history. We normalize for degradation state by calculating the proportion of tadpole craters in each degradation state category (1-4, i.e.

most to least degraded), then dividing these proportions by the highest proportion value to find weights such that the most common degradation state has a weight of 1, and the other degradation states have weights < 1. The largest proportion of pollywogs occurs for craters with a degradation state of 2 (Fig. 4.4). We then assign the calculated degradation state weight to each individual crater. When subsequently binning the Robbins crater database (e.g. in crater diameter or elevation), we calculate the mean degradation state weight for each bin, and multiply the total number of craters in each bin by this mean weight.

We divide the tadpole crater dataset and Robbins crater database into 11 equally-sized diameter bins for all craters with $D_c \geq$4 km. We choose this diameter cutoff as the database may be incomplete for smaller craters (Holo et al., 2021). The number of bins is chosen using the Rice rule ($k = 2n_a^{1/3}$) which is suitable for avoiding over-smoothing in non-normally distributed, continuous data (Terrell and Scott, 1985). Here, $n_a = 233$ is the total number of tadpole crater observations with $D_c \geq 4$ km. We sum the number of craters in each diameter bin, with Robbins crater database craters multiplied by their degradation state-dependent weights. We calculate a $\sqrt{n}$ error for each tadpole crater bin to account for shot-noise error, where n is the number of tadpole craters in that bin. We find the proportion of tadpole craters per bin and find a line of best fit to the proportion distribution per bin using the `scipy.optimize` package function `curve_fit` (Fig. 4.5). We then find the 95% confidence interval for each line of best fit using bootstrapping, generating 5000 samples of size $n_{R,4}$ =13,538 (the total number of craters in the Robbins database (Robbins and Hynek, 2012a) within the latitude band 24-52° S with $D_c \geq 4$ km).

Tadpole breaches preferentially form in craters with smaller diameters to better than 99.98% confidence (Fig. 4.5a, total number of tadpole craters with $D_c \geq$4 km $n_{a,4} = 233$). Of 5000 bootstrap fits of percentage tadpole craters as a function of binned diameter, 0 had a slope ≥ 0. To test that this result is not just a product of binning, we also used the Python package SKIKIT-LEARN to fit a linear least squares regression to tadpole occurrence

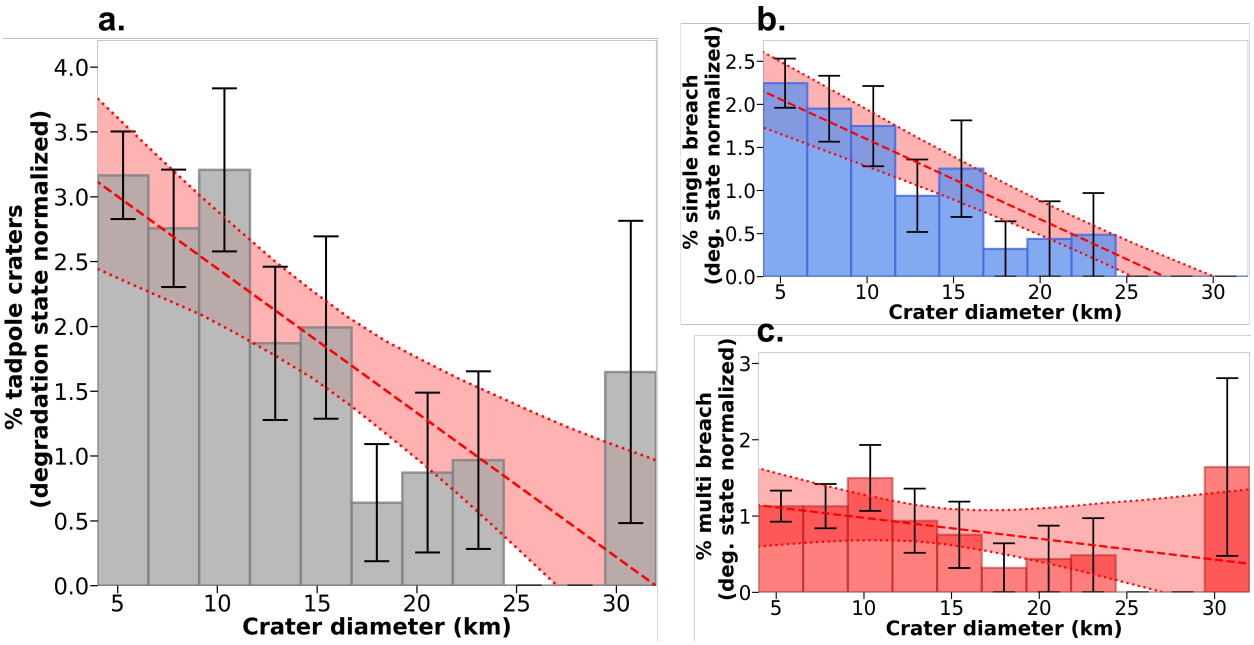

Figure 4.5: Tadpole craters show a statistically significant preference for smaller craters. **a.** Histogram of the proportion of all craters that are tadpole craters in the latitude band 24-52° S as a function of diameter, normalized for degradation state. **b.** Histogram of the proportion of all craters that are tadpole craters with a single exit breach by diameter. **c.** Histogram of the proportion of all craters that are tadpole craters with multiple breaches by diameter. For all panels, black bars show $\sqrt{n}$ error bars where n is the total number of tadpole craters in each bin ($n_a = 233$ is the total number of tadpole craters with $D_c \geq 4$ km for the full tadpole crater population, $n_s = 145$ for single exit breach tadpole craters, $n_m = 77$ for multiple breach tadpole craters). Dashed red lines show a linear best fit. Dotted red lines bounding red shaded areas indicate 99.8% confidence intervals for linear best fit found using 5000 bootstrapped samples of size n_R =13,538 (the total number of craters in latitude band 24-52° S with $D_c \geq 4$ km in the Robbins database (Robbins and Hynek, 2012a)) with replacement.

against diameter (tadpole craters assigned a score of 1, non-tadpole craters a score of -1) for each of the 5000 bootstrap-generated crater populations with all craters unbinned. 0 linear regressions had a slope ≥ 0. The small crater preference is dominated by the size preference of craters with a single exit breach (Fig. 4.5b, total single exit breach craters $n_{s,4} = 145$). Tadpole craters with multiple breaches show no clear crater diameter trend (Fig. 4.5, total multiple breach craters $n_{m,4} = 77$). However, the distribution of multiple breach craters is affected by small-number statistics, and a larger sample may reveal a clear trend not visible

among the 77 samples used in this analysis.

We interpret the preferential occurrence of tadpole breaches in smaller craters as an indication that the overspilling mechanism is limited by the column thickness of water (as either liquid or ice) available during the tadpole breach-forming period. The relative paucity of large tadpole craters, when corrected for crater degradation state, suggests that insufficient water (as liquid or ice) was available to fill deep topographic depressions. For example, a regionally compartmentalized groundwater system (Harrison and Grimm, 2009) may have limited the water volume available to flow into craters from discharge of a cryosphere-pressurized aquifer. Alternatively, deposition of a widespread but vertically thin ice sheet in the midlatitudes may have filled smaller craters to the rim with snow and ice, but left larger craters underfilled, so that meltwater ponds on the surface of the ice did not overtop crater rims. The largest tadpole crater in our dataset (D_c = 31.5 km) suggests the ice cover must have been $\lesssim$ 2500 m thick (Eqn. 4.1). However, local thickening of ice due to favorable conditions for precipitation or direct condensation is possible. 90% of tadpole craters in the latitude band 24-52° S have D_c < 12 km, which corresponds to an ice thickness < 1000 m (Eqn. 4.1). The low average height of mid-to-high latitude Amazonian pedestal craters (40.4 m in the S hemisphere), a proxy for ice-rich deposit thickness (Kadish et al., 2010), has been used to suggest that the total ice inventory available to fill craters and mantle high latitudes may have been limited by the combined water inventory of the polar layered deposits, shallow ice deposits, and regolith (Fastook and Head, 2013).

Elevation Dependence of Tadpole Craters

To determine whether there is an elevation preference for tadpole breach formation, we investigate not only MOLA gridded topography (Fig. 4.6a), but also smoothed topography on a variety of length scales to determine whether the occurrence of tadpole craters depends on local topography (e.g. a <100 km diameter hill) or regional topography (e.g. a several

100 km rise). We use the ArcGIS Geoprocessing Spatial Analyst Focal Statistics tool to generate smoothed MOLA topography with smoothing radii (r_s) of 50, 100, 200, 500, and 1000 km. This tool calculates the mean MOLA elevation of all cells within a circular radius r_s for each cell in the mosaic. We then subtract the smoothed topography from the original MOLA mosaic to find the residual MOLA topography. We then extract the elevation and residual topography for the central point of each tadpole crater and Robbins crater database crater in the 24-52° S latitude band with $D_c \geq 4$ km. We separate the craters into 11 evenly sized elevation bins and residual MOLA topography bins for each value of r_s. Again, the number of bins is chosen using the Rice rule: $k = 2n_a^{1/3}$(Terrell and Scott, 1985) where $n_a = 233$ is the total number of tadpole crater observations with $D_c \geq 4$ km. We restrict the residual MOLA topography bin range for each smoothing radius to exclude values beyond which there are 0 craters.

Following the same procedure as described in Section 4.3.1, we fit a linear best-fit line to the degradation state normalized tadpole crater percentage in each binned elevation and residual topography dataset, and find the 95% confidence intervals using bootstrapping. In our fitting procedure, the tadpole crater percentage in each bin is weighted proportional to the inverse of the $\sqrt{n}$ error such that the bin with the smallest $\sqrt{n}$ error has a weight of 1, and the bin with the largest error has a weight of $\min(\sqrt{n})/\max(\sqrt{n})$. This procedure reduces the impact of bins with very few craters on our fits. We repeat this process for the single exit breach and multiple breach tadpole crater datasets.

We find no elevation trend (Fig. 4.6). However, there is a peak in the percentage of tadpole craters at elevations between -2670 and -890 m which corresponds to the elevations of an apparent cluster of tadpole craters on the slopes of the Hellas Basin (Fig. 4.3). In the residual topography data, there is a consistent trend towards a greater tadpole crater fraction at higher elevations (Fig. 4.6b-f) in the full tadpole crater dataset, as well as the single exit breach and multiple breach subsets of the tadpole crater population (all 99.98%

confidence; 0 of 5000 bootstrap fits for each smoothing radius have slopes < 0). This trend is strongest for smaller smoothing radii, with a maximum best fit slope of 4.1% km^{-1} for a 50 km smoothing radius. We interpret this as a greater likelihood of tadpole breach formation for craters located on "local" highs within tens of kilometers of the crater, in addition to a slight preference for tadpole breach formation on regional highs, as indicated by the trend remaining present at a 1000 km smoothing radius (Fig. 4.6f). This interpretation disfavors a groundwater hypothesis for tadpole crater water source, as higher surface elevations act to reduce the pressure head driving groundwater discharge (Clifford and Parker, 2001) into a crater. A higher local elevation preference may also favor a precipitation or atmospheric deposition control on tadpole breach formation, for example, if local highs are cold enough to favor snow/ice accumulation as occurs at high elevations in climate models of a cold and icy early Mars under a thicker CO_2 atmosphere (Wordsworth et al., 2013) and models of Amazonian ice accumulation under high obliquity (Forget et al., 2006). Another possibility is that a preference for local highs indicates an orographic precipitation control on tadpole breach formation, where the local topography drives moisture-bearing parcels of atmosphere upwards, generating precipitation, e.g. of water ice, on relative highs (Scanlon et al., 2013).

The tadpole crater dataset used in this study is restricted to a narrow latitude band (24-52° S). Tadpole craters also occur outside this band (Warren et al., 2021; Wilson et al., 2016). A more complete global tadpole crater dataset might reveal elevation trends not distinguishable using the regional data presented here.

4.3.2 Tadpole crater DEMs

We analysed four digital elevation models (DEMs) of HiRISE stereopairs of multiple breach tadpole craters. Two fall within the latitude band 24-52° S analyzed in Section 4.3.1, and two are in Arabia Terra and have been previously studied (Warren et al., 2021). Throughout this paper, each multiple breach tadpole crater is referred to by a nickname corresponding

to the general region of Mars in which it occurs, listed in Table 4.1. We use HiRISE stereopairs and DEMs to measure topographic profiles of the crater rims (Fig. 4.1), and to make morphological observations of crater fill, rims, and breaches.

In this subsection, we present evidence that:

1. All multiple breach tadpole craters are partially filled with debris-mantled, ice-rich deposits

2. Crater rims have been modified by ice

3. Several breaches are filled with debris-mantled, ice-rich deposits, and therefore their depths may be underestimated

4. The two breaches from *Arabia Terra 1* have sections of valley floor that go upslope, which, if primary, would suggest a subglacial origin

This modern ice-fill and ice-related rim modification is not necessarily related to breach overspill as there is evidence for multiple ice ages on Mars (Butcher et al., 2017; Head et al., 2003; Fassett et al., 2014). We find that the morphology of tadpole craters does not favor a particular mechanism for crater overspill.

Busy readers may skip the remainder of this subsection.

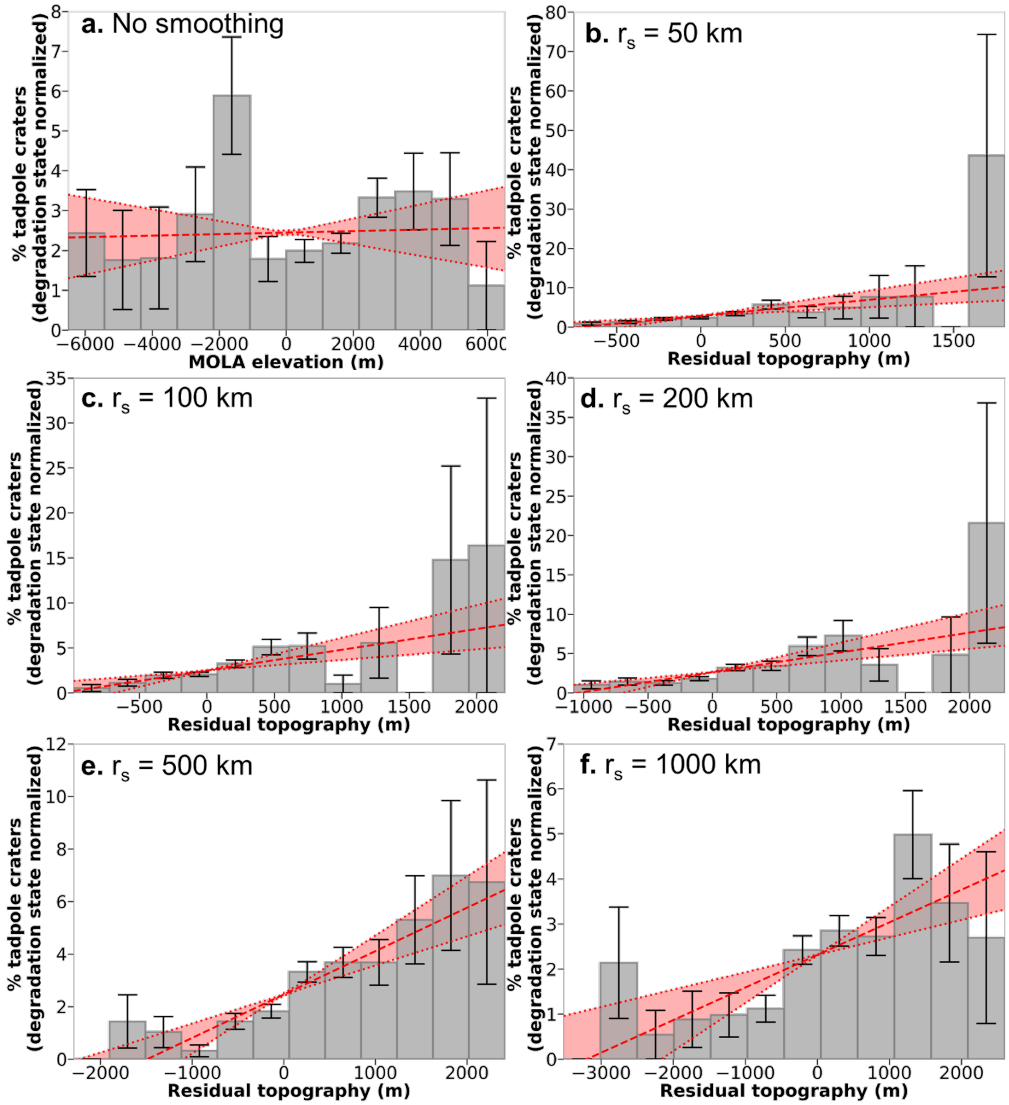

Figure 4.6: Tadpole craters do not show a clear elevation trend, but preferentially occur on relative highs across all length scales. **a.** Histogram of degradation-state-normalized (see Section 4.3.1) percentage of total crater population that is tadpole craters with MOLA elevation. b-f. Histogram of degradation-state-normalized percentage tadpole crater percentage with residual MOLA topography. We generate smoothed MOLA topography with smoothing radii (r_s) of 50, 100, 200, 500, and 1000 km. We then subtract the smoothed topography from the original MOLA mosaic to find the residual MOLA topography. Black bars show $\sqrt{n}$ error bars where n is the total number of tadpole craters in each bin ($n_a = 233$ is the total number of tadpole craters with $D_c \geq 4$ km for the full tadpole crater population). Dashed red lines show a linear best fit to inverse $\sqrt{n}$ weighted bin totals. Dotted red lines bounding red shaded areas indicate 95% confidence intervals for linear best fit found using 5000 bootstrapped samples of size n_R =13,538 (the total number of craters in latitude band 24-52° S with $D_c \geq 4$ km in the Robbins database (Robbins and Hynek, 2012a)) with replacement.

Nickname	**Lat**	**Lon**	n_b	D_c **(km)***	d_c **(m)**	$d_{c,0}$ **(m)**	$V_{c,0}$ **(km^3)**	**Crater ID***	**HiRISE ID (left)**
Arabia Terra 1	34.808	16.485	2	6.4	224	630	5.8	05_002270	ESP_052510_2150
Arabia Terra 2	37.625	21.347	5	3.6	195	390	1.2	05-001364	ESP_053736_2180
Hellas	-45.881	45.818	2	14.7	616	1290	53.6	27_000899	ESP_012014_1335
Noachis	-34.229	25.515	2	4.8	252	500	2.7	27_002296	ESP_074112_1455

Table 4.1: Summary of multiple breach tadpole craters investigated in this study. n_b is number of exit breaches, D_c is crater diameter, d_c is measured crater depth (errors $<$ 1m), $d_{c,0}$ and $V_{c,0}$ are calculated original crater depth and volume respectively (Eqns. 4.1 & 5.48; Garvin et al. 2000). *Database of Robbins and Hynek (2012a).

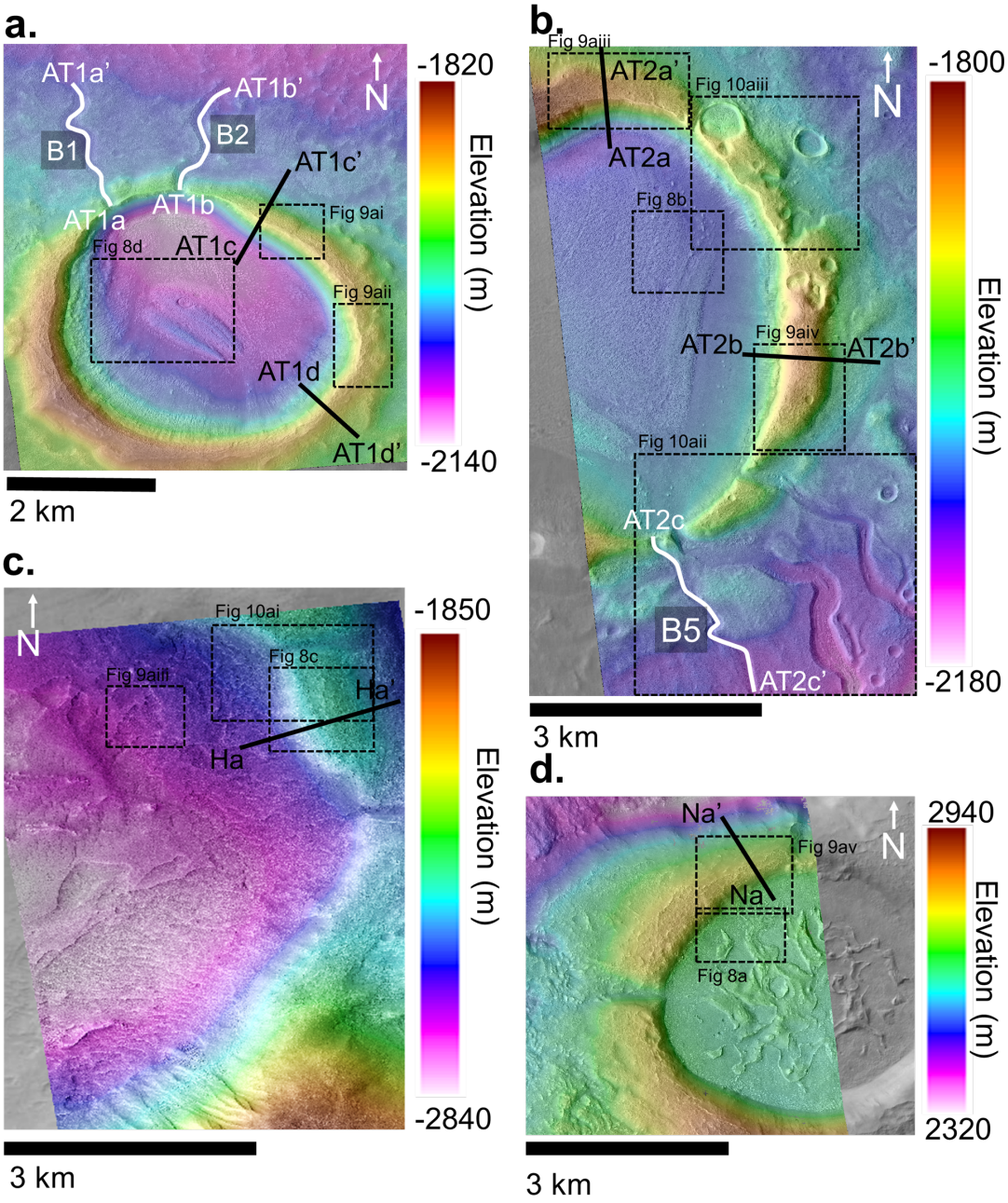

Figure 4.7: Digital Elevation Models (DEMs) of multiple breach tadpole craters showing measurement areas for other figures. **a.** *Arabia Terra 1* (left: ESP_052510_2150), **b.** *Arabia Terra 2* (left: ESP_053736_2180), **c.** *Hellas* (DEM: a. Noblet, left: ESP_012014_1335), **d.** *Noachis* (DEM: a. Noblet, left: ESP_074112_1455) (Table 4.1). White solid lines indicate breach long profiles (Fig. 4.10) with breach labels corresponding to those in Fig. 4.1, black solid lines indicate rim topographic profiles (Fig. 4.9), and black dashed boxes indicate regions shown in other figures.

Crater Fills

Using empirical equations for the depth and volume of craters on Mars based on MOLA observations (Garvin et al., 2000), we can calculate the expected depths (d_c, km) and volumes (V_c, km^3) for each tadpole crater (Table 4.1):

$$d_c = 0.131 D_c^{0.85} \tag{4.1}$$

$$V_c = 0.04 D_c^{2.68} \tag{4.2}$$

where D_c is the crater diameter in km. These equations span the simple-to-complex transition (Garvin et al., 2000), and are therefore appropriate for all four multiple breach tadpole craters in this study (Table 4.1).

Comparing the measured maximum crater depths from the DEMs with their predicted original depths (Garvin et al., 2000) (Table 4.1), all four craters have been infilled with hundreds of meters of material (*Arabia Terra 2*: 190 m (2 s.f.); *Hellas* (left: ESP_012014_1335): 670 m (2 s.f.)). Infilling is caused by processes including mass wasting, fluvial modification, and aeolian deposition, as sediment is moved from the crater walls or beyond to the crater floor over time (Mangold et al., 2012; Craddock et al., 1997b). Many mid-latitude craters also show evidence for debris-covered ice fill (e.g. Levy et al. 2009; Mangold 2003; Levy et al. 2014; Butcher et al. 2023), associated with other debris-covered glacial landforms poleward of around 30° that represent a water inventory of $> 1.25 \times 10^5$ km^3 (Levy et al., 2014). We also find evidence for debris-covered ice fill in these four multiple breach tadpole craters.

In HiRISE imagery, large areas of the crater floor fill of *Arabia Terra 1* and *Arabia Terra 2* show the distinctive interconnected knobs characteristic of "brain terrain" (Mangold, 2003; Levy et al., 2009; Butcher et al., 2023; Levy et al., 2014, 2010) (Fig. 4.8b & d). This texture is typically associated with lobate debris aprons (LDAs), lineated valley fill (LVF), and concentric crater fill (CCF), all of which show viscous flow features interpreted as the

result of buried ice 10-100 Myr old (Mangold, 2003). Mangold (2003) and Levy et al. (2009) propose differential sublimation of debris-mantled ice as the mechanism driving brain terrain formation. Periglacial freeze-thaw processes have also been proposed as a mechanism for forming brain terrain (Mellon et al., 2008; Hibbard, 2021), however, this interpretation is difficult to reconcile with the cold, arid conditions expected on recent Mars (Levy et al., 2016). Additionally, *Arabia Terra 1* has a candidate "ring mold" crater at its center (Fig. 4.9). Ring mold craters are characteristic of impacts into ice rich substrate (Kress and Head, 2008). We interpret the crater fill of *Arabia Terra 1* and *Arabia Terra 2* as between 30% (pore-filling) and 90% ice mixed with debris (Levy et al., 2014).

The crater floor fills observed in *Hellas* and *Noachis* lack clearly identifiable brain terrain (Fig. 4.8c & a respectively). The floor fill in *Hellas* is instead characterized by decameter-scale polygons visible in shallow depressions that act as windows into crater floor spanning mottled terrain (Fig. 4.8c). The sharp edges of these depressions and their scale are similar to sublimation pits observed surrounding mid- to high-latitude pedestal craters, indicating the presence of snow/ice in the substrate (Kadish et al., 2010). Their interior polygons resemble homogeneous patterned ground observed in the high latitudes (Mangold, 2005). Formation of decameter-scale polygons likely requires the presence of water ice. Polygonal patterned ground can form through desiccation and thermal variations in and/or sublimation from an ice-bearing layer, and may also suggest freeze-thaw processes (Mangold, 2005; Balme et al., 2013). Similar polygonal textures are also observed in latitude-dependent mantle in areas associated with concentric crater fill and brain terrain (Levy et al., 2009), and in transitions between different brain terrain textures in ice-filled craters (Mangold, 2003). We interpret the *Hellas* multiple breach tadpole crater floor textures as ice-rich fill.

In *Noachis*, the crater floor fill has a distinctive large-scale morphology, with irregularly shaped, slightly topographically elevated areas that from a distance resemble the surface of crumpled aluminum foil (Fig. 4.7). Up close, some surfaces of these topographically

elevated regions have decameter-scale polygons resembling those in *Hellas* (Fig. 4.8a), and their margins do not have a sharp contact with adjacent crater fill. Areas without polygons closely resemble material surrounding the brain terrain in *Arabia Terra 1* and *Arabia Terra 2* (e.g. Fig. 4.8d, top left). Additionally, at the boundary between the steep crater rim and the flatter crater floor, the infilling material exhibits wrinkles, which we interpret as indicative of viscous material, in this case, most likely ice. Therefore, our interpretation is that the crater fill in *Noachis* also includes ice.

Although we interpret all four multiple breach tadpole craters as filled with a mixture of ice and debris, this ice was not necessarily present at the time of crater overspill. The debris-covered glacial features observed in the Martian mid-latitudes may be as young as tens of millions of years (Mangold, 2003), but there is evidence for multiple ice ages on Mars (Butcher et al., 2017; Head et al., 2003; Fassett et al., 2014). If the breaches were incised on the earlier end of the tadpole crater age range in the late Hesperian or early Amazonian, then there may have been billions of years available for the contemporary crater-filling ice-rich deposits to accumulate (and potentially for any earlier crater-filling ice/ice-rich debris to be lost if the tadpole craters were ice-filled or subglacial, e.g. Fig. 4.2b & d). Therefore, the modern fill of multiple breach tadpole craters does not necessarily favor a particular mechanism for crater overspill.

Crater Rims

Tadpole craters have topographically elevated and sometimes fresh-appearing rims (Fig. 4.9). In our four DEMs, the highest portions of the crater rims have a "mottled" texture comprised of small meter to decameter scale, irregularly shaped pits with sharp edges (Fig. 4.9a). Occasionally, these small pits and their bounding ridges appear to form linear features persisting for a few hundred meters (e.g. Fig. 4.9**a.** iv, v, & vi). The tops of the observed tadpole crater rims also tend to be rounded (Fig. 4.9b), although the inner edge of the rim where

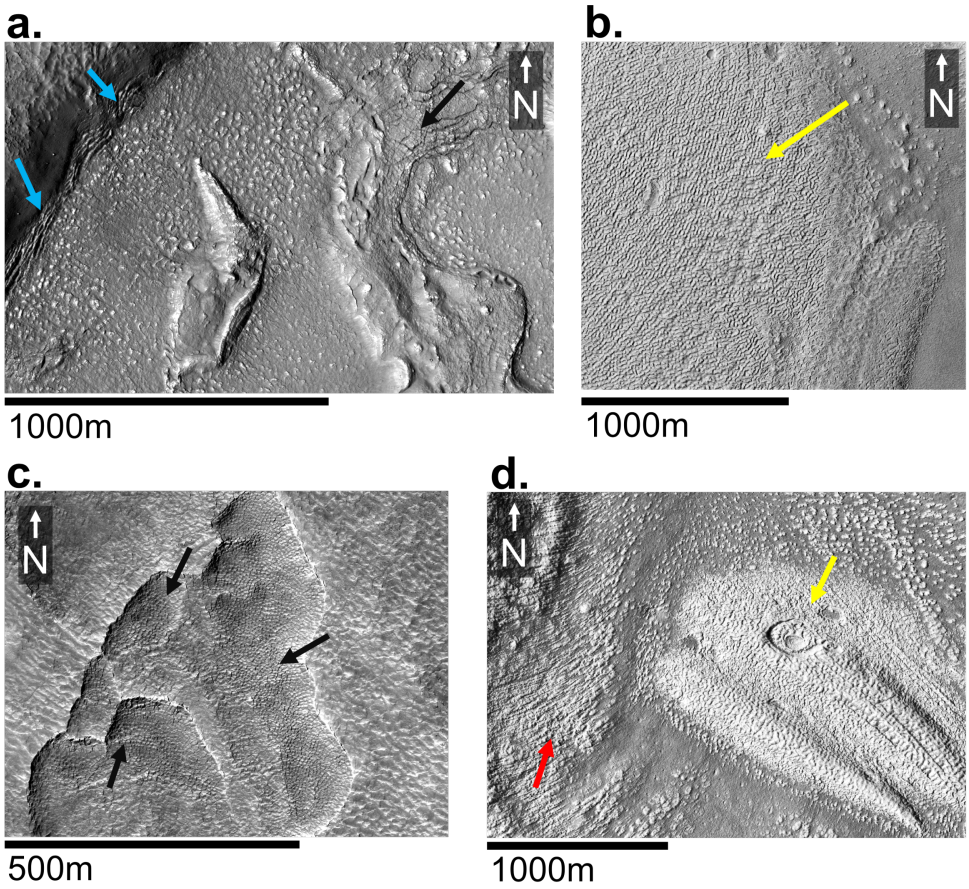

Figure 4.8: HiRISE imagery of crater floor fill, interpreted as crater-filling ice. Blue arrows indicate wrinkling at the boundary between the steep topography and texturally altered bedrock-like (Conway et al., 2018) appearance of the preserved crater rim and the flatter crater fill. Black arrows indicate decameter-scale polygonally-dissected crater fill resembling polygons observed in latitude-dependent mantle occurring alongside concentric crater fill and brain terrain (Levy et al., 2009), and in transitions between different brain terrain textures in ice and LDM-filled craters (Mangold, 2003). Yellow arrows indicate areas of closed-cell brain terrain (Levy et al., 2009), interpreted as indicators of crater-filling ice or ice-rich debris beneath LDM. Red arrows indicate arcuate, parallel ridges of light-toned, knobby material, interpreted as arcuate ridges (Conway et al., 2018), likely associated with ice fill. **a.** *Hellas* (left: ESP_012014_1335): decameter-scale bright mounds surrounded by mid-toned relatively smooth material throughout the image resemble buttes of partially-dissected brain terrain (Mangold, 2003) and knobby textures observed on lobate debris aprons (LDAs) (Pierce and Crown, 2003), **b.** *Arabia Terra 2* (left: ESP_053736_2180), **c.** *Noachis* (left: ESP_074112_1455), **d.** *Arabia Terra 1* (left: ESP_052510_2150): ring mold crater indicating impact into ice-rich substrate in center left of image (Kress and Head, 2008).

there is a break in slope towards the crater interior may remain sharp and appear fresh (4.9a.iv and b.iv). The combined mottled appearance and rounded rim profiles strongly resembles the distinctive "texturally altered bedrock" documented by Conway et al. (2018) in mid-high latitude craters and interpreted as an indicator of glacial processes, as texturally altered bedrock visually resembles terrestrial surfaces that have experienced ice-shattering and frost-segregation processes (Conway et al., 2018). On Earth, ice-shattering and frost-segregation typically require thin films of liquid water during the growth of ice lenses that break down rock (Matsuoka and Murton, 2008). However, accumulation of ice can proceed without liquid water in dry soils at the base of Antarctic ice (Lacelle et al., 2013), and dry ice lens growth may be able to occur under Martian conditions (Sizemore et al., 2015). We interpret the observed multiple breach tadpole crater rim textures as a signature of modification by ice. However, these textures need not be caused by the breach incising climate, as the craters also show evidence for contemporary ice fill (Section 4.3.2), therefore it is plausible that the rim texture is formed during a later episode of ice deposition.

Few craters of a similar size to typical tadpole craters (0.5-15 km) are preserved on Noachian terrains (Craddock and Howard, 2002); craters with $D_c < 4$ km are absent (Irwin III et al., 2013). Therefore it is difficult to make a direct textural comparison between tadpole crater rims and the rims of similar sized craters modified under enhanced fluvial activity. However, tadpole crater rims are not flattened as much as typical Noachian craters, definitionally lack fluvial channels superposing their rims, and do not show evidence for widespread small-scale gullies on the interior crater rim slope as observed for many degraded Noachian craters (Weiss and Head, 2015). Therefore, although our multiple breach tadpole crater rim observations indicate modification relative to fresh craters, our observations are consistent with the conclusion of Wilson et al. (2016) that these tadpole craters are Late Hesperian/Amazonian.

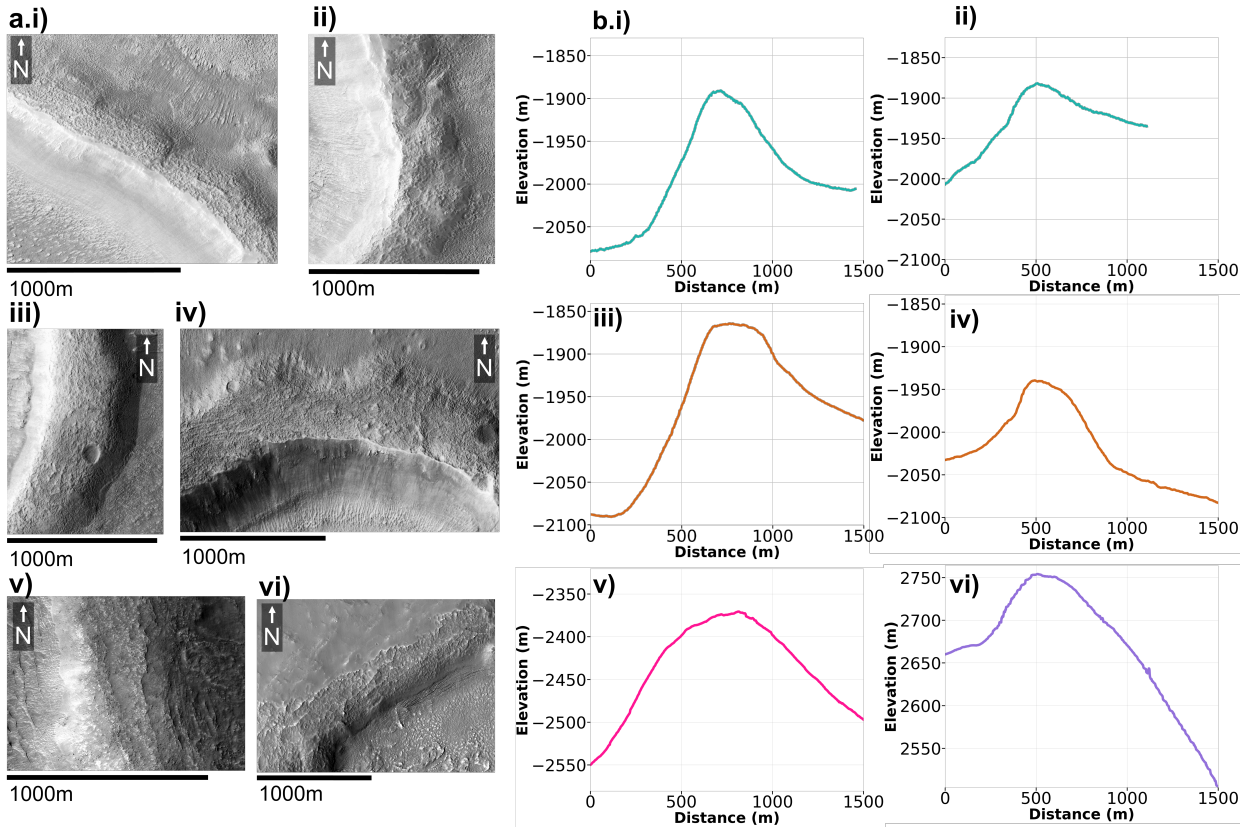

Figure 4.9: **a.** HiRISE imagery of unincised portions of multiple breach crater rims showing mottled rim textures resembling texturally altered bedrock (Conway et al., 2018) along the most topographically elevated portions of the rim in i & ii) *Arabia Terra 1* (left: ESP_053736_2180), iii & iv) *Arabia Terra 2* (left: ESP_053736_2180), v) *Hellas* (left: ESP_012014_1335), and vi) *Noachis* (left: ESP_074112_1455) (Table 4.1). **b.** Topographic profiles of crater rims (see Fig. 4.7 for profile traces) in i & ii) *Arabia Terra 1*, iii & iv) *Arabia Terra 2*, v) *Hellas*, and vi) *Noachis*, showing topographically rounded rims (e.g. ii, iii, vi) and sharper rim sections (e.g. i, iv) more closely resembling the steep, narrow shape of fresh crater rims (e.g. Robbins and Hynek 2012b). In all profiles, the crater interior is to the left.

Rim Breaches

We measured the dimensions of the exit breaches incising the rims of the four multiple breach tadpole craters using the measured rim topographic profiles (Fig. 4.1). The breaches have v-shaped cross sections (Fig. 4.1a-d ii) and are typically tens of meters deep and hundreds of meters wide where they intersect the rim (Table 4.2). We measure the length of the breaches by taking 3 downstream profiles of each breach until the point where the breach valley is

either no longer discernible from the surrounding terrain, or until another valley intersects the breach valley (e.g. Fig. 4.10a.ii. lower left).

Although some breach valleys have smooth floors and do not appear to be infilled, about half of the breaches of the four multiple breach tadpole craters have material morphologically resembling and/or continuous with the crater floor ice-rich deposits identified in Section 4.3.2 (Fig. 4.10a). As a result, we likely underestimate the depths of these breaches, and their downstream topographic profiles do not reflect the incised valley floor resulting from crater rim breaching. For breaches without ice-rich infill, we measure downstream topographic profiles (Fig. 4.10b). For *Arabia Terra 1*, the valley floor elevation increases downstream for some segments of both exit breaches (4.10b.i & ii). In terrestrial environments, such valley floor "undulations" with upslope valley reaches are diagnostic of subglacial drainage (Grau Galofre et al., 2018). Undulations have also been used as supporting evidence for subglacial drainage on Mars (Butcher et al., 2017; Grau Galofre et al., 2018, 2020). The breach valley walls and floors are smooth and featureless, and do not show evidence for overlying crater ejecta or mass wasting from the valley walls. However, if tadpole crater overspill was associated with widespread mid-latitude ice cover, there may have been subsequent loss of ice from the material at the base of and beneath the subglacial channel, leading to later modification of the downstream profile. In the absence of visible evidence for sublimation features or disruption of the breach valleys, we favor the interpretation that the undulations in the *Arabia Terra 1* breaches are a primary feature, but do not consider them to be diagnostic of a subglacial origin by themselves given the possibility of post-incision changes to topography that may not be detectable at HiRISE resolution. The downstream profiles of the remaining ice-free breaches (Fig. 4.10) do not show evidence for upslope reaches, which is consistent with either subglacial or subaerial erosion (Grau Galofre et al., 2018).

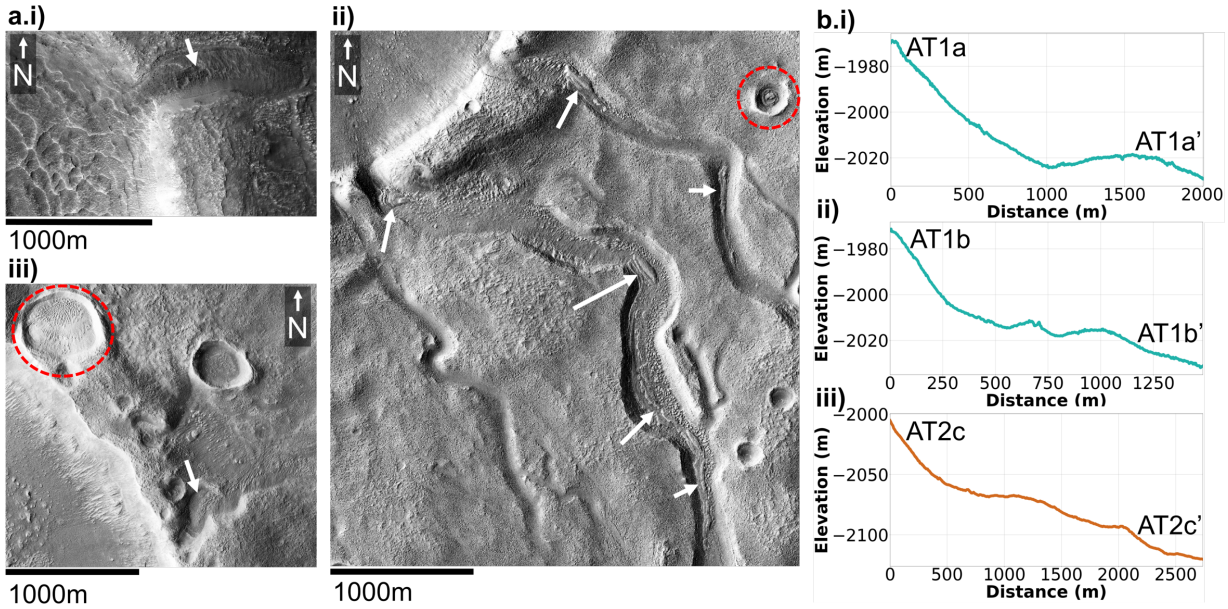

Figure 4.10: **a.** HiRISE imagery of crater rim breaches infilled with discontinuous material resembling crater-filling ice-rich deposits (white arrows, Section 4.3.2) in i) *Hellas* (left: ESP_012014_1335), ii & iii) *Arabia Terra 2* (left: ESP_053736_2180). Red dashed circles highlight small craters filled with material morphologically consistent with ice-rich deposits. **b.** Downstream topographic profiles of ice-rich deposit-free exit breaches (traces of profiles shown in Fig. 4.7) for i & ii) *Arabia Terra 1*, and iii) *Arabia Terra 2*.

4.4 Subaerial Overspill

In this section, we consider subaerial overspill mechanisms for tadpole crater breach formation (H1-H3, Fig. 4.2).

4.4.1 Water-filled crater

For a crater filled with water to form multiple exit breaches over the rim, the most straightforward explanation is that the crater rim was modified between overspilling episodes, creating a new lowest point on the rim. The preservation of tadpole craters with diameters <4 km precludes modification by the high (10^2-10^4 nm yr^{-1}) erosion rates during a wet climate predicted for Noachian Mars (Craddock and Howard, 2002; Salese et al., 2016), which erased craters of these sizes from Noachian-aged terrains (Irwin III et al., 2013). Using studies of

Tadpole Crater	**Breach**	d_b	w_b **(m)**	L **(m)** L **(m)**	V_b **(m^3**	$V_{w,min}$ **(m^3)**
Arabia Terra 1	B1	29±0.5	442±0.3	2140±4	4.07×10^6	1.36×10^7
	B2	28±0.3	338±0.2	1550±1	3.21×10^7	1.07×10^7
Arabia Terra 2	B1	32±0.4	199±0.5	400±4	6.05×10^5	2.02×10^6
	B2	28±0.5	362±0.1	810±3	3.64×10^6	1.21×10^7
	B3	34±0.1	466±0.1	3140±2	7.20×10^6	2.40×10^7
	B4	57±0.2	390±1	1210±1	6.32×10^6	2.11×10^7
	B5	27±0.1	282±0.5	580±4	1.32×10^6	4.41×10^7
Hellas	B1	19±0.1	351±0.1	1070±2	9.35×10^6	3.12×10^7
	B2	30±0.4	426±0.3	780±3	2.64×10^6	8.80×10^6
Noachis	B1	100±0.1	837±0.1	1020±2	2.66×10^7	8.87×10^7
	B2	17±0.4	277±0.3	980±1	5.93×10^6	1.98×10^7

Table 4.2: Breach measurements for each tadpole crater in this study (Table 4.1, see Fig. 4.1 for breach labels). d_b is maximum breach depth at the crater rim measured from profiles in Fig. 4.1, w_b is breach width on the crater rim measured from profiles in Fig. 4.1. L is the traced length of each breach until it either intersects another valley or becomes invisible. V_b is the breach volume calculated from the mean of at least 3 breach area profiles found in ArcGIS multiplied by L. All error bars come from the range of triplicate measurements. $V_{w,min}$ is the minimum water volume required to erode V_b assuming a maximum sediment:water ratio of 0.3.

small crater degradation from orbital and rover measurements, slower, aeolian erosion rates during the Hesperian and Amazonian have been estimated to be much lower, of order 0.01-10 nm yr^{-1} (Golombek and Bridges, 2000; Salese et al., 2016; Golombek et al., 2014). At an erosion rate of 10 nm yr^{-1}, it would take 4.5 Gyr for aeolian erosion to erode the rim of *Hellas* from the lowest point of B1 to the highest point on the pre-incision topography of B2 (Fig. 4.1cii), which is unrealistic because tadpole craters must post-date the Noachian. Additionally, for *Arabia Terra 1*, *Arabia Terra 2*, and *Noachis*, the lowest point in the highest incised breach is lower than the highest point on the pre-incision topography in another breach (e.g. *Noachis* B1 and B2, Fig. 4.1dii). This precludes the highest breach from incising first followed by a period of rim erosion because if the rim did not erode beneath the lowest point of an earlier breach, water should overspill from the first breach instead of forming a new breach above the highest point on the rim. Therefore, we exclude sequential overspill

with periods of rim modification in between each breach incision as a multiple breach-forming mechanism.

For multiple breaches to form simultaneously from a single crater filled with water, the water level must reach at least the lowest point of the pre-incision topography at the highest breach. In this scenario, water flows into the crater, filling it up. Once the water level reaches the lowest point on the rim, an outlet breach starts eroding. However, the flux of water into the crater exceeds the flux out of the first breach, and the water level continues to rise until new, higher elevation breaches form to accommodate the overspilling water (Fig. 4.11). In this scenario, water flows over the rim between breaches, and the total flux out of the crater through the eroding breaches and over the rim must be matched by the flux into the crater at least for a short time. Therefore, we can find the necessary water input flux to enable this multiple breach-forming mechanism to occur.

Using the 4 available Digital Elevation Models (DEMs) of multiple breach tadpole craters (Fig. 4.1), we measured topographic rim profiles by placing points on the highest elevation, well-preserved areas of the intact crater rim, excluding incised portions. Following Dussaillant et al. (2010), we use this first topographic profile to calculate an approximate, simplified pre-incision rim topography using linear interpolation between fresh crater rim points either side of each breach. We then measured a second topographic rim profile for each crater including the points from the first profile, in addition to points placed on well-preserved areas of the incised breaches along a straight line between the edges of each breach. We combine these two topographic profiles to make a composite topographic profile where the lowest elevation breach has formed, but all higher breaches still have their pre-incision topography. We then select a "water level" (z_w) such that the lowest part of the pre-incision topography of the highest elevation breach would be submerged, and use this z_w to calculate the wetted perimeter ($p_{w,i}$) and flow area ($a_{w,i}$) for each ith continuous section of the crater rim below

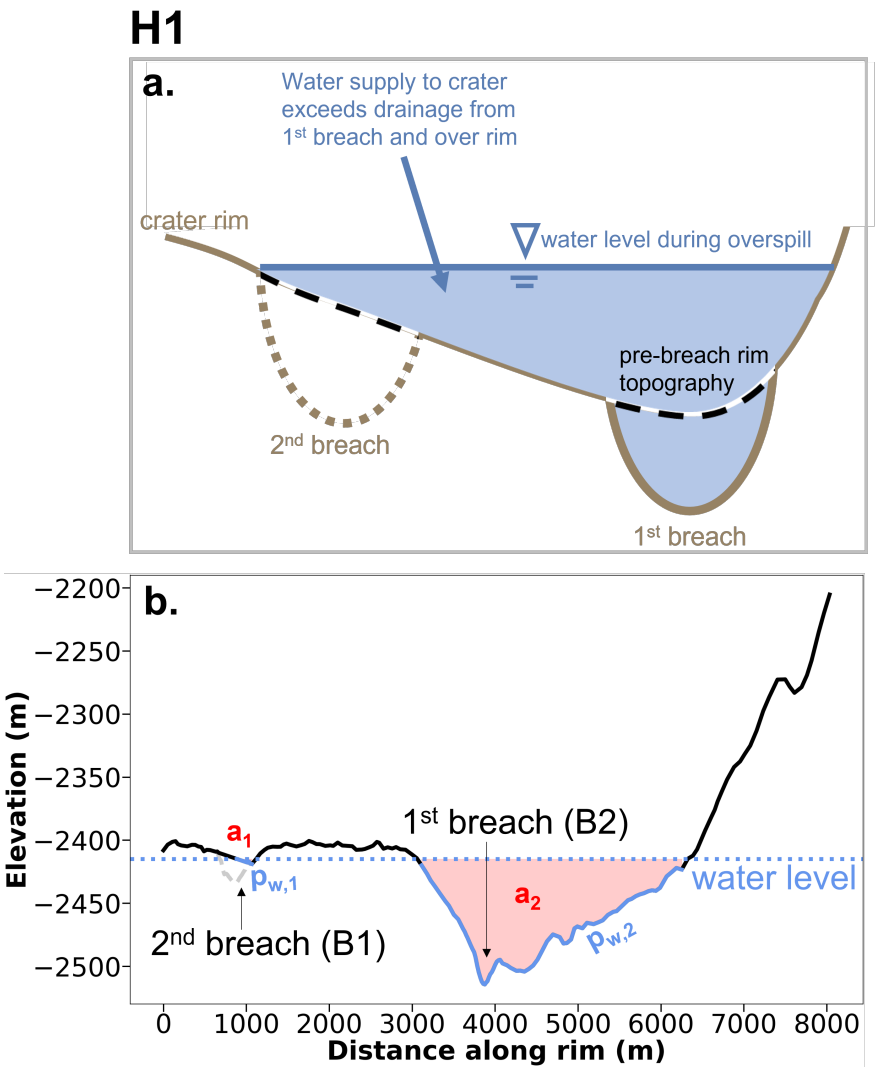

Figure 4.11: **a.** Sketch illustrating simultaneous erosion of multiple rim breaches in a water-filled crater. The crater is supplied by a continuous water source such as precipitation or groundwater. Once the water level reaches the lowest point on the rim, an outlet breach begins eroding, but the flux of water out of that breach can't keep up with the input flux. The water level continues to rise until new, higher breaches form to accommodate the overspilling water. In this scenario, the water source must be able to supply water at a rate greater than the combined flow rate out of the crater via the first breach and over the submerged crater rim. **b.** Topographic rim profile of *Hellas* tadpole crater (Table 4.1, Fig. 4.1) with pre-incision topography for Breach 1 (B1). Dotted blue line shows water level. Solid blue line on topographic profile shows wetted perimeters for portions of flow out of the crater ($p_{w,1}$ and $p_{w,2}$). Red hashed regions show cross-sectional areas (a_1 and a_2) of portions of flow out of the crater.

the water level to calculate hydraulic radius ($R_{H,i}$):

$$R_{H,i} = \frac{a_{w,i}}{p_{w,i}} \tag{4.3}$$

this allows us to use Manning's equation to find the average flow velocity ($\bar{u}$) over each submerged rim section:

$$\bar{u}_i = \frac{R_{H,i}^{2/3} S^{1/2}}{n} \tag{4.4}$$

where S is the slope for which we use values of 0.1 and 0.2 based on average measured rim slope values in Warren et al. (2021), and n is Manning's roughness coefficient, also known as Manning's n. We use a standard gravity scaling for Manning's n (Brownlie, 1983):

$$n = \frac{k^{1/6}}{8g^{1/2}} \tag{4.5}$$

where g is surface gravity and k is the channel bed roughness length scale which we set equal to grainsize d_g from 1 mm to 1 m (Table 4.4) in each model run (Warren et al., 2021).

We then calculate the total flux out of the crater:

$$Q_{out} = R_{H,1}\bar{u}_1 + ... + R_{H,i}\bar{u}_i \tag{4.6}$$

where 1 to i indicate the number of continuously submerged rim sections.

We can then compare Q_{out} for each crater (Table 4.3) to potential water sources for a water-filled crater (Sections 4.4.1 & 4.4.1).

Precipitation & Meltwater

As tadpole craters lack inlets and have intact rims, liquid water cannot be routed over land to tadpole craters from a catchment area larger than the crater itself. To find the precipitation/melt rate within each multiple breach tadpole crater required to generate Q_{out}

Tadpole Crater	Q_{out} ($m^3 s^{-1}$)	A_m to reach Q_{out} (km^2)	One-shot Groundwater: $Q_{in,max}$ ($m^3 s^{-1}$)	Multi-shot Melt pond overspill: $t_{melt,min}$ (days)
Arabia Terra 1	2.00×10^4	157,000	5.71×10^5	77
Arabia Terra 2	8.82×10^5	6,960,000	4.63×10^5	58
Hellas	1.63×10^6	12,900,000	3.47×10^5	4
Noachis	1.86×10^5	1,470,000	5.13×10^5	95

Table 4.3: Modelling results for subaerial crater overspill mechanisms. Q_{out} is the calculated flow out of the crater if all breaches are active simultaneously (Eqn. 4.6, Fig. 4.11, Section 4.4.1). A_m is the area over which melting would need to occur at 4 m yr^{-1} m^{-2} to supply Q_{out}. $Q_{in,max}$ is the maximum groundwater discharge rate found in our models, corresponding to groundwater flux from a pressurized aquifer with initial head $h_a = 5000$ m, permeability $k_h = 10^{-9}$ m^2 (Table 4.4), when the total volume of water discharged from the aquifer is 0.1 crater volumes (Section 4.4.1). $t_{melt,min}$ is the minimum time melting needs to occur at a rate of 4 m yr^{-1} m^{-2} to supply enough liquid water to melt ponds to repeatedly overspill and erode the observed breach depths for all tadpole crater rim breaches (Section 4.4.2).

required to activate all exit breaches simultaneously, we can simply divide Q_{out} (Table 4.3) by crater area. This gives values ranging from 0.6 mm s^{-1} for *Arabia Terra 1* to 8.5 mm s^{-1} for *Hellas*. Even the lowest value of 0.6 mm s^{-1} is equivalent to almost 52,000 mm day^{-1}, which is 35 times the maximum daily rainfall rate recorded on Earth (Chien and Kuo, 2011) – an unrealistically high precipitation or snowmelt rate for Earth or Mars. As expected from previous work (Warren et al., 2021), we can therefore exclude precipitation within the crater and snowmelt leading to simultaneous overspill at multiple breach locations as formation mechanisms for multiple breach tadpole craters.

Retreating Ice Sheet

A potential mechanism for expanding the catchment area of multiple breach tadpole craters without forming inlets is the intersection of a retreating ice sheet margin with the crater interior (Fig. 4.12a). In this scenario, the high meltwater supply rates required to match Q_{out} could be achieved by expanding the melting area rather than appealing to higher

melting rates, for example by routing meltwater from a large ice sheet area into a crater. We calculate the required melting area for each multiple breach tadpole crater by dividing Q_{out} by the melting rate on Mars, which is energy limited to around 4 m yr^{-1} m^{-2} (Kite et al. 2013; 100 W m^{-2} corresponds to $\sim$ 1 mm hr^{-1} m^{-2} of melt).

The results of this calculation yield melting areas 1,700 to 67,000 times larger than the multiple breach tadpole crater areas (Table 4.3), comparable to areas the size of Illinois and Russia for *Arabia Terra 1* and *Hellas* respectively. For *Hellas*, this would be equivalent to routing meltwater from an ice sheet covering the entire Hellas Basin into a single 14.6 km diameter crater. This would require unrealistic ice sheet topography. Therefore we exclude the *simultaneous* formation of multiple breaches by meltwater routed from a retreating ice sheet.

However, a rapidly retreating ice sheet is consistent with the *sequential* formation of multiple breaches in a tadpole crater. As the ice sheet retreats, it provides meltwater to the crater for overspilling and progressively exposes new areas of the rim. As topographically lower portions of rim are exposed, water overspills there, and earlier, higher elevation breaches are abandoned (Fig. 4.12).

Groundwater

One mechanism proposed for generating extremely high discharge rates and water volumes to carve outflow channels is groundwater discharge from cryosphere-confined aquifers (Carr, 1979; Harrison and Grimm, 2004; Manga, 2004; Andrews-Hanna and Phillips, 2007). Although tadpole crater outflow breaches are orders of magnitude smaller than these features, groundwater released from a pressurized aquifer might generate the high water fluxes required to sustain flow over the submerged rim of a tadpole crater, enabling multiple breaches to incise simultaneously.

To test this hypothesis, we find the groundwater flux into a tadpole crater. We consider

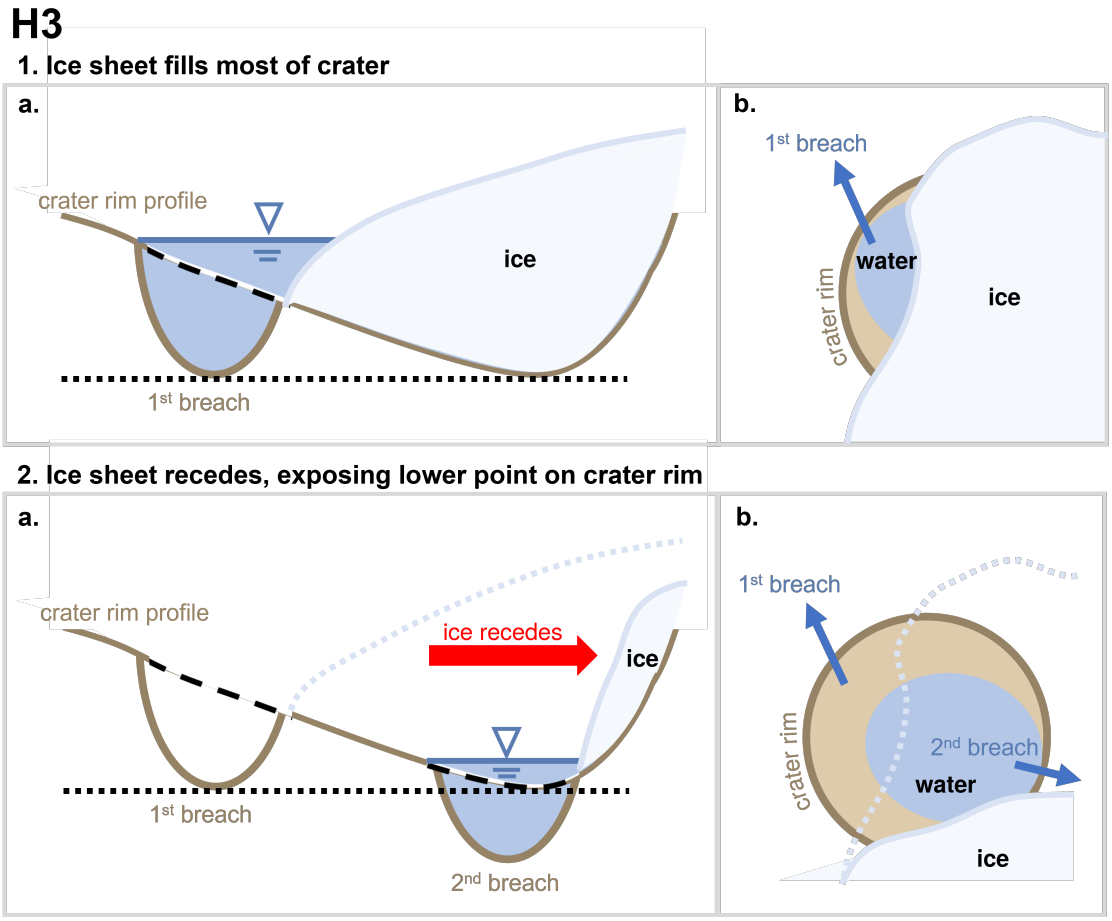

Figure 4.12: Schematic illustration of a retreating ice sheet progressively exposing lower rim topography in two stages (1 and 2), enabling multiple breaches to form. **1a & 2a.** profile view, **1b & 2b.** birds-eye view.

a case where there is a network of fractures beneath the crater, for example generated by impact fracturing (MacKinnon and Tanaka, 1989; Hanna and Phillips, 2005), that fully penetrates a homogeneous aquifer (Fig. 4.13). When water from the aquifer reaches the edge of the fracture network at a distance of $0.5D_c$ from the center of the crater, we assume it can begin filling the crater.

The radial flow of groundwater through a confined, homogeneous aquifer in 1-D can be found using (Domenico et al., 1998):

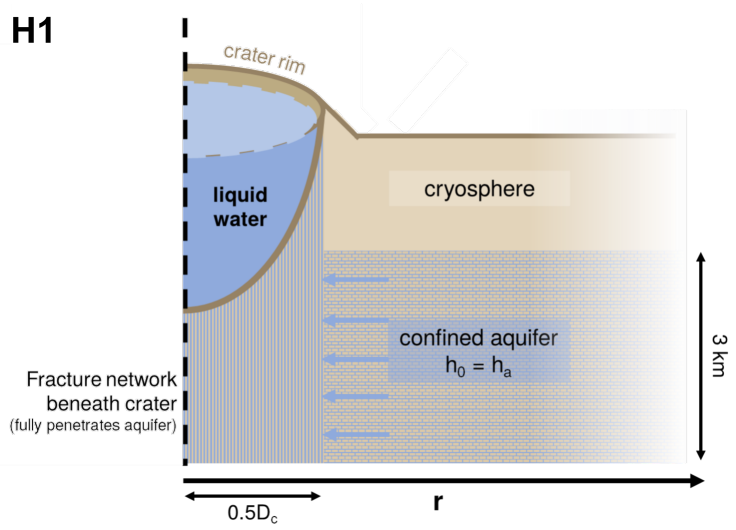

Figure 4.13: Sketch illustrating our groundwater model. A homogeneous, radially symmetrical confined aquifer 3 km thick pressurized by an overlying cryosphere is fully penetrated by a network of fractures beneath the tadpole crater, extending to the crater rim at $r = 0.5D_c$ where D_c is the crater diameter. Dashed black line indicates axis of radial symmetry. We assume that the flux of water to the crater is limited by flow through the confined aquifer to the edge of the fracture network (blue arrows). The aquifer starts with an initial head (h_0) of h_a, which is a free parameter in our groundwater model (Table 4.4).

$$\frac{\partial h}{\partial t} = \frac{k_h \rho_w g}{\mu S_s} \frac{\partial}{\partial r}\left(r \frac{\partial h}{\partial r}\right) \tag{4.7}$$

where h is hydraulic head in the aquifer, t is time, k_h is radial permeability, ρ_w is the density of water, μ is the viscosity of water, S_s is the specific storage of the aquifer, and r is radial distance from a central point (i.e. the center of the crater) (Table 4.4). We solve this equation using an explicit finite differences method for an aquifer of fixed thickness (3 km) to find the maximum groundwater flux into each multi-exit-breach tadpole crater using the parameters listed in Table 4.4. To maximize the groundwater discharge in our aquifer model, which is conservative in terms of rejecting the groundwater hypothesis, we neglect the turbulent upper limit on flow rate out of the aquifer as water moves through fractures to the tadpole crater (Manga, 2004). We investigate the groundwater flow rates for 10 evenly log-spaced values of both k_h and the initial pressure head in the aquifer (h_a) to capture a range of

possible pressurized aquifer conditions.

As expected, groundwater flow is maximized for the highest values of k_h (10^{-9} m^2, corresponding to the average horizontal permeability of a basaltic aquifer composed of stacked lava flows at the surface; Hanna and Phillips 2005; Manga 2004) and h_a (5000 m). However, even these conditions are not able to generate sufficient groundwater flow to match Q_{out} for tadpole craters *Arabia Terra 2* and *Hellas* for a 3 km thick aquifer (Table 4.3). In the case of *Noachis*, sufficient groundwater flow can only be sustained until the volume of water discharged from the aquifer has reached 0.9 crater volumes (Fig. 4.14) for the highest values of k_h (10^{-9} m^2) and h_a (5000 m).

As our models are 1D, Q_{in} scales linearly with aquifer thickness. For *Arabia Terra 2* an aquifer thickness of approximately 6 km would be required, and a 14 km thick aquifer would be required to match Q_{out} for *Hellas*. On Earth, crustal permeabilities decrease with depth by several orders of magnitude within a few kilometers (Huenges et al., 1997), and a factor 10^4 decrease in permeability is expected for the Martian subsurface as increasing lithostatic stresses lead to the closure of pore space and open fractures (Hanna and Phillips, 2005). Additionally, aquifer heads of $h_a = 5000$ m are equivalent to a pressure of 18.5 MPa, which are not achieved in models of aquifer pressurization by a downward-freezing aquifer following a rapid change in surface temperature from 270 to 220 K (Hanna and Phillips, 2005). Therefore, we conclude that discharge from a confined aquifer driving simultaneous overspill of multiple breaches is inconsistent with *Arabia Terra 2* and *Hellas*, and unlikely for *Noachis*.

Our calculations cannot exclude groundwater-driven simultaneous overspill of both breaches at *Arabia Terra 1*. However, the unrealistic combination of high permeabilities, aquifer pressures, and thick aquifers required to reconcile a groundwater source for Q_{out} for *Arabia Terra 2* and *Hellas*, the preferential occurrence of tadpole craters at high elevations relative to surrounding topography (Fig. 4.6, Section 4.3.1), and the absence of evidence for rim

incision or fluvial modification between breaches (Section 4.3.2) disfavors this mechanism for the overall tadpole crater population.

An additional consideration for a groundwater-driven crater overspilling mechanism is that a fracture network feeding the crater is required. Although we interpret the four multiple breach tadpole craters in this study to be ice filled (Section 4.3.2), thus burying any potential crater floor fractures, an impact-generated fracture system would likely extend up the crater wall, through the crater rim, and potentially into surrounding terrain (Polanskey and Ahrens, 1990; Kumar, 2005; Kumar and Kring, 2008). No fractures are visible on the scale of our HiRISE images. Therefore, any fractures (if present), must have apertures smaller than approximately 1 m. While the absence of these features in four tadpole craters does not exclude groundwater as a mechanism for all tadpole craters, noting the presence/absence of groundwater-related features and textures is important for future observations of tadpole craters.

4.4.2 Ice-filled crater

The 4 tadpole craters in this study all show features on the crater floor consistent with ice-fill, e.g. brain terrain and concentric ridges, and ice-filled craters are abundant poleward of around 30 degrees latitude. This ice fill may be a remnant of previous ice coverage, and the same ice (or an older generation of ice) may have infilled the crater at the time of breaching. If the crater was once ice-filled, subaerial drainage of supraglacial meltwater ponds could have drained over the crater rim (Warren et al., 2021). In this scenario, breach location would be dependent on ice surface topography and melt routing, not crater rim topography.

For each tadpole crater, we can calculate the number of meltwater overspill events needed to erode each crater rim breach to its observed depth as a function of meltwater pond diameter, and thus approximate the number of melt-years needed on Mars to generate multi-exit breach tadpole craters, constraining the Martian climate.

Symbol	Value(s)	Units	Description
		General parameters	
g	3.71	m s^{-2}	Mars gravity
ρ_w	1000	kg m^{-3}	Density of water
ρ_i	918	kg m^{-3}	Density of ice
ρ_r	2500	kg m^{-3}	Density of crust
		Groundwater model	
k_h	10^{-15} - 10^{-9}	m^2	Permeability *,$^+$
h_a	100 - 5000	m	Initial head in pressurized aquifer
S_s	10^{-6}	m^{-2}	Specific storage$^+$
z_a	3000	m	Aquifer thickness
μ	1×10^{-6}	m^2 s^{-1}	Viscosity of water
		Intrusion model	
T_{int}	1300	K	Initial temperature of intrusion
T_{surf}	230	K	Surface temperature
z_i	100 - 2000	m	Ice thickness
q_{geo}	25	mW m^{-2}	Geothermal heat flux
$c_{p,w}$	4180	J kg^{-1} K^{-1}	Specific heat capacity of water
$c_{p,i}$	2100	J kg^{-1} K^{-1}	Specific heat capacity of ice
$c_{p,r}$	1100	J kg^{-1} K^{-1}	Specific heat capacity of crust
L_i	330	kJ kg^{-1}	Latent heat of melting ice
		Melt pond overspill model	
h_0	0.1 - 1	m	Initial flow depth in breach (Warren et al., 2021)
d_g	0.001 - 1	m	Grainsize in breach (Warren et al., 2021)
f_a	0.001 - 1	-	Fraction of crater area covered by melt pond
S	0.1, 0.2	-	Slope

Table 4.4: Parameter values used for models of radial groundwater flow, ice melting above an intrusion, and overspill from a melt pond on the surface of an ice-filled crater. *Andrews-Hanna and Phillips (2007), $^+$Manga (2004)

To do this, we implement the coupled model of lake draining and breach erosion described in Warren et al. (2021) using our measured crater and breach properties in Tables 4.1 & 4.2 respectively. This model assumes no flow into the crater during erosion, no downstream changes in channel/valley geometry, flow depth, or flow velocity, and perfect downstream advection and removal of all eroded sediment. In order to find the minimum number of melt ponding events required, we assume that pond depth does not limit erosion, and instead that the pond depth for each erosion event is simply equal to the total eroded depth for that

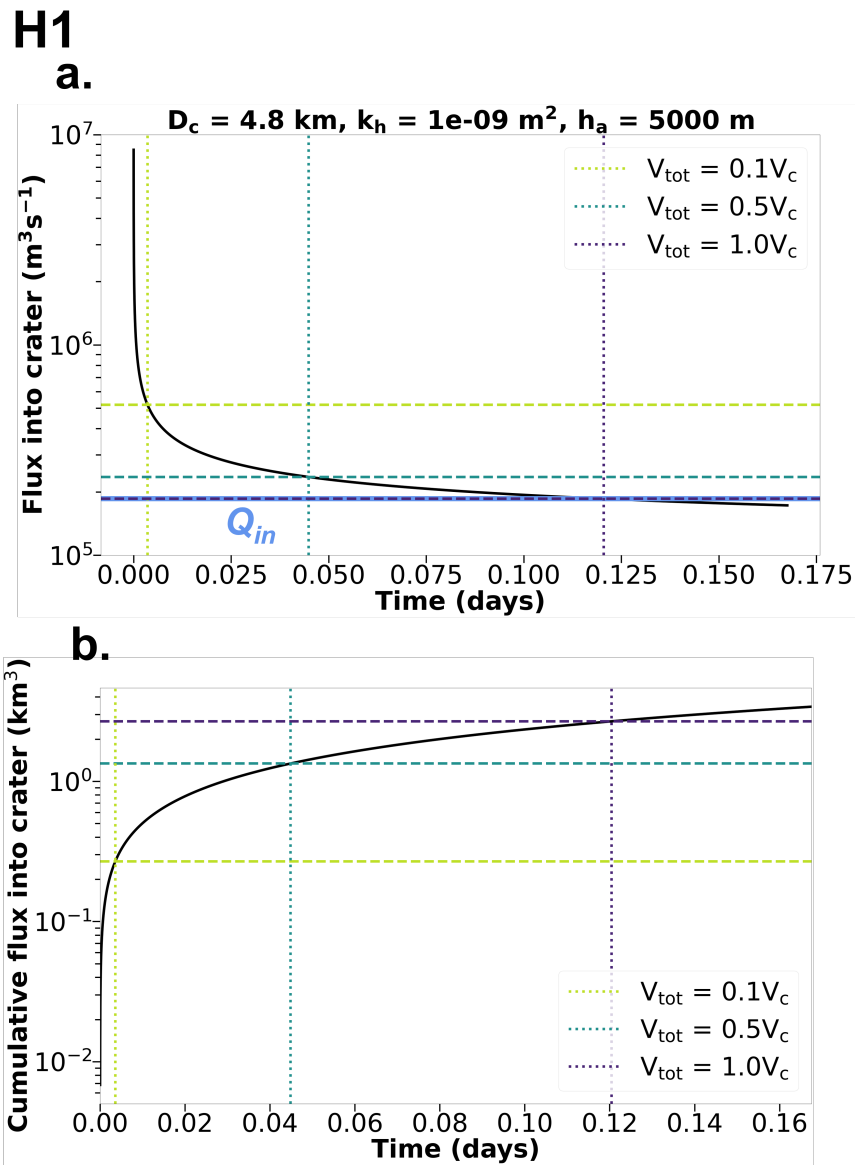

Figure 4.14: Example water fluxes into the crater from our groundwater model shows that confined aquifers with high permeability (k_h) and high initial pressure head (h_a) can exceed the calculated flow out of the crater required to activate all channels simultaneously (Q_{in}; Table 4.3, solid blue line) for *Noachis* (Table 4.1). **a.** Time evolution of groundwater flux into tadpole crater and **b.** cumulative groundwater flux into crater. Dotted vertical lines indicate the times when the groundwater discharge has filled 0.1, 0.5, and 1 times the crater volume (V_c). Dashed lines indicate the instantaneous and cumulative flux at these times.

event plus the initial water depth in the channel (Table 4.4). We set pond area for each breach as a fractional area (f_p) of the entire tadpole crater (A_c) and calculate the number

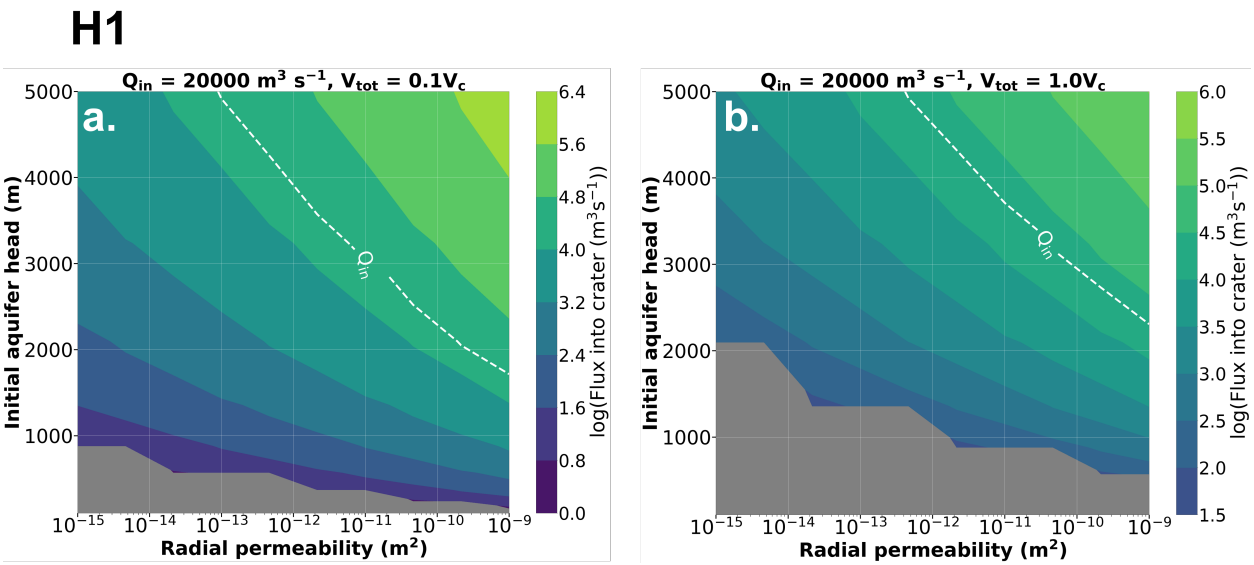

Figure 4.15: Groundwater flow through a confined aquifer with initial head >2000 m and permeability $> 10^{-12}$ m^2 can sustain the water supply rate necessary to overspill both breaches simultaneously for tadpole crater *Arabia Terra 2* (Table 4.3) from when the groundwater has supplied **a.** 0.1 crater volumes of water to **b.** 1 crater volume of water (i.e. the crater is filled to the brim with groundwater). However, higher initial aquifer head and permeabilities are required to sustain fluxes greater than Q_{in} until the crater is completely filled with water. Grey shaded areas indicate negligible groundwater flow into the crater on the timescale of one model timestep. Modeling results for other multiple breach tadpole craters are in Appendix C.1.

of melting days (t_m) represented by each breaching event (Table 4.3) using:

$$t_m = \frac{f_p A_c z_e}{r_m A_c} \tag{4.8}$$

where r_m is melt rate (4 m yr^{-1} m^{-2}; Kite et al. 2013). We assume no initial damming of the channel, which is conservative because it reduces the total erosion required to achieve the observed breach depths.

To find the minimum total magnitude of the climate excursion required to generate all exit breaches for all four multiple breach tadpole craters, we sum the minimum total number of melt days to carve each breach ($t_{melt,min}$, Table 4.3). This represents the minimum number of days that the temperature must exceed 273 K to form the observed exit breaches.

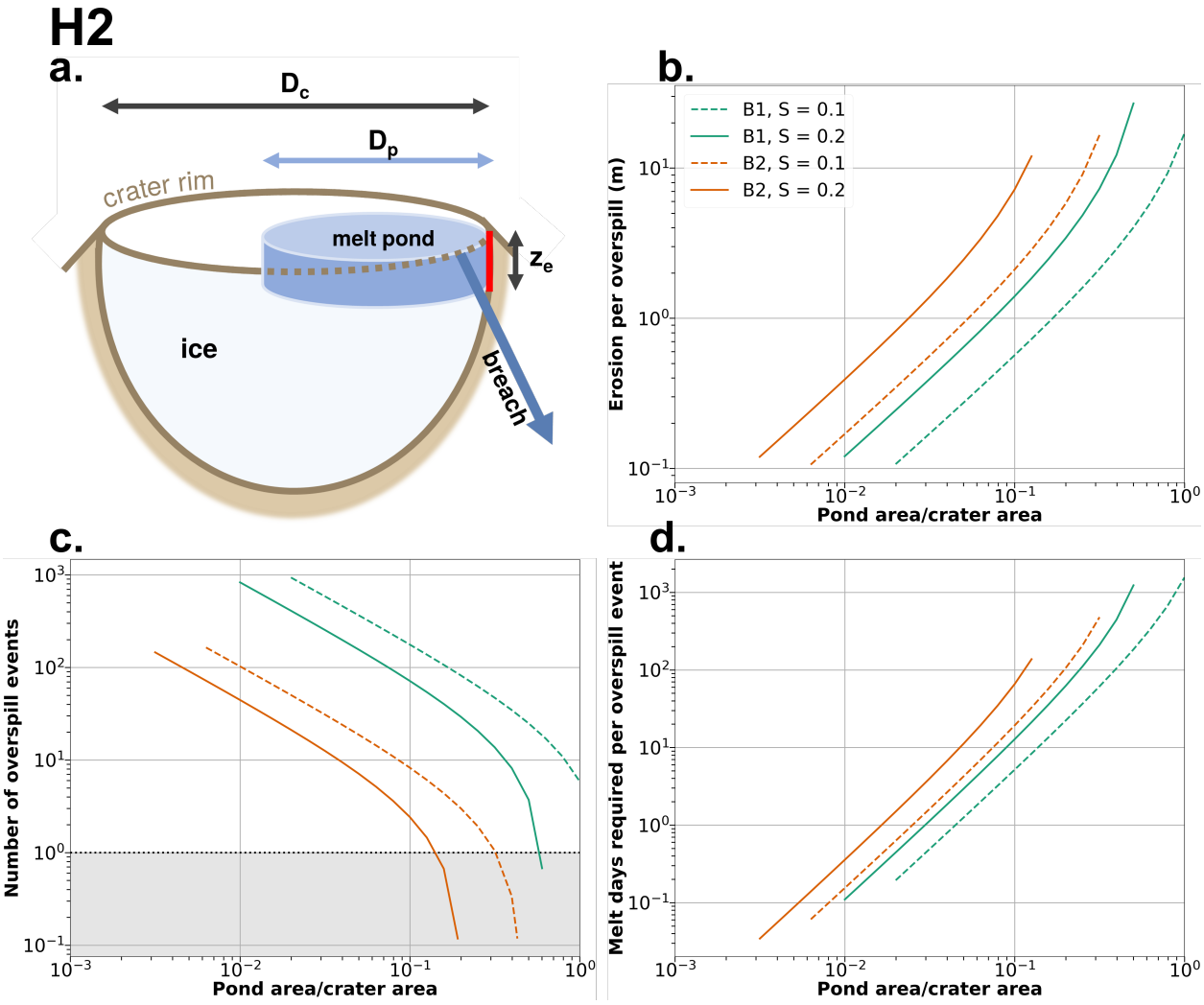

Figure 4.16: Meltwater pond overspill modelling results for *Noachis* B1 (teal) and B2 (orange) (Fig. 4.1) for measured breach parameters in Table 4.2 as a function of fractional melt pond area. **a.** Sketch of an ice-filled crater with a shallow melt pond smaller than the area of the crater with diameter D_p overspilling the rim via a breach. For each overspill event, the initial water depth in the melt pond must be at least the depth eroded in the overspill model (z_e, Warren et al. 2021). **b.** Downward erosion of breach base per individual overspilling event. Smaller melt pond areas generate less erosion when they overspill the rim. **c.** The number of overspill events required to carve each observed breach. The number of breaches required decreases as melt pond area increases. **d.** Melt days required to generate the water volumes required per overspill event in **c.** at a melt rate of 4 m yr^{-1} m^2 (Kite et al., 2013) across the entire crater area. Modeling results for other multiple breach tadpole craters are in Appendix C.2.

As this mechanism allows for each breach to form independently of any others, and each breach may be eroded by up to 10^3 small overspill events, these days do not necessarily need to be continuous. Rather, melting conditions need only persist continuously for as long as is needed to generate a sufficient volume of meltwater, which can be as little as hours (Fig. 4.16d).

Using the Mars Climate Database v6.1 (Forget et al., 1999; Millour et al., 2018), the modern surface temperature at *Noachis* exceeds 273 K for approximately 6 hrs a day during southern hemisphere summer, with peak temperatures of 310 K. Although peak temperatures vary, all four multiple breach tadpole craters in this study experience temperatures > 273 K for multiple hours during the warmest parts of the year. However, the high albedo and thermal inertia of ice and evaporitic cooling would prevent these temperatures alone from generating liquid water on modern Mars (Ingersoll, 1970), even if there were surface-exposed ice at these locations. Therefore, overspill of multiple breaches at this tadpole crater would require at least enough additional warming to overcome evaporitic cooling, in addition to stabilization of surface ice and ice accumulation in the southern mid-latitudes (which can occur under higher obliquity conditions in climate models, e.g. Forget et al. 2006; Fastook and Head 2014), and potentially increased atmospheric pressure depending on the dust content and crystalline structure of crater-filling ice/snowpack (Clow, 1987). However, if diurnal temperatures >273 K are required (for example to prevent re-freezing of a larger melt pond overnight), 50 K of warming is required at *Arabia Terra 2* in the northern hemisphere, and 25 K of warming at *Hellas* in the southern hemisphere. 50 K of warming is comparable to the warming invoked to explain the intense fluvial erosion and valley networks of the Noachian, and is difficult to achieve without either a much thicker (>1 bar) CO_2 atmosphere and additional greenhouse gases such as H_2 (Ramirez et al., 2014; Wordsworth et al., 2017; Kite et al., 2014; Ramirez, 2017; Batalha et al., 2015), H_2O-ice cloud warming (Kite et al., 2021), or another as yet unexplored warming mechanism. One potential warming mechanism

that may reduce the required warming to generate melt is a local increase in air temperature caused by the low albedo of exposed crater rim rock. This mechanism aids the formation of lakes on the surfaces of Antarctic glaciers even when summer temperatures remain below freezing (Stokes et al., 2019; Kingslake et al., 2017; Arthur et al., 2022), and supraglacial melt is often found in close association with exposed bedrock ridges and other areas of low albedo such as blue ice (Stokes et al., 2019; Bintanja and Reijmer, 2001). Overall, we favor repeated overspill of small melt ponds that require volumes of water than can be generated in < 1 day of melting, which is consistent with our overspill erosion results for all four multiple breach tadpole craters and can be achieved in a colder, more arid climate as expected for the Hesperian onwards on Mars.

4.5 Subglacial Overspill

4.5.1 Water Volume

An expression for the mean velocity of flow in a tunnel within or at the base of a glacier is (Nye, 1976):

$$\bar{u} = \frac{R_H^{2/3}}{n} \left[\frac{1}{\rho_w g} \left(\rho_w g \sin \alpha - \frac{\partial p}{\partial x} \right) \right]^{1/2} \tag{4.9}$$

where R_H is hydraulic radius, n is Manning's roughness coefficient, α is the bedrock channel slope and $\frac{\partial p}{\partial x}$ is the downstream pressure gradient.

The maximum driving pressure gradient for water exiting a subglacial channel is the difference in ice overburden pressure at the base of the tadpole crater and atmospheric pressure over the runout length of the measured outlet breaches, divided by the length of the outlet breach L (Table 4.2):

$$\frac{\partial p}{\partial x} \approx \frac{\rho_i g (d_c + h_i)}{(L + 0.5 D_c)} \tag{4.10}$$

where d_c is the depth of the tadpole crater (Table 4.1), and h_i is the ice thickness above the crater. This approach assumes that ice sheet thickness drops to zero by the end of the carved breach, maximizing the driving pressure gradient while also ensuring the full measured breach length remains subglacial.

Using our measured topographic profiles for each multiple breach tadpole crater, we can calculate the hydraulic radius of each individual breach using the same procedure as described for the multiple simultaneously active floods but adding the width of the submerged area to the wetted perimeter (p_w) to account for the top surface of the flow being in contact with ice. We assume that the ice has the same roughness as the rest of the channel perimeter (Nye, 1976). Then, we can use Equation 4.9 to calculate discharge out of each individual breach.

Terrestrial glacial lake outburst floods (GLOFs) can transport large volumes of coarse sediment and may dominate bedrock erosion in mountainous regions such as the Himalayas (e.g. Cook et al. 2018). If we assume a subglacial formation mechanism for tadpole craters in a glacial outburst flood-like event, we can use this discharge to estimate the volume of water V_L needed to erode each breach using the empirical relationship between peak tunnel channel discharge Q_p during terrestrial jökulhlaups (Walder and Costa, 1996):

$$Q_p = 46 V_L^{0.66} \tag{4.11}$$

A caveat of using this equation is that it does not include a scaling for Mars gravity, and is based on terrestrial observations only. We find that for subglacial flow driven by slope only, the empirical terrestrial jökulhlaup relationship generates water volumes (V_{sub}, Table 4.5) exceeding the initial fresh crater volume (V_c, Table 4.1) for all breaches in *Arabia Terra 2*, and one breach in *Noachis*, representing more than half of all breaches. However, the water volume cannot exceed the crater volume. Therefore, if the exit breaches did form via jökulhlaup-like GLOFs, we conclude that the terrestrial scaling between tunnel

channel discharge and total water volume does not hold. Alternatively, the breaches may represent consistent subglacial drainage maintained over a longer period of time, rather than a catastrophic GLOF-like event.

An alternative approach to calculate the minimum required subglacial water volume is to use the total eroded breach volumes (Table 4.2) to calculate the volume of water required to move that volume of sediment, given a range of sediment:water ratios. For the full range of dilute (i.e. clear water) to hyperconcentrated flows, sediment:water ratios typically vary from 0.0005 to 0.3 (Mangold et al., 2012). This factor of 600 difference yields a wide range of water volumes for each multiple breach tadpole crater breach, however, we only consider the minimum volume to constrain the minimum melting event necessary to generate sufficient water to erode each breach under subglacial conditions ($V_{w,min}$, Table 4.2).

We recommend future quantitative modeling of subglacial erosion for a variety of ice sheet geometeries to better constrain the total volume of water needed.

4.5.2 Ice Sheet Slope

Another factor in the subglacial routing of meltwater out of the tadpole craters is that the subglacial water pressure must be sufficient to overcome the steep topographic slope of the crater wall. Assuming that the basal meltwater pressure is static, which is appropriate for small discharges (Björnsson, 2003) (i.e. persistent subglacial flow rather than a catastrophic jökulhlaup-like event), the fluid potential gradient ($\frac{\partial p}{\partial x}$) at a given point beneath an ice sheet is given by the sum of the gravitational potential gradient and the overburden pressure gradient(Björnsson, 2003):

$$\frac{\partial p}{\partial x} = (\rho_w - \rho_i) g \frac{\partial z_b}{\partial x} + \rho_i g \frac{\partial (z_s - z_b)}{\partial x} \tag{4.12}$$

where ρ_i and ρ_w are the densities of ice and water respectively, z_b is the elevation at the base of the ice sheet relative to some datum (on Earth, sea level), and z_s is the elevation of the

				Slope only $\left(\frac{\partial p}{\partial x} = 0\right)$		*Crater ice only* ($h_i = 0$)		
Tadpole Crater		$p_{w,ice}$ **(m)**	$R_{h,ice}$ **(m)**	$Q_{out,ice}$ **(m^3s^{-1})**	V_{sub} **(km^3)**	$\frac{\partial p}{\partial x}$ **(Pa m^{-1})**	$Q_{out,ice}$ **(m^3s^{-1})**	V_{sub} **(km^3)**
Arabia Terra 1	B1	686	6.9	1.0×10^4	4	1.0×10^3	2.1×10^4	10
	B2	635	6.4	8.5×10^3	3	1.4×10^3	1.9×10^4	9
Arabia Terra 2	B1	446	7.8	8.4×10^3	3	3.3×10^3	2.7×10^4	16
	B2	706	6.4	9.5×10^3	3	1.6×10^3	2.3×10^4	12
	B3	922	8	1.8×10^4	8	4.2×10^2	2.7×10^4	16
	B4	676	16.6	4.4×10^4	33	1.1×10^3	9.1×10^4	99
	B5	605	7.4	1.0×10^4	4	2.3×10^3	2.9×10^4	17
Hellas	B1	642	6.6	9.0×10^3	3	4.1×10^3	3.3×10^4	21
	B2	489	7.1	7.8×10^3	2	5.6×10^3	3.3×10^4	21
Noachis	B1	1813	21	1.8×10^5	270	1.7×10^3	4.3×10^5	1000
	B2	624	4.5	4.7×10^3	1	1.7×10^3	1.2×10^4	4

Table 4.5: Calculations for subglacial breach scenarios for all tadpole craters (Tables 4.4 & 4.2, Fig. 4.7), assuming ice surface level with the top of the modern observable breach incision. We consider 2 cases: 1. Flow in each subglacial channel is driven only by a 0.1 slope. 2. Flow in the subglacial channel is driven by pressure gradient between crater bottom and surrounding terrain, roughly equivalent to the pressure exerted by a column of ice of thickness d_c. $p_{w,ice}$ is wetted perimeter including ice surface ($p_w + w_v$, Table 4.2), $R_{H,ice}$ is the hydraulic radius calculated using $p_{w,ice}$. $Q_{out,ice}$ is peak flow rate (Eqns. 4.9 & 4.6), V_{sub} is an empirical approximation of total subglacial water volume assuming jökulhlaup-like drainage of crater (Eqn. 4.11). $\frac{\partial p}{\partial x}$ is subglacial downstream pressure gradient (Eqn. 4.10). All calculated water volumes and fluxes are given to 2 s.f.

ice sheet surface. At a single point, ∇z_b and $\nabla(z_s - z_b)$ are equivalent to the slopes at the base of the ice sheet (S_b) and the surface of the ice sheet (S_s) respectively, and the driving pressure gradient at that point can be approximated by:

$$\frac{\Delta p}{\Delta x} = (\rho_w - \rho_i) g S_b + \rho_i g S_s \tag{4.13}$$

On the interior wall of the crater leading to the channel, S_b is negative. Therefore for the flow of water to proceed out of the crater, it must be exceeded by $\rho_i g S_s$ such that $\Delta\phi$ is positive. This leads to an expression for the minimum ice sheet surface slope required:

$$S_s > \frac{(\rho_w - \rho_i)}{\rho_i} S_b \tag{4.14}$$

The surface slope S_s must therefore be at least 9% of the basal slope in order to drive meltwater up and out of the crater. Therefore, for a basal slope of 0.6 (≈30 degrees, or close to the angle of repose), the ice surface slope would need to be greater than 0.054, or around 3 degrees. The slopes on the exterior edges of crater-filling ice mounds (Conway et al., 2012), and at the termini of lobate debris aprons (Mangold, 2003; Fastook et al., 2014) can be steeper than this. Therefore, we cannot exclude subglacial incision of exit breaches based on this simple calculation of the required ice surface slope.

4.5.3 Water Sources for Subglacial Flow

Supraglacial Melting

A lower limit on the duration of a climate event required to generate sufficient meltwater to form a multiple breach tadpole crater can be obtained from the volume of water required to move the total sediment volume of the breach channels (Table 4.2). These volumes are equivalent to a water depth of between 0.06 m and 2.76 m per unit crater area, which is equivalent to between 6 and 252 days per breach of meltwater generation at the crater surface at a rate of 4 m yr^{-1} m^{-2} (Kite et al., 2013), with a mean of 60 melting days to erode each breach if meltwater is sourced solely from the crater area. These values are comparable to the number of total melting days required in the surface melt pond mechanism (Section 4.4.2), and also need not be continuous as there is no requirement for the breaches to erode in a single subglacial event.

Other potential heat sources for melting include re-entry of ejecta following an impact (Goldin and Melosh, 2009; Toon et al., 1997), or the climate effects of very large impacts (impactors ≥ 100 km diameter) (Turbet et al., 2020; Segura et al., 2012). For heating by

ejecta re-entry, around 70 minutes of heating at 5 kW m^{-2} would generate the equivalent of 1 year's worth of melt, however, models of the thermal pulse following the Chicxulub Impact on Earth only achieve heating rates $\geq$ 5 kW m^{-2} for a few minutes (Goldin and Melosh, 2009). Therefore a single impact would not be able to generate the large melt ponds required to erode observed breaches in a single event (Fig. 4.16d), and tens to hundreds of Chicxulub-equivalent impacts (impactors tens of km in diameter) would be needed to explain breaches eroded by smaller ponds. For very large impacts, recent climate models suggest that short-lived high-intensity precipitation and high temperatures can last several years (Turbet et al., 2020). However, the intense, global precipitation caused by an impact on this scale would likely lead to intense fluvial weathering and crater degradation (Palumbo and Head, 2018), which is inconsistent with the small size and preserved rims of tadpole craters (Section 4.3.2). Regardless of the melting heat source, however, subglacial flow requires an ice sheet, which represents a greater total mid-latitude ice inventory than just crater-filling ice pods (Section 4.4.2, Fig. 4.2b) and therefore constrains the Martian climate during the Late Hesperian/Amazonian.

Magmatic Intrusions

Some recent glacial features on Mars, such as eskers, require wet-based glaciation to occur, such that there is meltwater available at the base of the ice (Gallagher and Balme, 2015; Butcher et al., 2023). For the expected climate regime and geothermal heat flux during the Amazonian, cold-based formation is expected for viscous flow features such as lineated valley fill and lobate debris aprons (Woodley et al., 2022; Gallagher and Balme, 2015). Previous studies have proposed magmatic intrusions as a source of enhanced geothermal heat flux to drive melting (Arnold et al., 2019). We use a forward Euler finite differences method in 1D to solve for the cooling of an intrusion of thickness H_{int} at depth d_{int} in the crust beneath a surface ice layer of thickness H_{ice} (Fig. 4.17) to calculate the conditions under

which meltwater can be generated at the base of a regional ice sheet through magmatic heat flux through the base of a tadpole crater.

The initial temperature profile with depth is set by the geothermal gradient through an ice layer with thickness h_{ice}, surface temperature T_{surf}, and the instantaneous emplacement of an intrusion with thickness h_{int} at temperature T_{int} at a depth of z_{int} (Table 4.4, Fig. 4.17).

Temperature then evolves diffusively in the crust and ice layer:

$$\frac{\partial T}{\partial z} = \frac{1}{\rho_z c_{p,z}} \frac{\partial}{\partial z} \left(k_z \frac{\partial T}{\partial z} \right) \tag{4.15}$$

where ρ_z, $c_{p,z}$, and k_z are the density, specific heat capacity, and thermal conductivity of the material at depth z (ice or rock).

Once the temperature at the base of the ice reaches the melting point of water, we fix the temperature at the ice-rock interface to 273 K (analogous to if a water layer were forming). We then calculate the heat flux across this boundary (q_{i-r}) at each timestep, and assume that all heat provided by the cooling intrusion at depth minus the conductive losses to the overlying ice layer is used to melt additional ice. We calculate the melting rate ($\dot{z}_m$) at each timestep:

$$\dot{z}_m = \frac{q_{i-r}}{L_i \rho_w} \tag{4.16}$$

We then calculate the maximum column thickness of meltwater produced by finding the cumulative sum of melt produced at each timestep (Fig. 4.17c). This approach implicitly assumes that the meltwater is removed instantaneously from the base of the ice, and artificially holds ice thickness constant. Therefore, once the base of the ice reaches 273 K, the conductive heat losses are fixed by the ice thickness and surface temperature, which set the thermal gradient in the ice. In reality, however, the progressive thinning of the ice layer would steepen the thermal gradient in the ice and therefore reduce the heat flux across the

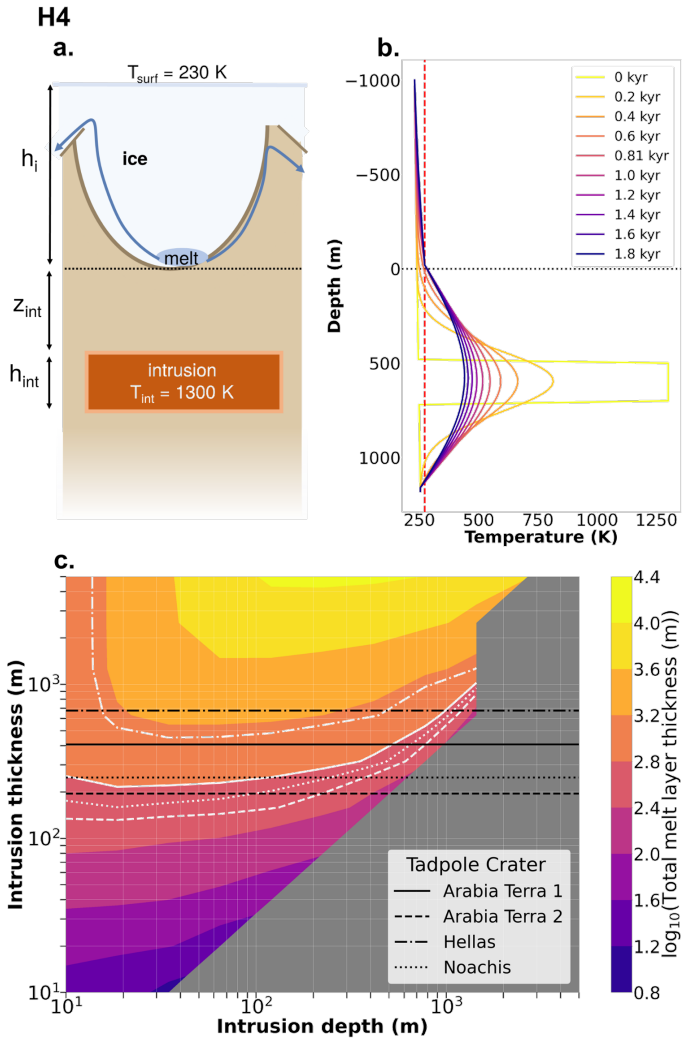

Figure 4.17: **a.** Sketch of 1D intrusion model. h_i is ice thickness, z_{int} is intrusion depth below the crater floor, h_{int} is the vertical thickness of the intrusion (assumed to have same diameter as the crater). Dashed line indicates base of ice at $z = 0$. **b.** Time evolution of vertical temperature profile (1D profile through central point of crater) for a 200 m thick intrusion with an initial temperature $T_{int} = 1300$ K emplaced 500 m below the crater floor for a crater overlain by 1 km of ice. Vertical red dashed line indicates indicates $T = 273$ K. Dashed line indicates base of ice at $z = 0$. **c.** total thickness of water melted per unit area at the base of a crater for intrusions of different thicknesses at a range of depths beneath the crater floor (Table 4.4). Black lines indicate maximum intrusion depth calculated from difference between predicted and measured crater floor depths (Table 4.1). White lines indicate predicted initial crater depth, i.e. where each crater would be filled to the brim with melt. Key shows line styles corresponding to different multiple breach tadpole craters.

rock-ice interface, leading to less melting.

To constrain the likelihood of magmatic intrusions as a melt-generating mechanism, we assume that all deformation related to intrusion emplacement is accommodated through fracturing and decoupling of the rock above the intrusion from the surrounding crust, leading to crater floor uplift (Walwer et al., 2021). In this scenario, the intrusion diameter is limited to D_c so that uplift due to intrusion inflation only occurs within the crater, and the total intrusion thickness is the difference between the predicted fresh crater depth and its current observed depth (Table 4.1, Walwer et al. 2021). To maximize the intrusion-driven melting, we neglect the cooling at the edges of the intrusion. Therefore our 1-D calculations best apply to the heating at the center of each crater, furthest from any additional conductive cooling at the intrusion's horizontal boundaries. This is conservative in the context of examining the feasibility of intrusion-driven basal melting because it maximizes the melt volume and melting duration for each intrusion.

We compare the total melt thickness to the depth of each multiple breach tadpole crater, and the crater area-averaged melt thickness required to erode the observed outlet breaches assuming a sediment:water ratio of 0.3 (Table 4.2). We find that intrusions beneath craters can readily provide sufficient heat to melt enough water to erode all the breaches for every multiple breach crater, and even to fill each crater to the brim with melt water (Fig. 4.17). Impact-induced decompression melting triggered by reduced pressure beneath craters when kilometers of material is removed has been proposed as a mechanism for generating volcanic activity on Martian and lunar crater floors (Edwards et al., 2014; Elkins-Tanton and Hager, 2005; Schultz, 1976), and there is evidence for impact-associated igneous activity in the Sudbury impact structure on Earth (e.g. Prevec et al. 2000). Infilled Martian craters with high thermal inertia flat floors consistent with volcanic fill by lavas or pyroclastic flows have an mean diameter $>$ 40 km (Edwards et al., 2014). In a survey of 2800 craters $>$ 1 km in diameter with high thermal inertia floor fill, the smallest crater with features consistent with

volcanic activity had a diameter of 8 km (Edwards et al., 2014). Floor fractured craters, which can form through intrusions beneath crater floors (Walwer et al., 2021; Schultz, 1976; Montigny et al., 2022), similarly have a mean diameter of 43 km, and the size-frequency distribution of floor fractured craters in Xanthe Terra suggests that larger craters preferentially have fractured floors (Sato et al., 2010). Therefore, if intrusions drive basal melting in tadpole craters, the preferential occurrence of tadpole breaches in small craters (Section 4.3.1, Fig. 4.5) may be inconsistent with intrusions beneath the craters themselves. However, larger, regional-scale intrusions could also trigger basal melting and may not lead to crater floor lava flows or fracture formation, therefore we cannot eliminate intrusions as a source for subglacial melt. Using our 1-D melting model, we can approximate the necessary intrusion depth to intrusion thickness relationship required to induce basal melting beneath a 1000 m thick ice sheet (Fig. 4.18). Our results show that laccoliths emplaced beneath the four multiple breach tadpole craters can provide a sufficient boost to geothermal heat flux to drive basal melting at the base of a 1000 m thick ice sheet for shallow intrusions. If large intrusions are the melt source for tadpole craters, a global database of tadpoles may show clustering of tadpole craters in regions with evidence for widespread volcanic activity.

If intrusions are the primary mechanism for generating liquid water in tadpole craters, this would require widespread intrusions at depths 0.5-5 km beneath both the northern (Fig. 4.3) and southern mid-latitudes (Wilson et al., 2016; Warren et al., 2021), at the same time as ice sheets were present. However, it is conceivable that some tadpole craters were fed by basal intrusion-triggered melting while the majority depended on climate-driving supraglacial melting (Section 4.5.3). Mapping volcanic features in these regions and comparing their spatial distributions to tadpole craters may provide further insight into the likelihood of this mechanism.

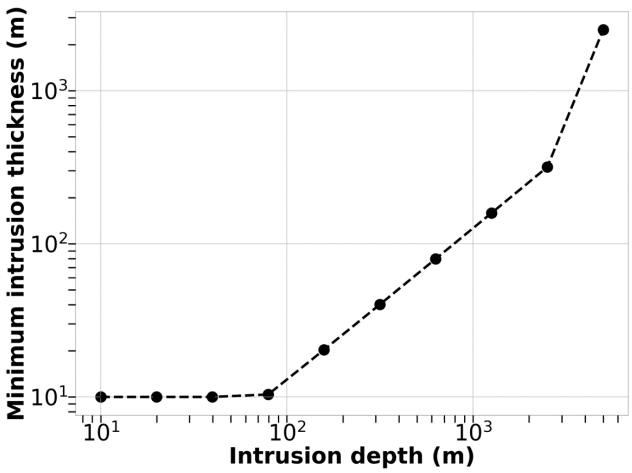

Figure 4.18: Minimum required intrusion thickness as a function of intrusion depth to trigger basal melting of an ice sheet filling a multiple breach tadpole crater. Minimum thickness is found by interpolating our melting model results to find the intrusion thickness at which 0 melting occurs, i.e. the intrusion is too deep for heating around the margins to raise the surface temperature above 273 K.

4.6 Discussion

4.6.1 Terrestrial analogs

Here, we examine three possible settings for multiple breach tadpole crater terrestrial analogs:

- Bedrock impact structures buried by ice
- Subaerial lake overspill from multiple breaches
- Subglacial lake overspill

However, it remains possible that the actual tadpole crater breach-forming mechanism has not yet been fingerprinted in a terrestrial environment.

Impact Craters Beneath Ice

Formerly subglacial bedrock impact craters, such as the 24 km diameter Haughton impact structure (Osinski and Lee, 2005), have been identified in the Canadian shield. Additionally,

radar studies have found craters that are still beneath ice sheets (e.g. Kjær et al. 2018; MacGregor et al. 2019). Most of these impact structures have been extensively eroded and feature inlet breaches, making them poor analogs for tadpole craters. For example, although Hiawatha Crater, Greenland, has an outlet to the northwest, the rim is cut by two subglacial inlet channels in the south (Kjær et al., 2018).

One exception and a strong candidate for a multiple breach tadpole crater terrestrial analog is Pingualuit Crater in Quebec, Canada (Fig. 4.19). Pingualuit (also referred to as Ungava Crater, Chubb Crater, and New-Quebec Crater in the literature) is a 3.4 km diameter crater dating to 1.4 Ma (Bouchard, 1989). Despite extensive glacial erosion (Bouchard et al., 1989), the topographic rim remains intact around the full circumference of the crater, extending more than 100 m above the surrounding terrain. The rim is incised by 10 outlet breaches at elevations between 553±5 m and 608±5 m above sea level (Desiage et al., 2015).

As the ice sheet retreated from the NE to SW (Gray and Lauriol, 1985), Desiage et al. (2015) propose that the highest elevation breaches on the eastern shore of the crater overspilled first. Then, as the ice retreated, lower points on the crater rim were exposed approximately anticlockwise where later breaches occurred. Evidence for subaerial breach drainage includes one breach coinciding with a paleoshoreline within the lake (Desiage et al., 2015). However, several esker segments close to the crater itself and parallel to downstream portions of the channel networks downstream of rim breaches suggest that subglacial drainage occurred in the vicinity of Pingualuit Crater during the last glaciation (Bouchard, 1989; Desiage et al., 2015). Desiage et al. (2015) suggest that the drainage of outlet 10 (Fig. 4.19) may have been subglacial, therefore not all breach events at Pingualuit or in tadpole craters need to have occurred as a result of the same climate and ice configuration.

This proposed mechanism for the overspilling of Pingualuit Crater, and the similarities between Pingualuit Crater's rim morphology and that of tadpole craters, provides support for the feasibility of our proposed "rapidly retreating glacier" mechanism (Section 4.4.1) for

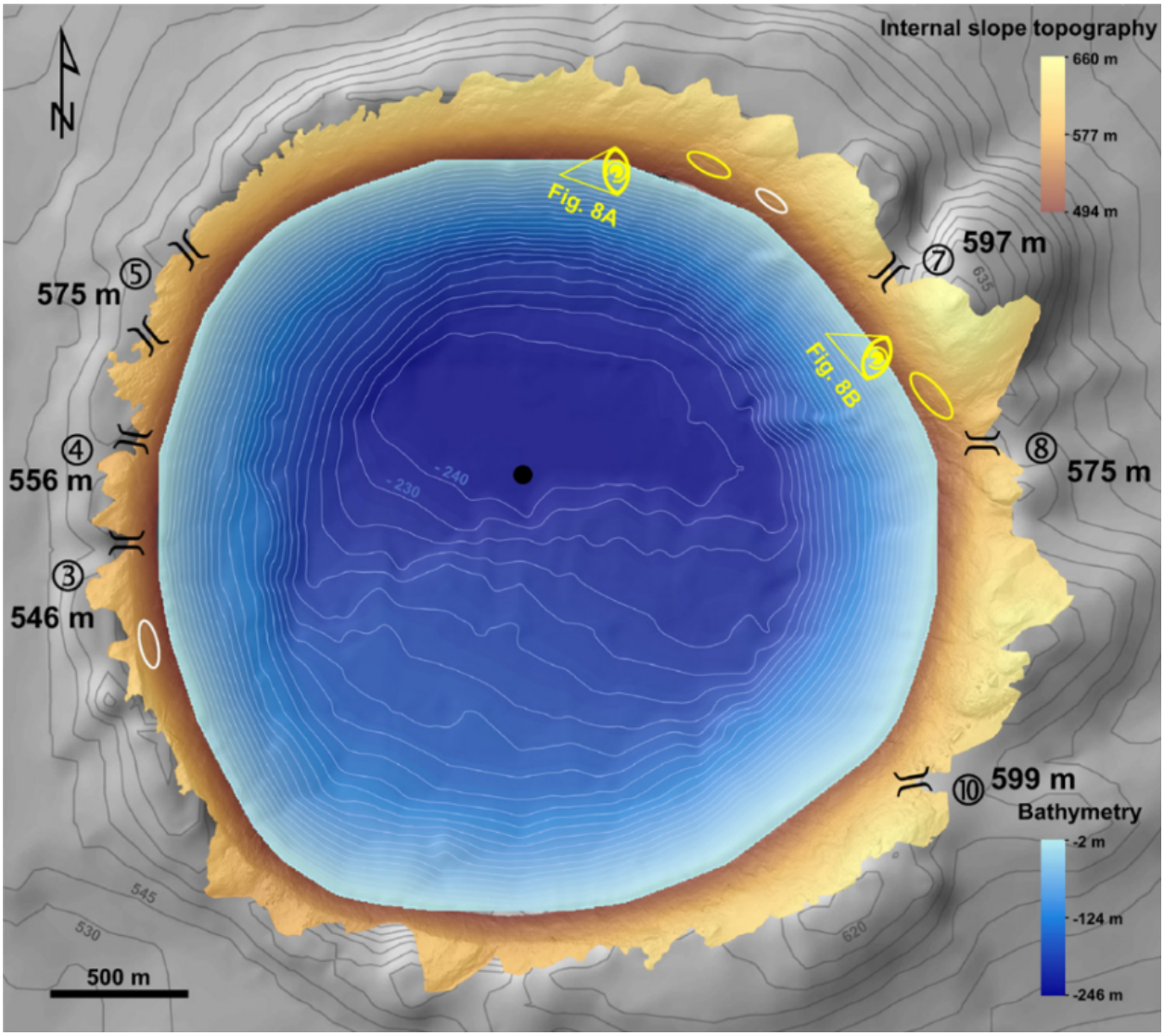

Figure 4.19: Reproduced from Fig. 7 in Desiage et al. (2015). Digital elevation model (DEM) of Pingualuit Crater. Black brackets indicate locations of breaches with elevations in meters above sea level. White and yellow ellipses highlight paleoshorelines corresponding to 575 m (the elevation of breach 3). All elevations have an error of ±1 m.

multiple breach tadpole crater formation.

Subaerial Lakes

Small terrestrial subaerial lakes with multiple outlet breaches are rare. One example is Lake Colonia in Patagonia, Chile (Dussaillant et al., 2010). Lake Colonia is fed by meltwater

generated by the rapid ablation of Colonia Glacier, and has a primary spillway active during a series of 5 jökulhlaup events in 2008 and 2009, and an earlier, now inactive spillway with a floor 10 m above the floor of the current spillway. If both spillways were active simultaneously, Dussaillant et al. (2010) calculate that the total flux of water out of the lake would have been 16,000 m^3 s^{-1}, which is of a similar order of magnitude to some of our calculated water fluxes (Table 4.3). This suggests that the crater inflow rate generated by meltwater routing from a terrestrial glacier is sufficient to activate multiple breaches in a single overspill event, which is likely due to the larger melting rates possible on Earth where the annual average temperature is closer to 273 K, even in high altitude environments.

On a scale far larger than tadpole craters, multiple spillways formed during the advance and retreat of the Laurentide Ice Sheet, which fed Glacial Lake Agassiz. As the Laurentide Ice Sheet retreated, it exposed lower topography, causing Lake Agassiz to abandon higher elevation breaches to the south, and routing megafloods through lower spillways to the north and east (Fisher, 2020). However, unlike tadpole craters, Lake Agassiz formed part of a network of connected proglacial lakes flooding into one another, as recorded by fan deposition into Lake Agassiz from lakes to the west (Kehew et al., 2009). At its maximum extent, Lake Agassiz had a volume of 38,700 km^3 (Mann et al., 1999), or 90 times the volume of the largest tadpole crater in the 24-52° S latitude band (Fig. 4.5a). Due to the vast difference in scale and the interconnected nature of large terrestrial proglacial lakes and the larger role of lithospheric flexure beneath ice sheets for proglacial flow routing on Earth, these are likely a poor analog for tadpole craters.

Subglacial Lakes

Since the discovery of the first subglacial lake in Antarctica (Robin et al., 1969), almost 800 subglacial lakes have been identified on Earth (Livingstone et al., 2022). Observations suggest that subglacial lakes in Antarctica and Greenland behave differently. In Antarctica, large,

stable lakes such as Lake Vostok tend to occur in large depressions in basal topography and can persist for thousands of years(Fricker et al., 2016). However, there are also smaller, active lakes that drain and refill on timescales of months to decades. These are associated with fast-flowing, wet-based ice streams and are associated with depressions in the ice surface rather than the basal topography (Fricker et al., 2016). The MacAyeal ice stream, for example, has ten known subglacial lakes (Smith et al., 2009). In Greenland, around 20% of subglacial lakes occur in regions where cold-based ice is expected and are also typically associated with slow-moving ice (Bowling et al., 2019). Lakes in cold-based regions of Greenland ice may be better analogies for tadpole craters given the preservation of topographically elevated crater rims in observed tadpole crater areas, with limited evidence for wet-based glacial features.

On Earth, satellite observations of the ice surface above known subglacial lakes can also reveal subglacial drainage and recharge events as the ice surface sinks and inflates respectively (Fricker et al., 2016), including recharge of a subglacial lake in northeast Greenland by routing of surface meltwater to the base of the ice by crevasses around the lake margins (Willis et al., 2015). This may be a good terrestrial analog for providing supraglacial meltwater to subglacial tadpole craters for subsequent overspill.

Additionally, evidence for catastrophic drainage of subglacial lakes leading to bedrock incision is visible in the Labyrinth in the Antarctic Dry Valleys. The Labyrinth is a network of multiple generations of cross-cutting channels extending 10s of km from the margin of the modern Wright Upper Glacier. Superposed ash fall deposits date date the channels to 12-14 Ma, with each incising 10-50 m into underlying bedrock (Lewis et al., 2006). This is similar to the depths of tadpole breaches (Table 4.2). The Labyrinth is hypothesized to have drained one or more subglacial lakes at a time when wet-based glaciation was more widespread beneath the Antarctic ice sheet (Marchant et al., 1993). Unfortunately, without knowing the configuration of the subglacial lake system(s), it is difficult to assess the similarity of the Labyrinth to multiple breach tadpole craters, as an interconnected network of subglacial

lakes is not consistent with the absence of inlets in tadpole craters.

4.7 Conclusions

Hundreds of tadpole craters exist on Mars (Wilson et al., 2016; Howard et al., 2022) (Fig. 4.3). In the 24-52° S latitude band, tadpole crater breaches preferentially form in smaller diameter craters (Fig. 4.5a). This demonstrates there was not enough water or ice available during tadpole breach formation to fill larger craters to the rim, suggesting a maximum ice thickness of approximately 1 to 2 km. When smoothed topography is subtracted from MOLA topography to generate residual topography, tadpole craters show a preference for occurring on relative highs at all lengthscales, with a steeper slope at shorter length scales (Fig. 4.6b-f). This favors a high-elevation dependent formation process for tadpole craters, for example accumulation of snow and ice at high altitudes, or orographic precipitation.

Forming multiple breaches exiting a single crater at different elevations without an inlet is an additional challenge to tadpole formation models. We consider four mechanisms for tadpole breach formation that can explain these features (Fig. 4.2).

Among subaerial mechanisms, we find that crater-interior precipitation or melting is too slow to drive simultaneous overspill of multiple breaches, and that appealing to increased melting area on a regional ice sheet routed into the crater requires unrealistically large melting areas. Additionally, we disfavor groundwater as a tadpole crater overspilling water source as this would require unrealistically high aquifer permeabilities, initial aquifer pressures, and aquifer thicknesses for three of the four multiple breach tadpole craters considered in this study. Overall, simultaneous overspill of multiple breaches (Fig. 4.2a) is unlikely. As a result, the only remaining subaerial mechanisms consistent with forming all four multiple breach tadpole craters are:

- **H2:** Draining of meltwater ponds smaller than the crater diameter formed on the surface of a crater-filling ice body and overspilling the crater rim (Section 4.16a,

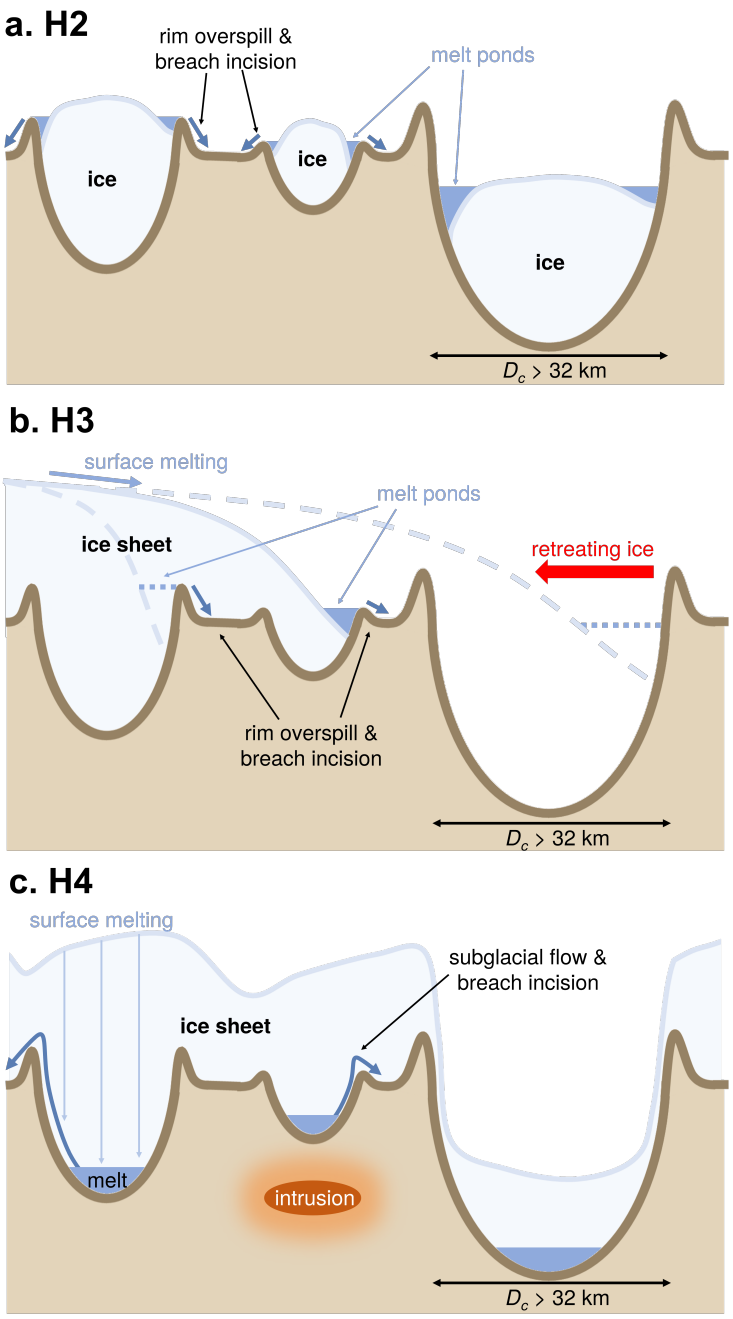

Figure 4.20: Sketch of the three remaining multiple breach tadpole crater forming mechanisms (Fig. 4.2) that are consistent with our morphological and modeling constraints on tadpole breach forming climate.

Figs. 4.2b & 4.20a)

- **H3:** Sequential breach overspill enabled by retreat of an ice sheet progressively exposing

lower rim topography and filling proglacial crater lakes with meltwater (Section 4.4.1, Figs. 4.2c & 4.20)

- **H4:** Subglacial flow with melt supplied by either supraglacial melting or basal melting triggered by a cooling intrusion (Section 4.5, Figs. 4.2c & 4.20c)

In the subglacial case (H4), we slightly disfavor intrusion-driven basal melting because crater floor volcanic features are typically associated with craters tens of kilometers in diameter (Edwards et al., 2014; Sato et al., 2010), whereas tadpole craters are typically <10 km in diameter (Fig. 4.5).

Finally, we suggest that Pingualuit Crater in Quebec, Canada (Bouchard et al., 1989) is the best currently known terrestrial analog for multiple breach tadpole craters. Pingualuit has a topographically elevated rim, ten exit breaches spanning tens of meters in elevation (Fig. 4.19), and lacks inlet breaches. The proposed formation mechanism for Pingualuit's series of exit breaches is the retreat of an ice sheet exposing progressively lower rim topography (Desiage et al., 2015). This demonstrates that our proposed ice sheet retreat mechanism for multiple breach tadpole crater formation (Fig. 4.2c & 4.12) does occur.

We conclude that the formation of multiple breach tadpole craters in the Martian midlatitudes requires the accumulation of at least hundreds of meters of ice, either as crater-filling ice bodies, or regional ice sheets (Fig. 4.20). Modeling studies have demonstrated that midlatitude ice accumulation can be achieved under Amazonian conditions if Mars' obliquity is higher (Forget et al., 2006; Madeleine et al., 2009; Fastook and Head, 2015). Our results also suggest that tens to hundreds of days of temperatures exceeding 273 K in the mid-latitudes are likely required to generate the liquid water for multiple breach tadpole crater overspill. If only small water volumes are required to enable meltwater pond accumulation or subglacial erosion, these melting days are consistent with annual peak temperatures at each multiple breach tadpole crater location on modern Mars (Forget et al., 1999; Millour et al., 2018) but would require an increase in greenhouse warming to overcome the cooling effects of ice

albedo, high thermal inertia, and evaporative cooling (Ingersoll, 1970). If melt needs to accumulate over continuous days, 25-50 K of warming is required.

Part II

Venus

CHAPTER 5

NARROW RANGE OF EARLY HABITABLE VENUS SCENARIOS PERMITTED BY MODELING OF OXYGEN LOSS AND RADIOGENIC ARGON DEGASSING

This chapter was originally published as: Warren, A. O., and Kite, E. S. "Narrow range of early habitable Venus scenarios permitted by modeling of oxygen loss and radiogenic argon degassing." *Proceedings of the National Academy of Sciences* (2023): 120 (11) e2209751120. Sections of the paper and accompanying supplementary have been reorganized to better fit a thesis format.

5.1 Abstract

Whether Venus was ever habitable is a key question driving missions to Earth's sister planet in the next decade. Venus today has a dry, O_2-poor atmosphere, but recent work has proposed that early Venus may have had liquid water (Krissansen-Totton et al., 2021), and reflective clouds that could have sustained habitable conditions until 0.7 Ga (Yang et al., 2014; Way and Del Genio, 2020). Water present at the end of a habitable era must since have been lost by photodissociation and H escape, causing buildup of atmospheric oxygen (Tian, 2015a). We present a new time-dependent model of Venus' atmospheric composition starting from the end of a hypothetical habitable era with surface liquid water. We find that O2 loss to space, oxidation of reduced atmospheric species, oxidation of lava, and oxidation of a surface magma layer formed in a runaway greenhouse climate can remove O_2 from up to 500 m Global Equivalent Layer (GEL) (around 30% of an Earth ocean), unless melts on Venus had a much lower oxygen fugacity than Mid Ocean Ridge melts on Earth, which increases the upper limit twofold. Volcanism is required to supply oxidizable fresh basalt and reduced gases to the atmosphere, but also contributes ^{40}Ar. Consistency with Venus'

modern atmospheric composition occurs in less than 0.4% of runs, in a narrow parameter range where the reducing power introduced by O_2 loss processes can balance O_2 introduced by H escape. Our models favor hypothetical habitable eras ending before 3 Ga and very reduced melt oxygen fugacities three log units below the fayalite-magnetite-quartz buffer (f_{O_2} <FMQ−3), among other constraints.

5.2 Introduction

Did Venus ever have liquid water? Answering this question is one of the core questions driving the fleet of new missions to Venus selected by NASA and ESA, the terrestrial planet most similar in size to the Earth in our solar system (O'Callaghan, 2021). Today, Venus has an average surface temperature of 720 K, and a dry 93 bar, predominantly CO_2 atmosphere. These conditions preclude the stability of water and most hydrous minerals on its present-day surface (Zolotov et al., 1997). Although some studies of Venus' climate evolution suggest that the planet has always been uninhabitably hot (Hamano et al., 2013; Gillmann et al., 2009; Turbet et al., 2021), other modeling studies propose that Venus may have been able to maintain surface temperatures low enough for liquid water for much of its past (Pollack, 1971; Yang et al., 2014; Way and Del Genio, 2020; Way et al., 2016; Kasting, 1988; Salvador et al., 2017). However, a vital question remains: How much water could early Venus have had, and when?

Recent modeling of Venus' magma ocean evolution and subsequent geodynamic and atmospheric evolution suggests that Venus may have retained sufficient water late enough in its history to form an ocean hundreds of meters deep, either through outgassing H_2O from volcanoes, or cooling a steam atmosphere (Krissansen-Totton et al., 2021). Even with modest water inventories of 10 m GEL, it has been proposed that habitable conditions on Venus might have persisted until as recently as 0.7 Ga, provided that the planet had a thinner (<10 bar) atmosphere, a faster rotation rate, and reflective cloud cover (Way and Del Genio,

2020; Yang et al., 2014).

If a liquid water layer persisted beyond the first few hundred million years of Venus' evolution, it may have left an imprint on Venus' modern atmosphere. This can be used to constrain the maximum thickness of a liquid water layer on Venus. The high deuterium to hydrogen ratio–150 times higher than Earth's (De Bergh et al., 1991)–in Venus' atmosphere has been proposed to suggest escape of up to an Earth ocean of water from Venus (Donahue et al., 1982; Kulikov et al., 2006). However, atmospheric D/H is ambiguous because a similar D/H ratio can be produced both by steady-state loss of water delivered over Venus' history, for example by degassing from a fractionated mantle source, through Raleigh fractionation of catastrophic recent water degassing, or through loss of water delivered by impacts (Grinspoon, 1993; Selsis et al., 2007). A further complication to interpreting Venus' D/H ratio is that the D/H fractionation factor in Venus' upper atmosphere may have varied 20-fold over time (Donahue, 1999). Additionally, the initial D/H ratio of Venus may have been higher than for Earth and Mars as a result of its impact history (Horner et al., 2009), or been modified by loss of H prior to condensation of water on Venus' surface during an early magma ocean period (Pahlevan et al., 2019). Therefore, although D/H is a useful constraint on loss of water from Venus, it is difficult to unpick the effects of Venus' formation and earliest evolution from later H_2O losses from a hypothetical habitable era with surface liquid water.

Fortunately, Venus' atmosphere also records the history of water on the planet through the concentration of atmospheric O (Krissansen-Totton et al., 2021; Gillmann et al., 2020). Any water in Venus' upper atmosphere is vulnerable to photodissociation to H and O (Ingersoll, 1969). H escapes to space at a higher rate than O, leading to accumulation of O (Tian, 2015b). O can then be lost through later non-thermal escape (Kulikov et al., 2006; Gillmann et al., 2020), oxidation of reduced atmospheric species such as CO and CH_4 released by volcanoes, and by oxidation of surface rocks (Heard and Kite, 2020). Crucial constraints are that Venus' present day atmosphere is exceedingly O_2 and CO-poor ($<$70 ppm O_2,

$<$ 50 ppm CO) and dry ($<$ 100 ppm H_2O) (Moroz, 1981; Johnson and de Oliveira, 2019). Therefore, if Venus ever had oceans, the O added to the atmosphere by the subsequent evaporation of this water during a moist or runaway greenhouse (RGH) period must since have been removed by oxygen sinks (Gillmann et al., 2020; Krissansen-Totton et al., 2021). In principle, this places an upper limit on the surface water inventory of any habitable period on Venus - i.e., whether or not Venus once had oceans - and also constrains the timing of any possible habitable periods in order to allow time for O sinks to remove essentially all of the O.

Here, we present a new time-dependent, mass-balance model of the evolution of Venus' atmospheric composition starting from the end of a hypothetical "habitable era," which we define here as a period able to maintain surface liquid water (Fig 5.1; Materials and Methods). Previous work has considered Venus' overall evolution from an initial magma ocean phase to explore whether condensation of surface liquid water and consistency with Venus' modern atmosphere is possible (Krissansen-Totton et al., 2021), but our approach specifically focuses on the consequences of a hypothetical habitable era for Venus' later evolution. As a result, our models are agnostic to Venus' formation, initial composition, magma ocean evolution, and the details of the habitable era itself. Our O_2 loss model tracks the post-habitable-era evolution of H_2O, CO_2, and O_2 in Venus' atmosphere. We assume that all surface liquid water present immediately before the end of habitability enters the atmosphere, either during a runaway greenhouse (RGH) phase, or a moist greenhouse phase, both of which could be triggered by the Sun brightening over time, or the outgassing of CO_2 through volcanism. We identify regions of parameter space using a regular grid of 7 parameters where the water (and therefore oxygen) added to Venus' atmosphere by the evaporation of habitable era surface liquid water and subsequent volcanic H_2O outgassing can be removed by (Fig. 5.1):

1. Non-thermal O escape

2. Oxidation of degassed CO and CH_4 to CO_2

3. Oxidation of lava, ash, and magma

Model runs are considered successful when the final atmospheric O_2, H_2O, and CO concentrations satisfy the upper limits on O_2, H_2O, and CO concentrations in Venus' modern atmosphere (Johnson and de Oliveira, 2019). We consider hypothetical habitable eras ending at 4.0, 3.0, and 1.5 Ga, with end-habitable-era water inventories between 10 and 1000 m GEL over a total of 94,080 model runs (parameters in Table 5.1, 47,040 runs each for the moist greenhouse case and the RGH case where oxidation of a molten surface occurs).

Two important processes in our O_2 loss model are the oxidation of degassed C and H species and oxidation of basalt lava flows. These processes both depend on Venus' crustal production and degassing history, which is constrained by the modern abundance of ^{40}Ar in Venus' atmosphere. This is because ^{40}Ar is produced by the decay of ^{40}K in the crust and in the mantle, and ^{40}Ar can be released from the mantle to the atmosphere through degassing from volcanic eruptions and intrusions. ^{40}Ar formed from ^{40}K decay in the crust can diffuse through the crust into the atmosphere (O'Rourke and Korenaga, 2015; Kaula, 1999). As little as 24% of the radiogenic ^{40}Ar in Venus' mantle has been degassed (O'Rourke and Korenaga, 2015), assuming an Earth-like K abundance on Venus. We construct a simple ^{40}Ar degassing model following (O'Rourke and Korenaga, 2015; Kaula, 1999) to determine whether the ^{40}Ar degassed by the crustal production histories used in our O_2 loss model falls within or below the $(1.61 \pm 0.54) \times 10^{16}$ kg range for ^{40}Ar abundance in Venus' modern atmosphere (Kaula, 1999).

5.3 Oxygen Loss Model

We combine simple models of degassing of basaltic melts (Surkov, Yu. A. and Barsukov, V. L. and Moskalyeva, L. P. and Kharyukova, V. P. and Kemurdzhian, A. L., 1984), atmospheric escape of H and O, and removal of O from the atmosphere by oxidation of reduced gases, lava flows and ash (when formed) to track the evolution of Venus' atmospheric composition since

Table 5.1: Parameter values used in O_2 loss model (see Materials and Methods for details). We implement a regular grid approach so all parameter combinations are explored.

Symbol	**Description**	**Values**	**Units**
t_0	End of habitable era (and model start time) in Gyr before present	4 (habitable for $\leq$0.5 Gyr) 3 (habitable for $\leq$1.5 Gyr) 1.5 (habitable for $\leq$3 Gyr)	Gyr
h_{hab}	Global Equivalent Layer (GEL) water released into atmosphere at end of habitable era (includes surface water, groundwater, and any water from minerals dehydrated during transition out of habitable conditions)	10, 50, 100, 300, 500, 700, 1000	m
c_{CO_2}	Concentration of CO_2 in Venusian basaltic melts	0.03, 0.05, 0.1, 0.2	wt%
c_{H_2O}	Concentration of H_2O in Venusian basaltic melts	0.001, 0.1, 0.2, 0.5, 700, 1000	wt%
f_{volc}	Fraction of CO_2 in Venus' present atmosphere derived from post-habitable era volcanic degassing	0.1, 0.5, 0.9, 1.0	
f_{ext}	Fraction of magmatism that is extrusive (reaches the surface as ash or lava rather than crystallizing deep underground)	0.1, 0.3, 0.9, 1.0	
$\log fO_2$	Oxygen fugacity of erupting melt relative to the fayalite-magnetite -quartz buffer	0, -1, -2, -3, -4	$\log fO_2\Delta$FMQ

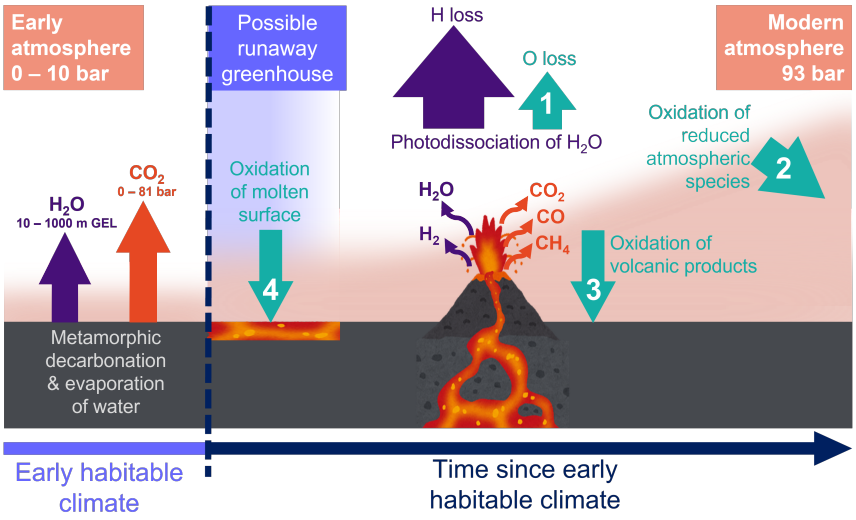

Figure 5.1: Schematic illustration of model for Venus' atmospheric evolution starting from the end of a hypothetical early habitable era. Prior to the model start, we set the total end-habitable era water inventory (Table 5.1). After the transition out of the habitable era: 1) additional volatiles are added to the atmosphere by volcanism. These volatiles are sourced from H and C species dissolved in the melt, and their speciation into H_2O, H_2, CO_2, CO, and CH_4 is set by the oxygen fugacity of the erupting melt. 2) water from volcanism and the early habitable era photodissociates to form H and O_2, 3) H escapes to space (purple arrow), 4) O is removed from the atmosphere by escape to space, oxidation of reduced atmospheric species such as H_2, CH_4 and CO to form H_2O and CO_2, and oxidation of FeO in volcanic products (teal arrows). In models where the habitable era ends in a runaway greenhouse (RGH), O can also be removed from the atmosphere by oxidation of a molten basalt layer if the surface temperature exceeds the basalt solidus.

the end of an early habitable period using a 4th-order Runge Kutte integration scheme. To identify post-habitable era scenarios that are compatible with Venus' present day atmospheric composition, we vary 7 key parameters in our model (Table 5.1) with each parameter value weighted equally. All parameter combinations resulting in final atmospheric H_2O, O_2, and CO concentrations below upper limits (Moroz, 1981) for Venus' atmosphere are marked as "successes."

5.3.1 Initial Conditions

Each model begins at time t_0, after the end of a hypothetical early habitable era on Venus. The initial column mass of CO_2 is:

$$M_{CO_2,0} = (1 - f_{volc}) M_{CO_2,f} \tag{5.1}$$

where f_{volc} (Table 5.1) is the fraction of CO_2 in Venus' present day atmosphere from post-habitable era volcanic degassing, and $M_{CO_2,f}$ is the column mass of CO_2 on Venus today. We consider values of f_{volc} greater than 0.1 because we assume some CO_2 must be degassed after the end of a habitable era due to Venus' young surface age (Phillips et al., 1992; Bottke et al., 2016). We extend the range to $f_{volc} = 1$ because a habitable atmosphere on Venus may have been CO_2 poor, as Earth's is today. Any CO_2 present at t_0 is assumed to have degassed prior to/during the habitable era, or through metamorphic decarbonation during the transition from habitable to uninhabitable conditions (Höning et al., 2021; Foley and Smye, 2018; Kerrick and Connolly, 2001).

We also initialize our model with H_2O added to the atmosphere by vaporization of any surface liquid water present during the habitable era (Table 5.1). We consider water inventories between 10 and 1000 m GEL. Our lower limit is based on water inventories required to sustain habitable surface temperatures in existing Venus climate model studies (Way and Del Genio, 2020). The loss of up to 3000 m GEL of water, or 1 Earth ocean, is one interpretation of Venus' modern D/H ratio (Donahue et al., 1982; Kulikov et al., 2006). We treat the initial atmospheric water in two different ways, corresponding to two different ways that water could have entered Venus' atmosphere during and at the end of a hypothetical habitable era. First, we consider a case where atmospheric water vapor does not lead to surface melting. This corresponds to a moist greenhouse where H is lost to space via a moist stratosphere (Wordsworth and Pierrehumbert, 2013), but the surface remains too cold to melt basalt. For simplicity, we do not explicitly model the time evolution of the moist

greenhouse phase, and instead assume that all H from the starting water inventory has already escaped, leaving behind O_2. Second, we consider a case where greenhouse warming from H_2O vaporized during a RGH causes melting of Venus' surface. We calculate surface temperatures as a function of partial pressure of water vapor in the atmosphere (Turbet et al., 2019). This enables us to quantify the potential importance of oxidation of a surface magma layer as an O_2 sink.

5.3.2 Runaway Greenhouse

Post-habitable-era surface temperatures on Venus may have exceeded the melting point of rock. For atmospheric water inventories as small as 0.1 Terrestrial Oceans (TO) and a solar flux twice that of present-day Earth, temperatures can exceed 2000 K (Turbet et al., 2019). Diffusion of oxygen into surface magma could oxidise Fe^{2+} to Fe^{3+}, serving as an O_2 sink. The duration of this O_2 sink depends on initial atmospheric water inventory and the combined H escape rate and dissolution of H_2O in the melt. These two processes both deplete atmospheric H_2O vapor, which reduces the surface temperature (the greenhouse effect of O_2 is negligible). We find surface temperature at each timestep, given the incoming solar flux relative to Earth's insolation (S_{eff}) and partial pressure of H_2O in the atmosphere in bars (p_{H_2O}), using a curve fit to existing numerical results (Turbet et al., 2020):

$$log_{10}\left(T_{surf}(x,y,z)\right) = c_1 + c_2x + c_3y + c_4z + c_5x^2 + c_6xy + c_8z^2 + c_9y^3 + c_{10}z^3 \quad (5.2)$$

where:

$$x = \left(log_{10}\left(P_{H_2O}\right) - k_1\right)/k_2 \quad (5.3)$$

$$y = \left(log_{10}\left(g\right) - k_3\right)/k_4 \tag{5.4}$$

$$z = \left(log_{10}\left(S_{eff}\right) - k_5\right)/k_6 \tag{5.5}$$

Coefficient values for c_{1-10} and k_{1-6} are given in Table D.1.

We neglect the greenhouse effect of background CO_2. The parameters that determine Venus' evolution during RGH melting are t_0, h_{hab}, f_{volc} and f_{ext} (Table 5.1), so for computational efficiency we model RGH evolution separately until the surface melt layer freezes then input the results as starting conditions for our baseline model.

To calculate removal of oxygen by oxidation of Fe^{2+} in basaltic melt at the surface, we calculate the temperature-depth profile of a 50 km thick crust at each timestep as the surface temperature evolves using a 1-D finite difference method. In the absence of any constraints on the crustal thickness on early Venus, we choose a maximum crustal thickness of 50 km because this is the thickness of basaltic crust required to remove the oxygen produced by the escape of 1 Earth ocean of water (Lécuyer et al., 2000), which exceeds the maximum habitable-era water inventory considered in our models. Temperature within the crust evolves by diffusion:

$$\rho c_p \frac{\partial T}{\partial t} = \frac{\partial}{\partial z}\left(k\frac{\partial T}{\partial z}\right) - q_L \tag{5.6}$$

where q_L is heat flux due to the latent heat of fusion:

$$q_L = \rho L \frac{\partial z_{melt}}{\partial t} \tag{5.7}$$

where z_{melt} is the effective magma layer thickness produced at each depth in the model. Our upper boundary condition in the model is the surface temperature, which is a function of insolation and water vapor in the atmosphere. We impose a heat flux of 50 mW m^{-2} as our lower boundary condition.

As the thickness of the melt layer and the partial pressure of H_2O in the atmosphere evolve, so does the amount of H_2O stored in the melt layer. As H escapes to space and as the melt layer thickens, less H_2O dissolves in the melt because the partial pressure of H_2O is reduced. However, as the melt layer re-freezes and partial pressure of H_2O drops, H_2O can also be re-exsolved into the atmosphere. The solubility of H_2O in the runaway greenhouse-triggered surface melt ($s_{\mathrm{H_2O},RGH}$) at a given timestep is (Schaefer et al., 2016):

$$s_{\mathrm{H_2O},RGH} = 3.44 \times 10^{-8} P_{\mathrm{H_2O}}^{0.74} \tag{5.8}$$

where $P_{\mathrm{H_2O}}$ is the partial pressure of H_2O in the atmosphere.

$$P_{\mathrm{H_2O}} = \frac{n_{\mathrm{H_2O},atm}}{n_{atm}} p_{atm} \tag{5.9}$$

where $n_{\mathrm{H_2O},atm}$ is number of moles H_2O per column mass in the atmosphere, n_{atm} is the total number of moles in the atmosphere, and p_{atm} is the total atmospheric pressure. We assume that dissolved H_2O is mixed throughout the melt layer, and that the dissolved H_2O content adjusts to match the H_2O solubility. Therefore, the change in atmospheric H_2O at each timestep is given by:

$$\frac{\partial n_{\mathrm{H_2O},atm}}{\partial t} = -\frac{\rho_{melt}}{m_{\mathrm{H_2O}}} \frac{\partial}{\partial t} \left(s_{\mathrm{H_2O},RGH} z_{melt} \right) \tag{5.10}$$

To calculate O_2 losses due to melt oxidation, we compute the melt fraction of a basalt with major element composition given by the Venera 14 surface measurements at a range of temperatures and pressures using alphaMELTS (Smith and Asimow, 2005; Asimow and Ghiorso, 1998; Ghiorso and Sack, 1995). We use these model runs to generate a lookup Table which we use to find melt fraction as a function of depth at each timestep. We assume that all Fe^{2+} in the melt can be completely oxidised, i.e. that O_2 can pervade the entire magma layer, for example by small-scale convection. We track both the cumulative melt

fraction ($f_{m,c}$) and the cumulative oxidized melt fraction ($f_{o,c}$) at each depth in the model. The oxidized melt fraction at each timestep is given by:

$$f_{o,c} = \frac{0.25 f_{m,c} \rho c_{\mathrm{FeO}}}{n_{O2,atm}} \tag{5.11}$$

where $n_{O2,atm}$ is the number of moles of O_2 per column atmosphere. The factor of 0.25 accounts for the stoichiometry of Eqn. 5.28. $f_{o,c}$ at a given depth is not allowed to exceed 1.

5.3.3 Atmospheric Escape

H Escape

The bulk composition of Venus' atmosphere evolves throughout our models based on expressions for escape of H from Venus (Tian, 2015a) which we use to track the accumulation of O_2 in the atmosphere. H is supplied by photodissociation of H_2O. Following previous work, we assume that the photodissociation rate does not limit H escape (Wordsworth and Pierrehumbert, 2013). Escape of a light species is limited by its ability to diffuse through the background atmosphere of heavier species that are not undergoing escape (Tian, 2015b). At high H_2O mixing ratios, H escape approaches the XUV (energy) limit (Eqn. 5.15). At each timestep in our model, we calculate the diffusion limited escape and the energy limited escape of H, and apply the lowest of the two.

The diffusion limit determines the maximum supply of the escaping species to the upper atmosphere. In this diffusion-limited case, the rate of atmospheric escape is:

$$\dot{M}_{H,esc} = X_H \frac{G M_V (m_{atm} - m_H)}{R^2} \frac{b}{k T_{upper}} \tag{5.12}$$

where X_H is the molar mixing ratio of H in the atmosphere, and m_{atm} is the mean molecular weight of the background atmosphere, set by the molar ratio of non-H species after photodissociation has occurred:

$$m_{atm} = X_{\mathrm{CO_2}} m_{\mathrm{CO_2}} + 2X_{\mathrm{O2}} m_{\mathrm{O}} + X_{\mathrm{CO}} m_{\mathrm{CO}} + X_{\mathrm{CH_4}} m_{\mathrm{CH_4}} \tag{5.13}$$

and b is the diffusion coefficient of H in the background atmosphere, which depends on the abundance of other species:(Tian, 2015a; Krissansen-Totton et al., 2021)

$$b_{H,atm} = \frac{b_{\mathrm{H-CO_2}}\, X_{\mathrm{CO_2}} + b_{\mathrm{H-CO}}\, X_{\mathrm{CO}} + b_{\mathrm{H-O}}\, X_{\mathrm{O}}}{X_{\mathrm{CO_2}} + X_{\mathrm{CO}} + X_{\mathrm{O}}} \tag{5.14}$$

$m_{\mathrm{CO_2}}$, m_{CO} $m_{\mathrm{O_2}}$ are the mean molar masses of CO_2 and O_2, and $X_{\mathrm{CO_2}}$, X_{CO} and $X_{\mathrm{O_2}}$ are the mixing ratios of CO_2, CO and O_2. $b_{\mathrm{H-CO_2}} = 8.4 \times 10^{19} T_{upper}^{0.6}$, $b_{\mathrm{H-CO}} = 6.5 \times 10^{19} T_{upper}^{0.7}$, and $b_{\mathrm{H-O}} = 4.8 \times 10^{19} T_{upper}^{0.75}$ are the binary diffusion coefficients of H in CO_2, CO, and O respectively in mol $\mathrm{m^{-1}\ s^{-1}}$ (Zahnle and Kasting, 1986; Marrero and Mason, 1972). Binary diffusion coefficients are derived from empirical fits to measured data and can deviate from the data by several tens of percent. To quantify the impact of this effect on our results, we conducted sensitivity tests with values of b_{atm} 30% lower and 30% higher than our baseline value and found that the total number of successful runs is not sensitive to ±30% variations in binary diffusion coefficient (Appendix Fig. D.4). $T_{upper} = 200$ K is the temperature of the upper atmosphere and is assumed constant in our models. We conducted sensitivity tests with values of T_{upper} at 215 K and 170 K to cover warmer, Earth-like upper atmosphere temperatures (Krissansen-Totton et al., 2021) through to modern Venus' more intensely CO_2-cooled stratosphere (Pätzold et al., 2007) and found that the total number of successful runs is not sensitive to these variations in stratospheric temperature (Appendix Fig. D.5).

We calculate the energy-limited escape rate, given by the mass loss rate of H in a pure H atmosphere, using: (Tian, 2015a; Zahnle and Catling, 2017)

$$\dot{M}_{H,ref} = \frac{\epsilon L_{XUV}(t) R^3}{4a^2 GM} \tag{5.15}$$

$\epsilon = 0.15$ (Tian, 2015a) is an efficiency factor, $L_{XUV}(t)$ is stellar XUV flux at time t, R is planet radius, a is Venus' semimajor axis, G is the gravitational constant, and M is the mass of Venus. To find $L_{XUV}(t)$, we use the following expression for solar XUV evolution, valid for solar age > 0.1 Gyr: (Zahnle and Catling, 2017; Ribas et al., 2005)

$$L_{XUV} = L_x(t/t_x)^{-\beta} \tag{5.16}$$

where $t_x = 0.1$ Gyr, $\beta = 1.24$, and $L_x = 1.6 \times 10^{23}$ J s^{-1} is an upper bound on the Sun's early XUV flux.

For present day Venus, the diffusion limit gives an H loss rate of order 10^{25} s^{-1}, depending on the mixing ratios of H and O in the resulting atmosphere, which is comparable to calculated modern H escape rates (Lammer et al., 2006). We set $T_{upper} = 200$ K, consistent with a CO_2 dominated atmosphere (Kulikov et al., 2006; Johnstone, C. P. et al., 2018).

If H escape to space is sufficiently rapid, the H can drag heavier species (such as O) along with it (Tian, 2015b). This process is active during the first few million years of our models with habitable eras beginning at 4.0 Ga, but is negligible relative to O loss through non-thermal escape and oxidation of lava flows and magma. To determine whether this process is active at a given timestep in our model, we calculate the critical mass (m_c) of the heaviest molecule escaping H can drag along with it in a background atmosphere of mass m_{atm} (Tian, 2015b):

$$m_c = \frac{X_H + q^2 X_{atm}}{X_H + q X_{atm}} m_H + \frac{kT\dot{M}_{H,ref}}{m_H bg\,(X_H + q X_{atm})} \tag{5.17}$$

where $q = m_{atm}/m_H$. In our model runs, we only see $m_c \geq m_O$ at the very beginning of models with > 700 m GEL H_2O with hypothetical habitable eras ending at 4 Ga and $f_{volc} \geq 0.9$, i.e. H escape is not limited by diffusion through the background CO_2 atmosphere. Under these conditions there is more than an order of magnitude more O in the background

atmosphere than CO_2, and we approximate the atmosphere as a mixture of H and O only to find the resulting H and O escape rates (Tian, 2015b):

$$\dot{M}_{O,esc} = \frac{\eta q}{1+\eta q}\dot{M}_{H,ref} \tag{5.18}$$

$$\dot{M}_{H,esc} = \frac{1}{1+\eta q}\dot{M}_{H,ref} \tag{5.19}$$

where:

$$\eta = \frac{Y-1}{YX_H/X_O + q} \tag{5.20}$$

$$Y = \frac{kT\dot{M}_{H,ref}}{(q-1)bgX_H m_H^2} \tag{5.21}$$

Escape of heavy species

For most of Venus' history, O loss to space has been via non-thermal escape processes. These depend on the XUV flux from the Sun and the properties of the solar wind (Kulikov et al., 2006; Gillmann et al., 2020). We use existing studies' (Gillmann et al., 2020) calculations of maximum loss of O_2 from Venus' atmosphere as a function of time. As O_2 is a minor constituent of the atmosphere relative to CO_2, we assume that O_2 loss from the upper atmosphere is limited by diffusion through the background atmosphere similar to Eqn. 5.13:

$$\begin{aligned} m_{atm} =& X_{\mathrm{CO_2}} m_{\mathrm{CO_2}} + X_{\mathrm{H_2O}} m_{\mathrm{H_2O}} + X_{\mathrm{CO}} m_{\mathrm{CO}} + X_{\mathrm{CH_4}} m_{\mathrm{CH_4}} \\ &+ X_{\mathrm{CO}} m_{\mathrm{CO}} + X_{\mathrm{H_2}} m_{\mathrm{H_2}} \end{aligned} \tag{5.22}$$

In this case, we apply a binary diffusion coefficient (b) relevant to the diffusion of O_2 through a mixture of CO_2 and CO (following the same approach as for diffusion of H through the upper atmosphere, Eqn. 5.14) (Marrero and Mason, 1972) as these are the dominant

constituent of the atmosphere in the majority of our models. As for H escape, we find the non-thermal escape rate and calculate the diffusion limit for O, and apply the smallest of the two to O escape in our models. Following other models of the long term evolution of Venus' atmosphere, we neglect nonthermal losses of CO_2 (Kulikov et al., 2006; Gillmann et al., 2016).

5.3.4 Degassing

For each model run, we set a melt H_2O and CO_2 concentration (c_{H_2O} and c_{CO_2} respectively, Table 5.1), based on the range observed in terrestrial Mid Ocean Ridge Basalts (MORB) (Saal et al., 2002; Danyushevsky, 2001; Soule et al., 2012; Helo et al., 2011), which have similar bulk compositions to Venus basalts (Kargel et al., 1993). We also set an oxidation state of the erupting melt between the fayalite-magnetite-quartz buffer ($\log fO_2$ =FMQ$\pm$0) and $\log fO_2$ =FMQ$-$4. We use VolcGasses (Wogan et al., 2020) to find H_2O and CO_2 solubility in basaltic melt (s_{H_2O} and s_{CO_2} respectively) and calculate the speciation of the exsolved H and C bearing gasses as a function of melt temperature and surface pressure. This degassing model assumes that bubbles and surrounding melt remain in thermodynamic equilibrium (Wogan et al., 2020). We assume that melts reaching the surface degas at Venus' time-varying surface pressure, and that all intrusive melts are emplaced at a shallow enough depth that all melt CO_2 can degas as CO_2, CO, or CH_4.

To calculate the degassing rate of H_2O per unit Venus surface area, we use:

$$\dot{M}_{H_2O,degas} = \dot{z}_{erupt}\rho_{melt}r_{H_2O}\left(c_{H_2O} - s_{H_2O}\right) \tag{5.23}$$

where $\dot{z}_{erupt}$ is the eruption rate (in m s^{-1}), ρ_{melt} is the density of the melt, and $r_{H_2O} = n_{H_2O}/(n_{H_2O}+n_{H_2})$ is the molar fraction of H_2O in the melt exsolved as H_2O. When $s_{H_2O} \geq c_{H_2O}$, $\dot{M}_{H_2O,degas} = 0$.

CO_2 solubilities in basaltic melt are much lower than our prescribed melt CO_2 concentrations at all pressures, so to calculate the degassing rate of CO_2 per unit Venus surface area, we use:

$$\dot{M}_{CO_2,degas} = \dot{z}_{erupt}\rho_{melt}r_{\mathrm{CO_2}}c_{\mathrm{CO_2}} \tag{5.24}$$

where $r_{\mathrm{CO_2}} = n_{\mathrm{CO_2}}/(n_{\mathrm{CO}} + n_{\mathrm{CH_4}}) + n_{\mathrm{CO_2}}$ is the molar fraction of CO_2 in the melt exsolved as CO_2. We also calculate H_2, CO and CH_4 degassing into the atmosphere at each time step using the same approach but substituting in r_{H2}, r_{CO}, and r_{CH4} as appropriate. After degassing, these species are oxidized by atmospheric O_2 (if present) to form H_2O and CO_2. If there are fewer moles of atmospheric O_2 in the atmosphere than would be needed to fully oxidize CO and CH_4, we assume that all the CO and CH_4 remaining after the O_2 is consumed stay in the atmosphere. This approach maximizes the likelihood of a model run matching both the modern O_2 and CO constraints on Venus' atmosphere because it both maximizes O_2 loss through this sink as well as maximizing oxidation of CO and CH_4 to CO_2.

The column mass of CO_2 in the atmosphere at the end of the habitable era is varied between 0% and 90% of Venus' present atmospheric CO_2. This accounts for any CO_2 either present in the atmosphere during the habitable era, or added at the end of the habitable era through thermal decomposition of habitable era carbonates. We do not consider the 100% case because without volcanism the sole O_2 sink on Venus is nonthermal escape, which has been quantified in existing studies (Gillmann et al., 2020). The remaining CO_2 is volcanically outgassed after the habitable era. Based on initial conditions, model start time (end of the habitable era) and prescribed $\mathrm{c_{CO_2}}$ We start each run by calculating z_{tot} i.e. the total thickness of a global layer of lava needed to degas sufficient C species for Venus' modern atmosphere to have 90 bar CO_2:

$$z_{tot} = \frac{f_{volc}}{c_{\mathrm{CO_2}}\rho_{melt}}M_{CO_2,f} \tag{5.25}$$

The evolution of Venus' eruption rate is unknown, but the present day eruption rate has been estimated at $\dot{z}_V$ =0.1-0.2 km^3 yr^{-1} (Basilevsky et al., 1997), and the total CO_2 concentration dependent erupted thickness (z_{tot}) is set by the need to outgas enough C-bearing atmospheric species for Venus' modern atmosphere to have 90 bar of CO_2 minus any CO_2 present in the atmosphere at the model start time. Although models of Venus' crustal production based on different possible tectonic regimes exist (Armann and Tackley, 2012; Weller and Kiefer, 2020), the exact crustal production history is not known. The crater retention age of Venus' surface is young, suggesting that the planet has been resurfaced geologically recently (Phillips et al., 1992; Bottke et al., 2016). However, the mechanism for resurfacing is debated. One hypothesis is a catastrophic resurfacing event 0.3 to 1 Gyr ago (Strom et al., 1994), for example by episodic subduction with complete renewal of Venus' lithosphere every few hundred million years (Turcotte, 1993; Armann and Tackley, 2012), but an alternative is equilibrium resurfacing by continuous volcanism (Bjonnes et al., 2012), which is also supported by evidence for ongoing volcanism (Smrekar et al., 2010). In our model, we use a highly simplified crustal production history for Venus that assumes continuous volcanism decreasing exponentially over time throughout Venus' history. This is consistent with exponentially decreasing volcanism is also similar to the pattern of melt production for full parameterized convection models of Venus (Krissansen-Totton et al., 2021). The total erupted volume is set by average melt CO_2 concentration, and the proportion of CO_2 in Venus' atmosphere that is sourced from post-habitable era volcanism. We parameterize eruption rate as an exponential (Fig. 5.2):

$$\dot{z}_{erupt} = a \exp(-bt) \tag{5.26}$$

where t is time since the end of the habitable period, b is the e-folding timescale of volcanism in Gyr, and a is a constant:

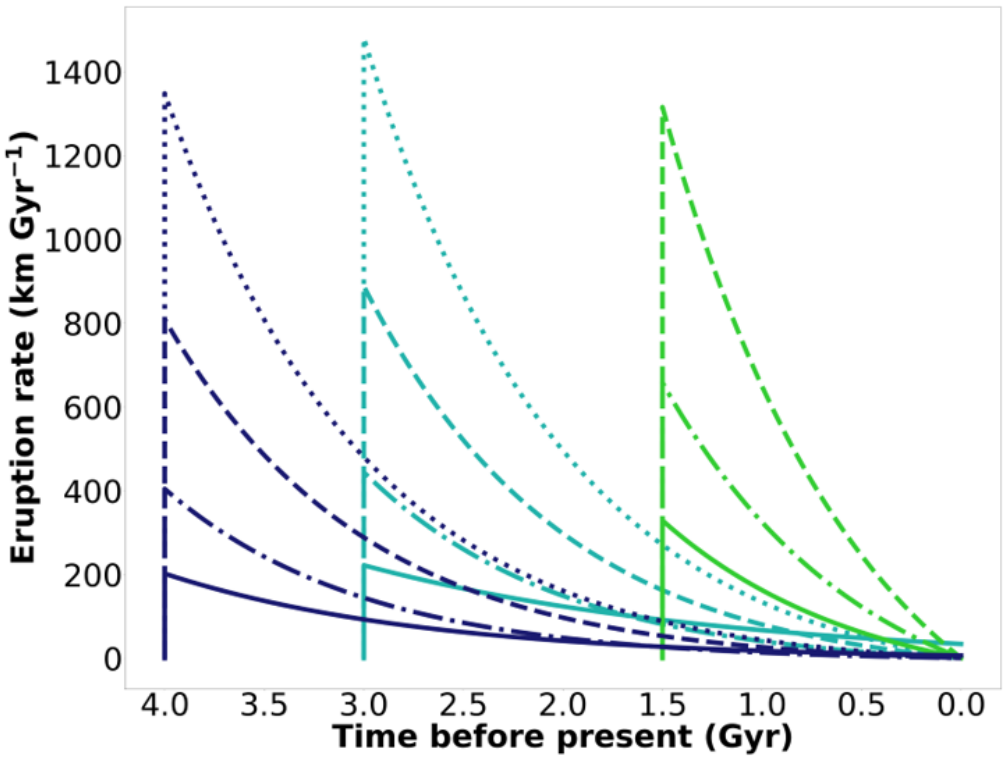

Figure 5.2: Magmatism rates (including both intrusive and extrusive volcanism) as a function of time in our model for end habitable era times $t_0 = 4.0$, 3.0, and 1.5 Ga (dark blue, blue, and green) and average melt $CO_2 = 300$, 500, 1000, and 2000 ppm (solid, dashed, dashed-dotted, dotted) with $f_{volc} = 1.0$. There is no eruption rate line for $t_0 = 1.5$ Ga and $CO_2 = 300$ ppm because this would lead to a total erupted volume requiring processing of more than 1.2× Venus' mantle volume in 1.5 Ga in order to degas the full 90 bar of CO_2 in Venus' modern atmosphere. The eruption rates shown in these curves will be lower for smaller values of f_{volc} as less of the total CO_2 in Venus' modern atmosphere is derived from volcanic degassing in these cases.

$$a = \frac{(\dot{z}_V / f_{ext}) + b\ z_{tot}}{1 - e^{-b\ t_{er}}} \tag{5.27}$$

where $\dot{z}_V$ is the present day crustal production rate, f_{ext} is the extrusive volcanism fraction, and t_{er} is either the end of the habitable era in model time (i.e. $4.5 - t_{start}$), or the model time at which the surface temperature drops below the basalt solidus in runs that begin with an RGH. We assume a modern crustal production rate of 0.1 km^3 yr^{-1} (Basilevsky et al., 1997; Strom et al., 1994; Ivanov and Head, 2013). We vary f_{ext} from

0.1 to 1 because some of Venus' volcanism must be extrusive to account for the young crater retention age of Venus' surface, and extending to $f_{ext} = 1$ captures both Earth-like extrusive:intrusive volcanism ratios at $f_{ext} = 0.3$ and 0.5 (White et al., 2006), and extreme heat-pipe tectonics at $f_{ext} = 1$ (Moore et al., 2017). All times are in Gyr. b and $\dot{z}_V$ are the most uncertain parameters in this equation as Venus' crustal production history and present extrusive volcanism fraction are poorly constrained.

5.3.5 Oxidation of basalt

O_2 left behind by H escape from the atmosphere may be removed by oxidation of basalt (Heard and Kite, 2020):

$$2FeO + 0.5O_2 \rightarrow Fe_2O_3 \tag{5.28}$$

The FeO concentrations at the Venera 13 and 14 landing sites are 9.3±2.2 wt% and 8.8±1.8 wt% respectively (Surkov, Yu. A. and Barsukov, V. L. and Moskalyeva, L. P. and Kharyukova, V. P. and Kemurdzhian, A. L., 1984), with bulk compositions at the Venera 14 and Vega 2 landing sites similar to terrestrial Mid Ocean Ridge Basalts (MORB) (Kargel et al., 1993). The typical FeO concentration in MOR basalts on Earth is between 7 and 12 wt% (Langmuir et al., 2013). We assume an average of 10 wt%, 0.1 kg of FeO are emplaced on Venus' surface for each kg of erupted lava. We follow (Gillmann et al., 2020) and assume that 1% of lava erupted on Venus is oxidized (Appendix 5.5.1), corresponding to the top 1 cm of a 1 m thick flow. We also assume that lava cannot continue to be oxidised past the timestep when it is produced because it will be buried by subsequent lava flows and diffusion in solid basalt is too slow for buried basalt to remain in contact with atmospheric O_2. The mass of O_2 removed from the atmosphere in a given timestep ($\dot{M}_{O_2,ox}$) is:

$$\dot{M}_{O2,ox} = M_{O2,atm} - 0.01 m_{\mathrm{O2}} \frac{0.25 \rho c_{\mathrm{FeO}} f_{ex} z_{erupt}(t)}{m_{\mathrm{FeO}}} \tag{5.29}$$

where m_{O2} and m_{FeO} are the molecular masses of O_2 and FeO, and c_{FeO} is the typical concentration of FeO in basalt in wt%. The factor of 0.25 accounts for the stoichiometry of Eqn. 5.28. $M_{O2,atm}$ is not allowed to fall below 0.

Volcanism on Venus may not always have been dominated by lava flows. Basaltic eruptions on Earth can be explosive, producing large volumes of ash and scoria (Houghton and Gonnermann, 2008). Although high atmospheric pressure disfavors explosive volcanism on Venus today, dissolved magmatic volatiles drive explosive volcanism at pressures greater than Venus' atmospheric pressure in subaqueous envrionments, such as MORs (Helo et al., 2011; Schipper et al., 2010). Several authors report observations of evidence for explosive volcanism on Venus, invoking volatile concentrations of order 1-3 wt% CO_2, SO_2 and H_2O (Ghail and Wilson, 2015; Campbell et al., 2017). However, CO_2 as the primary magmatic volatile phase is unlikely to drive explosive volcanism on present day Venus because concentrations above 6.5 wt% would be required (Airey et al., 2015).

The conditions required for explosive volcanism are sensitive not only to atmospheric pressure but also to melt ascent rates, magma temperatures, melt viscosity, and vent geometry (Airey et al., 2015; Glaze et al., 2011). We choose to implement the simplest possible threshold for the effusive-explosive transition, allowing explosive volcanism to occur when the volume fraction of gas (F_{gas}) exceeds ~75% (Sparks, 1978; Garvin et al., 1982). We find the volume of gas per m^3 melt delivered to the surface (V_{gas}) using the ideal gas law:

$$V_{gas} = \frac{n_{degas} R T_{melt}}{P_{atm}} \tag{5.30}$$

where n_{degas} is the number of moles of degassed CO_2 and H_2O. The corresponding volume fraction of gas is:

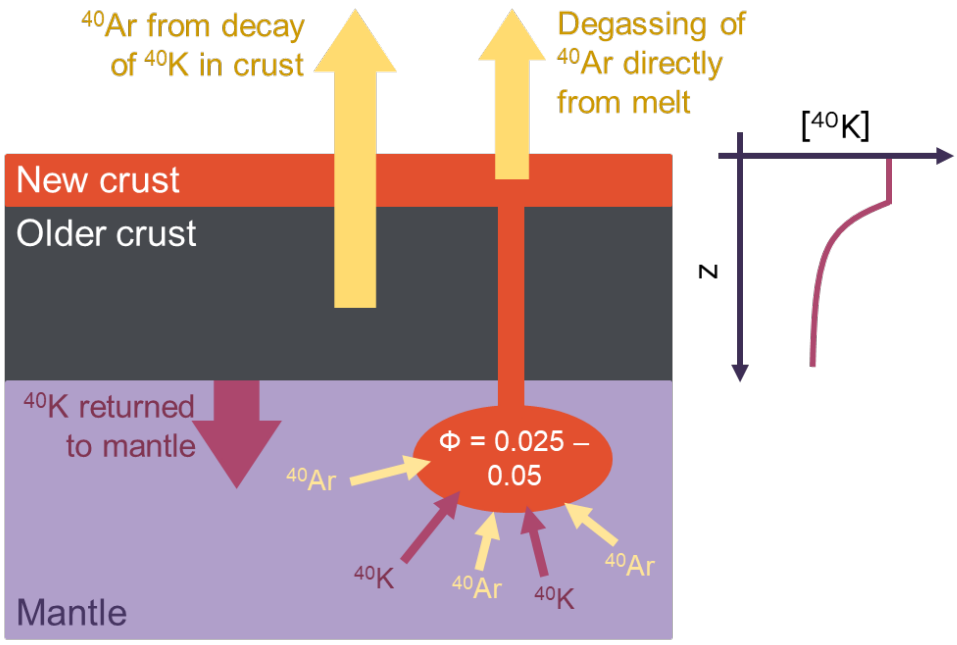

Figure 5.3: Schematic illustration of our ^{40}Ar degassing model based on: (Kaula, 1999; O'Rourke and Korenaga, 2015).

$$F_{gas} = \frac{V_{gas}}{V_{gas} + 1} \tag{5.31}$$

For $F_{gas} \geq 0.75$, the mass of O_2 removed from the atmosphere in a given timestep ($\dot{M}_{O_2,ox}$) is:

$$\dot{M}_{O2,ox} = M_{O2,atm} - m_{\mathrm{O2}} \frac{0.25 \rho c_{\mathrm{FeO}} f_{ex} z_{erupt}(t)}{m_{\mathrm{FeO}}} \tag{5.32}$$

5.4 Argon Degassing Model

Following previous work (Kaula, 1999; O'Rourke and Korenaga, 2015), we model the evolution of Venus' mantle, crust, and atmosphere ^{40}K and ^{40}Ar inventories forwards in time starting from the end of a hypothetical habitable era. Our models begin with mantle ^{40}K concentrations set by the decay of ^{40}K from Venus formation to the end of the habitable era, and with some fraction of the resulting radiogenic ^{40}Ar (f_{pre} ranging from 0 to 1) in

Table 5.2: Parameter values used in ^{40}Ar degassing model. [a]Kaula 1999, [b]O'Rourke and Korenaga 2015, [c]Arevalo Jr et al. 2009

Symbol	Description	Values	Units
t_0	End of habitable era	4, 3, 1.5	Ga
z_{crust}	Crust thickness	5, 10, 20, 30, 50	km
ϕ	Mantle melt fraction for crust production	0.025, 0.05	
c_{CO_2}	Melt CO_2 concentration	300, 500, 1000, 2000	ppm
f_{pre}	Fraction of present day atmospheric CO_2 degassed before end of habitable era	0, 0.1, 0.25, 0.5, 1	
f_{volc}	Fraction of present day atmospheric CO_2 degassed since end of habitable era	0.1, 0.5, 0.9, 1	
f_{ext}	Extrusive volcanism fraction	0.1, 0.3, 0.5, 1	
$c_{U,M}$	Primordial mantle U concentration	13, 17, 21[a,b]	ppb
$r_{K/U}$	K/U ratio	7200[a], 13800[c]	

the atmosphere.

^{40}Ar degassing occurs as a result of crustal production. New crust is produced by melting of the mantle at the crustal production rate set by the parameters t_{end}, f_{volc}, f_{ext}, and c_{CO_2} in our Oxygen Loss Model. We also consider an additional 4 parameters: crustal thickness, average melt fraction, and Venus' primordial mantle U concentration and K/U ratio (Table 5.2) (Kaula, 1999; O'Rourke and Korenaga, 2015). During partial melting, ^{40}K and ^{40}Ar preferentially partition into the melt, enriching the melt in these species. We assume that ^{40}Ar partitioned into the melt is released instantaneously into the atmosphere (Kaula, 1999) and the ^{40}K enters the crust. The ^{40}K in the newly erupted crust decays over time to produce more ^{40}Ar that we assume diffuses rapidly to the atmosphere (Kaula, 1999). To calculate this ^{40}Ar release at each timestep, we find the ^{40}K decay integrated across the entire depth of the crust, which we assume has a fixed thickness. We track the ^{40}K concentration throughout the crust at depth intervals of 1 m and consider cases both with and without recycling of ^{40}K back into the mantle.

The initial concentration of ^{40}K in Venus' mantle is given by (Kaula, 1999; O'Rourke and Korenaga, 2015):

$$[^{40}\mathrm{K}(0)] = r_{(^{40}\mathrm{K/K})} r_{(\mathrm{K/U})} c_{(\mathrm{U},M)} \exp\left(\lambda_{tot} t\right) \tag{5.33}$$

where $r_{(\mathrm{K/U})}$ is the ratio of K to U for Venus' crust as measured by spacecraft (Kaula, 1999), $r_{(^{40}\mathrm{K/K})} = 1.165 \times 10^{-4}$ is the present ^{40}K/K ratio (Kaula, 1999), $c_{(\mathrm{U},M)}$ is the primordial mantle U concentration based on values calculated for the Earth (Table 5.2) (O'Rourke and Korenaga, 2015), where t is present time after Venus' formation (4.5 Gyr), and λ_{tot} is the decay constant for ^{40}K:

$$\lambda_{tot} = \lambda_{\mathrm{Ar}} + \lambda_{\mathrm{Ca}} \tag{5.34}$$

Where $\lambda_{Ar} = 0.0581$ Gyr^{-1} and $\lambda_{Ca} = 0.4962$ Gyr^{-1} are the decay constants for decay of ^{40}K to ^{40}Ar and ^{40}Ca respectively (Kaula, 1999). Our models begin at the end of a hypothetical habitable era. We calculate the starting mantle ^{40}K concentration:

$$\left[^{40}\mathrm{K}(t_0)\right] = \left[^{40}\mathrm{K}(0)\right] \exp\left(-\lambda_{tot}(4.5 - t_0)\right) \tag{5.35}$$

starting mantle ^{40}Ar concentration:

$$\left[^{40}\mathrm{Ar}_M(t_0)\right] = (1 - f_{pre}) \left[^{40}\mathrm{K}(0)\right] \left(1 - \exp\left(-\lambda_{tot}(4.5 - t_0)\right)\right) \tag{5.36}$$

and starting atmospheric ^{40}Ar abundance:

$$^{40}\mathrm{Ar}(t_0)_a = f_{pre} V_M \rho_M \left[^{40}\mathrm{K}(0)\right] \left(1 - \exp\left(-\lambda_{tot}(4.5 - t_0)\right)\right) \tag{5.37}$$

where f_{pre} is the fraction of radiogenic ^{40}Ar degassed prior to the end of the habitable era, $\rho_M = 3550$ kg m^{-3} is the density of the mantle (Stevenson et al., 1983), and V_M is the mantle volume, taking Venus' core radius to be 3110 km (Spohn, 1991).

Next, we evolve the mantle and atmosphere ^{40}K and ^{40}Ar inventories forwards in time

(Fig. 5.7) until the present day based on the parameters in each of our O_2 loss models, calculating the crustal production rate using Equations 5.24-5.27. We assume that crustal thickness does not evolve over time, and instead consider a range of fixed thicknesses.

The concentration of ^{40}K in Venus' mantle at each new timestep ($\left[^{40}\mathrm{K}\right]_{M,i+1}$) is given by:

$$\begin{aligned}\left[^{40}\mathrm{K}\right]_{M,i+1} = &\left[^{40}\mathrm{K}\right]_{M,i} - \left[^{40}\mathrm{K}\right]_{M,i} \exp(-\Delta t \lambda_{\mathrm{K}}) \\ &- \frac{V_{new,i}\,\rho_c}{V_M \rho_M} \left[^{40}\mathrm{K}\right]_{m,i} \\ &+ \frac{V_{rec,i}\,\rho_c}{V_M \rho_M} \int_{D_c+z_{rec}}^{D_c} \left[^{40}\mathrm{K}(z)\right]_{c,i} dz\end{aligned} \tag{5.38}$$

where $\rho_c = 2800$ kg m^{-3} is the density of the crust, and D_c is the crustal thickness. $V_{new,i} = z_{new} A_{Venus}$ is the volume of new crust produced in one timestep.

V_{rec} is the volume of crust recycled back into the mantle at a given timestep, which is given by the difference between the total crustal thickness at timestep i and the fixed maximum crustal thickness, D_c. We track the concentration of ^{40}K throughout the crust with depth in 1 m intervals to calculate the amount of ^{40}K recycled back into Venus' mantle over time. We also consider a case in which recycled crust is not remixed into the mantle, and instead sinks into a separate mantle reservoir, in which case we set the final term of Equation 5.38 to 0. This depletes the melting mantle of ^{40}K over time, and permits a wider range of crustal production histories for Venus that can still fall within or below the measured range for Venus' atmospheric ^{40}Ar abundance.

New crust is produced by partial melting of the mantle. This sets the initial ^{40}K concentration of the crust. We consider melt fractions of $\Phi = 0.025$ and 0.05 (Table 5.2) (O'Rourke and Korenaga, 2015). During partial melting, ^{40}K and ^{40}Ar preferentially partition into the melt, enriching the melt in these species. The concentration of ^{40}K in new crust (which is also the concentration of ^{40}K in mantle melts) formed through fractional melting of the

mantle is:

$$[\mathrm{K}]_{c,i} = [\mathrm{K}]_{m,i} = [\mathrm{K}]_{M,i} \frac{1}{\phi} \left[1 - (1-\phi)^{1/D_{\mathrm{K}}}\right] \tag{5.39}$$

where D_{K} is the partition coefficient of K in the melt, which is very small (Shaw, 1970), so we make the approximation $(1-\phi)^{1/D} \approx 0$ (Kaula, 1999; O'Rourke and Korenaga, 2015). In our model, we assume that ^{40}Ar in the melt is released instantaneously to the atmosphere (O'Rourke and Korenaga, 2015). The mass of ^{40}Ar released to the atmosphere at each timestep by partial melting and crustal production is:

$$^{40}\mathrm{Ar}_{M\rightarrow a,i} = V_{new,i}\rho_c \left[\mathrm{Ar}\right]_M \frac{1}{\phi} \left[1 - (1-\phi)^{1/D_{\mathrm{Ar}}}\right] \tag{5.40}$$

where D_{Ar} is the partition coefficient of Ar in the melt, approximated in the same way as for ^{40}K (Kaula, 1999; O'Rourke and Korenaga, 2015).The concentration of ^{40}K in the crust at each timestep is given by:

$$\left[^{40}\mathrm{K}(z)\right]_{c,i} = \left[^{40}\mathrm{K}\right]_{c,i} - \left[^{40}\mathrm{K}\right]_{c,i} \exp(-\Delta t \lambda_{\mathrm{K}}) \tag{5.41}$$

The corresponding release of ^{40}Ar to the atmosphere by ^{40}K decay in the crust and rapid diffusion of ^{40}Ar to the surface (O'Rourke and Korenaga, 2015) is given by:

$$^{40}\mathrm{Ar}_{c\rightarrow a,i} = \rho_c A_{Venus} \frac{\lambda_{Ar}}{\lambda_K} \exp(-\Delta t \lambda_K) \int_{D_c}^{0} \left[^{40}\mathrm{K}(z)\right]_{c,i+1} dz \tag{5.42}$$

Therefore, the total ^{40}Ar in the atmosphere at each timestep is:

$$^{40}\mathrm{Ar}_{a,i+1} = ^{40}\mathrm{Ar}_{a,i} + ^{40}\mathrm{Ar}_{c\rightarrow a} + ^{40}\mathrm{Ar}_{M\rightarrow a,i} \tag{5.43}$$

Example ^{40}Ar degassing runs for a range of crustal production histories are shown in Fig 5.7. Model runs with final atmospheric ^{40}Ar inventories that match Venus' modern

atmospheric composition are marked as successful. We then find the proportion of successful Ar degassing runs overall and for each unique combination of t_{end}, f_{volc}, f_{ext}, and c_{CO_2}. We multiply these by our Oxygen Loss Model success rates to find the overall proportion of runs that can successfully match Venus' modern atmospheric composition (Fig. 5.9).

5.5 Results

5.5.1 Oxygen Loss Model

Our baseline O_2 loss model considers three oxygen sinks (Fig. 5.1:

1. Escape to space
2. Oxidation of reduced atmospheric species (CO, CH_4, and H_2) from degassing
3. Oxidation of basaltic lava flows and ash

Results for our baseline model show that these combined oxygen sinks are able to remove enough O_2 to make end-habitable-era water inventories of up to 300 m GEL ($\lesssim$10% of an Earth Ocean) consistent with Venus' present atmosphere. This volume of water would be readily supplied during Venus' formation, with estimates for Venus' initial water inventory ranging from around 0.5 to 5 Earth Oceans (Chassefière, 1996; Gillmann et al., 2009). The upper limit results from larger end-habitable-era water inventories contributing more O_2 to Venus' atmosphere than can be accommodated by the combined oxygen sinks in our model. The most important sinks are oxidation of reduced atmospheric species and oxidation of lava/ash. The relative contributions of these sinks to O_2 removal depends on the oxygen fugacity of erupting melts on Venus and the melt CO_2 and H_2O concentrations, which determine the speciation of degassed volatiles. For higher oxygen fugacities (e.g. $\log fO_2$=FMQ$\pm$0, where FMQ is the fayalite-magnetite-quartz buffer), oxidation of

lava/ash is the largest oxygen sink because less CO and CH_4 are degassed. As melt oxygen fugacity decreases and CO/CH_4 degassing increases, oxidation of CO/CH_4 becomes the primary O_2 sink. However, it is difficult for oxidation of CO/CH_4 to exactly balance O_2 introduced by end-habitable-era water inventories. Ongoing H_2O degassing is required in these runs to provide a continuous supply of O_2 and prevent Venus' atmosphere from becoming too CO-rich to satisfy modern CO constraints.

An exception to this 300 m GEL upper limit is if average melts on Venus have very reduced oxygen fugacities comparable to the most reduced Mars meteorite ($\log fO_2$=FMQ−4, Fig. 5.6). Models of mantle oxygen fugacities resulting from a magma ocean suggest that Earth and Venus-sized worlds will have more oxidized upper mantles (Deng et al., 2020), and Earth's upper mantle has an oxygen fugacity around $\log fO_2$=FMQ±0 (Cottrell and Kelley, 2011). However, mantle oxygen fugacities as low as $\log fO_2$=FMQ−4 have previously been proposed (Krissansen-Totton et al., 2021). For the $\log fO_2$=FMQ−4, end-habitable-era water inventories as large as 1000 m GEL (∼33% of an Earth ocean) remain consistent with Venus' modern atmosphere in our models, provided that melt H_2O concentration is >0.2 wt%. Model runs with 10 m GEL end-habitable-era water–an ocean three hundred times shallower than Earth's–can evolve to be at or below Venus' present day atmospheric O_2 levels for 5% of 10 m GEL runs overall; (Figs 5.5a, 5.8a, & 5.9). A 10 m GEL end-habitable era water inventory is the only case for which low modern atmospheric O_2 concentrations can be matched by habitable eras ending as late as 1.5 Ga.

When $\log fO_2 \geq$FMQ−3, 300 m GEL end-habitable-era water inventories are only compatible with Venus' modern atmosphere in runs where the habitable era ends early, at or before 3.0 Ga (Figs. 5.8 & 5.4). In runs with habitable eras that end early in Venus' history, the Sun's X-ray/extreme ultra-violet (XUV) flux is high, and can drive rapid H escape causing rapid build up of O_2 in the atmosphere. This is advantageous because volcanism rate decreases exponentially with time in our models, so oxidizable basalt–which can be a

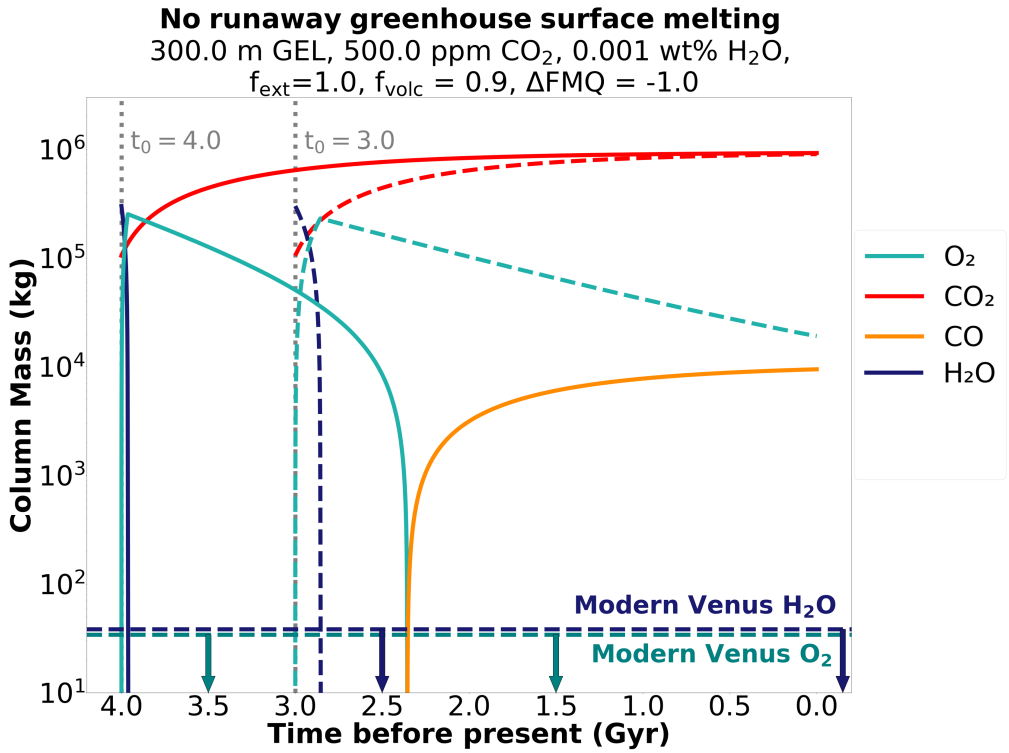

Figure 5.4: Timing of the end of a hypothetical habitable era is an important parameter for determining whether the habitable era can be reconciled with modern Venus' low atmospheric O_2. Time evolution of column masses of H_2O, H_2, O_2, CO_2, CO, and CH_4 for two post habitable era evolutions, each with a 300 m GEL water inventory, average melt H_2O 0.001 wt%, average melt CO_2 500 ppm, extrusive volcanism fraction f_{ext} =1.0, fraction of Venus' modern CO_2 volcanically degassed since the end of a hypothetical habitable era f_{volc} = 1.0, and melt oxygen fugacity log fO_2 = FMQ-1 in our baseline model (no runaway greenhouse surface melting). The solid line shows that a short-lived habitable era ending at 4.0 Ga can be reconciled with Venus' modern atmospheric O_2 (solid lines), whereas a habitable era ending at 3.0 Ga cannot (dashed line).

major oxygen sink –is most available soon after the end of the habitable era. An early end to the habitable era allows basalt oxidation to sequester the most O_2, as O_2 is available to be removed at the time of eruption.

When we add RGH surface melting to our baseline O_2 loss model, end habitable era water inventories $\geq$300 m GEL permit surface temperatures hot enough to melt basalt, enabling rapid diffusion of oxygen into a basaltic surface magma layer. This RGH is caused by vaporization of the end habitable era water inventory, and is distinct from a steam atmo-

sphere formed during accretion (Zahnle et al., 2007). The surface magma layer provides an additional O_2 sink as long as the H_2O greenhouse effect melts surface basalt (Turbet et al., 2019). However, adding this additional O sink only increases the total number of successful O_2 loss model runs from 2.2% to 2.6% (Figs 5.5b., 5.8b. & 5.9).

This is because:

1. In runs with large water inventories but little initial atmospheric CO_2, the surface magma layer is short-lived because H_2O loss rapidly reduces the greenhouse effect. This leads to a short-lived and thin surface magma layer that consumes only remove a small amount of O_2.

2. In runs with large water inventories and a large fraction of Venus's modern atmospheric CO_2 degassed prior to the end of the habitable era, H loss is slow because it must diffuse through a thick background atmosphere. This extends the lifetime of the oxidizable magma layer, but delays accumulation of atmospheric CO_2 because we do not include volcanic outgassing while the surface is molten. For habitable eras ending at 4.0 and 3.0 Ga, the surface magma layer can persist so long that it is no longer possible for all of Venus' present day CO_2 to volcanically degas after the surface of the magma layer freezes.

3. For habitable eras ending at 1.5 Ga and water inventories of 1000 m GEL, the increase in bolometric insolation and decrease in H loss rates due to the Sun's reduced XUV output (Ribas et al., 2005) enable a H_2O greenhouse with a surface magma layer to last until the present, which is inconsistent with data.

4. In runs with reducing melts, removal of atmospheric O_2 leftover from H escape of the end habitable era water inventory can remove so much O_2 from the atmosphere that there is no longer enough oxidizing power available to oxidize degassed CO and CH_4 fully to CO_2, leading to final atmospheric CO concentrations too high to match Venus'

modern atmosphere.

5.5.2 Argon Degassing Model

Oxidation of the degassed atmospheric species CO and CH_4 and oxidation of lava flows are the most important oxygen sinks in our baseline model. During degassing and volcanism, minor atmospheric constituents such as ^{40}Ar are released into the atmosphere alongside major C and H species and can be used to place constraints on the total crustal production on Venus (Kaula, 1999; O'Rourke and Korenaga, 2015). We model the ^{40}Ar degassing corresponding to the crustal production histories used in our O_2 loss models.

Overall, $\lesssim$0.4% of runs are consistent with Venus' present day atmospheric O_2 and ^{40}Ar for the parameter ranges investigated in this study. To match modern Venus' low atmospheric ^{40}Ar, our ^{40}Ar degassing model requires parameters that minimize the total production of new crust (Appendix Figs. D.1 & 5.7). High melt fractions reduce the concentration of ^{40}K and ^{40}Ar in mantle-derived melts, reducing the amount of ^{40}Ar degassed directly to the atmosphere during volcanism, and the amount of ^{40}K available in the crust to decay and also supply ^{40}Ar to the atmosphere. Thin crust promotes rapid recycling of ^{40}K enriched crust back into the mantle, reducing the amount of time available for crustal ^{40}K to decay and release ^{40}Ar to the atmosphere through the crust for a given crustal production rate. Low values of f_{volc}–which correspond most of Venus' modern CO_2 degassing before the end of a hypothetical habitable era–reduce the total amount of CO_2 that needs to be degassed during the model runs, which in turn reduces the necessary crustal production and the total amount of mantle melting and degassing required to achieve Venus' modern CO_2 atmosphere. This is advantageous for satisfying the the ^{40}Ar constraint because earlier degassing leaves less time for ^{40}K to decay, so the atmosphere by the end of the habitable era can have abundant CO_2 but still be ^{40}Ar poor. However, reducing the total crustal production (advantageous for matching the ^{40}Ar constraint) reduces the size of the basalt lava flow oxidation and degassed

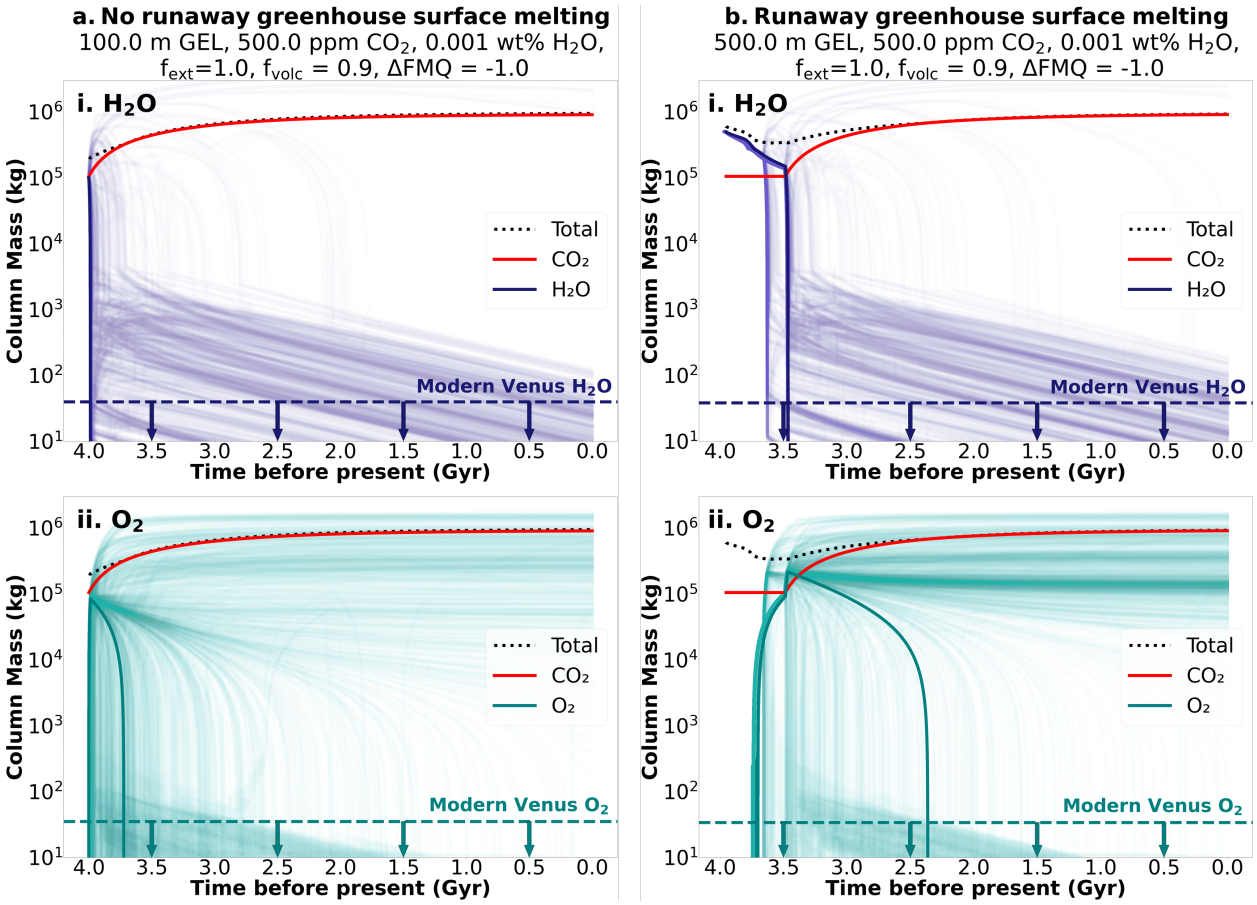

Figure 5.5: Example model output: Time evolution of column masses of i. H_2O (purple) and ii. O_2 (teal) for a. our baseline model, with all early habitable eras ending with 100 m GEL 4.0 Ga ago, and b. with RGH surface melting, showing all habitable eras ending with 500 m GEL at 4.0 Ga. Where red CO_2 curve is flat, surface is molten and volcanism does not occur. Runs are shown as translucent lines. Solid lines illustrate cases where atmospheric evolution is compatible with modern atmospheric H_2O and O_2. Dashed purple lines show upper limits for modern Venus H_2O, and dashed teal lines show upper limits for O_2. Adding runaway greenhouse (RGH) surface melting to our models enables slightly larger end-habitable-era water inventories to be compatible with modern atmospheric H_2O and O_2.

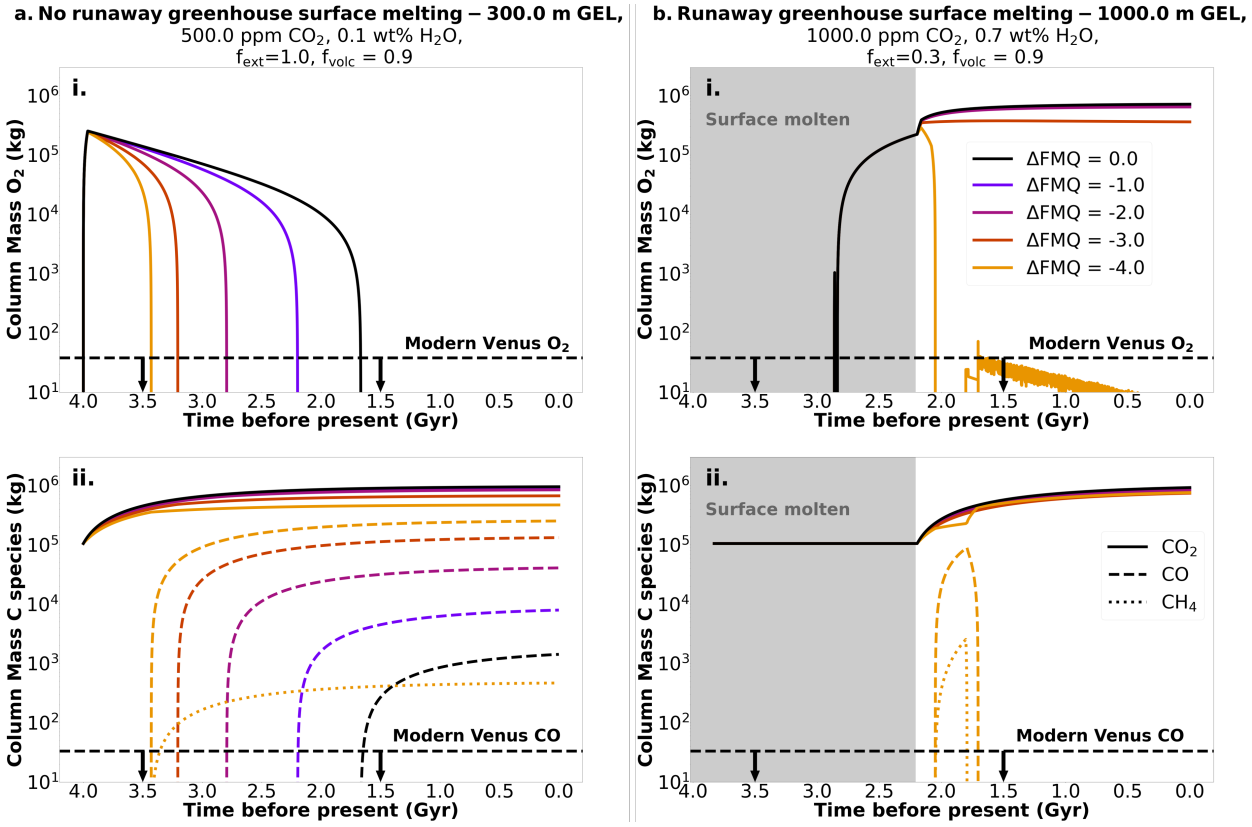

Figure 5.6: Example model output: Melts with lower oxygen fugacity can enable larger end-habitable-era water inventories to be compatible with modern atmospheric composition, however, melts with low oxygen fugacities also outgas reduced gasses such as CO which can overwhelm the O_2 available to oxidise them and produce an atmosphere with far greater CO than observed on modern Venus. Time evolution of column masses of i. O_2 and ii. C species for different melt oxygen fugacities in a. our baseline model, with all early habitable eras ending with 300 m GEL 4.0 Ga ago, and b. with 1000m GEL RGH surface melting. Line colors indicate melt oxygen fugacity. In ii., CO_2, CO, and CH_4 are indicated with solid, dashed, and dotted lines respectively. Black dashed horizontal lines show upper limits for modern Venus O_2 (<70 ppm) and CO (<52 ppm) in i and ii respectively (Johnson and de Oliveira, 2019). Only models that fall beneath both of these limits are considered successful.

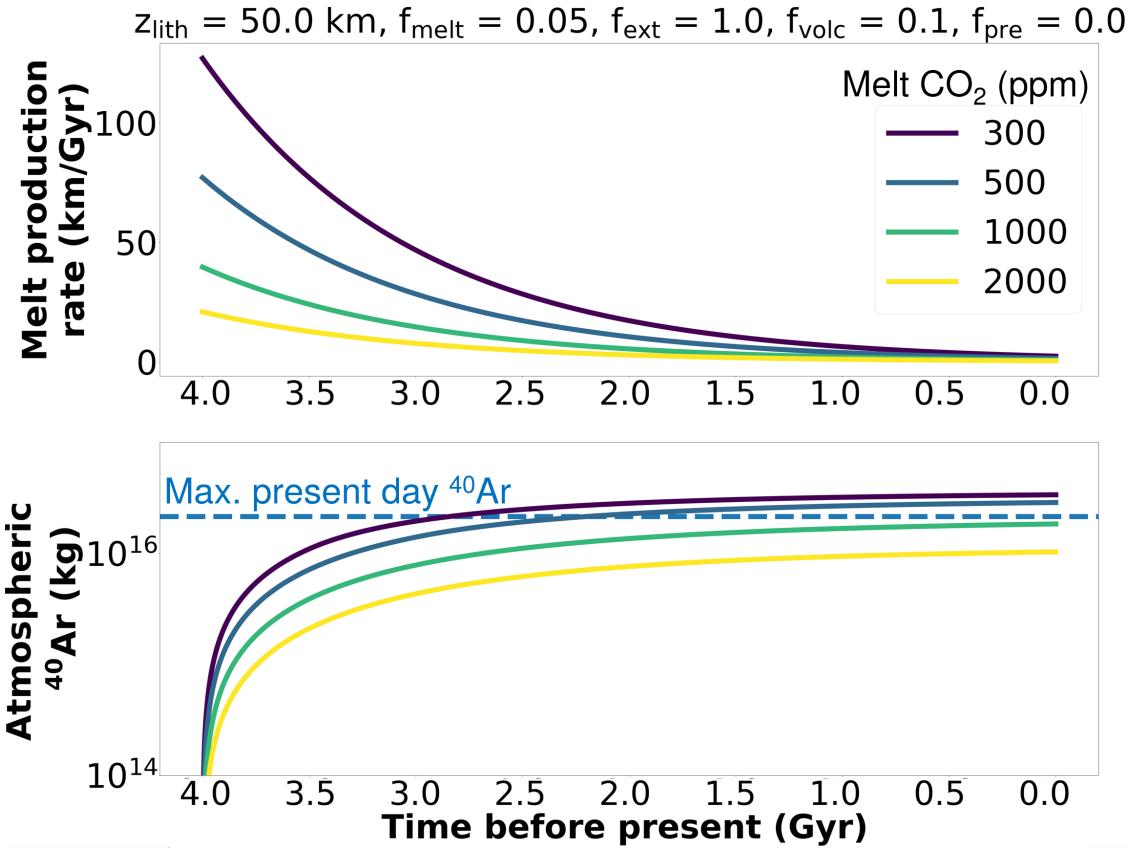

Figure 5.7: Example atmospheric ^{40}Ar accumulation for a range of crustal production rates, set by melt CO_2 concentrations (as in Fig. 5.2 and Equations 5.24&5.27).

reduced species O_2 sinks.

Together, these factors make it more difficult to reconcile a hypothetical early habitable era with data for modern Venus and narrow the range of parameters that reconcile a hypothetical habitable era with measurements of Venus' modern atmosphere. Within the framework of our model, only a small loophole in parameter space, corresponding to less than 0.4 % of model runs, remains when the ^{40}Ar and oxygen constraints are combined (light blue and light green columns in Fig. 5.9):

1. The habitable era must end prior to 3 Ga: In our models, volcanism is required to supply fresh basalt and reduced gases (particularly CO and CH_4) to Venus' surface and atmosphere to act as an oxygen sink. The later in Venus' history this volcanic

activity occurs, the longer mantle ^{40}K has to decay into ^{40}Ar, which is then degassed during volcanism. Extensive ^{40}Ar degassing in runs violates the observed low ^{40}Ar in Venus' modern atmosphere. Therefore, within the framework of our model, Venus must have been uninhabitable for at least ∼70% of its history, >4 times as long as some previous estimates (Way and Del Genio, 2020).

2. The end-habitable-era water inventory must be ≤300 m GEL, unless melt oxygen fugacity log fO_2 less than FMQ−3: For more oxidized average melts on Venus, oxygen sinks in our model can only remove the O left behind by H escape from 300 m GEL of water at the end of a habitable era. When erupted melts have lower oxygen fugacities, the corresponding increase in degassed CO and CH_4 can remove an additional 500 m GEL or more. Therefore, within the framework of our model, if Venusian melts have similar oxygen fugacity to mid ocean ridge (MOR) melts on Earth (i.e. log fO_2 ≈FMQ±0 (Cottrell and Kelley, 2011)), Venus' oceans were shallow by the end of the habitable era.

3. Average melts erupted on Venus after the habitable era must have had ≥ 0.2wt% dissolved H_2O, unless Venus melts have high oxygen fugacities: Oxidation of degassed CO and CH_4 is a major O_2 sink in our baseline model. Degassing of reduced species continues after all O_2 is consumed. As a result, degassing of CO and CH_4 often exceeds the O_2-reduction sink. Continued H_2O degassing through Venus' post-habitable history provides a supply of O_2 as H escapes to space to balance continued CO and CH_4 degassing. A given model run typically behaves in one of two ways: 1. Venus' post habitable evolution doesn't have sufficient O_2 sinks to remove O_2 from the atmosphere to match modern constraints. 2. Once O_2 from a large end-habitable-era water inventory is depleted in a run with larger cumulative O_2 sinks caused by either a surface melt layer during a runaway greenhouse or abundant extrusive volcanism, the O_2 available to oxidize CO and CH_4 to CO_2 has been used up and degassed CO

accumulates rapidly in the atmosphere. In other words, exactly matching the reducing capacity of the Venus surface-atmosphere system to the oxygen introduced by loss of an end-habitable-era H_2O inventory and degassed water requires fine tuning.

Only ∼10% of our 57,600 total ^{40}Ar degassing model runs (independent of our oxygen loss runs) fall within or below the measured range for Venus' modern atmospheric ^{40}Ar abundance. However, many of the ^{40}Ar degassing runs that can reproduce Venus' modern ^{40}Ar abundance have parameter combinations that cannot reproduce Venus' modern O_2, H_2O, and CO concentrations in our O_2 loss model. This reduces the proportion of our O_2 loss runs that are consistent with Venus' present day atmosphere when both oxygen and ^{40}Ar are considered to less than 0.4% (Fig 5.9).

5.6 Discussion

5.6.1 Habitable Era Water Recycling

Our models place an upper limit of 500 m GEL on the total water inventory supplied to the atmosphere at the end of a hypothetical habitable era on Venus, unless Venus' eruptive history has been dominated by melts with an oxygen fugacity of $\log fO_2$ less than FMQ−3 in which case the end habitable era inventory can extend to 1000m. Our O_2 loss model constrains only the final water inventory before conditions transitioned from habitable to uninhabitable. However, the surface water inventory during a hypothetical habitable era need not be constant. Eclogite formation before dehydration provides a mechanism for recycling of H_2O into the mantle. We consider the implications of removal of water to the mantle on the evolution of the total surface water inventory of a hypothetical habitable era. To quantify the evolution of a hypothetical habitable era's water inventory over time, we model the hydration of crust, and the recycling of hydrated crust into the mantle.

To determine the conditions under which hydrated crust can be recycled into the mantle

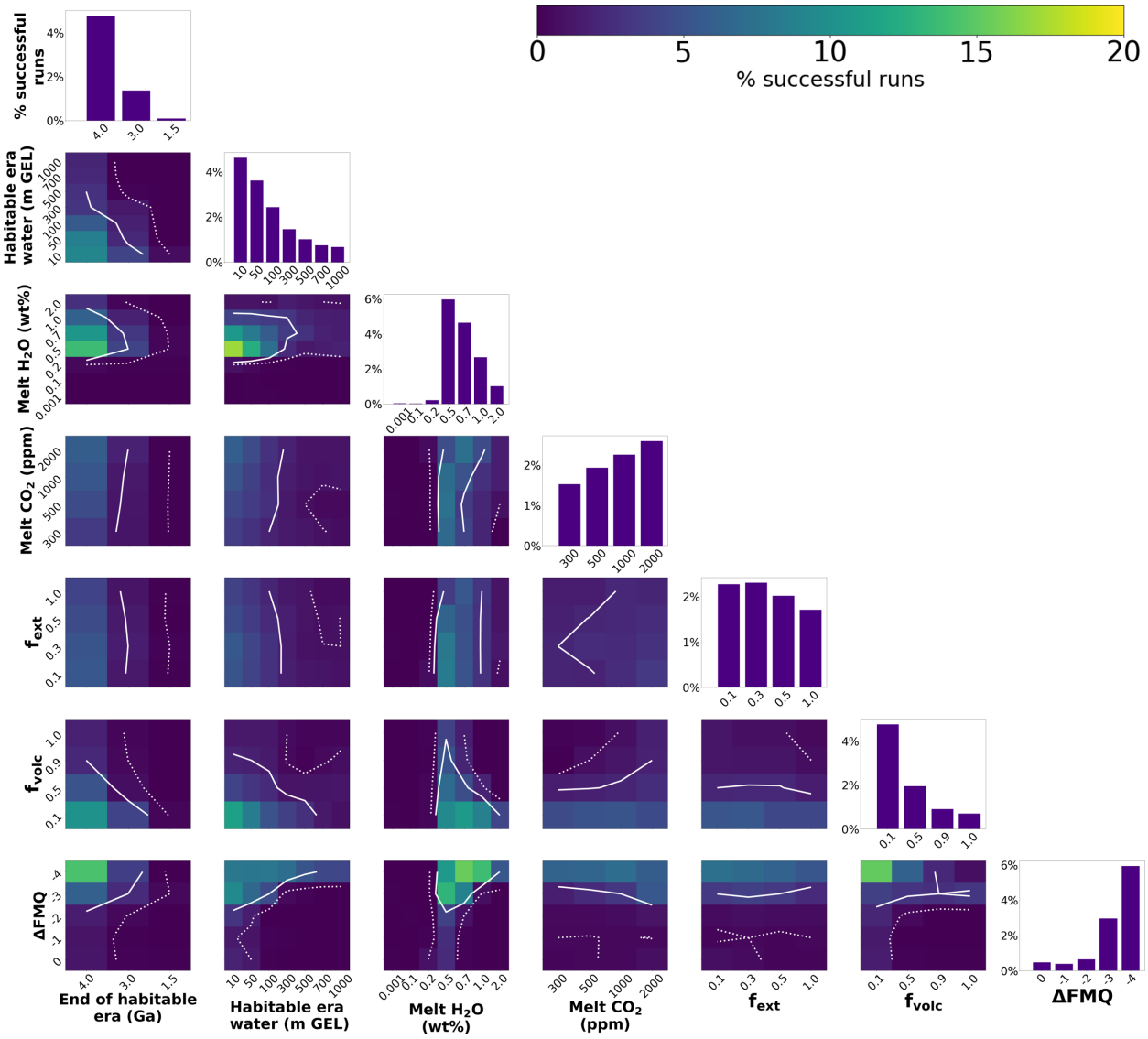

Figure 5.8: Percentage of model runs that end with atmospheric H_2O, O_2, and CO concentrations consistent with data for modern Venus (Moroz, 1981) for different combinations of parameters (Table 5.1) for runs without runaway greenhouse (RGH) surface melting. Contour plots show model success rates for combinations of different values of 2 parameters. Dashed and solid white lines indicate 2σ and 1σ levels, respectively. Summary bar charts show model success rates for different values of a single parameter. f_{ext} is extrusive magmatism fraction, f_{volc} is fraction of Venus' modern atmospheric CO_2 derived from post-habitable era volcanic degassing, and $\log fO_2\Delta\text{FMQ}$ is the oxygen fugacity of erupting melts since the end of the habitable era relative to the fayalite-magnetite-quartz buffer.

during a hypothetical habitable era, we calculate 1-D steady state geotherms for lithosphere of a fixed thickness z_{lith} and with a fixed downward advection velocity v equal to the crustal

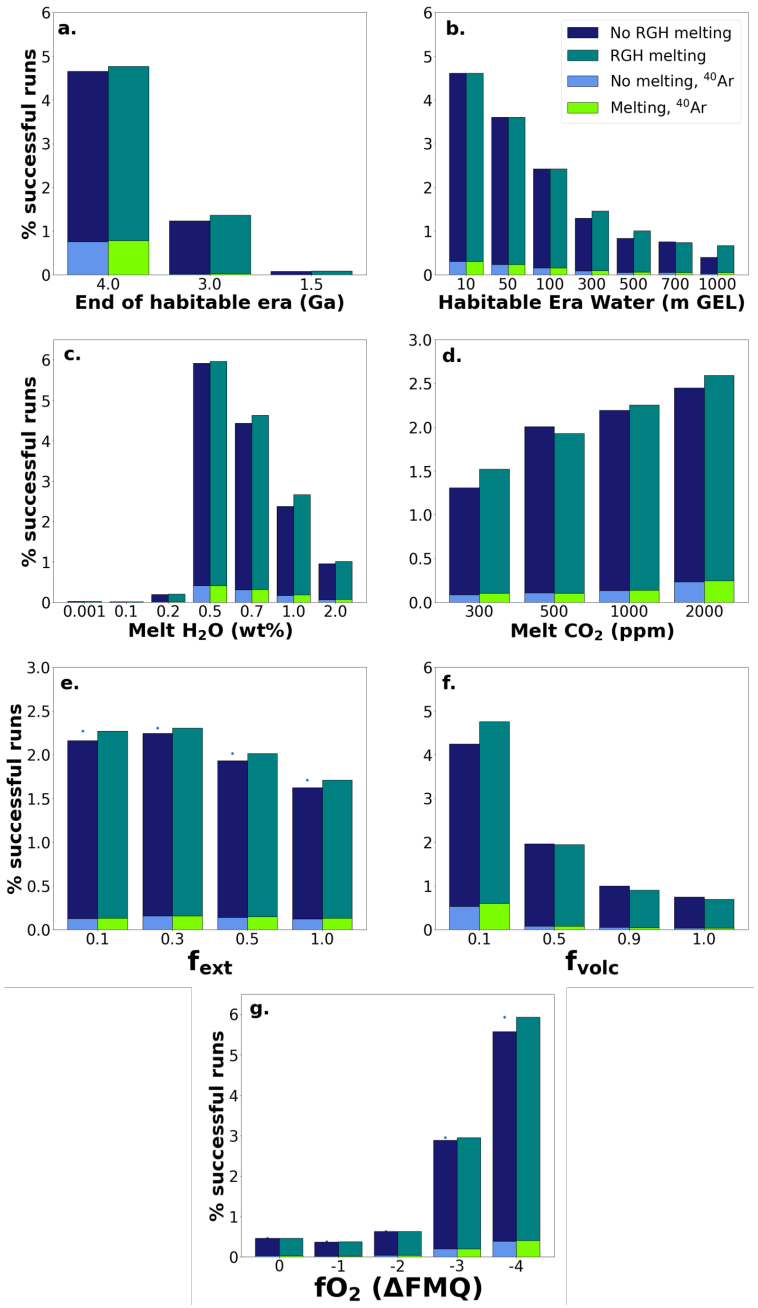

Figure 5.9: Comparison of fraction of successful runs (runs that have final atmospheric O_2, H_2O, and CO concentrations less than upper limits for Venus' present atmosphere) compatible with modern Venus atmosphere for models without runaway greenhouse (RGH) melting (dark blue), and with RGH melting (dark green). Successful runs that are also fall within or below the range of Venus' modern atmospheric ^{40}Ar abundance are also shown for models with (light blue) and without (light green) RGH. All parameter values correspond to Table 5.1.

production rate. We assume a heat pipe-style regime where new crust is produced through extrusive volcanism, leading to burial of older crust, and the eventual recycling of material from the base of the lithosphere into the underlying convecting mantle (Armann and Tackley, 2012). The resulting geotherm (O'Reilly and Davies, 1981; Kankanamge and Moore, 2019) is compared to phase boundaries for eclogite formation (Bucher and Frey, 2002) and serpentinite dehydration (Hacker et al., 2003). If eclogite formation is enabled first, then hydrated crust is recycled into the mantle.

We assume Venus produced enough crust to degas 80 bar of CO_2 prior to the end of the habitable era to maximize the potential for extensive recycling of hydrated crust into the mantle by increasing the rate of crustal burial. Heat transport in a stagnant lid regime with downwards advection of crust caused by continuous resurfacing by lava flows with diffusion of heat and internal radiogenic heat production, can be expressed as (O'Reilly and Davies, 1981; Kankanamge and Moore, 2019):

$$\alpha \frac{\partial^2 T}{\partial z^2} = v \frac{\partial T}{\partial z} + \frac{H}{\rho c_p} \tag{5.44}$$

where $\alpha = \frac{k}{\rho c_p}$ is the diffusion coefficient, k is conductivity, ρ is density, and c_p is specific heat capacity, and H is internal heat production by decay of radioactive elements. The steady state solution is (Kankanamge and Moore, 2019):

$$T(z) = \frac{z_{lith}}{v} \frac{H}{\rho c_p} + c_1 \frac{\alpha}{v} \exp \frac{v z_{lith}}{\alpha} + c_2 \tag{5.45}$$

where c_1 and c_2 are constants:

$$c_1 = \frac{v}{\alpha} \frac{\left(\Delta T - \frac{\rho c_p H z_{lith}}{v} \right)}{\exp\left(\frac{v z_{lith}}{\alpha} \right) - 1} \tag{5.46}$$

$$c_2 = T_s - c_1 \frac{\alpha}{v} \tag{5.47}$$

where $\Delta T = T(z_{lith}) - T(0)$.

The advection velocity v depends on the timing of the end of the habitable era (t_0 from our O_2 loss model), the proportion of Venus' modern CO_2 degassed prior to the end of the habitable era ($1 - f_{volc}$), and melt CO_2 concentration. We assume that the eruption rate (and therefore v) is constant over the period 4.4 Ga to t_0, such that:

$$v = \frac{1}{3.15 \times 10^{16} \, (4.4 - t_0)} \frac{(1 - f_{volc})}{c_{\mathrm{CO_2}} \rho_{melt}} M_{CO_2,f} \tag{5.48}$$

where the factor of 3.15×10^{16} converts from Gyrs to seconds.

We compare this geotherm to phase boundaries for eclogite formation (Bucher and Frey, 2002) and serpentinite dehydration (Hacker et al., 2003). When dense eclogite forms, crust is more likely to sink into the mantle (Morschhauser et al., 2011). Where the geotherm encounters the eclogite stability field before serpentine dehydrates, we assume that hydrated lithosphere returns water to the mantle through entrainment in convection (Armann and Tackley, 2012). When the geotherm crosses into the serpentinite dehydration field first, water is returned to the surface or shallow crustal reservoirs and not into the mantle. We investigate a range of internal radiogenic heating rates comparable to those observed in modern terrestrial basalts (Hasterok and Webb, 2017) to find combinations of lithosphere thickness and volumentric heat production rate that permit eclogite to form before serpentinite dehydration occurs. When the temperature-pressure profile crosses into the serpentinite dehydration field first, we assume that water returns to the surface or shallower depths in the crust, as suggested by the upward migration of water released by serpentinization during subduction on Earth. Additionally, we omit all geotherms where temperatures exceed 1573 K at depths shallower than z_{lith}, as the base of the lithosphere is defined by this temperature in our model. We find that eclogite forms before dehydration occurs when v and z_{lith} are large, and H is small (Fig. 5.10). Higher internal radiogenic heating rates (e.g. adjusted for a younger planet with a higher concentration of decaying radioactive elements) generate

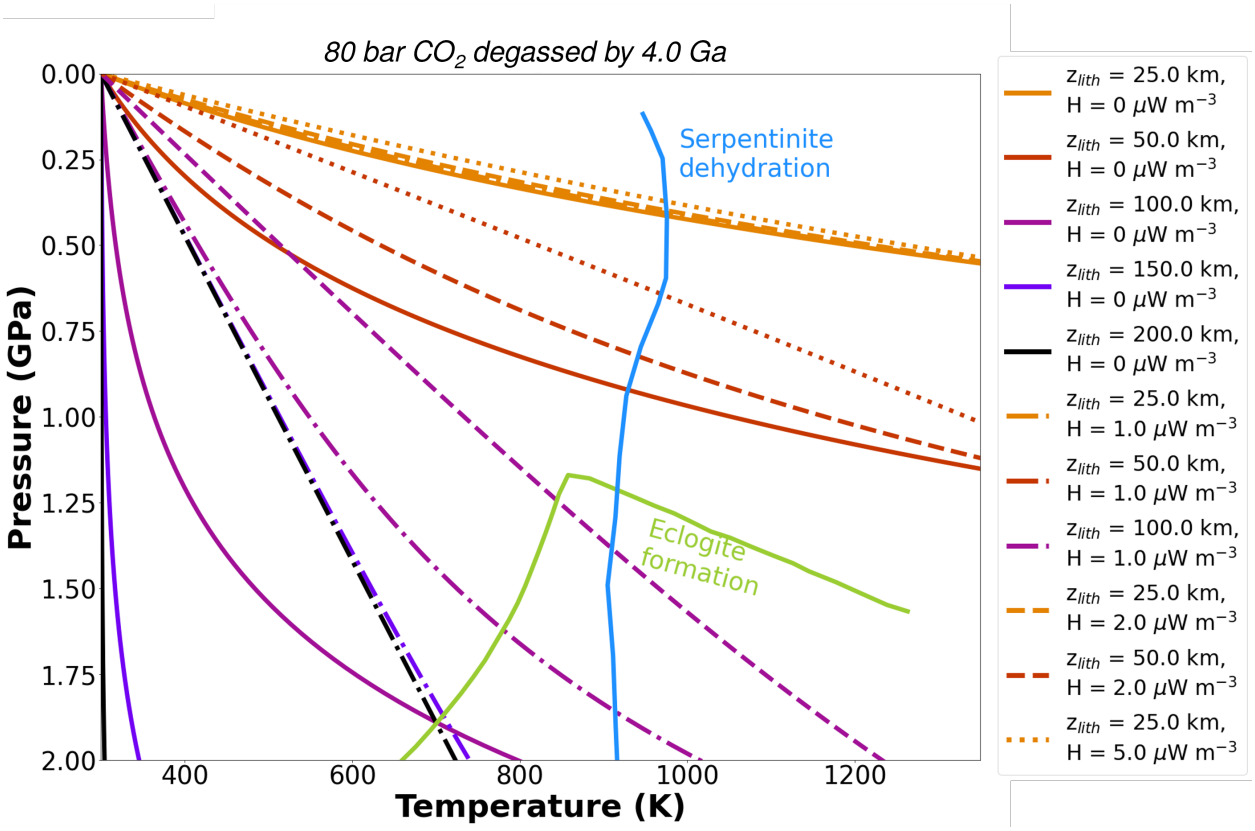

Figure 5.10: Steady-state pressure-temperature profiles for Venus lithosphere with a constant advection velocity of v = 400 km Gyr^{-1} (to degas a total of 90 bar CO_2 over the course of a 0.5 Gyr hypothetical habitable era on Venus). Colors indicate different lithospheric thicknesses ranging from z_{lith} = 25-200 km, and solid, dash-dotted, dashed, and dotted lines indicate crustal internal heat production rates from H = 0-5 μWm^{-3}. The blue and green lines show phase boundaries corresponding to serpentinite dehydration (Hacker et al., 2003) and eclogite formation (Bucher and Frey, 2002). We assume that all pressure-temperature profiles that cross into the eclogite formation field before the serpentinite dehydration field are able to recycle hydrated lithosphere into the mantle through entrainment of dense eclogite into the convecting mantle (Armann and Tackley, 2012).

geotherms with crusts thinner than 5 km, which is the lowest crustal thickness we consider in this model based on the range estimated for modern Venus (James et al., 2013). These thin, hot crusts do not pass through the eclogite stability field, and therefore do not lead to recycling of hydrated crust into the mantle within the framework of our model. Lithospheres thicker than 100 km with internal heating rates less than 5 μW m^{-3} (Fig. 5.10) are able to form eclogite before serpentinite dehydration occurs.

We initiate our models with an initial surface water inventory h_0 of up to 4000 m GEL, at the beginning of a hypothetical habitable era. At each timestep, we calculate the water removed from the surface inventory, and the water added by volcanic degassing. We assume that any hydrated crust is removed due to burial by new lava being erupted at the surface, so the crust moves downward at the advection velocity v (Equation 5.48). We use the same volcanic degassing procedure as for our initial O_2 loss models (Section 5.3.4), and the same range of melt H_2O concentrations (Table 5.1). However, we fix atmospheric pressure to <10 bar, based on climate models (Way et al., 2016), rather than tracking accumulation of atmospheric CO_2 as climate models for early Venus indicate that low atmospheric pressures are required to sustain surface liquid water (Way and Del Genio, 2020). The total GEL of water present at each timestep i is then:

$$\begin{aligned} h_i = h_{i-1} & \\ & - \frac{1}{\rho_w} \Delta t f_{hyd} A_h f_{ext} v \rho_c \\ & + \frac{1}{\rho_w} \Delta t f_{ext} v \rho_c \left(c_{\mathrm{H_2O}} - s_{\mathrm{H_2O}} \right) \end{aligned} \tag{5.49}$$

where $\rho_w = 1000$ kg m^{-3} is the density of water, $\rho_c = 2800$ kg m^{-3} is the density of the crust, f_{hyd} is the mass fraction of water in hydrated crust (up to 3 wt% (Schaefer and Sasselov, 2015)), A_h is the fraction of Venus' surface area submerged by the existing surface water inventory, and $s_{\mathrm{H_2O}}$ is the solubility of water in the crust-producing melt as calculated using VolcGasses. To obtain A_h, we use modern Venus hypsometry (Rosenblatt et al., 1994) to calculate the global equivalent layer of water that can be stored beneath any given elevation on Venus, and the cumulative area of Venus' surface beneath each elevation. We then interpolate to find the cumulative area of Venus' surface submerged at each timestep in our model.

In some cases, the surface water inventory approaches a steady state where removal by burial of hydrated crust (occurring at a rate set by the surface water inventory and crustal

production rate) matches water inputs by volcanic degassing. Models with low ($\leq$0.2 wt%) melt H_2O concentrations do not reach a steady state, and instead lose all of their water (Figs. D.2 & D.3).

In order for a habitable era with an evolving surface water inventory to be compatible with our O_2 loss and ^{40}Ar degassing model results, the surface water inventory by the end of the habitable era must be below 500 m GEL (Fig 5.9). This is favored by melt H_2O concentrations between 0.1 and 0.7 wt%, and high mass fractions ($\geq$0.5 wt%) of water in hydrated crust (Figs. D.2 & D.3). For cases where the final water inventory drops below 500 m GEL, the average surface water inventory over the course of the habitable era can be up to half an order of magnitude greater than the final water inventory for a few combinations of crust hydration and melt H_2O concentration, allowing for much deeper oceans on early Venus in some cases. However, this mechanism for net sequestration of water in the mantle through burial of hydrated crust does not affect the conclusion that only hypothetical habitable eras that ended prior to 3 Ga are consistent with ^{40}Ar, O_2, H_2O and CO concentrations in Venus' modern atmosphere

5.6.2 Limitations

The paucity of existing data for modern Venus severely restricts our understanding of Venus' past. This is one of the primary drivers for Venus exploration over the coming decades. It is currently unknown whether Venus has ongoing volcanism, what the planet's tectonic regime is, how thick the crust and lithosphere are, what the mantle composition is–let alone how all of these important factors have evolved over the past 4 Gyr (Smrekar et al., 2018). As a result, our treatment of Venus' post habitable evolution in both our oxygen loss and Ar degassing models is highly simplified.

First, to enable modeling with the least number of assumptions about Venus' interior, we have assumed that the composition of melts erupting on Venus does not change over

time. Thus, we model "average" melts on Venus. Eruptions resulting from mantle plumes (Smrekar et al., 2018) or local magmatic systems may have different volatile concentrations.

Second, we do not include degassing of S to reduce the number of parameters needed to describe melt compositions and degassing. Although this has a negligible impact on the speciation of the gasses included in our model (Wogan et al., 2020), Venus' modern atmosphere contains SO_2, SO, and other S species. This requires that Venus has recently degassed–and may still be degassing–S in some form (Bullock and Grinspoon, 2001). It follows that oxidation of S species may have acted as an O_2 sink analogous to the way oxidation of CO to CO_2 is an important mechanism for removing atmospheric O_2 in our model.

Third, our approach to modeling surface melting during a runaway greenhouse is highly simplified. To maximise the potential oxygen sink, we assume that diffusion of oxygen into the melt does not limit the rate at which the melt oxidizes such that all molten material at a given timestep is available to oxidize. Our approach also neglects the greenhouse effect of CO_2. CO_2 contributes around 420 K of greenhouse warming to Venus' modern atmosphere (Titov et al., 2007), which is not sufficient to melt Venus' surface under the bright modern Sun, and much less than the maximum greenhouse warming possible under the same insolation with H_2O (Turbet et al., 2019). Additionally, the absorption bands for CO_2 and H_2O overlap, so their greenhouse effects are not additive (Titov et al., 2013). Our modeling approach focuses on the feedback between the much stronger H_2O greenhouse effect and H escape to space, however, this may underestimate the surface temperature at a given timestep, which could extend the duration of the runaway greenhouse melting stage and lead to greater O_2 loss.

Fourth, we assume that Venus' eruptive history can be modelled as an exponential decay between the end of the habitable era and the present day. The crater retention age of Venus' surface suggests that the planet has been resurfaced geologically recently (Phillips

et al., 1992; Bottke et al., 2016). This crater retention age can be explained by either a catastrophic resurfacing event 0.3 to 1 Gyr ago (Strom et al., 1994), or equilibrium resurfacing by continuous volcanism (Bjonnes et al., 2012). We opt for continuous volcanism in our models because this maximizes the lava flow oxidation oxygen sink by erupting fresh lava, rather than having surface oxidation limited by diffusion. This, in turn, maximizes the end-habitable-era water inventory possible in our models, which is conservative relative to our conclusion that only a narrow range of parameters is consistent with Early Venus habitability. Differences in Venus' crustal production history will not change our fundamental conclusion that the reducing power introduced to Venus' surface-atmosphere system by non-thermal O escape, eruption of lava flows containing minerals that can be oxidized, and degassing of gasses such as CO and CH_4 must balance the total O_2 introduced by H escape from an end-habitable-era water inventory and any subsequently degassed H_2O in order to reconcile a past habitable era with Venus' modern atmosphere. However, differences in Venus' crustal production history are important for ^{40}Ar degassing. Our approach is also conservative with respect to ^{40}Ar degassing because degassing is greatest earlier in our models, reducing the time for ^{40}K decay to make ^{40}Ar available in the mantle for release by volcanism.

Fifth, our ^{40}Ar degassing model is based upon a large number of poorly-constrained parameters (Table 5.2) and requires assumptions about Venus' tectonic regime and pre-habitable-era evolution. There are several potential ways to reduce ^{40}Ar degassing over Venus' history that could make a larger proportion of our model results consistent with Venus' modern atmospheric composition. For example, the concentration of radioactive isotopes in Venus' mantle is poorly constrained (O'Rourke and Korenaga, 2015). A lower concentration of U and K in Venus' mantle would reduce the accumulation of ^{40}Ar in the mantle, and therefore ^{40}Ar degassing over time. Additionally, ^{40}Ar may not be distributed homogeneously through Venus' mantle. If Venus' mantle has incompatible-enriched reservoirs or a thick basal magma ocean (O'Rourke, 2020), ^{40}Ar may be prevented from degassing

to the atmosphere, increasing the number of our model runs compatible with Venus' modern atmospheric ^{40}Ar concentration.

5.6.3 Implications for upcoming Venus missions

Our model results suggest, in agreement with previous results (Krissansen-Totton et al., 2021), that a habitable era on Venus with abundant surface liquid water was unlikely and suggest a number of tests for upcoming Venus missions: VERITAS (Venus Emissivity, Radio science, InSAR, Topography, And Spectroscopy), DAVINCI (Deep Atmosphere Venus Investigation of Noble gases, Chemistry, and Imaging), and EnVision.

For example, VERITAS high resolution topography and gravity data could be used to better constrain Venus' present lithospheric thickness. At present, this parameter is not well enough constrained to distinguish between a range of possible tectonic regimes. Our results favor a tectonic regime with limited volcanism over the past 4 Gyr to reconcile any early habitable era with Venus' modern atmosphere. Determining Venus' modern (or recent) tectonic regime and lithospheric thickness is also important for better constraining ^{40}Ar degassing models, by providing constraints on the recycling depth of ^{40}K-enriched crust.

Both VERITAS and DAVINCI will to survey high SiO_2 rocks on Venus' surface. If these rocks resemble terrestrial andesites and rhyolites, this could imply H_2O in the melting zone and suggest high melt H_2O concentrations consistent with our successful model runs (Campbell and Taylor, 1983; Shellnutt, 2013). However, hydrous melting will need to be distinguished from anhydrous fractional crystallization processes, which can also produce silicic magmas (Shellnutt, 2013).

VERITAS also plans to measure FeO abundance. This can be used to narrow down the range of likely melting conditions and extent of fractional crystallization on Venus (Dyar et al., 2020), which also constrain melt volatile concentrations. Crustal FeO abundance can also be used to refine the estimate of FeO concentration in Venusian basalts used in our

models. If Venus' FeO is very high, this will increase the oxidizing potential per unit volume of lava, thus potentially driving our results towards higher required melt H_2O concentrations to compensate for greater loss of atmospheric O_2 to oxidizing Venus' basaltic surface while atmospheric O_2 is greatest early in Venus' post-habitable evolution.

5.7 Conclusions

Nonthermal O escape to space, oxidation of basaltic lava flows, and oxidation of degassed CO and CH_4 can remove oxygen from up to 300 m GEL on the total water inventory supplied to the atmosphere at the end of a hypothetical habitable era on Venus, unless Venus' eruptive history has been dominated by melts with an oxygen fugacity of $\log f\mathrm{O}_2$ less than FMQ-3 (Earth MORB is around $\log f\mathrm{O}_2$=FMQ$\pm$0 (Cottrell and Kelley, 2011)) in which case the end habitable era inventory can extend to 1000m. The oxidation of a transient layer of basaltic melt during an end-habitable-era runaway greenhouse (RGH) can remove oxygen corresponding to an additional 200 m GEL of water (Figs 5.8 & 5.9), raising the limit to 500 m GEL for Venus histories with melt oxygen fugacities $\log f\mathrm{O}_2 \geq$FMQ-3. Although these result reconcile a potential early habitable era on Venus with the paucity of O_2 in Venus' modern atmosphere, only 2.6% of parameter combinations in our models lead to post habitable era outcomes that satisfy atmospheric abundance data for modern Venus. These successful runs define a narrow loophole in parameter space where the reducing power of the Venus surface-atmosphere system since the end of a habitable era is able to balance the O_2 introduced by the escape of H from end-habitable-era water and degassed H_2O.

This loophole becomes even smaller when additional constraints on Venus' history are taken into consideration. The two most important oxygen sinks in our models are oxidation of degassed CO and CH_4 and oxidation of basaltic lava flows, both of which require volcanism and degassing on Venus since the end of a hypothetical habitable era. Degassing and volcanism due to crustal production on Venus leads to degassing of ^{40}Ar. When the ^{40}Ar

contributions to the atmosphere caused by the eruption of lava flows and degassing needed to remove oxygen from Venus' atmosphere through oxidation of basaltic volcanic products and reduced gasses like CO and CH_4 are taken into account, only models with habitable eras ending before 3.0 Ga are consistent with ^{40}Ar, O_2, H_2O, and CO measurements of Venus' modern atmosphere (Fig 5.9) reducing the success rate of our models to less than 0.4% of model runs.

Although our modeling results demonstrate that Venus must have had less than 500 m GEL water by around 4 Ga unless Venus' average melts had oxygen fugacities comparable to that of the most reduced Martian meteorite, we also find that the time-averaged water inventory on an early habitable Venus may have been much greater than this upper limit. Efficient recycling of hydrated basaltic crust into the mantle through eclogite formation (Bucher and Frey, 2002) might act to reduce Venus' surface water inventory during a habitable era. A 1-D model of this process suggests that habitable era averaged water inventories up to 1000 m GEL could be consistent with our O_2 loss and ^{40}Ar degassing modeling results even for melts with higher oxygen fugacities (Figs. D.2 & D.3), provided that Venus had a lithosphere greater than 100 km thick with internal radiogenic heat production rates less than 5 μW m^{-3} (Fig. 5.10).

Key measurements for the VERITAS, DAVINCI, and EnVision missions that would help further evaluate the likelihood of a past habitable era (based on our modeling results) are lithospheric thickness, and crustal SiO_2 and FeO abundances. For example, if hydrous melting is found to have been a significant process on Venus, this would support the existence of a past habitable era on Venus because our results suggest that high average melt H_2O concentrations are an important factor for preventing accumulation of abundant CO in Venus' atmosphere.

CHAPTER 6

SYNTHESIS

Mars and Venus are critical test beds for our understanding of what makes a planet habitable (Ehlmann et al., 2016; Kane et al., 2019). In this thesis, I have used observations, statistical analyses, and numerical modeling to integrate proxies for atmospheric pressure, climate, and composition from both Mars and Venus into our current understanding of how these planets may have passed in and out of habitable states over their lifetimes. Additionally, I have introduced several novel modeling approaches that can be used in future studies of both planets and potentially applied to exoplanets.

In Chapter 2, we used measured Martian crater populations in Mawrth Vallis and Meridiani Planum to constrain paleoatmospheric pressure on Noachian Mars (between ∼4.1 and 3.8 Ga) to either persistently below 1.5-2 bars, or varying between pressures above and below these paleopressure upper limits. To do this, we introduced a new workflow for incorporating the effects of preferential erasure of small craters and variations in atmospheric pressure during cratering into fits of measured crater populations to an impact model. Additionally, we integrated our new pressure upper limits with existing constraints using a basic model of Mars atmospheric pressure evolution to find a wide range of plausible atmospheric pressure histories for Mars. Our results demonstrated the sensitivity of our model to pressure estimates from more recent proxies, and the wide range of plausible pressure histories compatible with existing data. This highlights our as-yet limited understanding of atmospheric loss processes and rates on Mars. Our results motivate future searches for paleopressure proxies throughout Mars history, and for geologic evidence on Mars for processes that could facilitate multi-bar changes in atmospheric pressure on 0.1 Ga timescales, for example, catastrophic volcanism or atmospheric collapse. Of particular importance are paleopressure proxies recording Mars' atmosphere since 3.6 Ga. Potential opportunities include well-dated lava flows and caldera surfaces on Martian volcanoes, including Olympus

Mons (Robbins et al., 2011). An advantage of applying the crater size frequency distribution approach to these surfaces is that these populations have experienced modern 6 mbar pressures, so one end-member pressure for mixing models of contributions to the crater population is known. Additionally, these surfaces have been minimally modified, preserving the smallest craters which are most important for fitting modelled impact crater populations.

In Chapter 3, we used data from small, young craters with overspill channels but no visible inlets ("tadpole craters") and a model of erosion during overspill flooding tested against recorded terrestrial overspill events to determine that the majority of tadpole crater exit breach valleys are consistent with a single crater overspill event. In our modeling, we also introduced a novel workaround for the long-standing problem of unknown grainsizes in Martian fluvial systems. For craters not compatible with a single overspill event, we discussed potential crater-filling water sources and concluded that tadpole craters either formed in a single, groundwater-driven erosion event or through many small erosion events during draining of small meltwater lakes formed on crater-filling bodies of ice.

In Chapter 4, we built on our work in Chapter 3 by performing statistical analysis of a large tadpole crater dataset in the southern hemisphere to establish both a crater size and relative elevation preference for tadpole breach formation. We used data from tadpole craters with overspill breaches at multiple points on their rims to eliminate groundwater and rainfall as plausible water sources for these features. We concluded that the existence of multiple exit breach tadpole craters requires at least hundreds of meters of midlatitude ice relatively late in Mars history, in addition to intermittent melting mechanism such as sub-crater intrusions and/or surface warming. This suggests that ice has been an important control on Mars' surface processes and geomorphologic evolution since the end of the valley network forming era, and a cold climate a step on Mars' trajectory from wet to dry. Our results motivates future work into cataloging possible mechanisms for tens of K of surface warming in the Martian midlatitudes later in the planet's history, which may disfavor strongly atmospheric

pressure-dependent greenhouse warming mechanisms (e.g. CO_2-H_2 warming; Turbet et al. 2019) as Mars' atmospheric pressure has likely declined over time (e.g. Kite 2019; Hu et al. 2015; Manga et al. 2012). The preferential overspill of small craters on relative topographic highs found through our statistical analysis and our derived minimum required melt volumes under a range of conditions can be used to test future climate models. Overall, our results support a complex view of the decline of Martian habitability. Our observations require short-lived, spatially-restricted habitability even on an ice-dominated planet. As a larger inventory of tadpole craters becomes available, re-analyzing the size, spatial, and elevation distribution of these features will also be an important constraint on their formation, including ice distribution and volume. Additionally, this chapter provides a workflow for processing future HiRISE pairs of multiple breach tadpole craters to gather more observations that can be compared to our proposed water sources.

In Chapter 5, we used a novel numerical model of Venus' bulk atmospheric composition to demonstrate that reconciling a hypothetical habitable era on Venus with measurements of the low O_2, CO, and ^{40}Ar concentrations in the modern atmosphere is only possible for a narrow range of parameters. Our results suggest that a habitable era on Venus must have ended before 3 Ga, in contrast to previous modeling studies (e.g. Way and Del Genio 2020; Krissansen-Totton et al. 2021), and with less than 300 m GEL of water (10% of an Earth ocean) unless Venusian volcanism has been dominated by strongly reducing melts. In our model, we also introduced oxidation of a molten basalt layer at the planet's surface during a runaway greenhouse and efficient oxidation of explosive volcanic products like ash as possible oxygen sinks on terrestrial planets. We used our results to identify observations by upcoming missions (e.g. Smrekar et al. 2020; Garvin et al. 2020; Widemann et al. 2020) that may favor past habitability on Venus. The simplicity and flexibility of our numerical model also has applications beyond the Solar System, and may be suitable for modelling the multi billion year evolution of exoplanet atmospheres across a large parameter space.

REFERENCES

Abderrezzak, K. E. K. and A. Paquier (2011). Applicability of Sediment Transport Capacity Formulas to Dam-Break Flows over Movable Beds. *Journal of Hydraulic Engineering 137*(2), 209–221.

Aharonson, O., N. Schorghofer, and M. F. Gerstell (2003). Slope streak formation and dust deposition rates on Mars. *Journal of Geophysical Research: Planets 108*(E12).

Airapetian, V. S., R. Barnes, O. Cohen, G. A. Collinson, W. C. Danchi, C. F. Dong, A. D. Del Genio, K. France, K. Garcia-Sage, A. Glocer, and et al. (2020). Impact of space weather on climate and habitability of terrestrial-type exoplanets. *International Journal of Astrobiology 19*(2), 136–194.

Airey, M. W., T. Mather, D. Pyle, L. Glaze, R. Ghail, and C. Wilson (2015). Explosive volcanic activity on Venus: the roles of volatile contribution, degassing, and external environment. *Planetary and Space Science 113*, 33–48.

Amato, M. and D. Williams (2015). *Accessing the Venus Lower Atmosphere and Surface-from Venera and Pioneer Venus to VISE and VITaL*, pp. 71–100. Cham: Springer International Publishing.

Andrews-Hanna, J. C. and R. J. Phillips (2007). Hydrological modeling of outflow channels and chaos regions on Mars. *Journal of Geophysical Research: Planets 112*(E8).

Ansan, V. and N. Mangold (2006). New observations of Warrego Valles, Mars: Evidence for precipitation and surface runoff. *Planetary and Space Science 54*(3), 219–242.

Arevalo Jr, R., W. F. McDonough, and M. Luong (2009). The K/U ratio of the silicate Earth: Insights into mantle composition, structure and thermal evolution. *Earth and Planetary Science Letters 278*(3-4), 361–369.

Armann, M. and P. J. Tackley (2012). Simulating the thermochemical magmatic and tectonic evolution of Venus's mantle and lithosphere: Two-dimensional models. *Journal of Geophysical Research: Planets 117*(E12).

Arnold, N. S., S. J. Conway, F. E. G. Butcher, and M. R. Balme (2019). Modeled subglacial water flow routing supports localized intrusive heating as a possible cause of basal melting of Mars' south polar ice cap. *Journal of Geophysical Research: Planets 124*(8), 2101–2116.

Arthur, J. F., C. R. Stokes, S. S. R. Jamieson, J. Rachel Carr, A. A. Leeson, and V. Verjans (2022). Large interannual variability in supraglacial lakes around East Antarctica, journal=Nature Communications. *13*(1), 1711.

Asimow, P. D. and M. S. Ghiorso (1998). Algorithmic modifications extending MELTS to calculate subsolidus phase relations. *American Mineralogist 83*(9-10), 1127 – 1132.

Ayres, T. (1997). Evolution of the solar ionizing flux. *Journal of Geophysical Research 102*, 1641–1651.

Bahcall, J. N., M. H. Pinsonneault, and S. Basu (2001). Solar Models: Current Epoch and Time Dependences, Neutrinos, and Helioseismological Properties. *The Astrophysical Journal 555*(2), 990–1012.

Baker, L. L. (2017). Basalt Weathering and the Volatile Budget of Early Mars. In *Lunar and Planetary Science Conference*, Volume 2014, pp. 3081.

Balme, M., C. Gallagher, and E. Hauber (2013). Morphological evidence for geologically young thaw of ice on Mars: A review of recent studies using high-resolution imaging data. *Progress in Physical Geography: Earth and Environment 37*(3), 289–324.

Bamber, E. R., T. A. Goudge, C. I. Fassett, and G. R. Osinski (2022). Constraining the formation of paleolake inlet valleys across crater rims. *Icarus 378*, 114945.

Bamber, E. R., T. A. Goudge, C. I. Fassett, G. R. Osinski, and G. Stucky de Quay (2022). Paleolake inlet valley formation: Factors controlling which craters breached on early mars. *Geophysical Research Letters 49*(24), e2022GL101097.

Basilevsky, A., J. Head, G. Schaber, and R. Strom (1997). The resurfacing history of Venus. In R. P. SW Bougher, DM Hunten (Ed.), *Venus II*. University of Arizona Press, Tuscon.

Batalha, N., S. D. Domagal-Goldman, R. Ramirez, and J. F. Kasting (2015). Testing the early Mars H_2–CO_2 greenhouse hypothesis with a 1-D photochemical model. *Icarus 258*, 337–349.

Bergin, E. A., G. A. Blake, F. Ciesla, M. M. Hirschmann, and J. Li (2015). Tracing the ingredients for a habitable Earth from interstellar space through planet formation. *Proceedings of the National Academy of Sciences 112*(29), 8965–8970.

Bierson, C. J., R. J. Phillips, I. B. Smith, S. E. Wood, N. E. Putzig, D. Nunes, and S. Byrne (2016). Stratigraphy and evolution of the buried CO_2 deposit in the Martian south polar cap. *Geophysical Research Letters 43*(9), 4172–4179.

Bintanja, R. and C. H. Reijmer (2001). Meteorological conditions over Antarctic blue-ice areas and their influence on the local surface mass balance. *Journal of Glaciology 47*(156), 37–50.

Bishop, J. L., E. Z. N. Dobrea, N. K. McKeown, M. Parente, B. L. Ehlmann, J. R. Michalski, R. E. Milliken, F. Poulet, G. A. Swayze, J. F. Mustard, S. L. Murchie, and J.-P. Bibring (2008). Phyllosilicate Diversity and Past Aqueous Activity Revealed at Mawrth Vallis, Mars. *Science 321(5890)*, 830–833.

Bishop, J. L., A. G. Fairén, J. R. Michalski, L. Gago-Duport, L. L. Baker, M. A. Velbel, C. Gross, and E. B. Rampe (2018). Surface clay formation during short-term warmer and wetter conditions on a largely cold ancient Mars. *Nature Astronomy 2*(3), 206.

Bishop, J. L. and E. B. Rampe (2016). Evidence for a changing Martian climate from the mineralogy at Mawrth Vallis. *Earth and Planetary Science Letters 448*, 42–48.

Bjonnes, E., V. L. Hansen, B. James, and J. B. Swenson (2012). Equilibrium resurfacing of Venus: Results from new Monte Carlo modeling and implications for Venus surface histories. *Icarus 217*(2), 451–461.

Björnsson, H. (2003). Subglacial lakes and jökulhlaups in Iceland. *Global and Planetary Change 35*(3-4), 255–271.

Bland, P. A. and N. A. Artemieva (2006). The rate of small impacts on Earth. *Meteoritics & Planetary Science 41*(4), 607–631.

Boslough, M. and D. Crawford (2008). Low-altitude airbursts and the impact threat. *International Journal of Impact Engineering 35*(12), 1441–1448.

Bottke, W. F. and J. C. Andrews-Hanna (2017). A post-accretionary lull in large impacts on early Mars. *Nature Geoscience 10*(5), 344–348.

Bottke, W. F., D. Vokrouhlicky, B. Ghent, S. Mazrouei, S. Robbins, and S. Marchi (2016). On Asteroid Impacts, Crater Scaling Laws, and a Proposed Younger Surface Age for Venus. In *Lunar and Planetary Science Conference*, Lunar and Planetary Science Conference, pp. 2036.

Bouchard, M., B. Marsan, S. Péloquin, G. Fortin, M. Saarnisto, W. Shilts, P. David, and A. Fliszár (1989). Géologie glaciaire du cratère du nouveau-québec. In S. Péloquin and M. A. Bouchard (Eds.), *L'histoire Naturelle du Cratère du Nouveau-Québec, Collection environnement et géologie 7*, pp. 101–138. Université de Montréal.

Bouchard, M. A. (1989). Englaciation et glaciation du cratère du nouveau-québec, un modèle théorique. In S. Péloquin and M. A. Bouchard (Eds.), *L'histoire Naturelle du Cratère du Nouveau-Québec, Collection environnement et géologie 7*, pp. 139–163. Université de Montréal.

Bowling, J., S. Livingstone, A. Sole, and W. Chu (2019). Distribution and dynamics of Greenland subglacial lakes. *Nature Communications 10*(1), 2810.

Brain, D. A., F. Bagenal, Y.-J. Ma, H. Nilsson, and G. S. Wieser (2016). Atmospheric escape from unmagnetized bodies. *Journal of Geophysical Research: Planets 121*(12), 2364–2385.

Bristow, T. F., R. M. Haberle, D. F. Blake, D. J. D. Marais, J. L. Eigenbrode, A. G. Fairén, J. P. Grotzinger, K. M. Stack, M. A. Mischna, E. B. Rampe, K. L. Siebach, B. Sutter, D. T. Vaniman, and A. R. Vasavada (2017). Low Hesperian pCO_2 constrained from in situ mineralogical analysis at Gale Crater, Mars. *Proceedings of the National Academy of Sciences 114*(9), 2166–2170.

Brown, P., R. E. Spalding, D. O. ReVelle, E. Tagliaferri, and S. P. Worden (2002). The flux of small near-Earth objects colliding with the Earth. *Nature 420*(6913), 294.

Brownlie, W. R. (1983). Flow depth in sand-bed channels. *Journal of Hydraulic Engineering 109*(7), 959–990.

Bryson, C. E., V. Cazcarra, and L. L. Levenson (1974). Sublimation rates and vapor pressures of water, carbon dioxide, nitrous oxide, and xenon. *Journal of Chemical & Engineering Data 19*(2), 107–110.

Bucher, K. and M. Frey (2002). Metamorphism of mafic rocks. In *Petrogenesis of Metamorphic Rocks*, pp. 279–324. Springer.

Bullock, M. A. and D. H. Grinspoon (2001). The recent evolution of climate on Venus. *Icarus 150*(1), 19–37.

Buratti, B. J., J. M. Bauer, M. D. Hicks, J. K. Hillier, A. Verbiscer, H. Hammel, B. Schmidt, B. Cobb, B. Herbert, M. Garsky, J. Warda, and J. Fousta (2011). Photometry of Triton 1992–2004: Surface volatile transport and discovery of a remarkable opposition surge. *Icarus 212*, 835–846.

Butcher, F. E., N. S. Arnold, M. R. Balme, S. J. Conway, C. D. Clark, C. Gallagher, A. Hagermann, S. R. Lewis, A. M. Rutledge, R. D. Storrar, et al. (2023). Eskers associated with buried glaciers in Mars' mid latitudes: recent advances and future directions. *Annals of Glaciology*, 1–6.

Butcher, F. E., M. R. Balme, C. Gallagher, N. S. Arnold, S. J. Conway, A. Hagermann, and S. R. Lewis (2017). Recent basal melting of a mid-latitude glacier on Mars. *Journal of Geophysical Research: Planets 122*(12), 2445–2468.

Byrne, P. K., R. C. Ghail, M. S. Gilmore, A. C. Şengör, C. Klimczak, D. A. Senske, J. L. Whitten, S. Khawja, R. E. Ernst, and S. C. Solomon (2020). Venus tesserae feature layered, folded, and eroded rocks. *Geology 49*(1), 81–85.

Campbell, B. A., G. A. Morgan, J. L. Whitten, L. M. Carter, L. S. Glaze, and D. B. Campbell (2017). Pyroclastic flow deposits on Venus as indicators of renewed magmatic activity. *Journal of Geophysical Research: Planets 122*(7), 1580–1596.

Campbell, I. H. and S. R. Taylor (1983). No water, no granites - No oceans, no continents. *Geophysical Research Letters 10*(11), 1061–1064.

Cardenas, B. T. and M. P. Lamb (2022). Paleogeographic Reconstructions of an Ocean Margin on Mars Based on Deltaic Sedimentology at Aeolis Dorsa. *Journal of Geophysical Research: Planets 127*(10), e2022JE007390.

Carr, M. H. (1979). Formation of Martian flood features by release of water from confined aquifers. *Journal of Geophysical Research: Solid Earth 84*(B6), 2995–3007.

Cassata, W. S., D. L. Shuster, P. R. Renne, and B. P. Weiss (2012). Trapped Ar isotopes in meteorite ALH 84001 indicate Mars did not have a thick ancient atmosphere. *Icarus 221*(1), 461–465.

Cassata, W. S., K. J. Zahnle, K. M. Samperton, P. C. Stephenson, and J. Wimpenny (2022). Xenon isotope constraints on ancient Martian atmospheric escape. *Earth and Planetary Science Letters 580*, 117349.

Ceplecha, Z., J. Borovička, W. G. Elford, D. O. ReVelle, R. L. Hawkes, V. Porubčan, and M. Šimek (1998). Meteor Phenomena and Bodies. *Space Science Reviews 84*(3), 327–471.

Chappelow, J. E. and V. L. Sharpton (2005). Influences of atmospheric variations on Mars's record of small craters. *Icarus 178*(1), 40–55.

Chassefière, E. (1996). Hydrodynamic escape of oxygen from primitive atmospheres: applications to the cases of Venus and Mars. *Icarus 124*(2), 537–552.

Chassefière, E. and F. Leblanc (2004). Mars atmospheric escape and evolution; interaction with the solar wind. *Planetary and Space Science 52*, 1039–1058.

Chassefière, E., F. Leblanc, and B. Langlais (2007). The combined effects of escape and magnetic field histories at Mars. *Planetary and Space Science 55*(3), 343–357.

Cheng, N.-S. and X. Chen (2014). Slope correction for calculation of bedload sediment transport rates in steep channels. *Journal of Hydraulic Engineering 140*(6), 04014018.

Chien, F.-C. and H.-C. Kuo (2011). On the extreme rainfall of Typhoon Morakot (2009). *Journal of Geophysical Research: Atmospheres 116*(D5).

Chitwood, L. A. and R. A. Jensen (2000). Large Prehistoric Flood Along Paulina Creek, Newberry Volcano, Oregon. *What's New at Newberry Volcano, Oregon: Guidebook for the Friends of the Pleistocene Eighth Annual Pacific Northwest Cell Field Trip*, 31–40.

Ciesla, F. J., G. D. Mulders, I. Pascucci, and D. Apai (2015). Volatile delivery to planets from water-rich planetesimals around low-mass stars. *The Astrophysical Journal 804*(1), 9.

Citron, R. I., M. Manga, and D. J. Hemingway (2018). Timing of oceans on Mars from shoreline deformation. *Nature 555*(7698), 643–646.

Clague, J. J. and S. G. Evans (2000). A review of catastrophic drainage of moraine-dammed lakes in British Columbia. *Quaternary Science Reviews 19*(17-18), 1763–1783.

Clifford, S. M., J. Lasue, E. Heggy, J. Boisson, P. McGovern, and M. D. Max (2010). Depth of the Martian cryosphere: Revised estimates and implications for the existence and detection of subpermafrost groundwater. *Journal of Geophysical Research: Planets 115*(E7).

Clifford, S. M. and T. J. Parker (2001). The Evolution of the Martian Hydrosphere: Implications for the Fate of a Primordial Ocean and the Current State of the Northern Plains. *Icarus 154*(1), 40–79.

Clow, G. D. (1987). Generation of liquid water on Mars through the melting of a dusty snowpack. *Icarus 72*(1), 95–127.

Cockell, C. S., T. Bush, C. Bryce, S. Direito, M. Fox-Powell, J. Harrison, H. Lammer, H. Landenmark, J. Martin-Torres, N. Nicholson, et al. (2016). Habitability: a review. *Astrobiology 16*(1), 89–117.

Coleman, N. M. (2005). Martian megaflood-triggered chaos formation, revealing groundwater depth, cryosphere thickness, and crustal heat flux. *Journal of Geophysical Research: Planets 110*(E12).

Conway, S. J., F. E. Butcher, T. de Haas, A. A. Deijns, P. M. Grindrod, and J. M. Davis (2018). Glacial and gully erosion on Mars: A terrestrial perspective. *Geomorphology 318*, 26–57.

Conway, S. J., N. Hovius, T. Barnie, J. Besserer, S. Le Mouélic, R. Orosei, and N. A. Read (2012). Climate-driven deposition of water ice and the formation of mounds in craters in Mars' north polar region. *Icarus 220*(1), 174–193.

Cook, K. L., C. Andermann, F. Gimbert, B. R. Adhikari, and N. Hovius (2018). Glacial lake outburst floods as drivers of fluvial erosion in the himalaya. *Science 362*(6410), 53–57.

Costa, F., R. Dohmen, and S. Chakraborty (2008). Time scales of magmatic processes from modeling the zoning patterns of crystals. *Reviews in Mineralogy and Geochemistry 69*, 545–594.

Costa, J. E. and R. L. Schuster (1988). The formation and failure of natural dams. *GSA Bulletin 100*(7), 1054–1068.

Cottrell, E. and K. A. Kelley (2011). The oxidation state of fe in morb glasses and the oxygen fugacity of the upper mantle. *Earth and Planetary Science Letters 305*(3-4), 270–282.

Craddock, R. A. and A. D. Howard (2002). The case for rainfall on a warm, wet early Mars. *Journal of Geophysical Research: Planets 107*(E11), 21–1.

Craddock, R. A., T. A. Maxwell, and A. D. Howard (1997a). Crater morphometry and modification in the Sinus Sabaeus and Margaritifer Sinus regions of Mars. *Journal of Geophysical Research: Planets 102*(E6), 13321–13340.

Craddock, R. A., T. A. Maxwell, and A. D. Howard (1997b). Crater morphometry and modification in the sinus sabaeus and margaritifer sinus regions of Mars. *Journal of Geophysical Research: Planets 102*(E6), 13321–13340.

Damgaard, J. S., R. J. Whitehouse, and R. L. Soulsby (1997). Bed-load sediment transport on steep longitudinal slopes. *Journal of Hydraulic Engineering 123*(12), 1130–1138.

Danyushevsky, L. V. (2001). The effect of small amounts of H_2O on crystallisation of mid-ocean ridge and backarc basin magmas. *Journal of Volcanology and Geothermal Research 110*(3-4), 265–280.

Davis, J., M. Balme, P. Grindrod, R. Williams, and S. Gupta (2016). Extensive Noachian fluvial systems in Arabia Terra: Implications for early Martian climate. *Geology 44*, 847–850.

Davis, P. M. (1993). Meteoroid Impacts as Seismic Sources on Mars. *Icarus 105*(2), 469–478.

De Bergh, C., B. Bezard, T. Owen, D. Crisp, J.-P. Maillard, and B. L. Lutz (1991). Deuterium on Venus: observations from Earth. *Science 251*(4993), 547–549.

Deng, J., Z. Du, B. B. Karki, D. B. Ghosh, and K. K. Lee (2020). A magma ocean origin to divergent redox evolutions of rocky planetary bodies and early atmospheres. *Nature Communications 11*(1), 1–7.

Desiage, P.-A., P. Lajeunesse, G. St-Onge, A. Normandeau, G. Ledoux, H. Guyard, and R. Pienitz (2015). Deglacial and postglacial evolution of the pingualuit crater lake basin, northern québec (Canada). *Geomorphology 248*, 327–343.

di Achille, G. and B. M. Hynek (2010). Ancient ocean on Mars supported by global distribution of deltas and valleys. *Nature Geoscience 3*, 459–463.

Dickson, J., L. Kerber, C. Fassett, and B. Ehlmann (2018). A global, blended ctx mosaic of Mars with vectorized seam mapping: A new mosaicking pipeline using principles of non-destructive image editing. In *49th Lunar and Planetary Science Conference*, Volume 49, pp. 2083.

Dickson, J. L., C. I. Fassett, and J. W. Head (2009). Amazonian-aged fluvial valley systems in a climatic microenvironment on Mars: Melting of ice deposits on the interior of Lyot Crater. *Geophysical Research Letters 36*(8).

Domenico, P. A., F. W. Schwartz, et al. (1998). *Physical and chemical hydrogeology*, Volume 506. Wiley New York.

Donahue, T. M. (1999). New analysis of hydrogen and deuterium escape from Venus. *Icarus 141*(2), 226–235.

Donahue, T. M., J. H. Hoffman, R. R. Hodges, and A. J. Watson (1982). Venus Was Wet: A Measurement of the Ratio of Deuterium to Hydrogen. *Science 216*(4546), 630–633.

Dong, C., Y. Lee, Y. Ma, M. Lingam, S. Bougher, J. Luhmann, S. Curry, G. Toth, A. Nagy, V. Tenishev, X. Fang, D. Mitchell, D. Brain, and B. Jakosky (2018). Modeling Martian Atmospheric Losses over Time: Implications for Exoplanetary Climate Evolution and Habitability. *The Astrophysical Journal 859*(1), L14.

Dorren, D. and E. F. Guinan (1994). HD 129333: the Sun in its infancy. *The Astrophysical Journal 428*, 805–818.

Dussaillant, A., G. Benito, W. Buytaert, P. Carling, C. Meier, and F. Espinoza (2010). Repeated glacial-lake outburst floods in Patagonia: an increasing hazard? *Natural Hazards 54*(2), 469–481.

Dyar, M. D., J. Helbert, A. Maturilli, N. T. Müller, and D. Kappel (2020). Probing Venus Surface Iron Contents With Six-Band Visible Near-Infrared Spectroscopy From Orbit. *Geophysical Research Letters 47*(23), e2020GL090497.

Edwards, C., J. Bandfield, P. Christensen, and A. Rogers (2014). The formation of infilled craters on Mars: Evidence for widespread impact induced decompression of the early Martian mantle? *Icarus 228*, 149–166.

Ehlmann, B. L., F. S. Anderson, J. Andrews-Hanna, D. C. Catling, P. R. Christensen, B. A. Cohen, C. D. Dressing, C. S. Edwards, L. T. Elkins-Tanton, K. A. Farley, C. I. Fassett, W. W. Fischer, A. A. Fraeman, M. P. Golombek, V. E. Hamilton, A. G. Hayes, C. D. K. Herd, B. Horgan, R. Hu, B. M. Jakosky, J. R. Johnson, J. F. Kasting, L. Kerber, K. M. Kinch, E. S. Kite, H. A. Knutson, J. I. Lunine, P. R. Mahaffy, N. Mangold, F. M. McCubbin, J. F. Mustard, P. B. Niles, C. Quantin-Nataf, M. S. Rice, K. M. Stack, D. J. Stevenson, S. T. Stewart, M. J. Toplis, T. Usui, B. P. Weiss, S. C. Werner, R. D. Wordsworth, J. J. Wray, R. A. Yingst, Y. L. Yung, and K. J. Zahnle (2016). The sustainability of habitability on terrestrial planets: Insights, questions, and needed measurements from Mars for understanding the evolution of Earth-like worlds. *Journal of Geophysical Research: Planets 121*(10), 1927–1961.

Elkins-Tanton, L. (2008). Linked magma ocean solidification and atmospheric growth for Earth and Mars. *Earth and Planetary Science Letters 271*(1), 181–191.

Elkins-Tanton, L. T. and B. H. Hager (2005). Giant meteoroid impacts can cause volcanism. *Earth and Planetary Science Letters 239*(3), 219–232.

Elkins-Tanton, L. T., S. E. Smrekar, P. C. Hess, and E. M. Parmentier (2007). Volcanism and volatile recycling on a one-plate planet: Applications to Venus. *Journal of Geophysical Research: Planets 112*(E4).

Fassett, C. I., J. L. Dickson, J. W. Head, J. S. Levy, and D. R. Marchant (2010). Supraglacial and proglacial valleys on Amazonian Mars. *Icarus 208*(1), 86–100.

Fassett, C. I. and J. W. Head (2005). Fluvial sedimentary deposits on Mars: Ancient deltas in a crater lake in the Nili Fossae region. *Geophysical Research Letters 32*(14).

Fassett, C. I. and J. W. Head (2008). Valley network-fed, open-basin lakes on Mars: Distribution and implications for Noachian surface and subsurface hydrology. *Icarus 198*(1), 37–56.

Fassett, C. I., J. S. Levy, J. L. Dickson, and J. W. Head (2014). An extended period of episodic northern mid-latitude glaciation on Mars during the Middle to Late Amazonian: Implications for long-term obliquity history. *Geology 42*(9), 763–766.

Fastook, J. and J. Head (2013). Amazonian non-polar glaciation: supply-limited glacial history and the role of ice sequestration. In *44th Annual Lunar and Planetary Science Conference*, Number 1719, pp. 1256.

Fastook, J. L. and J. W. Head (2014). Amazonian mid- to high-latitude glaciation on Mars: Supply-limited ice sources, ice accumulation patterns, and concentric crater fill glacial flow and ice sequestration. *Planetary and Space Science 91*, 60–76.

Fastook, J. L. and J. W. Head (2015). Glaciation in the Late Noachian Icy Highlands: Ice accumulation, distribution, flow rates, basal melting, and top-down melting rates and patterns. *Planetary and Space Science 106*, 82–98.

Fastook, J. L., J. W. Head, and D. R. Marchant (2014). Formation of lobate debris aprons on Mars: Assessment of regional ice sheet collapse and debris-cover armoring. *Icarus 228*, 54–63.

Fastook, J. L., J. W. Head, D. R. Marchant, and F. Forget (2008). Tropical mountain glaciers on Mars: Altitude-dependence of ice accumulation, accumulation conditions, formation times, glacier dynamics, and implications for planetary spin-axis/orbital history. *Icarus 198*(2), 305–317.

Fernández-Fassnacht, E. and F. D. Río (1984). The vapour pressure of CO_2 from 194 to 243 K. *The Journal of Chemical Thermodynamics 16*(5), 469–474.

Fisher, T. G. (2020). Megaflooding associated with glacial Lake Agassiz. *Earth-Science Reviews 201*, 102974.

Folco, L., M. D. Martino, A. E. Barkooky, M. D'Orazio, A. Lethy, S. Urbini, I. Nicolosi, M. Hafez, C. Cordier, M. v. Ginneken, A. Zeoli, A. M. Radwan, S. E. Khrepy, M. E. Gabry, M. Gomaa, A. A. Barakat, R. Serra, and M. E. Sharkawi (2011). Kamil Crater (Egypt): Ground truth for small-scale meteorite impacts on Earth. *Geology 39*(2), 179–182.

Foley, B. J. (2015). The role of plate tectonic–climate coupling and exposed land area in the development of habitable climates on rocky planets. *The Astrophysical Journal 812*(1), 36.

Foley, B. J. and A. J. Smye (2018). Carbon cycling and habitability of Earth-sized stagnant lid planets. *Astrobiology 18*(7), 873–896.

Forget, F., R. Haberle, F. Montmessin, B. Levrard, and J. Head (2006). Formation of glaciers on Mars by atmospheric precipitation at high obliquity. *science 311*(5759), 368–371.

Forget, F., F. Hourdin, R. Fournier, C. Hourdin, O. Talagrand, M. Collins, S. R. Lewis, P. L. Read, and J.-P. Huot (1999). Improved general circulation models of the Martian atmosphere from the surface to above 80 km. *Journal of Geophysical Research: Planets 104*(E10), 24155–24176.

Forget, F., R. Wordsworth, E. Millour, J.-B. Madeleine, L. Kerber, J. Leconte, E. Marcq, and R. Haberle (2013). 3D modelling of the early Martian climate under a denser CO_2 atmosphere: Temperatures and CO_2 ice clouds. *Icarus 222(1)*, 81–99.

French, R. H. (1985). *Open-channel hydraulics*. McGraw-Hill, Stuggart. New York.

Fricker, H. A., M. R. Siegfried, S. P. Carter, and T. A. Scambos (2016). A decade of progress in observing and modelling Antarctic subglacial water systems. *Philosophical Transactions of the Royal Society of London Series A 374*(2059), 20140294.

Gallagher, C. and M. Balme (2015). Eskers in a complete, wet-based glacial system in the Phlegra Montes region, Mars. *Earth and Planetary Science Letters 431*, 96–109.

Garvin, J. B., G. Arney, S. Getty, N. Johnson, W. Kiefer, R. Lorenz, M. Ravine, C. Malespin, C. Webster, B. Campbell, N. Izenberg, and V. Cottini (2020). DAVINCI+: Deep Atmosphere of Venus Investigation of Noble Gases, Chemistry, and Imaging Plus. In *Lunar and Planetary Science Conference*, Lunar and Planetary Science Conference, pp. 2599.

Garvin, J. B., J. W. Head, and L. Wilson (1982). Magma vesiculation and pyroclastic volcanism on Venus. *Icarus 52*(2), 365–372.

Garvin, J. B., S. E. Sakimoto, J. J. Frawley, and C. Schnetzler (2000). North polar region craterforms on Mars: Geometric characteristics from the Mars orbiter laser altimeter. *Icarus 144*(2), 329–352.

Ghail, R. C. and L. Wilson (2015). A pyroclastic flow deposit on Venus. *Geological Society, London, Special Publications 401*(1), 97–106.

Ghiorso, M. S. and R. O. Sack (1995). Chemical mass transfer in magmatic processes IV. A revised and internally consistent thermodynamic model for the interpolation and extrapolation of liquid-solid equilibria in magmatic systems at elevated temperatures and pressures. *Contributions to Mineralogy and Petrology 119*(2), 197–212.

Gillmann, C., E. Chassefière, and P. Lognonné (2009). A consistent picture of early hydrodynamic escape of Venus atmosphere explaining present Ne and Ar isotopic ratios and low oxygen atmospheric content. *Earth and Planetary Science Letters 286*(3-4), 503–513.

Gillmann, C., G. J. Golabek, S. N. Raymond, M. Schönbächler, P. J. Tackley, V. Dehant, and V. Debaille (2020). Dry late accretion inferred from Venus's coupled atmosphere and internal evolution. *Nature Geoscience 13*(4), 265–269.

Gillmann, C., G. J. Golabek, and P. J. Tackley (2016). Effect of a single large impact on the coupled atmosphere-interior evolution of Venus. *Icarus 268*, 295 – 312.

Glaze, L. S., S. M. Baloga, and J. Wimert (2011). Explosive volcanic eruptions from linear vents on Earth, Venus, and Mars: Comparisons with circular vent eruptions. *Journal of Geophysical Research: Planets 116*(E1).

Glotch, T. D. and A. D. Rogers (2013). Evidence for magma-carbonate interaction beneath Syrtis Major, Mars. *Journal of Geophysical Research: Planets 118*(1), 126–137.

Goddard, K., N. H. Warner, S. Gupta, and J.-R. Kim (2014). Mechanisms and timescales of fluvial activity at Mojave and other young Martian craters. *Journal of Geophysical Research: Planets 119*(3), 604–634.

Goldin, T. J. and H. J. Melosh (2009). Self-shielding of thermal radiation by Chicxulub impact ejecta: Firestorm or fizzle? *Geology 37*(12), 1135–1138.

Golombek, M. and N. Bridges (2000). Erosion rates on Mars and implications for climate change: Constraints from the Pathfinder landing site. *Journal of Geophysical Research: Planets 105*(E1), 1841–1853.

Golombek, M., N. Warner, V. Ganti, M. Lamb, T. Parker, R. L. Fergason, and R. Sullivan (2014). Small crater modification on Meridiani Planum and implications for erosion rates and climate change on Mars. *Journal of Geophysical Research: Planets 119*(12), 2522–2547.

Golombek, M. P., J. A. Grant, L. S. Crumpler, R. Greeley, R. E. Arvidson, J. F. Bell, C. M. Weitz, R. Sullivan, P. R. Christensen, L. Soderblom, et al. (2006). Erosion rates at the Mars Exploration Rover landing sites and long-term climate change on Mars. *Journal of Geophysical Research: Planets 111*(E12).

Goudge, T. A., C. I. Fassett, M. Coholich, and E. R. Bamber (2023). Assessing controls on the incomplete draining of martian open-basin lakes. *Journal of Geophysical Research: Planets 128*(1), e2022JE007443.

Goudge, T. A., C. I. Fassett, J. W. Head, J. F. Mustard, and K. L. Aureli (2016). Insights into surface runoff on early Mars from paleolake basin morphology and stratigraphy. *Geology 44*(6), 419–422.

Goudge, T. A., C. I. Fassett, and D. Mohrig (2019). Incision of paleolake outlet canyons on Mars from overflow flooding. *Geology 47*(1), 7–10.

Gough, D. O. (1981, Nov). Solar interior structure and luminosity variations. *Solar Physics 74*(1), 21–34.

Grant, J. A., I. Irwin, Rossman P., J. P. Grotzinger, R. E. Milliken, L. L. Tornabene, A. S. McEwen, C. M. Weitz, S. W. Squyres, T. D. Glotch, and B. J. Thomson (2008). HiRISE imaging of impact megabreccia and sub-meter aqueous strata in Holden Crater, Mars. *Geology 36*(3), 195–198.

Grant, J. A. and P. H. Schultz (1993). Degradation of selected terrestrial and Martian impact craters. *Journal of Geophysical Research: Planets 98*(E6), 11025–11042.

Grant, J. A. and S. A. Wilson (2011). Late alluvial fan formation in southern Margaritifer Terra, Mars. *Geophysical Research Letters 38*(8).

Grant, J. A. and S. A. Wilson (2019). Evidence for late alluvial activity in Gale crater, Mars. *Geophysical Research Letters 46*(13), 7287–7294.

Grau Galofre, A., A. M. Jellinek, and G. R. Osinski (2020). Valley formation on early Mars by subglacial and fluvial erosion. *Nature Geoscience 13*(10), 663–668.

Grau Galofre, A., A. M. Jellinek, G. R. Osinski, M. Zanetti, and A. Kukko (2018). Subglacial drainage patterns of Devon Island, Canada: detailed comparison of rivers and subglacial meltwater channels. *The Cryosphere 12*(4), 1461–1478.

Gray, J. T. and B. Lauriol (1985). Dynamics of the late Wisconsin ice sheet in the Ungava Peninsula interpreted from geomorphological evidence. *Arctic and Alpine Research 17*(3), 289–310.

Greeley, R. and B. Schneid (1991). Magma generation on Mars—amounts, rates, and comparisons with Earth, Moon, and Venus. *Science 254*, 996–998.

Grimm, Simon L., Demory, Brice-Olivier, Gillon, Michaël, Dorn, Caroline, Agol, Eric, Burdanov, Artem, Delrez, Laetitia, Sestovic, Marko, Triaud, Amaury H. M. J., Turbet, Martin, Bolmont, Émeline, Caldas, Anthony, de Wit, Julien, Jehin, Emmanuël, Leconte, Jérémy, Raymond, Sean N., Van Grootel, Valérie, Burgasser, Adam J., Carey, Sean, Fabrycky, Daniel, Heng, Kevin, Hernandez, David M., Ingalls, James G., Lederer, Susan, Selsis, Franck, and Queloz, Didier (2018). The nature of the TRAPPIST-1 exoplanets. *Astronomy & Astrophysics 613*, A68.

Grinspoon, D. H. (1993). Implications of the high D/H ratio for the sources of water in Venus' atmosphere. *Nature 363*(6428), 428–431.

Gronoff, G., P. Arras, S. Baraka, J. M. Bell, G. Cessateur, O. Cohen, S. M. Curry, J. J. Drake, M. Elrod, J. Erwin, K. Garcia-Sage, C. Garraffo, A. Glocer, N. G. Heavens, K. Lovato, R. Maggiolo, C. D. Parkinson, C. Simon Wedlund, D. R. Weimer, and W. B. Moore (2020). Atmospheric escape processes and planetary atmospheric evolution. *Journal of Geophysical Research: Space Physics 125*(8), e2019JA027639.

Grotzinger, J. P., S. Gupta, M. C. Malin, D. M. Rubin, J. Schieber, K. Siebach, D. Y. Sumner, K. M. Stack, A. R. Vasavada, R. E. Arvidson, F. Calef, L. Edgar, W. F. Fischer, J. A. Grant, J. Griffes, L. C. Kah, M. P. Lamb, K. W. Lewis, N. Mangold, M. E. Minitti, M. Palucis, M. Rice, R. M. E. Williams, R. A. Yingst, D. Blake, D. Blaney, P. Conrad, J. Crisp, W. E. Dietrich, G. Dromart, K. S. Edgett, R. C. Ewing, R. Gellert, J. A. Hurowitz, G. Kocurek, P. Mahaffy, M. J. McBride, S. M. McLennan, M. Mischna, D. Ming, R. Milliken, H. Newsom, D. Oehler, T. J. Parker, D. Vaniman, R. C. Wiens, and S. A.

Wilson (2015). Deposition, exhumation, and paleoclimate of an ancient lake deposit, Gale crater, Mars. *Science 350*(6257).

Grotzinger, J. P. and R. E. Milliken (2012). The Sedimentary Rock Record of Mars: Distribution, Origins, and Global Stratigraphy. In *Sedimentary Geology of Mars*. SEPM Society for Sedimentary Geology.

Grotzinger, J. P., D. Y. Sumner, L. C. Kah, K. Stack, S. Gupta, L. Edgar, D. Rubin, K. Lewis, J. Schieber, N. Mangold, R. Milliken, P. G. Conrad, D. DesMarais, J. Farmer, K. Siebach, F. Calef, J. Hurowitz, S. M. McLennan, D. Ming, D. Vaniman, J. Crisp, A. Vasavada, K. S. Edgett, M. Malin, D. Blake, R. Gellert, P. Mahaffy, R. C. Wiens, S. Maurice, J. A. Grant, S. Wilson, R. C. Anderson, L. Beegle, R. Arvidson, B. Hallet, R. S. Sletten, M. Rice, J. Bell, J. Griffes, B. Ehlmann, R. B. Anderson, T. F. Bristow, W. E. Dietrich, G. Dromart, J. Eigenbrode, A. Fraeman, C. Hardgrove, K. Herkenhoff, L. Jandura, G. Kocurek, S. Lee, L. A. Leshin, R. Leveille, D. Limonadi, J. Maki, S. McCloskey, M. Meyer, M. Minitti, H. Newsom, D. Oehler, A. Okon, M. Palucis, T. Parker, S. Rowland, M. Schmidt, S. Squyres, A. Steele, E. Stolper, R. Summons, A. Treiman, R. Williams, A. Yingst, and MSL Science Team (2014). A Habitable Fluvio-Lacustrine Environment at Yellowknife Bay, Gale Crater, Mars. *Science 343*(6169), 1242777.

Haberle, R. M. (1998). Early Mars Climate Models. *Journal of Geophysical Research: Planets 103*(E12), 28467–28479.

Haberle, R. M., R. T. Clancy, F. Forget, M. D. Smith, and R. W. Zurek (2017). *The Atmosphere and Climate of Mars*. Cambridge University Press.

Haberle, R. M., D. Tyler, C. P. McKay, and W. L. Davis (1994). A Model for the Evolution of CO_2 on Mars. *Icarus 109*(1), 102–120.

Hacker, B. R., G. A. Abers, and S. M. Peacock (2003). Subduction factory 1. Theoretical mineralogy, densities, seismic wave speeds, and H_2O contents. *Journal of Geophysical Research: Solid Earth 108*(B1).

Halevy, I. and J. W. Head (2014). Episodic warming of early Mars by punctuated volcanism. *Nature Geoscience 7*(12), 865–868.

Hamano, K., Y. Abe, and H. Genda (2013). Emergence of two types of terrestrial planet on solidification of magma ocean. *Nature 497*(7451), 607–610.

Hancox, G. T., M. J. McSaveney, V. R. Manville, and T. R. Davies (2005). The October 1999 Mt Adams rock avalanche and subsequent landslide dam-break flood and effects in Poerua River, Westland, New Zealand. *New Zealand Journal of Geology and Geophysics 48*(4), 683–705.

Hanna, J. C. and R. J. Phillips (2005). Hydrological modeling of the Martian crust with application to the pressurization of aquifers. *Journal of Geophysical Research: Planets 110*(E1).

Harrison, K. P. and R. E. Grimm (2004). Tharsis recharge: A source of groundwater for Martian outflow channels. *Geophysical Research Letters 31*(14).

Harrison, K. P. and R. E. Grimm (2005). Groundwater-controlled valley networks and the decline of surface runoff on early Mars. *Journal of Geophysical Research: Planets 110*(E12).

Harrison, K. P. and R. E. Grimm (2009). Regionally compartmented groundwater flow on Mars. *Journal of Geophysical Research: Planets 114*(E4).

Hart, M. H. (1979). Habitable zones about main sequence stars. *Icarus 37*(1), 351–357.

Hartmann, W. K. (2005). Martian cratering 8: Isochron refinement and the chronology of Mars. *Icarus 174*(2), 294–320.

Hasterok, D. and J. Webb (2017). On the radiogenic heat production of igneous rocks. *Geoscience Frontiers 8*(5), 919–940.

Hauber, E., T. Platz, D. Reiss, L. Le Deit, M. Kleinhans, W. Marra, T. de Haas, and P. Carbonneau (2013). Asynchronous formation of Hesperian and Amazonian-aged deltas on Mars and implications for climate. *Journal of Geophysical Research: Planets 118*(7), 1529–1544.

Hauck, S. A. and R. J. Phillips (2002). Thermal and crustal evolution of Mars. *Journal of Geophysical Research: Planets 107*, 6–19.

Head, J., G. Neukum, R. Jaumann, H. Hiesinger, E. Hauber, M. Carr, P. Masson, B. Foing, H. Hoffmann, M. Kreslavsky, et al. (2005). Tropical to mid-latitude snow and ice accumulation, flow and glaciation on Mars. *Nature 434*(7031), 346–351.

Head, J. W., C. I. Fassett, S. J. Kadish, D. E. Smith, M. T. Zuber, G. A. Neumann, and E. Mazarico (2010). Global distribution of large lunar craters: Implications for resurfacing and impactor populations. *science 329*(5998), 1504–1507.

Head, J. W. and D. R. Marchant (2014). The climate history of early Mars: insights from the Antarctic McMurdo Dry Valleys hydrologic system. *Antarctic Science 26*(6), 774–800.

Head, J. W., J. F. Mustard, M. A. Kreslavsky, R. E. Milliken, and D. R. Marchant (2003). Recent ice ages on Mars. *Nature 426*(6968), 797–802.

Heard, A. W. and E. S. Kite (2020). A probabilistic case for a large missing carbon sink on Mars after 3.5 billion years ago. *Earth and Planetary Science Letters 531*, 116001.

Hecht, M. H. (2002). Metastability of Liquid Water on Mars. *Icarus 156*(2), 373–386.

Helo, C., M.-A. Longpré, N. Shimizu, D. A. Clague, and J. Stix (2011). Explosive eruptions at mid-ocean ridges driven by CO_2-rich magmas. *Nature Geoscience 4*(4), 260–263.

Herrick, R. R. and S. Hensley (2023). Surface changes observed on a Venusian volcano during the Magellan mission. *Science 379*(6638), 1205–1208.

Hibbard, S. M. (2021). *Surface Morphology and Subsurface Ice Content Relationships in Arcadia Planitia, Mars and the Canadian High Arctic*. Ph. D. thesis, The University of Western Ontario.

Hills, J. G. and M. P. Goda (1993). The Fragmentation of Small Asteroids in the Atmosphere. *Astronomical Journal 105*, 1114.

Hoffert, M., A. Callegari, C. Hsieh, and W. Ziegler (1981). Liquid water on Mars: An energy balance climate model for co2/h2o atmospheres. *Icarus 47*(1), 112–129.

Holo, S. and E. Kite (2019). Dynamics of Mars Lake-Overflow Valley Incision. In *Lunar and Planetary Science Conference*, Volume 50, abstract number 2481.

Holo, S. J., E. S. Kite, S. A. Wilson, and A. M. Morgan (2021). The timing of alluvial fan formation on Mars. *The Planetary Science Journal 2*(5), 210.

Holsapple, K. A. (1993). The scaling of impact processes in planetary sciences. *Annual Review of Earth and Planetary Sciences 21*, 333–373.

Holt, J. W., A. Safaeinili, J. J. Plaut, J. W. Head, R. J. Phillips, R. Seu, S. D. Kempf, P. Choudhary, D. A. Young, N. E. Putzig, et al. (2008). Radar sounding evidence for buried glaciers in the southern mid-latitudes of Mars. *Science 322*(5905), 1235–1238.

Höning, D., P. Baumeister, J. L. Grenfell, N. Tosi, and M. J. Way (2021). Early Habitability and Crustal Decarbonation of a Stagnant-Lid Venus. *Journal of Geophysical Research: Planets 126*(10), e2021JE006895.

Horner, J., O. Mousis, J.-M. Petit, and B. Jones (2009). Differences between the impact regimes of the terrestrial planets: Implications for primordial D:H ratios. *Planetary and Space Science 57*(12), 1338–1345.

Houghton, B. and H. Gonnermann (2008). Basaltic explosive volcanism: Constraints from deposits and models. *Geochemistry 68*(2), 117 – 140.

Howard, A., S. Wilson, and J. Moore (2022). Fresh Shallow Valleys and Exit Breach Mid-Latitude Craters: Formation Below a Thick Ice Cover. In *European Planetary Science Congress*, pp. EPSC2022–180.

Hu, R., D. M. Kass, B. L. Ehlmann, and Y. L. Yung (2015). Tracing the fate of carbon and the atmospheric evolution of Mars. *Nature Communications 6*, 10003.

Huenges, E., J. Erzinger, J. Kück, B. Engeser, and W. Kessels (1997). The permeable crust: Geohydraulic properties down to 9101 m depth. *Journal of Geophysical Research: Planets 102*(B8), 18,255–18,265.

Huntsberger, T., G. Rodriguez, and P. S. Schenker (2000). Robotics Challenges for Robotic and Human Mars Exploration. In *Fourth International Conference and Exposition on Robotics for Challenging Situations and Environments*, pp. 340–346.

Hynek, B. and G. di Achille (2017). Geologic map of Meridiani Planum, Mars. *US Geological Survey Scientific Investigations Map 3356*.

Hynek, B. M., M. Beach, and M. R. T. Hoke (2010). Updated global map of Martian valley networks and implications for climate and hydrologic processes. *Journal of Geophysical Research 115*(E9).

Ingersoll, A. P. (1969). The runaway greenhouse: A history of water on Venus. *Journal of Atmospheric Sciences 26*(6), 1191–1198.

Ingersoll, A. P. (1970). Mars: Occurrence of liquid water. *Science 168*(3934), 972–973.

Irwin, R. P. (2013). Testing Links Between Impacts and Fluvial Erosion on Post-Noachian Mars. In *44th Lunar and Planetary Science Conference*, Houston, pp. Abstract #2958. Lunar and Planetary Institute.

Irwin III, R. P., K. L. Tanaka, and S. J. Robbins (2013). Distribution of early, middle, and late Noachian cratered surfaces in the Martian highlands: Implications for resurfacing events and processes. *Journal of Geophysical Research: Planets 118*(2), 278–291.

Ivanov, B. A., G. Neukum, and R. Wagner (2001). *Size-Frequency Distributions of Planetary Impact Craters and Asteroids*, pp. 1–34. Dordrecht: Springer Netherlands.

Ivanov, M. A. and J. W. Head (2013). The history of volcanism on Venus. *Planetary and Space Science 84*, 66–92.

Jakosky, B. M. (2019). The CO_2 inventory on Mars. *Planetary and Space Science 175*, 52–59.

Jakosky, B. M., D. Brain, M. Chaffin, S. Curry, J. Deighan, J. Grebowsky, J. Halekas, F. Leblanc, R. Lillis, J. G. Luhmann, L. Andersson, N. Andre, D. Andrews, D. Baird, D. Baker, J. Bell, M. Benna, D. Bhattacharyya, S. Bougher, C. Bowers, P. Chamberlin, J. Y. Chaufray, J. Clarke, G. Collinson, M. Combi, J. Connerney, K. Connour, J. Correira, K. Crabb, F. Crary, T. Cravens, M. Crismani, G. Delory, R. Dewey, G. DiBraccio, C. Dong, Y. Dong, P. Dunn, H. Egan, M. Elrod, S. England, F. Eparvier, R. Ergun, A. Eriksson, T. Esman, J. Espley, S. Evans, K. Fallows, X. Fang, M. Fillingim, C. Flynn, A. Fogle, C. Fowler, J. Fox, M. Fujimoto, P. Garnier, Z. Girazian, H. Groeller, J. Gruesbeck, O. Hamil, K. G. Hanley, T. Hara, Y. Harada, J. Hermann, M. Holmberg, G. Holsclaw, S. Houston, S. Inui, S. Jain, R. Jolitz, A. Kotova, T. Kuroda, D. Larson, Y. Lee, C. Lee, F. Lefevre, C. Lentz, D. Lo, R. Lugo, Y. J. Ma, P. Mahaffy, M. L. Marquette, Y. Matsumoto, M. Mayyasi, C. Mazelle, W. McClintock, J. McFadden, A. Medvedev, M. Mendillo, K. Meziane, Z. Milby, D. Mitchell, R. Modolo, F. Montmessin, A. Nagy, H. Nakagawa, C. Narvaez, K. Olsen, D. Pawlowski, W. Peterson, A. Rahmati, K. Roeten, N. Romanelli, S. Ruhunusiri, C. Russell, S. Sakai, N. Schneider, K. Seki, R. Sharrar, S. Shaver, D. E. Siskind, M. Slipski, Y. Soobiah, M. Steckiewicz, M. H. Stevens, I. Stewart, A. Stiepen, S. Stone, V. Tenishev, N. Terada, K. Terada, E. Thiemann, R. Tolson, G. Toth, J. Trovato, M. Vogt, T. Weber, P. Withers, S. Xu, R. Yelle,

E. Yiğit, and R. Zurek (2018). Loss of the Martian atmosphere to space: Present-day loss rates determined from MAVEN observations and integrated loss through time. *Icarus 315*, 146–157.

Jakosky, B. M., B. G. Henderson, and M. T. Mellon (1995). Chaotic obliquity and the nature of the Martian climate. *Journal of Geophysical Research: Planets 100*(E1), 1579–1584.

Jakosky, B. M. and R. J. Phillips (2001). Mars' volatile and climate history. *Nature 412*(6843), 237.

James, P. B., M. T. Zuber, and R. J. Phillips (2013). Crustal thickness and support of topography on Venus. *Journal of Geophysical Research: Planets 118*(4), 859–875.

Jellinek, A. M. and M. G. Jackson. Connections between the bulk composition, geodynamics and habitability of Earth. *Nature Geosc volume=8, number=8, pages=587-593, issn=1752-0908, doi=10.1038/ngeo2488, url=https://doi.org/10.1038/ngeo2488*.

Jerolmack, D. J. and P. Sadler (2018). Transience and persistence in the depositional record of continental margins. *Journal of Geophysical Research: Earth Surface*, F03S13.

Jessup, K. L., J. R. Spencer, G. E. Ballester, R. R. Howell, F. Roesler, M. Vigel, and R. Yelle (2004). The atmospheric signature of Io's Prometheus plume and anti-jovian hemisphere: evidence for a sublimation atmosphere. *Icarus 169*, 197–215.

Johnson, N. M. and M. R. R. de Oliveira (2019). Venus Atmospheric Composition In Situ Data: A Compilation. *Earth and Space Science 6*(7), 1299–1318.

Johnstone, C. P., Güdel, M., Lammer, H., and Kislyakova, K. G. (2018). Upper atmospheres of terrestrial planets: Carbon dioxide cooling and the Earth´s thermospheric evolution. *Astronomy and Astrophysics 617*, A107.

Kadish, S. J., J. W. Head, and N. G. Barlow (2010). Pedestal crater heights on Mars: A proxy for the thicknesses of past, ice-rich, Amazonian deposits. *Icarus 210*(1), 92–101.

Kamphuis, J. (1974). Determination of sand roughness for fixed beds. *Journal of Hydraulic Research 12*(2), 193–203.

Kane, S. R., G. Arney, D. Crisp, S. Domagal-Goldman, L. S. Glaze, C. Goldblatt, D. Grinspoon, J. W. Head, A. Lenardic, C. Unterborn, M. J. Way, and K. J. Zahnle (2019). Venus as a Laboratory for Exoplanetary Science. *Journal of Geophysical Research: Planets 124*(8), 2015–2028.

Kankanamge, D. G. and W. B. Moore (2019). A parameterization for volcanic heat flux in heat pipe planets. *Journal of Geophysical Research: Planets 124*(1), 114–127.

Kargel, J., G. Komatsu, V. Baker, and R. Strom (1993). The Volcanology of Venera and VEGA Landing Sites and the Geochemistry of Venus. *Icarus 103*(2), 253–275.

Kaspi, Y. and A. P. Showman (2015). Atmospheric dynamics of terrestrial exoplanets over a wide range of orbital and atmospheric parameters. *The Astrophysical Journal 804*(1), 60.

Kasting, J. F. (1988). Runaway and moist greenhouse atmospheres and the evolution of Earth and Venus. *Icarus 74*(3), 472–494.

Kasting, J. F., D. P. Whitmire, and R. T. Reynolds (1993). Habitable zones around main sequence stars. *Icarus 101*(1), 108–128.

Kaula, W. M. (1999). Constraints on Venus Evolution from Radiogenic Argon. *Icarus 139*(1), 32 – 39.

Kehew, A. E., M. L. Lord, A. L. Kozlowski, and T. G. Fisher (2009). *Proglacial megaflooding along the margins of the Laurentide ice sheet*, pp. 104 – 127.

Kerber, L., F. Forget, and R. Wordsworth (2015). Sulfur in the early Martian atmosphere revisited: Experiments with a 3-D Global Climate Model. *Icarus 261*, 133–148.

Kerrick, D. and J. Connolly (2001). Metamorphic devolatilization of subducted marine sediments and the transport of volatiles into the Earth's mantle. *Nature 411*(6835), 293–296.

Khawja, S., R. Ernst, C. Samson, P. Byrne, R. Ghail, and L. MacLellan (2020). Tesserae on Venus may preserve evidence of fluvial erosion. *Nature Communications 11*(1), 1–8.

King, J., I. Loveday, and R. L. Schuster (1989). The 1985 Bairaman landslide dam and resulting debris flow, Papua New Guinea. *Quarterly Journal of Engineering Geology and Hydrogeology 22*(4), 257–270.

Kingslake, J., J. C. Ely, I. Das, and R. E. Bell (2017). Widespread movement of meltwater onto and across Antarctic ice shelves. *Nature 544*(7650), 349–352.

Kite, E. S. (2019). Geologic Constraints on Early Mars Climate. *Space Science Reviews 215*(1), 10.

Kite, E. S., P. Gao, C. Goldblatt, M. A. Mischna, D. P. Mayer, and Y. L. Yung (2017). Methane bursts as a trigger for intermittent lake-forming climates on post-Noachian Mars. *Nature Geoscience 10*(10), 737–740.

Kite, E. S., I. Halevy, M. A. Kahre, M. J. Wolff, and M. Manga (2013). Seasonal melting and the formation of sedimentary rocks on Mars, with predictions for the Gale Crater mound. *Icarus 223*(1), 181–210.

Kite, E. S., A. Lucas, and C. I. Fassett (2013). Pacing early Mars river activity: Embedded craters in the Aeolis Dorsa region imply river activity spanned $\geq$(1–20)Myr. *Icarus 225*(1), 850–855.

Kite, E. S., D. P. Mayer, S. A. Wilson, J. M. Davis, A. S. Lucas, and G. Stucky de Quay (2019). Persistence of intense, climate-driven runoff late in Mars history. *Science Advances 5*(3), eaav7710.

Kite, E. S., M. A. Mischna, B. Fan, A. M. Morgan, S. A. Wilson, and M. I. Richardson (2022). Changing spatial distribution of water flow charts major change in Mars's greenhouse effect. *Science Advances 8*(21), eabo5894.

Kite, E. S. and A. Noblet (2022). High and dry: Billion-year trends in the aridity of river-forming climates on Mars. *Geophysical Research Letters*, e2022GL101150.

Kite, E. S., L. J. Steele, M. A. Mischna, and M. I. Richardson (2021). Warm early Mars surface enabled by high-altitude water ice clouds. *Proceedings of the National Academy of Sciences 118*(18), e2101959118.

Kite, E. S., J.-P. Williams, A. Lucas, and O. Aharonson (2014). Low palaeopressure of the Martian atmosphere estimated from the size distribution of ancient craters. *Nature Geoscience 7*, 335–339.

Kjær, K. H., N. K. Larsen, T. Binder, A. A. Bjørk, O. Eisen, M. A. Fahnestock, S. Funder, A. A. Garde, H. Haack, V. Helm, et al. (2018). A large impact crater beneath Hiawatha glacier in northwest Greenland. *Science Advances 4*(11), eaar8173.

Kopparapu, R. K., R. Ramirez, J. F. Kasting, V. Eymet, T. D. Robinson, S. Mahadevan, R. C. Terrien, S. Domagal-Goldman, V. Meadows, and R. Deshpande (2013). Habitable zones around main-sequence stars: new estimates. *The Astrophysical Journal 765*(2), 131.

Kopparapu, R. K., R. M. Ramirez, J. SchottelKotte, J. F. Kasting, S. Domagal-Goldman, and V. Eymet (2014). Habitable zones around main-sequence stars: Dependence on planetary mass. *The Astrophysical Journal Letters 787*(2), L29.

Korycansky, D. and K. Zahnle (2005). Modeling crater populations on Venus and Titan. *Planetary and Space Science 53*(7), 695–710.

Korycansky, D. and K. J. Zahnle (2004). Atmospheric impacts, fragmentation, and small craters on Venus. *Icarus 169*(2), 287–299.

Kreslavsky, M. A. and J. W. Head (2005). Mars at very low obliquity: Atmospheric collapse and the fate of volatiles. *Geophysical Research Letters 32*.

Kress, A. M. and J. W. Head (2008). Ring-mold craters in lineated valley fill and lobate debris aprons on Mars: Evidence for subsurface glacial ice. *Geophysical Research Letters 35*(23).

Krissansen-Totton, J., J. J. Fortney, and F. Nimmo (2021). Was Venus Ever Habitable? Constraints from a Coupled Interior–Atmosphere–Redox Evolution Model. *Planetary Science Journal 2*(5), 216.

Krissansen-Totton, J., J. J. Fortney, F. Nimmo, and N. Wogan (2021). Oxygen False Positives on Habitable Zone Planets Around Sun-Like Stars. *AGU Advances 2*(2), e2020AV000294.

Krissansen-Totton, J., M. Thompson, M. L. Galloway, and J. J. Fortney (2022). Understanding planetary context to enable life detection on exoplanets and test the Copernican principle. *Nature Astronomy 6*(2), 189–198.

Kruijver, A., D. Höning, and W. van Westrenen (2021). Carbon cycling and habitability of massive Earth-like exoplanets. *The Planetary Science Journal 2*(5), 208.

Kulikov, Y., H. Lammer, H. Lichtenegger, N. Terada, I. Ribas, C. Kolb, D. Langmayr, R. Lundin, E. Guinan, S. Barabash, and H. Biernat (2006). Atmospheric and water loss from early Venus. *Planetary and Space Science 54*(13), 1425 – 1444.

Kumar, P. S. (2005). Structural effects of meteorite impact on basalt: Evidence from Lonar crater, India. *Journal of Geophysical Research: Solid Earth 110*(B12).

Kumar, P. S. and D. A. Kring (2008). Impact fracturing and structural modification of sedimentary rocks at Meteor Crater, Arizona. *Journal of Geophysical Research: Planets 113*(E9).

Kurahashi-Nakamura, T. and E. Tajika (2006). Atmospheric collapse and transport of carbon dioxide into the subsurface on early Mars. *Geophysical Research Letters 33*(18).

Kurokawa, H., K. Kurosawa, and T. Usui (2018). A lower limit of atmospheric pressure on early Mars inferred from nitrogen and argon isotopic compositions. *Icarus 299*, 443–459.

Lacelle, D., A. F. Davila, D. Fisher, W. H. Pollard, R. DeWitt, J. Heldmann, M. M. Marinova, and C. P. McKay (2013). Excess ground ice of condensation–diffusion origin in university valley, Dry Valleys of Antarctica: Evidence from isotope geochemistry and numerical modeling. *Geochimica et Cosmochimica Acta 120*, 280–297.

Lagmay, A. M. F., K. S. Rodolfo, F. P. Siringan, H. Uy, C. Remotigue, P. Zamora, M. Lapus, R. Rodolfo, and J. Ong (2007). Geology and hazard implications of the Maraunot notch in the Pinatubo Caldera, Philippines. *Bulletin of Volcanology 69*(7), 797–809.

Lamb, M. P., W. E. Dietrich, and J. G. Venditti (2008). Is the critical shields stress for incipient sediment motion dependent on channel-bed slope? *Journal of Geophysical Research: Earth Surface 113*(F2).

Lamb, M. P., N. J. Finnegan, J. S. Scheingross, and L. S. Sklar (2015). New insights into the mechanics of fluvial bedrock erosion through flume experiments and theory. *Geomorphology 244*, 33–55.

Lammer, H., J. H. Bredehöft, A. Coustenis, M. L. Khodachenko, L. Kaltenegger, O. Grasset, D. Prieur, F. Raulin, P. Ehrenfreund, M. Yamauchi, J.-E. Wahlund, J.-M. Grießmeier, G. Stangl, C. S. Cockell, Y. N. Kulikov, J. L. Grenfell, and H. Rauer (2009). What makes a planet habitable? *The Astronomy and Astrophysics Review 17*(2), 181–249.

Lammer, H., E. Chassefière, O. Karatekin, A. Morschhauser, P. B. Niles, O. Mousis, P. Odert, U. V. Möstl, D. Breuer, V. Dehant, M. Grott, H. Gröller, E. Hauber, and L. B. S. Pham (2013). Outgassing History and Escape of the Martian Atmosphere and Water Inventory. *Space Science Reviews 174*(1), 113–154.

Lammer, H., J. F. Kasting, E. Chassefière, R. E. Johnson, Y. N. Kulikov, and F. Tian (2008). Atmospheric escape and evolution of terrestrial planets and satellites. *Space Science Reviews 139*(1), 399–436.

Lammer, H., H. Lichtenegger, H. Biernat, N. Erkaev, I. Arshukova, C. Kolb, H. Gunell, A. Lukyanov, M. Holmstrom, S. Barabash, T. Zhang, and W. Baumjohann (2006). Loss of hydrogen and oxygen from the upper atmosphere of Venus. *Planetary and Space Science 54*(13), 1445 – 1456.

Lammer, H., A. L. Zerkle, S. Gebauer, N. Tosi, L. Noack, M. Scherf, E. Pilat-Lohinger, M. Güdel, J. L. Grenfell, M. Godolt, and A. Nikolaou (2018). Origin and evolution of the atmospheres of early Venus, Earth and Mars. *The Astronomy and Astrophysics Review 26*(1), 2.

Langmuir, C. H., E. M. Klein, and T. Plank (2013). *Petrological Systematics of Mid-Ocean Ridge Basalts: Constraints on Melt Generation Beneath Ocean Ridges*, pp. 183–280. American Geophysical Union (AGU).

Lapotre, M. G. A., R. C. Ewing, M. P. Lamb, W. W. Fischer, J. P. Grotzinger, D. M. Rubin, K. W. Lewis, M. J. Ballard, M. Day, S. Gupta, S. G. Banham, N. T. Bridges, D. J. D. Marais, A. A. Fraeman, J. A. Grant, K. E. Herkenhoff, D. W. Ming, M. A. Mischna, M. S. Rice, D. Y. Sumner, A. R. Vasavada, and R. A. Yingst (2016). Large wind ripples on Mars: A record of atmospheric evolution. *Science 353*, 55–58.

Larsen, I. J. and M. P. Lamb (2016). Progressive incision of the Channeled Scablands by outburst floods. *Nature 538*(7624), 229–232.

Laskar, J., A. C. M. Correia, M. Gastineau, F. Joutel, B. Levrard, and P. Robutel (2004). Long term evolution and chaotic diffusion of the insolation quantities of Mars. *Icarus 170*(2), 343–364.

Lasne, J. (2021). Heterogeneous Physical Chemistry in the Atmospheres of Earth, Mars, and Venus: Perspectives for Rocky Exoplanets. *ACS Earth and Space Chemistry 5*(2), 149–162.

Lécuyer, C., L. Simon, and F. Guyot (2000). Comparison of carbon, nitrogen and water budgets on Venus and the Earth. *Earth and Planetary Science Letters 181*(1-2), 33–40.

Levy, J., J. W. Head, and D. R. Marchant (2010). Concentric crater fill in the northern mid-latitudes of Mars: Formation processes and relationships to similar landforms of glacial origin. *Icarus 209*(2), 390–404.

Levy, J. S., C. I. Fassett, and J. W. Head (2016). Enhanced erosion rates on Mars during Amazonian glaciation. *Icarus 264*, 213–219.

Levy, J. S., C. I. Fassett, J. W. Head, C. Schwartz, and J. L. Watters (2014). Sequestered glacial ice contribution to the global Martian water budget: Geometric constraints on the volume of remnant, midlatitude debris-covered glaciers. *Journal of Geophysical Research: Planets 119*(10), 2188–2196.

Levy, J. S., J. W. Head, and D. R. Marchant (2009). Concentric crater fill in Utopia Planitia: History and interaction between glacial "brain terrain" and periglacial mantle processes. *Icarus 202*(2), 462–476.

Lewis, A. R., D. R. Marchant, D. E. Kowalewski, S. L. Baldwin, and L. E. Webb (2006). The age and origin of the Labyrinth, western Dry Valleys, Antarctica: Evidence for extensive middle Miocene subglacial floods and freshwater discharge to the Southern Ocean. *Geology 34*(7), 513–516.

Lillis, R. J., D. A. Brain, S. W. Bougher, F. Leblanc, J. G. Luhmann, B. M. Jakosky, R. Modolo, J. Fox, J. Deighan, X. Fang, Y. C. Wang, Y. Lee, C. Dong, Y. Ma, T. Cravens, L. Andersson, S. M. Curry, N. Schneider, M. Combi, I. Stewart, J. Clarke, J. Grebowsky, D. L. Mitchell, R. Yelle, A. F. Nagy, D. Baker, and R. P. Lin (2015). Characterizing Atmospheric Escape from Mars Today and Through Time, with MAVEN. *Space Science Reviews 195*(1), 357–422.

Livingstone, S. J., Y. Li, A. Rutishauser, R. J. Sanderson, K. Winter, J. A. Mikucki, H. Björnsson, J. S. Bowling, W. Chu, C. F. Dow, et al. (2022). Subglacial lakes and their changing role in a warming climate. *Nature Reviews Earth & Environment 3*(2), 106–124.

Loizeau, D., N. Mangold, F. Poulet, V. Ansan, E. Hauber, J.-P. Bibring, B. Gondet, Y. Langevin, P. Masson, and G. Neukum (2010). Stratigraphy in the Mawrth Vallis region through OMEGA, HRSC color imagery and DTM. *Icarus 205*, 396–418.

Loizeau, D., N. Mangold, F. Poulet, J. Bibring, A. Gendrin, V. Ansan, C. Gomez, B. Gondet, Y. Langevin, P. Masson, and G. Neukum (2007). Phyllosilicates in the Mawrth Vallis region of Mars. *Journal of Geophysical Research: Planets 112*, E8.

Loizeau, D., S. C. Werner, N. Mangold, J.-P. Bibring, and J. L. Vago (2012). Chronology of deposition and alteration in the Mawrth Vallis region, Mars. *Planetary and Space Science 72*, 31–43.

Lundin, R., H. Lammer, and I. Ribas (2007). Planetary magnetic fields and solar forcing: Implications for atmospheric evolution. *Space Science Reviews 129*(1), 245–278.

Lunine, J. I. (2006). Physical conditions on the early Earth. *Philosophical Transactions of the Royal Society B: Biological Sciences 361*(1474), 1721–1731.

Lustig-Yaeger, J., G. Fu, E. M. May, K. N. O. Ceballos, S. E. Moran, S. Peacock, K. B. Stevenson, M. López-Morales, R. J. MacDonald, L. C. Mayorga, D. K. Sing, K. S. Sotzen, J. A. Valenti, J. Adams, M. K. Alam, N. E. Batalha, K. A. Bennett, J. Gonzalez-Quiles, J. Kirk, E. Kruse, J. D. Lothringer, Z. Rustamkulov, and H. R. Wakeford (2023). A JWST transmission spectrum of a nearby Earth-sized exoplanet. *arXiv preprint arXiv:2301.04191*.

Lyne, J. E., M. Tauber, and R. Fought (1996). An analytical model of the atmospheric entry of large meteors and its application to the tunguska event. *Journal of Geophysical Research: Planets 101*(E10), 23207–23212.

MacGregor, J. A., W. F. Bottke Jr., M. A. Fahnestock, J. P. Harbeck, K. H. Kjaer, J. D. Paden, D. E. Stillman, and M. Studinger (2019). A Possible Second Large Subglacial Impact Crater in Northwest Greenland. *Geophysical Research Letters 46*(3), 1496–1504.

Macías, J., L. Capra, K. Scott, J. Espíndola, A. García-Palomo, and J. Costa (2004). The 26 May 1982 breakout flows derived from failure of a volcanic dam at El Chichón, Chiapas, Mexico. *Geological Society of America Bulletin 116*(1-2), 233–246.

MacKinnon, D. J. and K. L. Tanaka (1989). The impacted Martian crust: structure, hydrology, and some geologic implications. *Journal of Geophysical Research: Planets 94*, 17359–17370.

Madeleine, J.-B., F. Forget, J. W. Head, B. Levrard, F. Montmessin, and E. Millour (2009). Amazonian northern mid-latitude glaciation on Mars: A proposed climate scenario. *Icarus 203*(2), 390–405.

Madeleine, J.-B., J. W. Head, F. Forget, T. Navarro, E. Millour, A. Spiga, A. Colaïtis, A. Määttänen, F. Montmessin, and J. L. Dickson (2014). Recent ice ages on Mars: The role of radiatively active clouds and cloud microphysics. *Geophysical Research Letters 41*(14), 4873–4879.

Mahaffy, P. R., C. R. Webster, J. C. Stern, A. E. Brunner, S. K. Atreya, P. G. Conrad, S. Domagal-Goldman, J. L. Eigenbrode, G. J. Flesch, L. E. Christensen, H. B. Franz, C. Freissinet, D. P. Glavin, J. P. Grotzinger, J. H. Jones, L. A. Leshin, C. Malespin, A. C. McAdam, D. W. Ming, R. Navarro-Gonzalez, P. B. Niles, T. Owen, A. A. Pavlov, A. Steele, M. G. Trainer, K. H. Williford, J. J. Wray, and the MSL Science Team (2015). The imprint of atmospheric evolution in the D/H of Hesperian clay minerals on Mars. *Science 347*(6220), 412–414.

Malin, M. C. and K. S. Edgett (2000). Sedimentary Rocks of Early Mars. *Science 290*(5498), 1927–1937.

Manga, M. (2004). Martian floods at Cerberus Fossae can be produced by groundwater discharge. *Geophysical Research Letters 31*(2).

Manga, M., A. Patel, J. Dufek, and E. S. Kite (2012). Wet surface and dense atmosphere on early Mars suggested by the bomb sag at Home Plate, Mars. *Geophysical Research Letters 39*(1), L01202.

Mangold, N. (2003). Geomorphic analysis of lobate debris aprons on Mars at Mars orbiter camera scale: Evidence for ice sublimation initiated by fractures. *Journal of Geophysical Research: Planets 108*(E4).

Mangold, N. (2005). High latitude patterned grounds on Mars: Classification, distribution and climatic control. *Icarus 174*(2), 336–359.

Mangold, N., S. Adeli, S. Conway, V. Ansan, and B. Langlais (2012). A chronology of early Mars climatic evolution from impact crater degradation. *Journal of Geophysical Research: Planets 117*(E4).

Mangold, N., V. Ansan, P. Masson, C. Quantin, and G. Neukum (2008). Geomorphic study of fluvial landforms on the northern Valles Marineris plateau, Mars. *Journal of Geophysical Research: Planets 113*, E08009.

Mangold, N., S. Gupta, O. Gasnault, G. Dromart, J. D. Tarnas, S. F. Sholes, B. Horgan, C. Quantin-Nataf, A. J. Brown, S. L. Mouélic, R. A. Yingst, J. F. Bell, O. Beyssac, T. Bosak, F. Calef, B. L. Ehlmann, K. A. Farley, J. P. Grotzinger, K. Hickman-Lewis, S. Holm-Alwmark, L. C. Kah, J. Martinez-Frias, S. M. McLennan, S. Maurice, J. I. Nuñez, A. M. Ollila, P. Pilleri, J. W. Rice, M. Rice, J. I. Simon, D. L. Shuster, K. M. Stack, V. Z. Sun, A. H. Treiman, B. P. Weiss, R. C. Wiens, A. J. Williams, N. R. Williams, and K. H. Williford (2021). Perseverance rover reveals an ancient delta-lake system and flood deposits at Jezero crater, Mars. *Science 374*(6568), 711–717.

Mangold, N., E. Kite, M. Kleinhans, H. Newsom, V. Ansan, E. Hauber, E. Kraal, C. Quantin, and K. Tanaka (2012). The origin and timing of fluvial activity at eberswalde crater, Mars. *Icarus 220*(2), 530–551.

Mangold, N., C. Quantin, V. Ansan, C. Delacourt, and P. Allemand (2004). Evidence for Precipitation on Mars from Dendritic Valleys in the Valles Marineris Area. *Science 305*(5680), 78–81.

Mann, J. D., D. W. Leverington, J. Rayburn, and J. T. Teller (1999). The volume and paleobathymetry of glacial Lake Agassiz. *Journal of Paleolimnology 22*(1), 71–80.

Manning, C. V., C. Bierson, N. E. Putzig, and C. P. McKay (2019). The formation and stability of buried polar CO2 deposits on Mars. *Icarus 317*, 509–517.

Marchant, D. R., G. H. Denton, D. E. Sugden, and C. C. S. III (1993). Miocene Glacial Stratigraphy and Landscape Evolution of the Western Asgard Range, Antarctica. *Geografiska Annaler: Series A, Physical Geography 75*(4), 303–330.

Marchant, D. R. and J. W. Head (2007). Antarctic Dry Valleys: Microclimate zonation, variable geomorphic processes, and implications for assessing climate change on Mars. *Icarus 192*(1), 187–222.

Marra, W. A., L. Braat, A. W. Baar, and M. G. Kleinhans (2014). Valley formation by groundwater seepage, pressurized groundwater outbursts and crater-lake overflow in flume experiments with implications for Mars. *Icarus 232*, 97–117.

Marrero, T. R. and E. A. Mason (1972). Gaseous diffusion coefficients. *Journal of Physical and Chemical Reference Data 1*(1), 3–118.

Matson, D. L., A. G. Davies, G. J. Veeder, J. A. Rathbun, T. V. Johnson, and J. C. Castillo (2006). Io: Loki Patera as a magma sea. *Journal of Geophysical Research: Planets 111*(E9).

Matsubara, Y., A. D. Howard, and J. P. Gochenour (2013). Hydrology of early Mars: Valley network incision. *Journal of Geophysical Research: Planets 118*(6), 1365–1387.

Matsuoka, N. and J. Murton (2008). Frost weathering: recent advances and future directions. *Permafrost and Periglacial Processes 19*(2), 195–210.

Mayer, D. P. and E. S. Kite (2016). An Integrated Workflow for Producing Digital Terrain Models of Mars from CTX and HiRISE Stereo Data Using the NASA Ames Stereo Pipeline. In *Lunar and Planetary Science Conference*, Volume 47, pp. 1241.

McEwen, A. S., L. Ojha, C. M. Dundas, S. S. Mattson, S. Byrne, J. J. Wray, S. C. Cull, S. L. Murchie, N. Thomas, and V. C. Gulick (2011). Seasonal flows on warm Martian slopes. *Science 333*(6043), 740–743.

McEwen, A. S., B. S. Preblich, E. P. Turtle, N. A. Artemieva, M. P. Golombek, M. Hurst, R. L. Kirk, Devon M. Burr, and P. R. Christensen (2005). The rayed crater Zunil and interpretations of small impact craters on Mars. *Icarus 176*, 351–381.

Meadows, V. S. and R. K. Barnes (2018). Factors Affecting Exoplanet Habitability. In H. J. Deeg and J. A. Belmonte (Eds.), *Handbook of Exoplanets*, pp. 57.

Meadows, V. S., C. T. Reinhard, G. N. Arney, M. N. Parenteau, E. W. Schwieterman, S. D. Domagal-Goldman, A. P. Lincowski, K. R. Stapelfeldt, H. Rauer, S. DasSarma, S. Hegde, N. Narita, R. Deitrick, J. Lustig-Yaeger, T. W. Lyons, N. Siegler, and J. L. Grenfell (2018). Exoplanet biosignatures: Understanding oxygen as a biosignature in the context of its environment. *Astrobiology 18*(6), 630–662.

Mellon, M. T., R. E. Arvidson, J. J. Marlow, R. J. Phillips, and E. Asphaug (2008). Periglacial landforms at the Phoenix landing site and the northern plains of Mars. *Journal of Geophysical Research: Planets 113*(E3).

Melosh, H. J. (1981). Atmospheric breakup of terrestrial impactors. In R. B. Merill and P. H. Schultz (Eds.), *Multi-ring basins: Formation and Evolution*, pp. 29–35.

Meyer-Peter, E. and R. Mueller (1948). Formulas for bed-load transport. In *IAHSR 2nd meeting, Stockholm, appendix 2*. IAHR.

Michael, G. and G. Neukum (2010). Planetary surface dating from crater size–frequency distribution measurements: Partial resurfacing events and statistical age uncertainty. *Earth and Planetary Science Letters 294*(3-4), 223–229.

Michael, G. G. (2013). Planetary surface dating from crater size–frequency distribution measurements: Multiple resurfacing episodes and differential isochron fitting. *Icarus 226*(1), 885–890.

Michalski, J. R., J.-P. Bibring, F. Poulet, D. Loizeau, N. Mangold, E. N. Dobrea, J. L. Bishop, J. J. Wray, N. K. McKeown, M. Parente, E. Hauber, F. Altieri, F. G. Carrozzo, , and P. B. Niles (2010). The Mawrth Vallis Region of Mars: A Potential Landing Site for the Mars Science Laboratory (MSL) Mission. *Astrobiology 10(7)*, 687–703.

Millour, E., F. Forget, M. Lopez-Valverde, F. Lefevre, F. Gonzalez-Galindo, S. Lewis, J.-Y. Chaufray, L. Montabone, V. Zakharov, A. Spiga, and M. Vals (2018). Exploring the interannual variablitity of the Martian atmosphere with the Mars Climate Database v5.3. In *42nd COSPAR Scientific Assembly*, Volume 42, pp. C4.3–6–18.

Mills, F. P., J. I. Moses, P. Gao, and S.-M. Tsai (2021). The diversity of planetary atmospheric chemistry. *Space Science Reviews 217*(3), 43.

Mischna, M. A., V. Baker, R. Milliken, M. Richardson, and C. Lee (2013). Effects of obliquity and water vapor/trace gas greenhouses in the Early Martian climate. *Journal of Geophysical Research: Planets 118*(3), 560–576.

Mischna, M. A., M. I. Richardson, R. J. Wilson, and D. J. McCleese (2003). On the orbital forcing of Martian water and CO_2cycles: A general circulation model study with simplified volatile schemes. *Journal of Geophysical Research: Planets 108*(E6).

Montigny, A., D. Walwer, and C. Michaut (2022). The origin of hierarchical cracks in floor-fractured craters on Mars and the Moon. *Earth and Planetary Science Letters 600*, 117887.

Moore, J. M., A. D. Howard, W. E. Dietrich, and P. M. Schenk (2003). Martian Layered Fluvial Deposits: Implications for Noachian Climate Scenarios. *Geophysical Research Letters 30(24)*, 665–671.

Moore, W. B., J. I. Simon, and A. A. G. Webb (2017). Heat-pipe planets. *Earth and Planetary Science Letters 474*, 13–19.

Moroz, V. (1981). The atmosphere of Venus. *Space Science Reviews 29*(1), 3–127.

Morris, M., M. Hassan, A. Kortenhaus, and P. Visser (2009). Breaching processes: A state of the art review. *FLOODsite Report T06-06-03*.

Morschhauser, A., M. Grott, and D. Breuer (2011). Crustal recycling, mantle dehydration, and the thermal evolution of Mars. *Icarus 212*(2), 541–558.

Moser, D. E., G. A. Arcuri, D. A. Reinhard, L. F. White, J. R. Darling, I. R. Barker, D. J. Larson, A. J. Irving, F. M. McCubbin, K. T. Tait, J. Roszjar, A. Wittmann, and C. Davis (2019). Decline of giant impacts on Mars by 4.48 billion years ago and an early Opportunity for habitability. *Nature Geoscience 12*(7), 522–527.

Mouginis-Mark, P. J., J. Boyce, V. L. Sharpton, and H. Garbeil (2018). Determination of Mars crater geometric data: Insights from high-resolution digital elevation models. *Meteoritics & Planetary Science 53*(4), 726–740.

Mueller, E. R., J. Pitlick, and J. M. Nelson (2005). Variation in the reference shields stress for bed load transport in gravel-bed streams and rivers. *Water Resources Research 41*(4).

Mueller, P. A. and A. P. Nutman (2017). The Archean–Hadean Earth: Modern paradigms and ancient processes. In *The Web of Geological Sciences: Advances, Impacts, and Interactions II*. Geological Society of America.

Murphy, D. M. and T. Koop (2005). Review of the vapour pressures of ice and supercooled water for atmospheric applications. *Quarterly Journal of the Royal Meteorological Society 131*(608), 1539–1565.

Nakamura, T. and E. Tajika (2003). Climate change of Mars-like planets due to obliquity variations: implications for Mars. *Geophysical Research Letters 30*(13).

Nash, T., D. Bell, T. Davies, and S. Nathan (2008). Analysis of the formation and failure of Ram Creek landslide dam, South Island, New Zealand. *New Zealand journal of geology and geophysics 51*(3), 187–193.

National Academies of Sciences (2022). *Origins, Worlds, and Life: A Decadal Strategy for Planetary Science and Astrobiology 2023-2032*. Washington, DC: The National Academies Press.

Neupane, R., H. Chen, and C. Cao (2019). Review of moraine dam failure mechanism. *Geomatics, Natural Hazards and Risk 10*(1), 1948–1966.

Nimmo, F. and K. Tanaka (2005). Early crustal evolution of Mars. *Annual Review of Earth and Planetary Sciences 33*, 133–161.

Nininger, H. H. and J. D. Figgins (1933). The excavation of a meteorite crater near haviland, kiowa county, kansas. *Colorado Museum of Natural History, Proceedings 12*(3), 9–15.

Noack, L., M. Godolt, P. von Paris, A.-C. Plesa, B. Stracke, D. Breuer, and H. Rauer (2014). Can the interior structure influence the habitability of a rocky planet? *Planetary and Space Science 98*, 14–29.

Nowajewski, P., M. Rojas, P. Rojo, and S. Kimeswenger (2018). Atmospheric dynamics and habitability range in Earth-like aquaplanets obliquity simulations. *Icarus 305*, 84–90.

Nuno, R. G. and D. A. Paige (2019). Martian Microcraters as Evidence for Obliquity-Driven Pressure Variations. In *Lunar and Planetary Science Conference*, Volume 50 of *Lunar and Planetary Science Conference*, pp. 3096.

Nye, J. F. (1976). Water flow in glaciers: jökulhlaups, tunnels and veins. *Journal of Glaciology 17*(76), 181–207.

O'Callaghan, J. (2021). How three missions to Venus could solve the planet's biggest mysteries. *Nature 594*(7864), 486–487.

Oehler, D. Z. and C. C. Allen (2012). Giant Polygons and Mounds in the Lowlands of Mars: Signatures of an Ancient Ocean? *Astrobiology 12*, 601–615.

Öpik, E. J. (1966). The Martian Surface. *Science 15*, 255–265.

O'Reilly, T. C. and G. F. Davies (1981). Magma transport of heat on Io: A mechanism allowing a thick lithosphere. *Geophysical Research Letters 8*(4), 313–316.

O'Rourke, J. G. (2020). Venus: A thick basal magma ocean may exist today. *Geophysical Research Letters 47*(4), e2019GL086126.

Osinski, G. R. and P. Lee (2005). Intra-crater sedimentary deposits at the Haughton impact structure, Devon Island, Canadian high Arctic. *Meteoritics & Planetary Science 40*(12), 1887–1899.

Ostberg, C., S. R. Kane, Z. Li, E. W. Schwieterman, M. L. Hill, K. Bott, P. A. Dalba, T. Fetherolf, J. W. Head, and C. T. Unterborn (2023). The demographics of terrestrial planets in the Venus zone. *The Astronomical Journal 165*(4), 168.

Osti, R. and S. Egashira (2009). Hydrodynamic characteristics of the Tam Pokhari Glacial Lake outburst flood in the Mt. Everest region, Nepal. *Hydrological Processes: An International Journal 23*(20), 2943–2955.

O'Rourke, J. G. and J. Korenaga (2015). Thermal evolution of Venus with argon degassing. *Icarus 260*, 128 – 140.

Pahlevan, K., L. Schaefer, and M. M. Hirschmann (2019). Hydrogen isotopic evidence for early oxidation of silicate Earth. *Earth and planetary science letters 526*, 115770.

Palucis, M. C., W. E. Dietrich, R. M. Williams, A. G. Hayes, T. Parker, D. Y. Sumner, N. Mangold, K. Lewis, and H. Newsom (2016). Sequence and relative timing of large lakes in Gale crater (Mars) after the formation of Mount Sharp. *Journal of Geophysical Research: Planets 121*(3), 472–496.

Palumbo, A. M. and J. W. Head (2018). Impact cratering as a cause of climate change, surface alteration, and resurfacing during the early history of Mars. *Meteoritics & Planetary Science 53*(4), 687–725.

Passey, Q. R. and H. Melosh (1980). Effects of atmospheric breakup on crater field formation. *Icarus 42*(2), 211–233.

Pätzold, M., B. Häusler, M. Bird, S. Tellmann, R. Mattei, S. Asmar, V. Dehant, W. Eidel, T. Imamura, R. Simpson, et al. (2007). The structure of Venus' middle atmosphere and ionosphere. *Nature 450*(7170), 657–660.

Pepin, R. O. (1994). Evolution of the Martian Atmosphere. *Icarus 111*(2), 289–304.

Pepin, R. O. (2006). Atmospheres on the terrestrial planets: Clues to origin and evolution. *Earth and Planetary Science Letters 252*(1), 1–14.

Petigura, E. A., A. W. Howard, and G. W. Marcy (2013). Prevalence of Earth-size planets orbiting Sun-like stars. *Proceedings of the National Academy of Sciences 110*(48), 19273–19278.

Pham, L. B. S. and O. Karatekin (2016). Scenarios of atmospheric mass evolution on Mars influenced by asteroid and comet impacts since the late Noachian. *Planetary and Space Science 125*, 1–11.

Phillips, R. J., R. F. Raubertas, R. E. Arvidson, I. C. Sarkar, R. R. Herrick, N. Izenberg, and R. E. Grimm (1992). Impact craters and Venus resurfacing history. *Journal of Geophysical Research: Planets 97*(E10), 15923–15948.

Phillips, R. J., M. T. Zuber, S. C. Solomon, M. P. Golombek, B. M. Jakosky, W. B. Banerdt, D. E. Smith, R. M. E. Williams, B. M. Hynek, O. Aharonson, and S. A. H. Ii (2001). Ancient Geodynamics and Global-Scale Hydrology on Mars. *Science 291*(5513), 2587–2591.

Pierce, T. L. and D. A. Crown (2003). Morphologic and topographic analyses of debris aprons in the eastern Hellas region, Mars. *Icarus 163*(1), 46–65.

Pierson, T. C. (2005). Hyperconcentrated flow—transitional process between water flow and debris flow. In *Debris-flow hazards and related phenomena*, pp. 159–202. Springer.

Plaza, G., O. Zevallos, and É. Cadier (2011). La Josefina Landslide Dam and Its Catastrophic Breaching in the Andean Region of Ecuador. In *Natural and artificial rockslide dams*, pp. 389–406. Springer.

Podolak, M., J. B. Pollack, and R. T. Reynolds (1988). Interactions of planetesimals with protoplanetary atmospheres. *Icarus 73*(1), 163–179.

Polanskey, C. A. and T. J. Ahrens (1990). Impact spallation experiments: Fracture patterns and spall velocities. *Icarus 87*(1), 140–155.

Pollack, J. B. (1971). A nongrey calculation of the runaway greenhouse: Implications for Venus' past and present. *Icarus 14*(3), 295–306.

Pollack, J. B., J. F. Kasting, S. M. Richardson, and K. Poliakoff (1987). The case for a wet, warm climate on early Mars. *Icarus 71*(2), 203–224.

Popova, O., I. Nemtchinov, and W. K. Hartmann (2003). Bolides in the present and past Martian atmosphere and effects on cratering processes. *Meteoritics & Planetary Science 38*(6), 905–925.

Prevec, S., P. Lightfoot, and R. Keays (2000). Evolution of the sublayer of the Sudbury Igneous Complex: geochemical, Sm–Nd isotopic and petrologic evidence. *Lithos 51*(4), 271–292.

Ramirez, R. M. (2017). A warmer and wetter solution for early Mars and the challenges with transient warming. *Icarus 297*, 71–82.

Ramirez, R. M. and L. Kaltenegger (2014). The habitable zones of pre-main-sequence stars. *The Astrophysical Journal Letters 797*(2), L25.

Ramirez, R. M., R. Kopparapu, M. E. Zugger, T. D. Robinson, R. Freedman, and J. F. Kasting (2014). Warming early Mars with CO_2 and H_2. *Nature Geoscience 7*, 59–63.

Rapin, W., G. Dromart, D. Rubin, L. L. Deit, N. Mangold, L. Edgar, O. Gasnault, K. Herkenhoff, S. Le Mouélic, R. Anderson, S. Maurice, V. Fox, B. Ehlmann, J. Dickson, and R. Wiens (2021). Alternating wet and dry depositional environments recorded in the stratigraphy of Mount Sharp at Gale crater, Mars. *Geology 49*(7), 842–846.

Ribas, I., E. F. Guinan, M. Gudel, and M. Audard (2005). Evolution of the Solar Activity over Time and Effects on Planetary Atmospheres. I. High-Energy Irradiances (1–1700 Å). *Astrophysical Journal 622*(1), 680–694.

Rickenmann, D. (1991). Bed load transport and hyperconcentrated flow at steep slopes. In A. Armanini and G. Di Silvio (Eds.), *Fluvial Hydraulics of Mountain Regions*, Berlin, Heidelberg, pp. 429–441. Springer Berlin Heidelberg.

Robbins, S. J., G. di Achille, and B. M. Hynek (2011). The volcanic history of Mars: High-resolution crater-based studies of the calderas of 20 volcanoes. *Icarus 211*(2), 1179–1203.

Robbins, S. J. and B. M. Hynek (2012a). A new global database of Mars impact craters $\geq$1 km: 1. database creation, properties, and parameters. *Journal of Geophysical Research: Planets 117*(E5).

Robbins, S. J. and B. M. Hynek (2012b). A new global database of Mars impact craters $\geq$1 km: 2. Global crater properties and regional variations of the simple-to-complex transition diameter. *Journal of Geophysical Research: Planets 117*(E6).

Robin, G. d. Q., S. Evans, and J. T. Bailey (1969). Interpretation of radio echo sounding in polar ice sheets. *Philosophical Transactions of the Royal Society of London. Series A, Mathematical and Physical Sciences 265*(1166), 437–505.

Rodriguez, J. A. P., J. S. Kargel, V. R. Baker, V. C. Gulick, D. C. Berman, A. G. Fairén, R. Linares, M. Zarroca, J. Yan, H. Miyamoto, et al. (2015). Martian outflow channels: How did their source aquifers form, and why did they drain so rapidly? *Scientific Reports 5*(1), 13404.

Rosenblatt, P., P. Pinet, and E. Thouvenot (1994). Comparative hypsometric analysis of Earth and Venus. *Geophysical Research Letters 21*(6), 465–468.

Saal, A. E., E. H. Hauri, C. H. Langmuir, and M. R. Perfit (2002). Vapour undersaturation in primitive mid-ocean-ridge basalt and the volatile content of Earth's upper mantle. *Nature 419*(6906), 451–455.

Saito, H. and K. Kuramoto (2017). Formation of a hybrid-type proto-atmosphere on Mars accreting in the solar nebula. *Monthly Notices of the Royal Astronomical Society 475*, 1274–1287.

Sakuraba, H., H. Kurokawa, and H. Genda (2019). Impact degassing and atmospheric erosion on Venus, Earth, and Mars during the late accretion. *Icarus 317*, 48–58.

Salese, F., V. Ansan, N. Mangold, J. Carter, A. Ody, F. Poulet, and G. G. Ori (2016). A sedimentary origin for intercrater plains north of the Hellas basin: Implications for climate conditions and erosion rates on early Mars. *Journal of Geophysical Research: Planets 121*(11), 2239–2267.

Salvador, A., H. Massol, A. Davaille, E. Marcq, P. Sarda, and E. Chassefière (2017). The relative influence of H_2O and CO_2 on the primitive surface conditions and evolution of rocky planets. *Journal of Geophysical Research: Planets 122*(7), 1458–1486.

Sato, H., K. Kurita, and D. Baratoux (2010). The formation of floor-fractured craters in Xanthe Terra. *Icarus 207*(1), 248–264.

Scanlon, K. E., J. W. Head, J.-B. Madeleine, R. D. Wordsworth, and F. Forget (2013). Orographic precipitation in valley network headwaters: Constraints on the ancient Martian atmosphere. *Geophysical Research Letters 40*(16), 4182–4187.

Schaefer, L. and D. Sasselov (2015). The persistence of oceans on Earth-like planets: Insights from the deep-water cycle. *Astrophysical Journal 801*(1), 40.

Schaefer, L., R. D. Wordsworth, Z. Berta-Thompson, and D. Sasselov (2016). Predictions of the atmospheric composition of GJ 1132b. *The Astrophysical Journal 829*(2), 63.

Scheller, E. L., B. L. Ehlmann, R. Hu, D. J. Adams, and Y. L. Yung (2021). Long-term drying of Mars by sequestration of ocean-scale volumes of water in the crust. *Science 372*(6537), 56–62.

Schipper, C. I., J. D. White, B. Houghton, N. Shimizu, and R. B. Stewart (2010). Explosive submarine eruptions driven by volatile-coupled degassing at Lō'ihi Seamount, Hawai'i. *Earth and Planetary Science Letters 295*(3), 497 – 510.

Schlichting, H. E., R. Sari, and A. Yalinewich (2015). Atmospheric mass loss during planet formation: The importance of planetesimal impacts. *Icarus 247*, 81–94.

Schultz, P. H. (1976). Floor-fractured lunar craters. *The Moon 15*(3), 241–273.

Schultz, R. A. (1993). Brittle strength of basaltic rock masses with applications to Venus. *Journal of Geophysical Research: Planets 98*(E6), 10883–10895.

Schulze-Makuch, D. and L. N. Irwin (2018). *Astrobiological Potential of Planetary Bodies Within the Solar System*, pp. 203–228. Cham: Springer International Publishing.

Segura, T. L., C. P. McKay, and O. B. Toon (2012). An impact-induced, stable, runaway climate on Mars. *Icarus 220*(1), 144–148.

Selsis, F., J. F. Kasting, B. Levrard, J. Paillet, I. Ribas, and X. Delfosse (2007). Habitable planets around the star Gliese 581? *Astronomy & Astrophysics 476*(3), 1373–1387.

Shaw, D. M. (1970). Trace element fractionation during anatexis. *Geochimica et Cosmochimica Acta 34*(2), 237–243.

Shellnutt, J. G. (2013). Petrological modeling of basaltic rocks from Venus: A case for the presence of silicic rocks. *Journal of Geophysical Research: Planets 118*(6), 1350–1364.

Shoemaker, E. M., F. A. Macdonald, and C. S. Shoemaker (2005). Geology of five small Australian impact craters. *Australian Journal of Earth Sciences 52*(4-5), 529–544.

Sizemore, H. G., A. P. Zent, and A. W. Rempel (2015). Initiation and growth of Martian ice lenses. *Icarus 251*, 191–210.

Slipski, M. and B. M. Jakosky (2016). Argon isotopes as tracers for Martian atmospheric loss. *Icarus 272*, 212–227.

Smith, B. E., H. A. Fricker, I. R. Joughin, and S. Tulaczyk (2009). An inventory of active subglacial lakes in Antarctica detected by ICESat (2003–2008). *Journal of Glaciology 55*(192), 573–595.

Smith, D. E., M. T. Zuber, H. V. Frey, J. B. Garvin, J. W. Head, D. O. Muhleman, G. H. Pettengill, R. J. Phillips, S. C. Solomon, H. J. Zwally, et al. (2001). Mars Orbiter Laser Altimeter: Experiment summary after the first year of global mapping of Mars. *Journal of Geophysical Research: Planets 106*(E10), 23689–23722.

Smith, M. R., A. R. Gillespie, and D. R. Montgomery (2008). Effect of obliteration on crater-count chronologies for Martian surfaces. *Geophysical Research Letters 35*(10).

Smith, P. M. and P. D. Asimow (2005). Adiabat_1ph: A new public front-end to the MELTS, pMELTS, and pHMELTS models. *Geochemistry, Geophysics, Geosystems 6*(2).

Smrekar, S., D. Dyar, J. Helbert, S. Hensley, D. Nunes, and J. Whitten (2020). VERITAS (Venus Emissivity, Radio Science, InSAR, Topography And Spectroscopy): A Proposed Discovery Mission. In *European Planetary Science Congress*, pp. EPSC2020–447.

Smrekar, S. E., A. Davaille, and C. Sotin (2018). Venus interior structure and dynamics. *Space Science Reviews 214*(5), 1–34.

Smrekar, S. E., E. R. Stofan, N. Mueller, A. Treiman, L. Elkins-Tanton, J. Helbert, G. Piccioni, and P. Drossart (2010). Recent hotspot volcanism on Venus from VIRTIS emissivity data. *Science 328*(5978), 605–608.

Soto, A., M. Mischna, T. Schneider, C. Lee, and M. Richardson (2015). Martian atmospheric collapse: Idealized GCM studies. *Icarus 250*, 553–569.

Soule, S., D. Nakata, D. Fornari, A. Fundis, M. Perfit, and M. Kurz (2012). CO_2 variability in mid-ocean ridge basalts from syn-emplacement degassing: Constraints on eruption dynamics. *Earth and Planetary Science Letters 327*, 39–49.

Sparks, R. (1978). The dynamics of bubble formation and growth in magmas: A review and analysis. *Journal of Volcanology and Geothermal Research 3*(1), 1 – 37.

Spohn, T. (1991). Mantle differentiation and thermal evolution of Mars, Mercury, and Venus. *Icarus 90*(2), 222–236.

Squyres, S. W., A. H. Knoll, R. E. Arvidson, J. W. Ashley, J. Bell, W. M. Calvin, P. R. Christensen, B. C. Clark, B. A. Cohen, P. De Souza, et al. (2009). Exploration of Victoria crater by the Mars rover Opportunity. *Science 324*(5930), 1058–1061.

Stanley, B. D., M. M. Hirschmann, and A. C. Withers (2011). CO_2 solubility in Martian basalts and Martian atmospheric evolution. *Geochimica et Cosmochimica Acta 75*(20), 5987–6003.

Steakley, K., J. Murphy, M. Kahre, R. Haberle, and A. Kling (2019). Testing the impact heating hypothesis for early Mars with a 3-D global climate model. *Icarus 330*, 169–188.

Steele, L. J., M. R. Balme, and S. R. Lewis (2017). Regolith-atmosphere exchange of water in Mars' recent past. *Icarus 284*, 233–248.

Stephens, S. K. and D. J. Stevenson (1990). Dry Carbonate Formation on Mars: A Plausible Sink for an Early Dense CO_2 Atmosphere? In *Lunar and Planetary Science Conference*, Volume 21.

Stevenson, D. J., T. Spohn, and G. Schubert (1983). Magnetism and thermal evolution of the terrestrial planets. *Icarus 54*(3), 466–489.

Stokes, C. R., J. E. Sanderson, B. W. J. Miles, S. S. R. Jamieson, and A. A. Leeson (2019). Widespread distribution of supraglacial lakes around the margin of the East Antarctic Ice Sheet. *Scientific Reports 9*(1), 13823.

Strom, R. G., R. Malhotra, T. Ito, F. Yoshida, and D. A. Kring (2005). The Origin of Planetary Impactors in the Inner Solar System. *Science 309*(5742), 1847–1850.

Strom, R. G., R. Malhotra, Z.-Y. Xiao, T. Ito, F. Yoshida, and L. R. Ostrach (2015). The inner solar system cratering record and the evolution of impactor populations. *Research in Astronomy and Astrophysics 15*(3), 407.

Strom, R. G., G. G. Schaber, and D. D. Dawson (1994). The global resurfacing of Venus. *Journal of Geophysical Research: Planets 99*(E5), 10899–10926.

Sturm, S., T. Kenkmann, and S. Hergarten (2016). Ejecta thickness and structural rim uplift measurements of Martian impact craters: Implications for the rim formation of complex impact craters. *Journal of Geophysical Research: Planets 121*(6), 1026–1053.

Sun, V. Z., K. P. Hand, K. M. Stack, K. A. Farley, J. I. Simon, C. Newman, S. Sharma, Y. Liu, R. C. Wiens, A. J. Williams, N. Tosca, S. Alwmark, O. Beyssac, A. Brown, F. Calef, E. L. Cardarelli, E. Clavé, B. Cohen, A. Corpolongo, A. D. Czaja, T. Del Sesto, A. Fairen, T. Fornaro, T. Fouchet, B. Garczynski, S. Gupta, C. D. K. Herd, K. Hickman-Lewis, B. Horgan, J. Johnson, K. Kinch, T. Kizovski, R. Kronyak, R. Lange, L. Mandon, S. Milkovich, R. Moeller, J. Núñez, G. Paar, G. Pyrzak, C. Quantin-Nataf, D. L. Shuster, S. Siljestrom, A. Steele, M. Tice, O. Toupet, A. Udry, A. Vaughan, and B. Wogsland. Overview and Results from the Mars 2020 Perseverance Rover's First Science Campaign on the Jezero Crater Floor. *Journal of Geophysical Research: Planets*, e2022JE007613.

Surkov, Yu. A. and Barsukov, V. L. and Moskalyeva, L. P. and Kharyukova, V. P. and Kemurdzhian, A. L. (1984). New data on the composition, structure, and properties of Venus rock obtained by Venera 13 and Venera 14. *Journal of Geophysical Research: Solid Earth 89*(S02), B393–B402.

Svetsov, V., I. Nemtchinov, and A. Teterev (1995). Disintegration of Large Meteoroids in Earth's Atmosphere: Theoretical Models. *Icarus 116*(1), 131–153.

Tanaka, K. L., S. Robbins, C. Fortezzo, J. Skinner Jr, and T. M. Hare (2014). The digital global geologic map of Mars: Chronostratigraphic ages, topographic and crater morphologic characteristics, and updated resurfacing history. *Planetary and Space Science 95*, 11–24.

Tanaka, K. L., J. A. Skinner, T. M. Hare, T. Joyal, and A. Wenker (2003). Resurfacing history of the northern plains of Mars based on geologic mapping of Mars Global Surveyor data. *Journal of Geophysical Research: Planets 108*(E4).

Tancredi, G., J. Ishitsuka, P. H. Schultz, R. S. Harris, P. Brown, D. O. Revelle, K. Antier, A. L. Pichon, D. Rosales, E. Vidal, M. E. Varela, L. Sánchez, S. Benavente, J. Bojorquez,

D. Cabezas, and A. Dalmau (2009). A meteorite crater on Earth formed on September 15, 2007: The Carancas hypervelocity impact. *Meteoritics & Planetary Science 44*(12), 1967–1984.

Tauber, M. E. and D. B. Kirk (1976). Impact craters on Venus. *Icarus 28(3)*, 351–357.

Terrell, G. R. and D. W. Scott (1985). Oversmoothed nonparametric density estimates. *Journal of the American Statistical Association 80*(389), 209–214.

Tian, F. (2015a). Atmospheric Escape from Solar System Terrestrial Planets and Exoplanets. *Annual Review of Earth and Planetary Sciences 43*(1), 459–476.

Tian, F. (2015b). History of water loss and atmospheric O_2 buildup on rocky exoplanets near M dwarfs. *Earth and Planetary Science Letters 432*, 126–132.

Tian, F., J. F. Kasting, and S. C. Solomon (2009). Thermal escape of carbon from the early Martian atmosphere. *Geophysical Research Letters 36*(2).

Titov, D. V., M. A. Bullock, D. Crisp, N. O. Renno, F. W. Taylor, and L. V. Zasova (2007). *Radiation in the Atmosphere of Venus*, pp. 121–138. American Geophysical Union (AGU).

Titov, D. V., G. Piccioni, P. Drossart, and W. J. Markiewicz (2013). *Radiative Energy Balance in the Venus Atmosphere*, pp. 23–53. New York, NY: Springer New York.

Toon, O. B., K. Zahnle, D. Morrison, R. P. Turco, and C. Covey (1997). Environmental perturbations caused by the impacts of asteroids and comets. *Reviews of Geophysics 35*(1), 41–78.

Tosca, N. J., I. A. M. Ahmed, B. M. Tutolo, A. Ashpitel, and J. A. Hurowitz (2018). Magnetite authigenesis and the warming of early Mars. *Nature Geoscience 11*(9), 635.

Touma, J. and J. Wisdom (1993). The Chaotic Obliquity of Mars. *Science 259*(5099), 1294–1297.

Trenberth, K. E., J. R. Christy, and J. G. Olson (1987). Global atmospheric mass, surface pressure, and water vapor variations. *Journal of Geophysical Research 92*(D12), 14815.

Tu, Lin, Johnstone, Colin P., Güdel, Manuel, and Lammer, Helmut (2015). The extreme ultraviolet and X-ray Sun in Time: High-energy evolutionary tracks of a solar-like star. *Astronomy & Astrophysics 577*, L3.

Turbet, M., E. Bolmont, G. Chaverot, D. Ehrenreich, J. Leconte, and E. Marcq (2021). Day–night cloud asymmetry prevents early oceans on Venus but not on Earth. *Nature 598*(7880), 276–280.

Turbet, M., E. Bolmont, D. Ehrenreich, P. Gratier, J. Leconte, F. Selsis, N. Hara, and C. Lovis (2020). Revised mass-radius relationships for water-rich rocky planets more irradiated than the runaway greenhouse limit. *Astronomy & Astrophysics 638*, A41.

Turbet, M., D. Ehrenreich, C. Lovis, E. Bolmont, and T. Fauchez (2019). The runaway greenhouse radius inflation effect - An observational diagnostic to probe water on Earth-sized planets and test the habitable zone concept. *Astronomy & Astrophysics 628*, A12.

Turbet, M., C. Gillmann, F. Forget, B. Baudin, A. Palumbo, J. Head, and O. Karatekin (2020). The environmental effects of very large bolide impacts on early Mars explored with a hierarchy of numerical models. *Icarus 335*, 113419.

Turbet, M., H. Tran, O. Pirali, F. Forget, C. Boulet, and J.-M. Hartmann (2019). Far infrared measurements of absorptions by CH_4+CO_2 and H_2+CO_2 mixtures and implications for greenhouse warming on early Mars. *Icarus 321*, 189–199.

Turcotte, D. L. (1993). An episodic hypothesis for Venusian tectonics. *Journal of Geophysical Research: Planets 98*(E9), 17061–17068.

van Berk, W., Y. Fu, and J. Ilger (2012). Reproducing early Martian atmospheric carbon dioxide partial pressure by modeling the formation of Mg-Fe-Ca carbonate identified in the Comanche rock outcrops on Mars. *Journal of Geophysical Research: Planets 117*.

Van Rijn, L. C. (1984). Sediment transport, part I: bed load transport. *Journal of hydraulic engineering 110*(10), 1431–1456.

Vasavada, A. R., T. J. Milavec, and D. A. Paige (1993). Microcraters on Mars: Evidence for past climate variations. *Journal of Geophysical Research: Planets 98*(E2), 3469–3476.

Vida, K., Z. Kővári, A. Pál, K. Oláh, and L. Kriskovics (2017). Frequent flaring in the TRAPPIST-1 system—unsuited for life? *The Astrophysical Journal 841*(2), 124.

Vinson, A. M. and B. M. Hansen (2017). On the spin states of habitable zone exoplanets around M dwarfs: the effect of a near-resonant companion. *Monthly Notices of the Royal Astronomical Society 472*(3), 3217–3229.

Walder, J. S. and J. E. Costa (1996). Outburst floods from glacier-dammed lakes: The effect of mode of lake drainage on flood magnitude. *Earth Surface Processes and Landforms 21*(8), 701–723.

Walder, J. S. and J. E. O'Connor (1997). Methods for predicting peak discharge of floods caused by failure of natural and constructed Earthen dams. *Water Resources Research 33*(10), 2337–2348.

Walwer, D., C. Michaut, V. Pinel, and M. Adda-Bedia (2021). Magma ascent and emplacement below floor fractured craters on the Moon from floor uplift and fracture length. *Physics of the Earth and Planetary Interiors 312*, 106658.

Wang, C.-y., M. Manga, and J. C. Hanna (2006). Can freezing cause floods on Mars? *Geophysical research letters 33*(20).

Warner, N., S. Gupta, S.-Y. Lin, J.-R. Kim, J.-P. Muller, and J. Morley (2010). Late Noachian to Hesperian climate change on Mars: Evidence of episodic warming from transient crater lakes near Ares Vallis. *Journal of Geophysical Research: Planets 115*(E6).

Warner, N. H., S. Gupta, F. Calef, P. Grindrod, N. Boll, and K. Goddard (2015). Minimum effective area for high resolution crater counting of Martian terrains. *Icarus 245*, 198–240.

Warren, A., S. Holo, E. Kite, and S. Wilson (2021). Overspilling small craters on a dry Mars: Insights from breach erosion modeling. *Earth and Planetary Science Letters 554*, 116671.

Watters, W. A., L. M. Geiger, M. Fendrock, and R. Gibson (2015). Morphometry of small recent impact craters on Mars: Size and terrain dependence, short-term modification. *Journal of Geophysical Research: Planets 120*(2), 226–254.

Way, M. J. and A. D. Del Genio (2020). Venusian Habitable Climate Scenarios: Modeling Venus Through Time and Applications to Slowly Rotating Venus-Like Exoplanets. *Journal of Geophysical Research: Planets 125*(5), e2019JE006276.

Way, M. J., A. D. Del Genio, N. Y. Kiang, L. E. Sohl, D. H. Grinspoon, I. Aleinov, M. Kelley, and T. Clune (2016). Was Venus the first habitable world of our solar system? *Geophysical Research Letters 43*(16), 8376–8383.

Way, M. J., C. Ostberg, B. J. Foley, C. Gillmann, D. Höning, H. Lammer, J. O'Rourke, M. Persson, A.-C. Plesa, A. Salvador, M. Scherf, and M. Weller (2023). Synergies Between Venus & Exoplanetary Observations. *Space Science Reviews 219*(1), 13.

Weiss, D. K. and J. W. Head (2015). Crater degradation in the Noachian highlands of Mars: Assessing the hypothesis of regional snow and ice deposits on a cold and icy early Mars. *Planetary and Space Science 117*, 401–420.

Weller, M. B. and W. S. Kiefer (2020). The Physics of Changing Tectonic Regimes: Implications for the Temporal Evolution of Mantle Convection and the Thermal History of Venus. *Journal of Geophysical Research: Planets 125*(1), e2019JE005960.

Whipple, K. X., R. A. Di Biase, and B. T. Crosby (2013). Bedrock rivers. In J. Shroder and E. Wohl (Eds.), *Treatise on Geomorphology*, Chapter 9, pp. 550–573. San Diego: Academic Press.

White, S. M., J. A. Crisp, and F. J. Spera (2006). Long-term volumetric eruption rates and magma budgets. *Geochemistry, Geophysics, Geosystems 7*(3).

Whittaker, E. A., M. Malik, J. Ih, E. M.-R. Kempton, M. Mansfield, J. L. Bean, E. S. Kite, D. D. B. Koll, T. W. Cronin, and R. Hu (2022). The Detectability of Rocky Planet Surface and Atmosphere Composition with the JWST: The Case of LHS 3844b. *The Astronomical Journal 164*(6), 258.

Widemann, T., R. Ghail, C. F. Wilson, and D. V. Titov (2020). EnVision: Europe's Proposed Mission to Venus. In *AGU Fall Meeting Abstracts*, pp. P022–02.

Williams, J.-P., A. V. Pathare, and O. Aharonson (2014). The production of small primary craters on Mars and the Moon. *Icarus 235*, 23–36.

Williams, J.-P., C. H. van der Bogert, A. V. Pathare, G. G. Michael, M. R. Kirchoff, and H. Hiesinger (2017). Dating very young planetary surfaces from crater statistics: A review of issues and challenges. *Meteoritics & Planetary Science 53*, 554–582.

Willis, M. J., B. G. Herried, M. G. Bevis, and R. E. Bell (2015). Recharge of a subglacial lake by surface meltwater in northeast Greenland. *Nature 518*(7538), 223–227.

Wilson, S. A., A. D. Howard, J. M. Moore, and J. A. Grant (2016). A cold-wet middle-latitude environment on Mars during the Hesperian-Amazonian transition: Evidence from northern Arabia valleys and paleolakes: A Late, Cold, and Wet Climate on Mars. *Journal of Geophysical Research: Planets 121*(9), 1667–1694.

Wilson, S. A., A. M. Morgan, A. D. Howard, and J. A. Grant (2021). The Global Distribution of Craters With Alluvial Fans and Deltas on Mars. *Geophysical Research Letters 48*(4), e91653.

Wogan, N., J. Krissansen-Totton, and D. C. Catling (2020). Abundant Atmospheric Methane from Volcanism on Terrestrial Planets Is Unlikely and Strengthens the Case for Methane as a Biosignature. *Planetary Science Journal 1*(3), 58.

Wolf, E. T. (2017). Assessing the habitability of the TRAPPIST-1 system using a 3D climate model. *The Astrophysical Journal Letters 839*(1), L1.

Woodley, S. Z., F. E. Butcher, P. Fawdon, C. D. Clark, F. S. Ng, J. M. Davis, and C. Gallagher (2022). Multiple sites of recent wet-based glaciation identified from eskers in western Tempe Terra, Mars. *Icarus 386*, 115147.

Wordsworth, R., F. Forget, E. Millour, J. Head, J.-B. Madeleine, and B. Charnay (2013). Global modelling of the early Martian climate under a denser CO_2 atmosphere: Water cycle and ice evolution. *Icarus 222*(1), 1–19.

Wordsworth, R., Y. Kalugina, S. Lokshtanov, A. Vigasin, B. Ehlmann, J. Head, C. Sanders, and H. Wang (2017). Transient reducing greenhouse warming on early Mars. *Geophysical Research Letters 44(2)*, 665–671.

Wordsworth, R., A. H. Knoll, J. Hurowitz, M. Baum, B. L. Ehlmann, J. W. Head, and K. Steakley (2021). A coupled model of episodic warming, oxidation and geochemical transitions on early Mars. *Nature Geoscience 14*(3), 127–132.

Wordsworth, R. D. (2016). The climate of early Mars. *Annual Review of Earth and Planetary Sciences 44*, 381–408.

Wordsworth, R. D., L. Kerber, R. T. Pierrehumbert, F. Forget, and J. W. Head (2015). Comparison of "warm and wet" and "cold and icy" scenarios for early Mars in a 3-D climate model. *Journal of Geophysical Research: Planets 120*(6), 1201–1219.

Wordsworth, R. D. and R. T. Pierrehumbert (2013). Water loss from terrestrial planets with CO_2-rich atmospheres. *Astrophysical Journal 778*(2), 154.

Worni, R., M. Stoffel, C. Huggel, C. Volz, A. Casteller, and B. Luckman (2012). Analysis and dynamic modeling of a moraine failure and glacier lake outburst flood at Ventisquero Negro, Patagonian Andes (Argentina). *Journal of Hydrology 444*, 134–145.

Wray, J. J., S. L. Murchie, J. L. Bishop, B. L. Ehlmann, R. E. Milliken, M. B. Wilhelm, K. D. Seelos, and M. Chojnacki (2016). Orbital evidence for more widespread carbonate-bearing rocks on Mars. *Journal of Geophysical Research: Planets 121*(4), 652–677.

Yang, J., G. Boué, D. C. Fabrycky, and D. S. Abbot (2014). Strong dependence of the inner edge of the habitable zone on planetary rotation rate. *Astrophysical Journal 787*(1), L2.

Yang, J., N. B. Cowan, and D. S. Abbot (2013). Stabilizing cloud feedback dramatically expands the habitable zone of tidally locked planets. *The Astrophysical Journal Letters 771*(2), L45.

Zahnle, K., N. Arndt, C. Cockell, A. Halliday, E. Nisbet, F. Selsis, and N. H. Sleep (2007). Emergence of a habitable planet. *Space Science Reviews 129*(1), 35–78.

Zahnle, K., R. M. Haberle, D. C. Catling, and J. F. Kasting (2008). Photochemical instability of the ancient Martian atmosphere. *Journal of Geophysical Research: Planets 113*(E11).

Zahnle, K. J. and D. C. Catling (2017). The Cosmic Shoreline: The Evidence that Escape Determines which Planets Have Atmospheres, and what this May Mean for Proxima Centauri B. *Astrophysical Journal 843*(2), 122.

Zahnle, K. J. and J. F. Kasting (1986). Mass fractionation during transonic escape and implications for loss of water from Mars and Venus. *Icarus 68*(3), 462–480.

Zhan, Z., S. Seager, J. J. Petkowski, C. Sousa-Silva, S. Ranjan, J. Huang, and W. Bains (2021). Assessment of isoprene as a possible biosignature gas in exoplanets with anoxic atmospheres. *Astrobiology 21*(7), 765–792.

Zolotov, M. Y., B. Fegley Jr, and K. Lodders (1997). Hydrous silicates and water on Venus. *Icarus 130*(2), 475–494.

APPENDIX A

SUPPLEMENTARY INFORMATION FOR CHAPTER 2

A.1 Fitting Procedure

To find our upper limits on atmospheric pressure from measured CSFDs, we used a Bayesian fitting method and treated impacts as a Poisson process (Kite et al., 2014; Aharonson et al., 2003). We fit our data to modelled crater densities at 8 different atmospheric pressures from 7 mbar to 5.5 bar. For each 1 m crater diameter bin, we evaluated the probability of seeing the number of observed craters (Y) measured from our HiRISE images, anaglyphs, and DTMs using Poisson statistics:

$$p(Y \| D,\ P) = \bar{\lambda}^{Y} \frac{\exp\left(-\bar{\lambda}^{Y}\right)}{Y!} \tag{A.1}$$

where $\bar{\lambda} = p(D, P)$ is the distribution of crater densities (D) as a function of atmospheric pressure (P) scaled to the overall number of impacts observed for a fixed impactor frequency. To find the likelihood of our observed data given our atmosphere-impactor interaction model, we summed the logarithms of the probabilities of seeing the number of craters from our CSFDs in each diameter bin.

We used the bootstrapping procedure of Kite et al. (2014) to calculate the best fit paleopressure upper estimates and the 2σ error bars shown in Fig. 5.

A.2 Synthetic time-varying, modified cumulative size frequency distributions

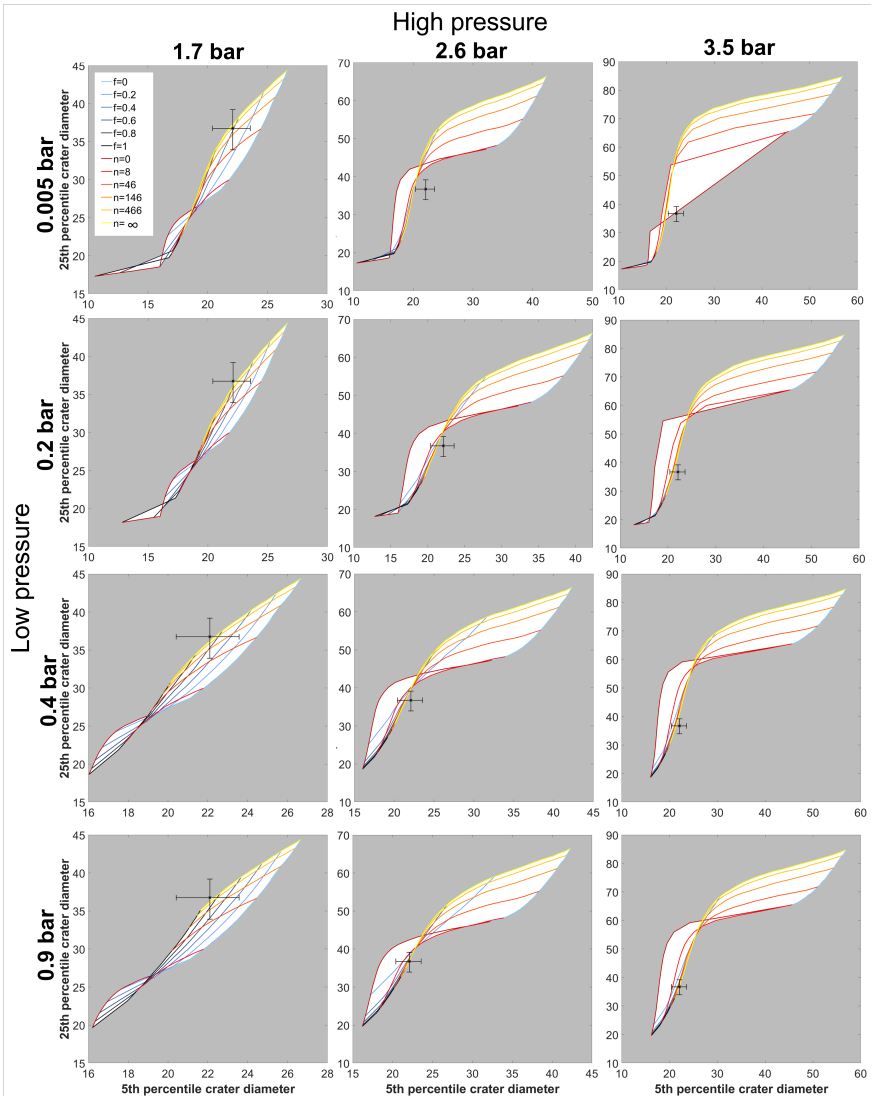

Figure A.1: Contours of 5th and 25th crater diameter for different fractions of time spent at low pressure (f, cool colours) and different degrees of modification by preferential obliteration of small craters (n, warm colors, n = large — greater small crater removal). Black crosses with error bars are the measured 5th and 25th crater diameter for the Mawrth phyllosilicates plotted on the same axes. Error bars indicate mean fractional difference between best-fit crater diameter and maximum and minimum crater diameters found using `circfit`. Grey indicates regions of parameter space for which it is not possible to reproduce 5th and 25th percentile diameters.

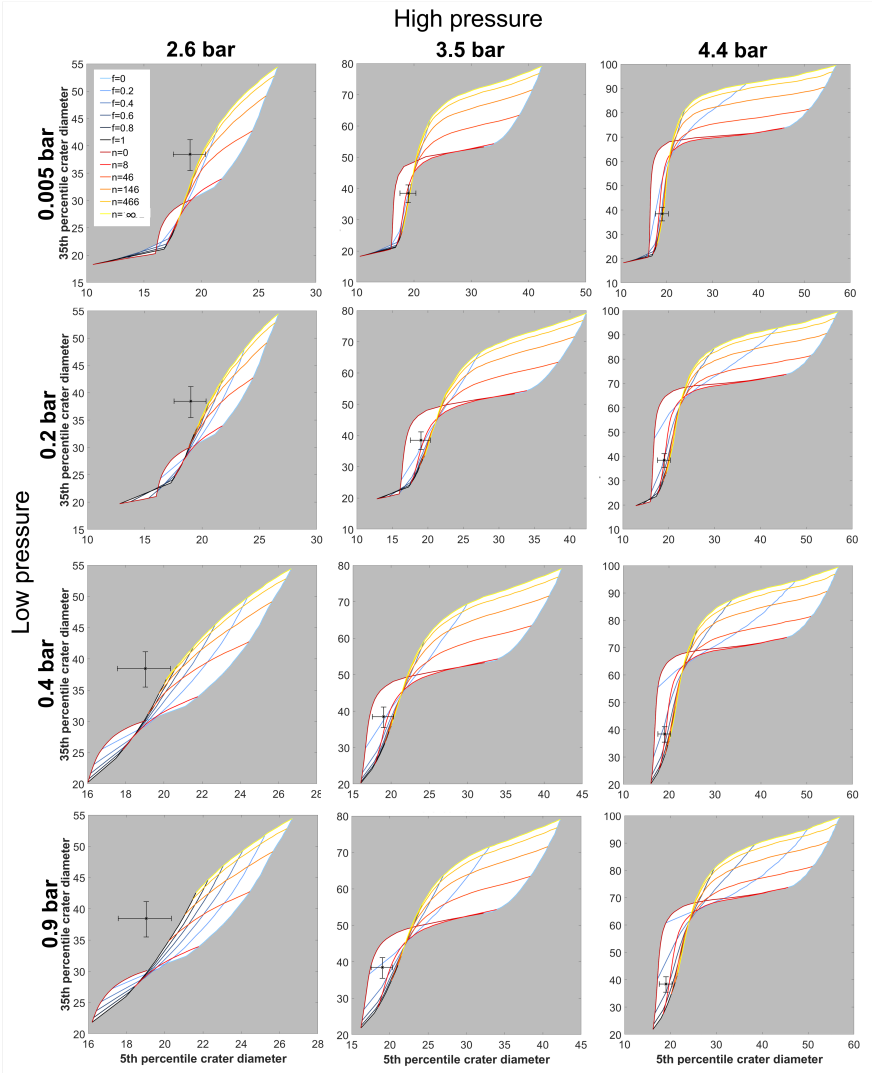

Figure A.2: Contours of 5th and 35th crater diameter for different fractions of time spent at low pressure (f, cool colours) and different degrees of modification by preferential obliteration of small craters (n, warm colors, n = large — greater small crater removal). Black crosses with error bars are the measured 5th and 25th crater diameter for the Meridiani deposits plotted on the same axes. Error bars indicate mean fractional difference between best-fit crater diameter and maximum and minimum crater diameters found using `circfit`. Grey indicates regions of parameter space for which it is not possible to reproduce 5th and 35th percentile diameters.

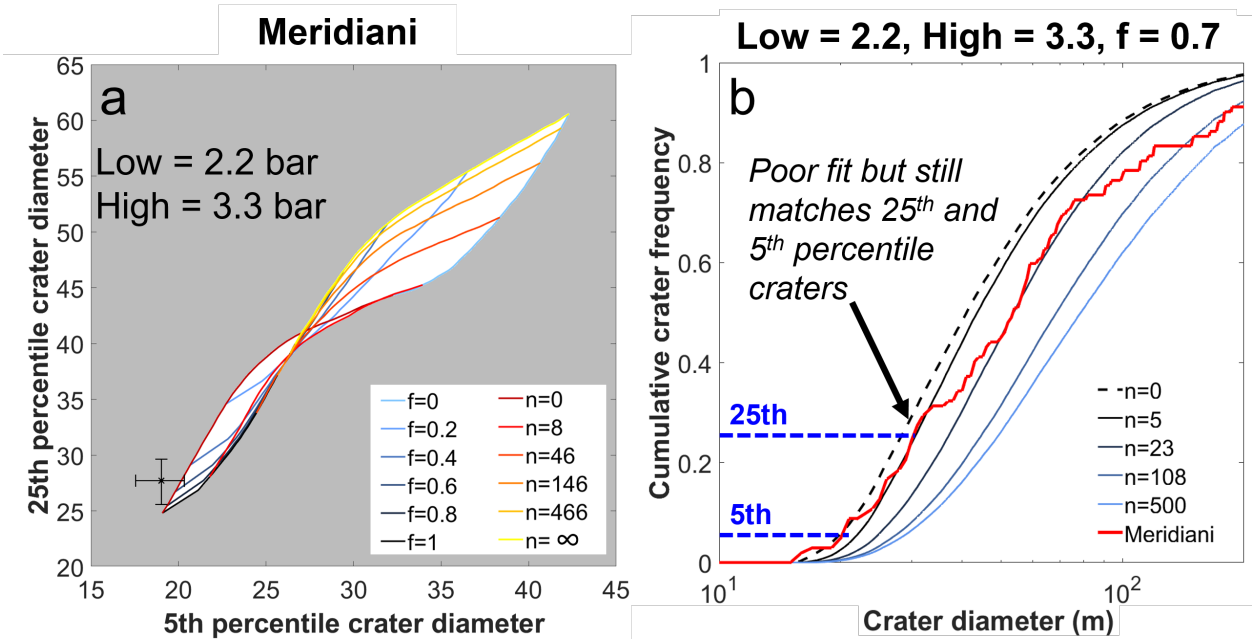

Figure A.3: a) Contours of 5th and 35th crater diameter for different fractions of time spent at low pressure (f, cool colours) and different degrees of modification by preferential obliteration of small craters (n, warm colors, n = large — greater small crater removal) for Meridiani data for an atmosphere alternating between zero-elevation-corrected pressures of 3.3 and 2.2 bar. Greyed out areas indicate regions of parameter space that cannot reproduce the measured CSFD. b) Comparison of measured Meridiani CSFD with region of allowed parameter space overlapped by error bars on diameter measurement showing that although 5th and 25th percentile crater diameters come close to f=0.8, n=0 curve, the overall fit of the synthetic, modified, time-varying CSFDs to the measured CSFD is poor. This is due to the stepwise nature of the small end of the Meridiani CSFD. Therefore, we chose to compare the 5th and 35th percentile crater diameters to reduce the impact of this effect.

APPENDIX B

SUPPLEMENTARY INFORMATION FOR CHAPTER 3

B.1 Justification of Model Assumptions

In our model derivation, we assume that pressure gradients in the flow diffuse on a shorter timescale than that of downwards erosion of the outflow valley (uniform flow), and that the timescales for the valley to erode by one grain diameter is smaller than the timescale for variations in flow depth (quasi-steady flow). The uniform flow assumption is justified because we assume that valley geometry does not change with downstream length. However, we can also demonstrate that these assumptions are justified by considering the relevant timescale for transport stage evolution. Eq. can be re-written in terms of T:

$$\frac{3}{2}\frac{Rd\tau_{*c}}{S}\frac{dT}{dt} = \frac{4Q_{in}}{\pi D^2} - \frac{32w_c g^{1/2}R^{5/3}d^{3/2}\tau_{*c}^{5/3}}{\pi D^2 S^{7/6}}T^{5/3} + \frac{8w_c}{w_v L}\sqrt{Rgd^3\tau_{*c}^3}(T-1)^{3/2} \tag{B.1}$$

This can be further re-written as:

$$\frac{3}{16}\frac{w_v L}{w_c}\sqrt{\frac{R}{gd\tau_{*c}}}\frac{dT}{dt} = \frac{w_v L}{2\pi D^2 w_c\sqrt{Rgd^3\tau_{*c}^3}} - \frac{4w_v L}{\pi D^2}\left(\frac{R}{S}\right)^{7/6}\tau_{*c}^{1/6}T^{5/3} + (T-1)^{3/2} \tag{B.2}$$

Where:

$$\frac{t}{t_*} = \frac{3}{16}\frac{w_v L}{w_c}\sqrt{\frac{R}{gd\tau_{*c}}} \tag{B.3}$$

Is the characteristic timescale for transport stage variation and t_* is dimensionless time. We can compare this to the characteristic timescale for a shallow-water gravity wave to travel up the valley:

$$t_w = \frac{L}{gH} \tag{B.4}$$

In our model, $\tau_{*c} < 1$, $S < 1$, and $H \geq d$, therefore the characteristic timescale for transport stage variation is much longer than the timescale for a pressure gradient to diffuse up the valley. This further justifies the uniform flow assumption.

To justify the quasi-steady assumption, we can consider the timescale t_d for erosion of the channel bed by one grain diameter d:

$$\frac{dB}{dt} \approx \frac{d}{t_d} \tag{B.5}$$

$$t_d = \frac{w_v L}{8 w_c \sqrt{Rgd\tau_{*c}}} \frac{1}{(T-1)^{3/2}} \tag{B.6}$$

Therefore, for all values of T where $T > \left(\frac{R}{S}\right)^{2/3} - 1$ ($T > 4$ for a typical tadpole crater slope), the quasi-steady flow assumption holds because the channel erodes on a shorter timescale than the transport stage changes, i.e., the transport stage remains approximately the same over the characteristic timescale for changes to the channel bed to occur. As T approaches 1, t_d approaches infinity, which violates the quasi-steady flow assumption because transport stage changes will outpace channel erosion. However, most erosion occurs shortly after breach erosion while T is high, where the quasi-steady flow assumption is valid, so we do not expect this assumption to strongly affect our results.

B.2 Supplementary Tables

Table B.1: Compilation of potential tadpole crater terrestrial analogue data.

Event Name	D (km)	L (km)	w_v (m)	S_{min}	S_{max}	z (m)	Reference
Nostetuko, Canada	2.5	2.5	100	0.19	0.83	40	Clague and Evans (2000)
Queen Bess, Canada	2.8	0.3	75	0.19	0.83	15	Clague and Evans (2000)
Tats Lake, Canada	0.113	0.5	25	0.19	0.83	9	Clague and Evans (2000)
Pinatubo, Philippines	0.95	2	60	0.2	0.5	23	Lagmay et al. (2007)
Paulina Creek, United States	2.8	2.8	30	0.017	0.13	4.6	Chitwood and Jensen (2000)
Ram Creek, New Zealand	0.35	0.5	30	0.26	0.36	40	Nash et al. (2008)
Bairaman, Papua New Guinea	3	2	400	0.2	0.3	70	King et al. (1989)
El Chichon, Mexico	1.4	1	50	0.03	0.42	30	Macías et al. (2004)
Khumbu Humal, Nepal	0.8	0.3	200	0.47	0.58	60	Vuichard and Zimmermann (1987)
La Josephina, Ecuador	1.9	1.9	200	0.25	0.45	40	Plaza et al. (2011)
Poerua River, New Zealand	0.7	0.4	150	0.18	0.44	45	Hancox et al. (2005)
Ventisquero Negro, Argentina	0.7	0.35	70	0.1	0.84	27	Worni et al. (2012)
Tam Pokhari, Nepal	0.68	0.68	60	0.2	0.6	50	Osti and Egashira (2009)

APPENDIX C

SUPPLEMENTARY INFORMATION FOR CHAPTER 4

C.1 Groundwater Model Output

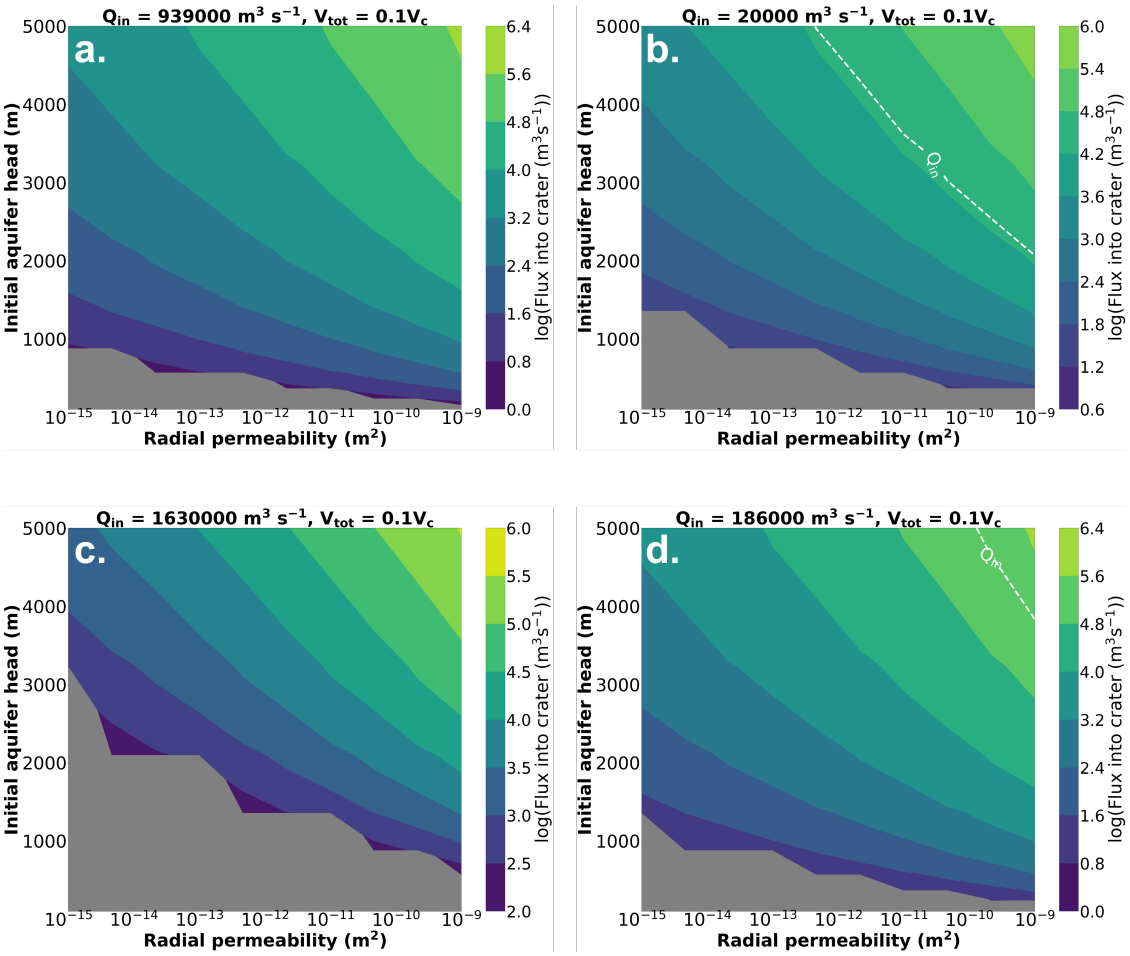

Figure C.1: Groundwater flux into each multiple exit breach tadpole crater as a function of radial permeability and initial aquifer head when 0.1 crater volumes of water have been discharged from the aquifer. **a.** *Arabia Terra 1*, **b.** *Arabia Terra 2*, **c.** *Hellas*, **d.** *Noachis*. Dashed white lines indicate the water supply rate necessary to overspill all breaches simultaneously (Table 4.3). There is no dashed line on a because the required input flux is not reached in our model. Grey shaded areas indicate negligible groundwater flow into the crater.

C.2 Pond Overspill Model Output

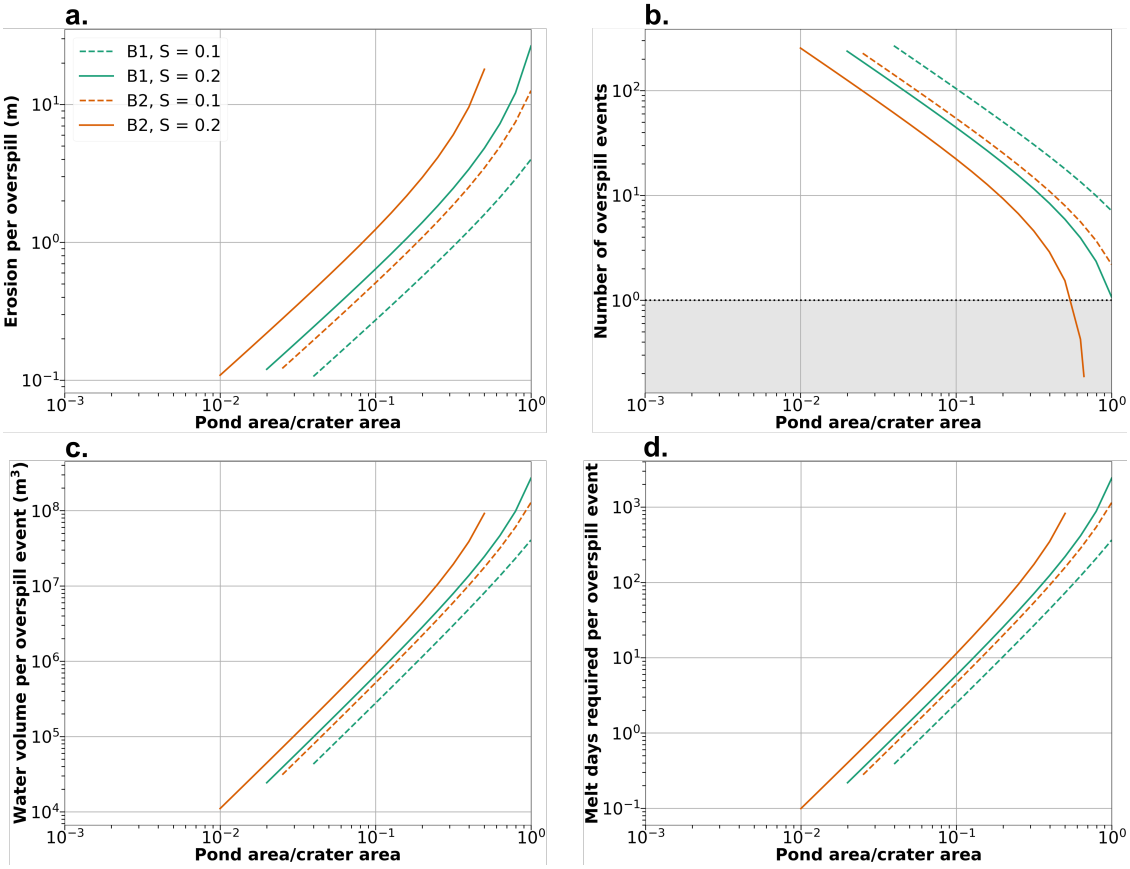

Figure C.2: Meltwater pond overspill modelling results for *Arabia Terra 1* B1 and B2 (Fig. 4.1a) for measured breach parameters in Table 4.2 as a function of fractional melt pond area. S is slope. **a.** Downward erosion of breach base per individual overspilling event. Smaller melt pond areas generate less erosion when they overspill the rim. **b.** The number of overspill events required to carve each observed breach. The number of breaches required decreases as melt pond area increases. **d.** Total water volume required per overspill event in **b**. **d.** Melt days required to generate the water volumes required in **c.** at a melt rate of 4 m yr^{-1} m^2 (Kite et al., 2013) across the entire crater area.

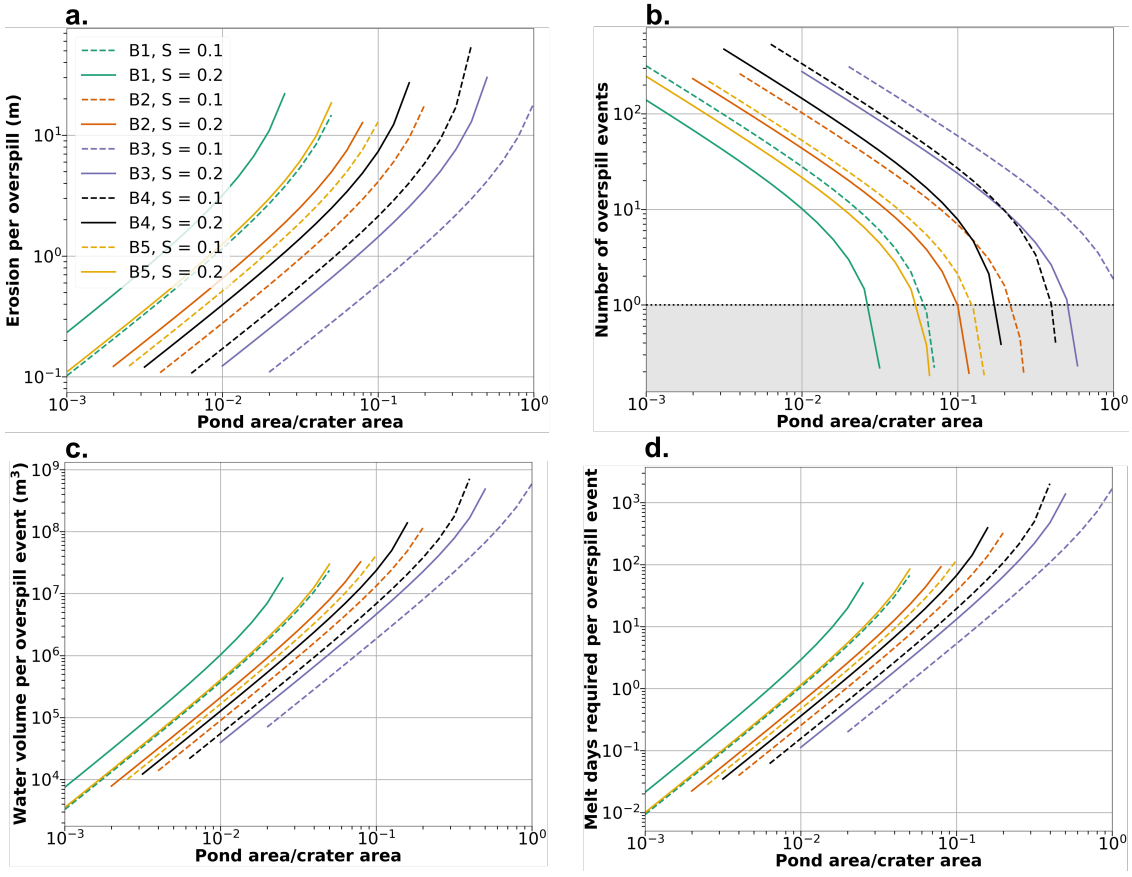

Figure C.3: Meltwater pond overspill modelling results for *Arabia Terra 2* B1, B2, B3, B4, and B5 (Fig. 4.1b) for measured breach parameters in Table 4.2 as a function of fractional melt pond area. S is slope. **a.** Downward erosion of breach base per individual overspilling event. Smaller melt pond areas generate less erosion when they overspill the rim. **b.** The number of overspill events required to carve each observed breach. The number of breaches required decreases as melt pond area increases. **d.** Total water volume required per overspill event in **b**. **d.** Melt days required to generate the water volumes required in **c.** at a melt rate of 4 m yr^{-1} m^2 (Kite et al., 2013) across the entire crater area.

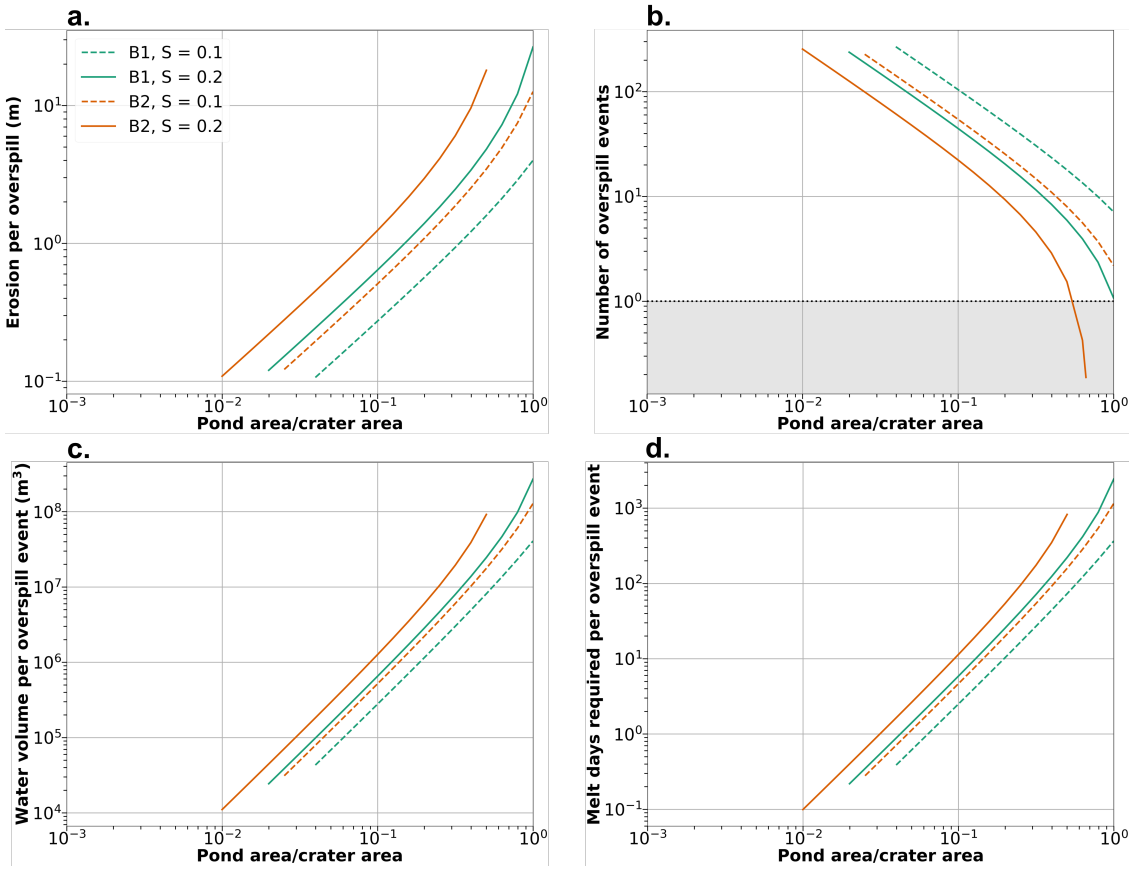

Figure C.4: Meltwater pond overspill modelling results for *Hellas* B1 and B2 (Fig. 4.1c) for measured breach parameters in Table 4.2 as a function of fractional melt pond area. S is slope. **a.** Downward erosion of breach base per individual overspilling event. Smaller melt pond areas generate less erosion when they overspill the rim. **b.** The number of overspill events required to carve each observed breach. The number of breaches required decreases as melt pond area increases. **d.** Total water volume required per overspill event in **b**. **d.** Melt days required to generate the water volumes required in **c.** at a melt rate of 4 m yr^{-1} m^2 (Kite et al., 2013) across the entire crater area.

APPENDIX D

SUPPLEMENTARY INFORMATION FOR CHAPTER 5

D.1 Oxygen loss model

D.1.1 Crustal production upper limit

For an Earth-like internal heating rate and a 500 K temperature drop between the melting region and the surface the maximum crustal production rate is ∼175 km^3 yr^{-1}(Armann and Tackley, 2012). Volcanism at this rate over 4 Gyr would produce ∼1500 km of crust (not accounting for changing heating rate over time or mantle cooling), implying substantial crustal recycling, and eruption of 80% of Venus' mantle. For a melt fraction of 15%, at the upper end of terrestrial Mid Ocean Ridge melting, this crustal production rate would imply melt processing of Venus' mantle volume 5 times. Crustal recycling may aid Venus in retaining its water (Elkins-Tanton et al., 2007). Parameterized stagnant lid convection models constrained by ^{40}Ar measurements suggest total crustal production of a global layer <65 km, and melt processing of up to 1.2 Venus mantle volumes (O'Rourke and Korenaga, 2015). However, 2D simulations (Armann and Tackley, 2012) of Venus' thermal evolution including episodic lid convection are able to produce up to 1.2 mantle volumes of crust over Venus' lifetime (implying crustal recycling).

D.1.2 Runaway Greenhouse Surface Temperature

We find surface temperature at each timestep, given the incoming solar flux relative to Earth's insolation (S_{eff}) and partial pressure of H_2O in the atmosphere in bars (p_{H_2O}), using a curve fit to existing numerical results (Turbet et al., 2020):

$$log_{10}\left(T_{surf}(x,y,z)\right) = c_1 + c_2x + c_3y + c_4z + c_5x^2 + c_6xy + c_8z^2 + c_9y^3 + c_{10}z^3 \quad \text{(D.1)}$$

Coefficient	Value	Coefficient	Value
c_1	3.401 $\times 10^{0}$	k_1	2.668
c_2	1.501 $\times 10^{-1}$	k_2	1.019
c_3	-3.401 $\times 10^{-2}$	k_3	1.099
c_4	4.702 $\times 10^{-2}$	k_4	0.4683
c_5	-4.911 $\times 10^{-3}$	k_5	0.7664
c_6	8.519 $\times 10^{-1}$	k_6	0.4224
c_7	-1.467 $\times 10^{-2}$		
c_8	-7.091 $\times 10^{-3}$		
c_9	-7.627 $\times 10^{-3}$		
c_{10}	8.348 $\times 10^{-3}$		

Table D.1: Coefficient values used in calculation of surface temperature as a function of effective stellar luminosity and partial pressure of water in the atmosphere (Turbet et al., 2020).

where:

$$x = \left(log_{10}\left(P_{\mathrm{H_2O}}\right) - k_1\right)/k_2 \tag{D.2}$$

$$y = \left(log_{10}\left(g\right) - k_3\right)/k_4 \tag{D.3}$$

$$z = \left(log_{10}\left(S_{eff}\right) - k_5\right)/k_6 \tag{D.4}$$

Coefficient values for c_{1-10} and k_{1-6} are given in Table D.1.

D.1.3 Drag of Heavy Species During H Escape

If H escape to space is sufficiently rapid, the H can drag heavier species (such as O) along with it (Tian, 2015b). To determine whether this process is active at a given timestep in our model, we calculate the critical mass (m_c) of the heaviest molecule escaping H can drag along with it in a background atmosphere of mass m_{atm} (Tian, 2015b):

$$m_c = \frac{X_H + q^2 X_{atm}}{X_H + q X_{atm}} m_H + \frac{kT\dot{M}_{H,ref}}{m_H b g \left(X_H + q X_{atm}\right)} \tag{D.5}$$

where $q = m_{atm}/m_H$. In our model runs, we only see $m_c \geq m_O$ at the very beginning of models with $>$ 700 m GEL H_2O with hypothetical habitable eras ending at 4 Ga and $f_{volc} \geq 0.9$, i.e. H escape is not limited by diffusion through the background CO_2 atmosphere. Under these conditions there is more than an order of magnitude more O in the background atmosphere than CO_2, and we approximate the atmosphere as a mixture of H and O only to find the resulting H and O escape rates (Tian, 2015b):

$$\dot{M}_{O,esc} = \frac{\eta q}{1 + \eta q} \dot{M}_{H,ref} \tag{D.6}$$

$$\dot{M}_{H,esc} = \frac{1}{1 + \eta q} \dot{M}_{H,ref} \tag{D.7}$$

where:

$$\eta = \frac{Y - 1}{Y X_H / X_O + q} \tag{D.8}$$

$$Y = \frac{kT\dot{M}_{H,ref}}{(q-1) b g X_H m_H^2} \tag{D.9}$$

D.1.4 Explosive Volcanism

Although high atmospheric pressure disfavors explosive volcanism on Venus today, dissolved magmatic volatiles drive explosive volcanism at pressures greater than Venus' atmospheric pressure in subaqueous envrionments, such as MORs (Helo et al., 2011; Schipper et al., 2010). Several authors report observations of evidence for explosive volcanism on Venus, invoking volatile concentrations of order 1-3 wt% CO_2, SO_2 and H_2O (Ghail and Wilson, 2015;

Campbell et al., 2017). However, CO_2 as the primary magmatic volatile phase is unlikely to drive explosive volcanism on present day Venus because concentrations above 6.5 wt% would be required (Airey et al., 2015). The conditions required for explosive volcanism are sensitive not only to atmospheric pressure but also to melt ascent rates, magma temperatures, melt viscosity, and vent geometry (Airey et al., 2015; Glaze et al., 2011). We choose to implement the simplest possible threshold for the effusive-explosive transition, allowing explosive volcanism to occur when the volume fraction of gas (F_{gas}) exceeds ~75% (Sparks, 1978; Garvin et al., 1982). We find the volume of gas per m^3 melt delivered to the surface (V_{gas}) using the ideal gas law:

$$V_{gas} = \frac{n_{degas} R T_{melt}}{P_{atm}} \tag{D.10}$$

where n_{degas} is the number of moles of degassed CO_2 and H_2O. The corresponding volume fraction of gas is:

$$F_{gas} = \frac{V_{gas}}{V_{gas} + 1} \tag{D.11}$$

For $F_{gas} \geq 0.75$, the mass of O_2 removed from the atmosphere in a given timestep ($\dot{M}_{O_2,ox}$) is:

$$\dot{M}_{O2,ox} = M_{O2,atm} - m_{\mathrm{O2}} \frac{0.25 \rho c_{\mathrm{FeO}} f_{ex} z_{erupt}(t)}{m_{\mathrm{FeO}}} \tag{D.12}$$

D.2 Supplementary Figures

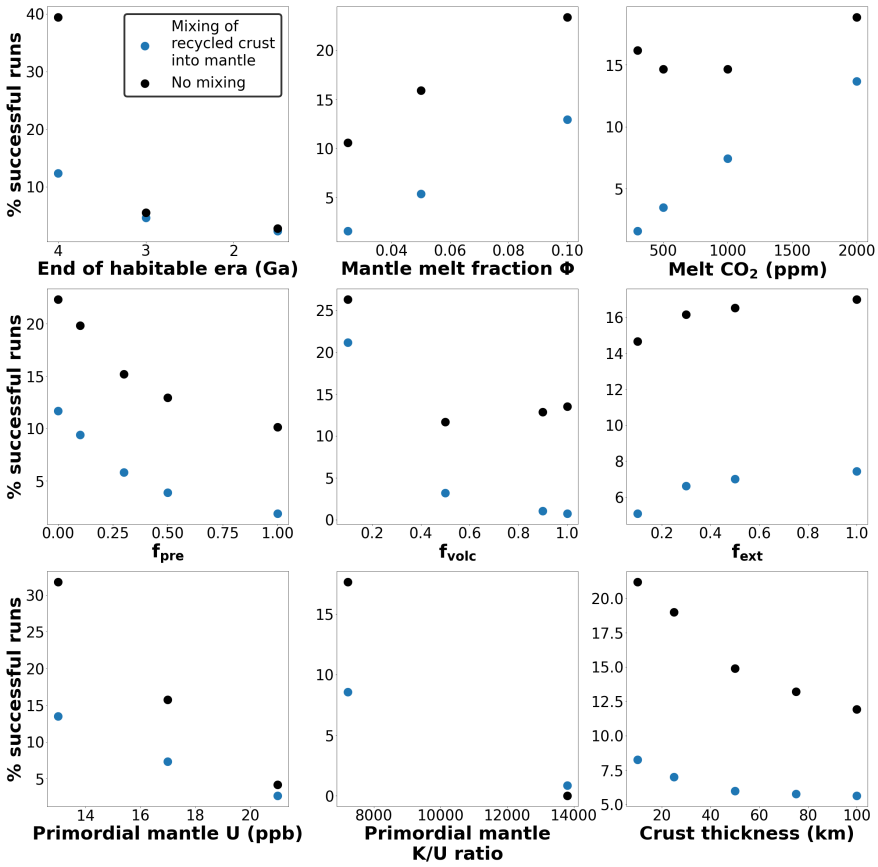

Figure D.1: Summary of ^{40}Ar degassing model results shown as the percentage of ^{40}Ar evolution models (e.g. Fig. 5.7) that contribute less than $1.61 \pm 0.54 \times 10^{16}$ kg ^{40}Ar (Kaula, 1999) to Venus' atmosphere over the course of Venus' post-habitable era evolution. The most favorable parameters for successful Ar degassing model runs are anticorrelated with parameters that reconcile a hypothetical early habitable era with Venus' modern atmospheric O_2. ^{40}Ar degassing models where ^{40}K crust is not re-mixed into the mantle after recycling at the base of the crust permit a wider range of parameter space to be compatible with modern ^{40}Ar in Venus' atmosphere. Blue circles correspond to results of 57,000 models where material recycled from the base of the crust is mixed uniformly throughout the mantle. Black circles correspond to results of 57,000 models where recycled crust becomes part of a separate mantle reservoir and does not alter the ^{40}K concentration of the mantle from which new crust is derived. f_{pre} is the fraction of mantle ^{40}Ar produced from the formation of Venus until the end of the hypothetical habitable era that is assumed to have already degassed and remained in the atmosphere. Melt CO_2 concentration, fraction of Venus' present day atmosphere contributed by post-habitable era volcanic degassing (f_{volc}), and extrusive volcanism fraction (f_{ext}) have the same values as in the O_2 loss models. Table 5.2 lists all model variables and their values.

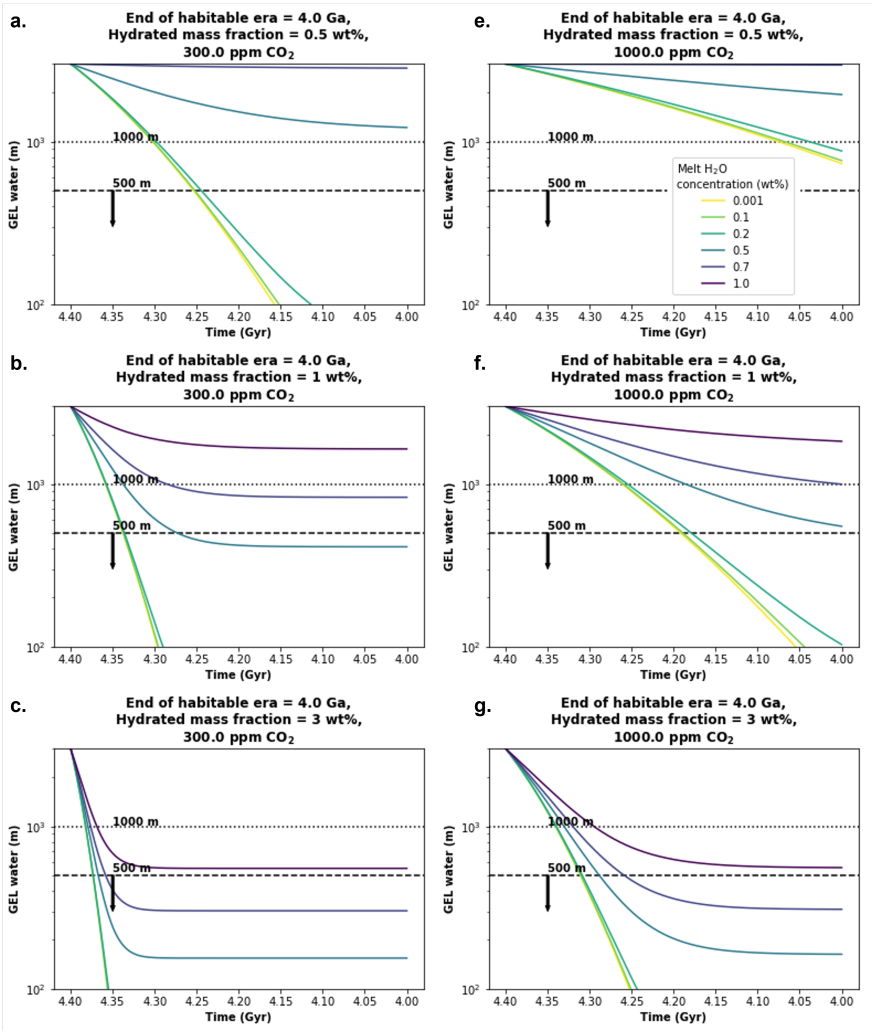

Figure D.2: Example evolutions of habitable era water inventory in km GEL for a habitable era starting with 4000 m water on the surface, with a constant atmospheric CO_2 pressure of 1 bar, for a range of H_2O mass fractions in hydrated crust (a & d. 0.5 wt%; b & e. 1 wt%; c & f. 3 wt%) and melt CO_2 concentrations (a,b, & c. 300 ppm; d, e & f. 1000 ppm). Dashed lines indicate upper limits on end-habitable-era surface water inventory from O_2 loss and ^{40}Ar degassing models (500 m–black dashed, 1000 m–black dotted for very reduced melt oxygen fugacities). The final size of the surface liquid water inventory must fall below these lines by the end of the habitable era at 4.0 Ga to be consistent with Venus' modern atmospheric composition.

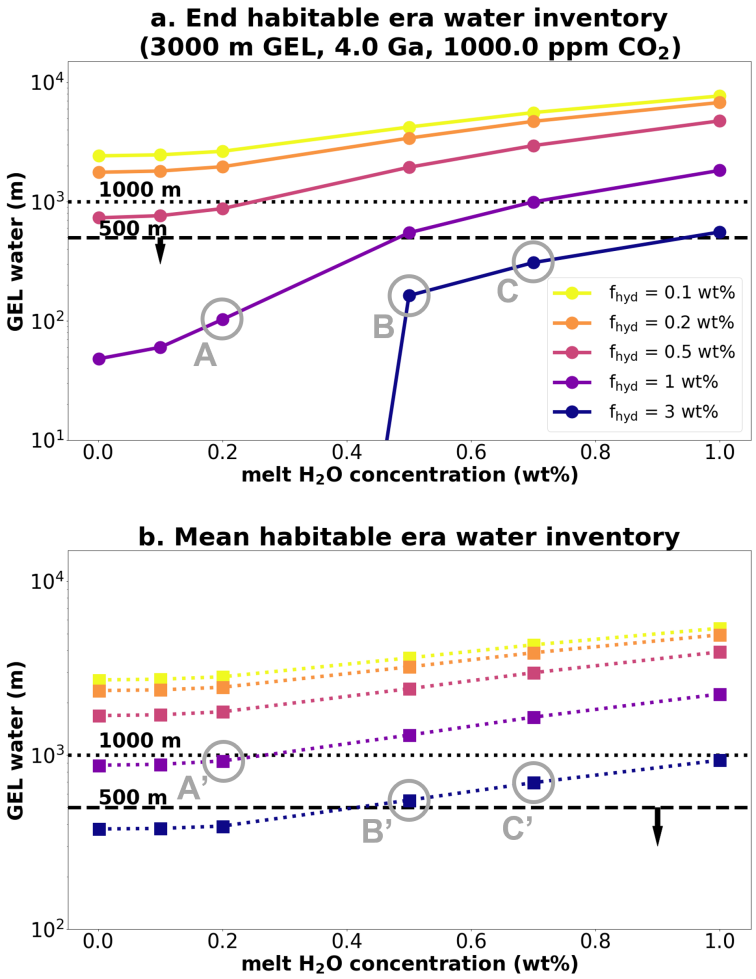

Figure D.3: Although the final surface water inventory at the end of the habitable era must be less than 500 m GEL (or 1000 m GEL for a very reducing melt oxygen fugacity), recycling of water into the mantle during the habitable era can lead to an average surface water inventory larger than these upper limits. Example runs that meet these conditions are shown by the circled points A (Panel a.) and A' (Panel b.), B (Panel a.) and B' (Panel b.), C (Panel a.) and C' (Panel b.). a. Final size of the habitable era water inventory after evolution of the surface water inventory in km GEL. Horizontal dashed line indicates upper limit on end-habitable-era surface water inventory from O_2 loss and ^{40}Ar models. The final size of the surface liquid water inventory must fall below these lines to be consistent with Venus' modern atmospheric composition based on our O_2 loss model. b. Time-averaged size of the habitable era water inventory during the same habitable era. Horizontal black line is the same as for a., but the average water inventory does not need to fall beneath these lines to be consistent with oxygen and ^{40}Ar in Venus' modern atmosphere.

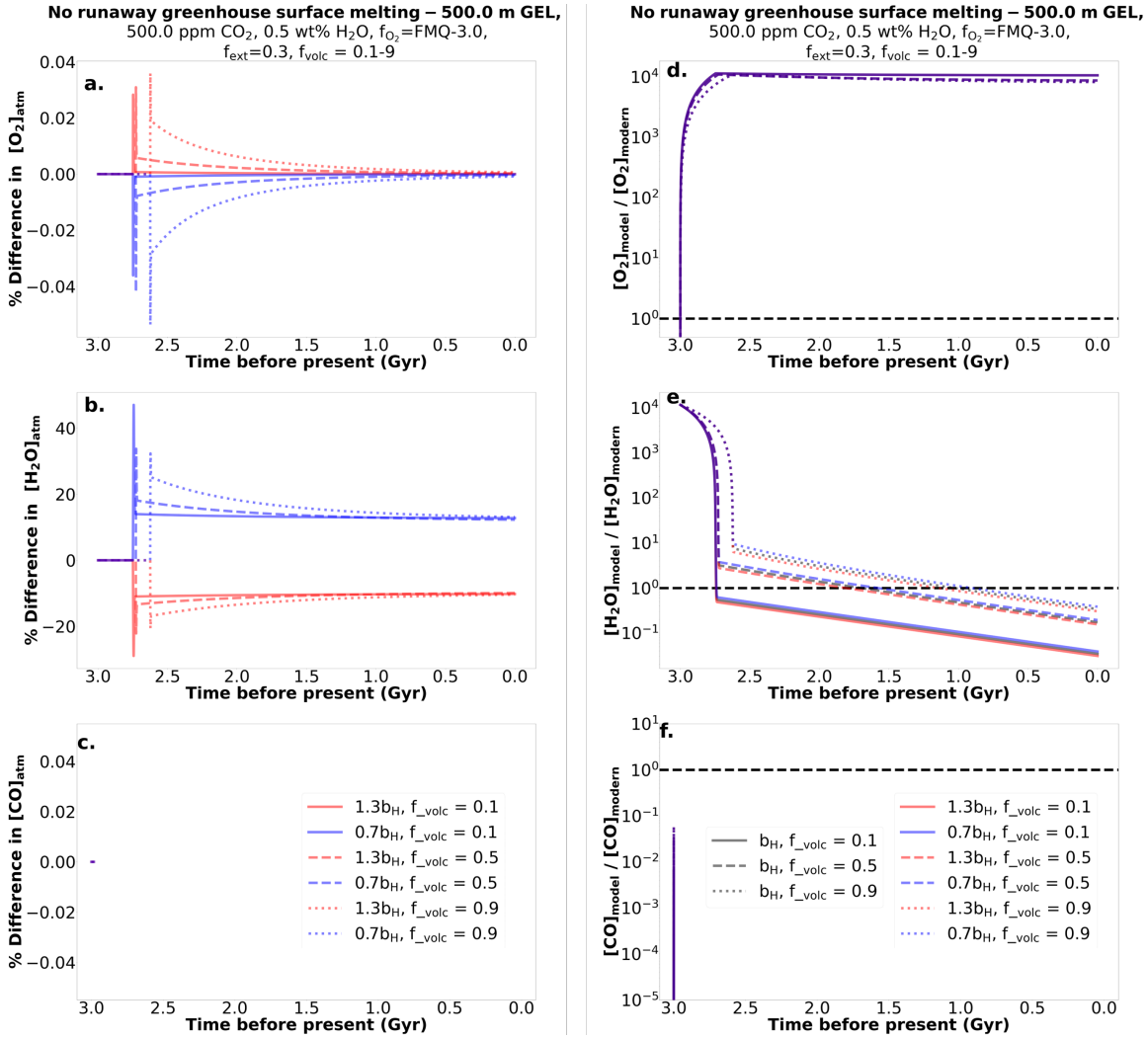

Figure D.4: Example sensitivity tests with values of binary diffusion coefficient of hydrogen through the background atmosphere (b_H) 30% lower ($0.7b_H$, blue) and 30% higher ($1.3b_H$, red) than our baseline model (black, shown in d, e, and f). Colors are transparent and curves appear purple where $0.7b_H$, baseline b_H, and $1.3b_H$ results overlap. We set 500m GEL end habitable era water inventory, 500 ppm melt CO_2, 0.5 wt% melt H_2O, f_{ext} = 0.3, $\log fO_2$ =FMQ-3, and a f_{volc} = ranging from 0.1 to 0.9 (indicated by solid, dotted, and dashed lines). a-c show the percent difference in the atmospheric concentration of O_2, H_2O, and CO relative to the baseline b_H used in our O_2 loss model. CO curves are absent where the atmospheric CO concentration in the baseline model is 0. Initial, short-lived spikes in CO concentration are due to CO degassing prior to O_2 accumulation due to H escape to space. d-f show the atmospheric concentration of each species in the model divided by the maximum atmospheric concentration as constrained by modern Venus measurements. The horizontal dashed black line indicates where atmospheric concentration exactly matches the relevant modern constraint–curves that end below this line are deemed "successful" in our model. ±30% variations in b_H do not affect whether a given model run is successful for any parameter combination.

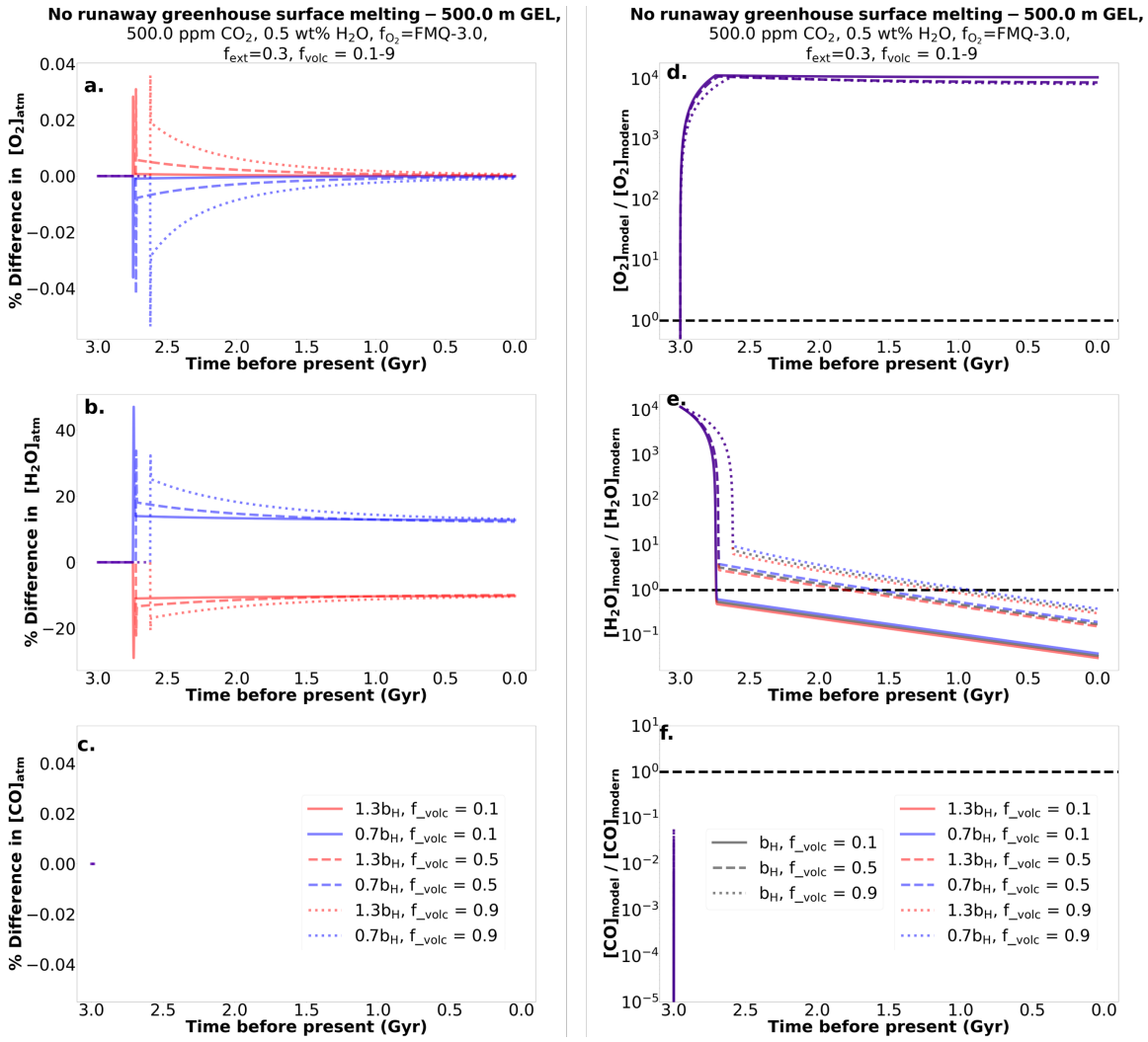

Figure D.5: Example sensitivity tests with values of T_{atm} = 170 K and 215 K compared with our baseline model that uses T_{atm} = 215 K (black, shown in d, e, and f). Colors are transparent and curves appear purple where 170 K, baseline, and 215 K results overlap. We set 500m GEL end habitable era water inventory, 500 ppm melt CO_2, 0.5 wt% melt H_2O, f_{ext} = 0.3, $\log fO_2$ =FMQ-3, and a f_{volc} = ranging from 0.1 to 1.0 (indicated by solid, dotted, dashed lines, and dashed-dotted lines). a-c show the percent difference in the atmospheric concentration of O_2, H_2O, and CO relative to the baseline b_H used in our O_2 loss model. CO curves are absent where the atmospheric CO concentration in the baseline model is 0. Initial, short-lived spikes in CO concentration are due to CO degassing prior to O_2 accumulation due to H escape to space. d-f show the atmospheric concentration of each species in the model divided by the maximum atmospheric concentration as constrained by modern Venus measurements. The horizontal dashed black line indicates where atmospheric concentration exactly matches the relevant modern constraint–curves that end below this line are deemed "successful" in our model. These variations in T_{atm} do not affect whether a given model run is successful for any parameter combination.